Electrochemical studies of the automotive lubricant additive zinc n-dibutyldithiophosphate

Sarah R. Jacob
Physical and Theoretical Chemistry Laboratory
University of Oxford

Hilary 1998

Sarah Jacob
Christ Church

Doctor of Philosophy
Hilary 1998

Electrochemical studies of the automotive lubricant additive zinc n-dibutyldithiophosphate

Abstract

Zinc dialkyldithiophosphates (ZDTPs) are widely incorporated in lubricant formulations as anti-oxidant and anti-wear additives. Recent years have seen the emergence of considerable research aimed at defining the mode of action of these compounds. Despite this, the mechanistic action of ZDTPs in their capacity as both anti-wear and anti-oxidant agents remains ill defined. Previous investigations have used a wide variety of techniques, however, electrochemical methods have been poorly exploited.

This thesis describes application of electrochemical techniques to the study of zinc n-dibutyldithiophosphate (Bu^n-ZDTP) in an investigation of the value of such methods as a tool for ZDTP analysis. A comprehensive study of Bu^n-ZDTP redox activity under standard electrochemical conditions has been implemented. Using cyclic voltammetry, Bu^n-ZDTP has been shown to be oxidised in an irreversible 2 electron transfer process. The diffusion co-efficient of this species in DMF has been calculated via rotating disc electrode (RDE) voltammetry. Bu^n-ZDTP reduction proceeds via nucleation of zinc at the electrode surface. The limiting current of the 2 electron reduction process is lower than previously observed for Bu^n-ZDTP oxidation. This occurs since zinc deposition is confined to growth centres which effectively limit the electroactive area of the electrode. A more thorough investigation of zinc nucleation at the electrode surface was undertaken using chronoamperometry. Transients plotted in dimensionless form were compared to theoretical models of nuclear growth.

The potential of atomic force microscopy as a promising technique for the imaging of ZDTP filming action has been demonstrated. Ex-situ atomic force microscopy was conducted of electrode surfaces following reduction in Bu^n-ZDTP solution under cyclic and RDE voltammetric conditions.

Development of a variable elevated temperature apparatus for the study of Bu^n-ZDTP under conditions more typical of an engine environment has been described. Application of the system to a wide range of electrochemical problems was demonstrated as an illustration of the advantages of this novel experimental approach. Studies of N, N, N$'$, N$'$-tetramethyl-p-phenylenediamine and tris(4-bromophenyl)amine oxidation yielded diffusion co-efficients (D) at elevated temperatures from which activation parameters for diffusion were obtained. Variation of D with temperature was compared to predicted theory according to the Stokes-Einstein and Wilke-Chang relationships. Studies of ortho-bromonitrobenzene and 9-chloroanthracene reduction demonstrated the elevated temperature apparatus to be a viable method for the interrogation of rapid kinetic processes. Both compounds are reduced according to an ECE mechanistic scheme where halide bond cleavage constitutes the chemical step. Since the use of microelectrodes permits "outrunning" of bond cleavage kinetics to give an n_{eff} of less than two, rate constants at varying temperatures were evaluated. Arrhenius plots were used to deduce activation parameters of halide bond cleavage in both compounds.

Preliminary studies of Bu^n-ZDTP redox activity under conditions more typical of an engine environment are discussed. Application of the novel microelectrode apparatus to an elevated temperature study of Bu^n-ZDTP is described. Voltammetric investigations in toluene, a resistive solvent which serves as a convenient model for oil, are discussed.

Acknowledgements

First I would like to thank my supervisor Prof. Richard Compton for his support over the past 3½ years. A big thank you also to all the members of the Compton group for providing such a friendly working atmosphere especially Jo and Emma who were always up for a good 'ol moan wherever the need arose! Other Compton group people who warrant a special mention are Frank Marken, Rob Dryfe and Richard Webster for their many helpful discussions; Qi Hong and Marco Suarez for help with atomic force microscopy experiments and John Alden for writing the data analysis program used during elevated temperature work. An especially big thank you must go to Dr. Barry Coles for his assistance in particular in the fabrication of the variable temperature voltammetric apparatus.

Other members of PTCL staff also deserve a special mention for their help throughout my DPhil, particularly the electronics and workshops departments, John Freeman in the drawing office and Tony and Merv in stores.

Outside of the lab, I am indebted to the EPSRC for financial support and also Thornton Research Centre, Shell UK, Ltd. for financial support and for providing the zinc n-dibutyldithiophosphate lubricant additive.

I must thank all my friends in the Christ Church GCR who made college life so special. A big hello to the lasses of the Christ Church Womens' 1st VIII and thank you for making my last year particularly memorable and just about keeping me sane while I was writing up! Thanks also to all my other friends from Wokingham and Southampton for their friendship and support throughout my time in Oxford in particular I would like to mention Julia, Ros and Jo.

More than anyone else, I would like to thank my parents and my brother Steve for their patience, tolerance and support throughout my DPhil .And last but not least, I would like to thank Kevin, without his regular pep-talks and our numerous cake-eating expeditions, I don't think I would have made it through the past 3½ years!

1 INTRODUCTION **1**

1.1 OVERVIEW 1
1.2 LUBRICANT COMPOSITION 2
1.3 LUBRICANT ADDITIVES 3
1.3.1 Friction and wear control 3
1.3.2 Contamination control and cleanliness 5
1.3.3 Fluid properties 6
1.4 ZDTPS 6
1.4.1 Anti-wear behaviour 7
1.4.2 Anti-oxidant behaviour 8
1.4.3 Inter-relationship between anti-wear and anti-oxidant behaviour 10
1.4.4 Interaction of ZDTP with other lubricant additives 11
1.5 TECHNIQUES IMPLEMENTED IN THE STUDY OF ZDTPS 12
1.5.1 Nuclear magnetic resonance 12
1.5.2 Infrared and raman spectroscopies 13
1.5.3 X-ray photoelectron spectroscopy 13
1.5.4 X-ray absorption spectroscopy 14
1.5.5 Scanning electron microscopy, electron microprobe analysis and mass spectrometry 14
1.6 PREVIOUS ELECTROCHEMICAL STUDIES OF ZDTPS 14
1.7 INTRODUCTION TO ZDTP STUDIES UNDERTAKEN IN THE PRESENT WORK 16
1.8 MODELLING THE ENGINE ENVIRONMENT 16
1.8.1 Working in resistive solvents 16
1.8.2 Working at elevated temperatures 18
1.9 OVERVIEW OF WORK PRESENTED IN THIS THESIS 20
REFERENCES 21

2 THEORY **24**

2.1 INTRODUCTION 24
2.2 NATURE OF ELECTRON TRANSFER 24
2.2.1 Mass transport 25
2.3 EXPERIMENTAL DESIGN FOR ELECTROANALYTICAL INVESTIGATIONS 28
2.3.1 Working electrode 28
2.3.2 Reference electrode 28
2.3.3 Counter electrode 29
2.3.4 Control and measurement of potential 30
2.3.5 Supporting electrolyte 31
2.4 CYCLIC VOLTAMMETRY 31
2.4.1 Applications of cyclic voltammetry 34
2.5 ROTATING DISC ELECTRODE VOLTAMMETRY 34
2.5.1 Hydrodynamics of a rotating disc electrode 36
2.5.2 Transport to a rotating disc electrode 37
2.5.3 Applications of rotating disc electrode voltammetry 39
2.6 CHRONOAMPEROMETRY 40
2.6.1 Applications of chronoamperometry 40
2.7 MICRODISC VOLTAMMETRY 41
2.7.1 Characteristics of microdisc electrodes 42
2.7.2 Uses of microdisc electrodes 44
2.8 SURFACE STUDIES USING ATOMIC FORCE MICROSCOPY 45
2.8.1 Scanning probe microscopy 45
2.8.2 The atomic force microscope (AFM) 51
2.8.3 Previous applications of the AFM 60
2.8.4 Application of the AFM to nanotribology 63
REFERENCES 65

3 EXPERIMENTAL PROTOCOL.......... 69
3.1 INTRODUCTION.......... 69
3.2 MICRODISC VOLTAMMETRY.......... 69
3.2.1 Cell configuration.......... 69
3.2.2 Microdisc electrodes.......... 70
3.2.3 Electronics.......... 72
3.3 CYCLIC VOLTAMMETRY.......... 73
3.3.1 Cell configuration.......... 73
3.3.2 Working electrodes.......... 73
3.3.3 Electronics.......... 74
3.3.4 Cyclic voltammetry in conjunction with ex-situ atomic force microscopy.......... 74
3.4 ROTATING DISC ELECTRODE VOLTAMMETRY.......... 75
3.4.1 Cell configuration.......... 75
3.4.2 Rotating disc electrodes.......... 76
3.4.3 Electronics.......... 77
3.4.4 Rotating disc electrode voltammetry in conjunction with ex-situ atomic force microscopy.......... 77
3.5 CHRONOAMPEROMETRY.......... 78
3.5.1 Cell configuration.......... 78
3.5.2 Working electrodes.......... 78
3.5.3 Electronics.......... 78
3.6 ATOMIC FORCE MICROSCOPY.......... 78
3.6.1 The AFM.......... 78
3.6.2 Ex-situ atomic force microscopy.......... 79
3.6.3 In-situ atomic force microscopy.......... 79
3.7 DATA ANALYSIS.......... 80
3.8 SOLVENTS AND SOLUTION PREPARATION.......... 80
3.9 CHEMICALS.......... 81
REFERENCES.......... 82

4 DEVELOPMENT OF A VARIABLE TEMPERATURE MICROELECTRODE APPARATUS.......... 83
4.1 INTRODUCTION.......... 83
4.2 APPARATUS DESIGN.......... 83
4.3 HEATED VOLTAMMETRIC CELL.......... 84
4.4 TEMPERATURE CONTROL.......... 85
4.4.1 Feedback temperature control system.......... 86
4.4.2 PID temperature control system.......... 87
4.4.3 Characterisation of solution temperature.......... 88
4.5 FLOW SYSTEM.......... 90
4.5.1 Flow rate control.......... 90
4.5.2 Characterisation of flow rate effects on limiting current.......... 93
4.5.3 Characterisation of flow rate effects on temperature stability.......... 95
4.5.4 Solution reservoir and pre-treatment.......... 96
4.5.5 Flow system construction.......... 97
4.6 COMPUTER CONTROL SYSTEM.......... 98
4.7 SUMMARY.......... 98
REFERENCES.......... 99

5 APPLICATION OF THE VARIABLE TEMPERATURE MICROELECTRODE APPARATUS.......... 100
5.1 INTRODUCTION.......... 100
5.2 N,N,N',N'-TETRAMETHYL-P-PHENYLENEDIAMINE (TMPD).......... 100
5.2.1 TMPD oxidation.......... 100
5.2.2 Application of the elevated temperature apparatus to the study of TMPD.......... 102
5.2.3 Experimental determination of diffusion coefficients at elevated temperatures in

acetonitrile 102
5.2.4 Estimation of diffusion coefficients using Wilke-Chang theory 105
5.2.5 Determination of activation parameters for diffusion 107
5.2.6 Comparison of variable temperature data with Wilke-Chang relationship 109
5.2.7 Calculation of effective radius 111
5.2.8 Experimental determination of diffusion coefficients at elevated temperatures in water 113
5.2.9 Experimental determination of activation parameters for diffusion 114
5.2.10 Comparison of variable temperature data with the Wilke-Chang relationship 115
5.2.11 Calculation of effective radius 116
5.2.12 Summary 117
5.3 TRIS(4-BROMOPHENYL)AMIME (TBPA) 118
5.3.1 TBPA oxidation 118
5.3.2 Application of the elevated temperature apparatus to the study of TBPA 119
5.3.3 Experimental determination of diffusion coefficients 119
5.3.4 Experimental determination of activation parameters for diffusion 121
5.3.5 Comparison of variable temperature data with the Wilke-Chang relationship 122
5.3.6 Calculation of effective radius 123
5.3.7 Summary 124
5.4 ORTHO-BROMONITROBENZENE (oBNB) 124
5.4.1 Mechanism of oBNB reduction 124
5.4.2 Application of microelectrode voltammetry to oBNB reduction 129
5.4.3 Previous kinetic analyses of oBNB 130
5.4.4 Previous determination of activation parameters for halonitrobenzenes 131
5.4.5 Application of the variable temperature electrochemical apparatus to the study of oBNB 132
5.4.6 Experimental determination of rate constants for halide bond cleavage of oBNB 133
5.4.7 Experimental determination of the rate constant at room temperature using microelectrodes of variable radii 137
5.4.8 Experimental determination of activation parameters for halide bond cleavage of oBNB 139
5.4.9 Comparison of data with literature values derived for other halonitrobenzene compounds 143
5.4.10 Summary 144
5.5 9-CHLOROANTHRACENE (9-ArCl) 145
5.5.1 Mechanism of 9-ArCl reduction 145
5.5.2 Previous kinetic analyses of 9-ArCl halide bond cleavage 148
5.5.3 Previous determination of activation parameters for halide bond cleavage of 9-ArCl 148
5.5.4 Application of the elevated temperature voltammetric apparatus to the study of 9-ArCl 150
5.5.5 Experimental determination of rate constants for halide bond cleavage of 9-ArCl 150
5.5.6 Experimental determination of activation parameters for halide bond cleavage of 9-ArCl 153
5.5.7 Comparison of data with previous literature studies 157
5.5.8 Summary 159
5.6 CONCLUSIONS 160
REFERENCES 161

6 VOLTAMMETRY OF BU^n-ZDTP 164

6.1 INTRODUCTION 164
6.2 INTRODUCTION TO BU^n-ZDTP VOLTAMMETRY UNDERTAKEN IN THE PRESENT WORK 164
6.3 CYCLIC VOLTAMMETRY OF BU^n-ZDTP 165
6.3.1 Experimental 165
6.3.2 Results and discussion 165
6.4 RDE VOLTAMMETRY OF BU^n-ZDTP 180
6.4.1 Experimental 180
6.4.2 Results and Discussion 181
6.5 SUMMARY 190
REFERENCES 190

7 CHRONOAMPEROMETRIC STUDIES OF BU^n-ZDTP 192
- 7.1 INTRODUCTION 192
- 7.2 THEORETICAL TREATMENT OF NUCLEATION AND GROWTH 192
- 7.3 OVERVIEW OF NUCLEATION STUDIES OF ZINC 195
- 7.4 EXPERIMENTAL 195
- 7.5 RESULTS 196
  - 7.5.1 Glassy carbon 196
  - 7.5.2 Platinum 198
- 7.6 MODELLING OF THE NUCLEATION PROCESS 200
  - 7.6.1 Theoretical model for the growth of hemispherical nuclei under diffusion limited conditions 200
  - 7.6.2 Previous applications of model 203
  - 7.6.3 Application of model to deposition of Bu^N-ZDTP 204
- 7.7 SUMMARY 209
- REFERENCES 212

8 ATOMIC FORCE MICROSCOPY OF BU^n-ZDTP 213
- 8.1 INTRODUCTION 213
- 8.2 SURVEY OF LITERATURE RELATING TO AFM STUDIES OF METAL ELECTRODEPOSITION 213
  - 8.2.1 Literature reports of AFM studies of zinc electrodeposition 217
- 8.3 APPLICATION OF ATOMIC FORCE MICROSCOPY TO THE STUDY OF ZINC DEPOSITION IN THE PRESENT WORK 218
- 8.4 EX-SITU ATOMIC FORCE MICROSCOPY IN CONJUNCTION WITH CYCLIC VOLTAMMETRY 219
  - 8.4.1 Experimental 219
  - 8.4.2 Results 220
- 8.5 EX-SITU ATOMIC FORCE MICROSCOPY IN CONJUNCTION WITH RDE VOLTAMMETRY 224
  - 8.5.1 Experimental 224
  - 8.5.2 Results 224
- 8.6 IN-SITU ATOMIC FORCE MICROSCOPY 229
- 8.7 SUMMARY 230
- REFERENCES 231

9 PRELIMINARY STUDIES OF BU^n-ZDTP VOLTAMMETRY AT ELEVATED TEMPERATURES AND IN RESISTIVE SOLVENT MEDIA .. 233
- 9.1 INTRODUCTION 233
- 9.2 HIGH TEMPERATURE INVESTIGATIONS 233
  - 9.2.1 Application of the elevated temperature voltammetric apparatus to the study of Bu^n-ZDTP 233
  - 9.2.2 Experimental 233
  - 9.2.3 Results 234
  - 9.2.4 Conclusions 236
- 9.3 RESISTIVE SOLVENT INVESTIGATIONS 236
  - 9.3.1 Application of resistive solvents to the study of Bu^n-ZDTP 236
  - 9.3.2 Literature reports of voltammetry in toluene 237
  - 9.3.3 Experimental 238
  - 9.3.4 Results 239
  - 9.3.5 Conclusions 241
- 9.4 SUMMARY 241
- REFERENCES 242

10 CONCLUSIONS AND FUTURE DIRECTIONS 243
- 10.1 INTRODUCTION 243

10.2 REVIEW....243
10.3 FUTURE DIRECTIONS....246
  10.3.1 Extension of ZDTP studies....247
  10.3.2 Refinement of elevated temperature apparatus for the study of ZDTPs....248
10.4 MAJOR CONTRIBUTIONS OF THIS THESIS....250
REFERENCES....250

Chapter 1

Introduction

1.1 Overview

The broad aim of the work reported in this thesis is the electrochemical study of zinc n-dibutyldithiophosphate (Bu^n-ZDTP). This species is a typical zinc dialkyldithiophosphate (ZDTP) which constitutes a class of compounds used routinely in the automotive industry as lubricant additives. Motivation for this was driven in part by the fact that in spite of the widespread use and importance of ZDTP additives, their mode of action is not well-defined. Electrochemical techniques offer analytical possibilities for the study of ZDTPs. Primarily they provide a means of studying oxidation and reduction processes undergone by the ZDTP which are fundamental to its role as an anti-oxidant agent. The use of such techniques in the elucidation of ZDTP redox processes is seldom exploited and literature reports pertaining to such investigations are few.

Electrochemical studies of an oil additive encompass certain challenges if reaction conditions are to be a true model of the engine conditions under which the ZDTP is normally active. Typical operating conditions of a ZDTP include first, the elevated temperatures and pressures of the working engine and secondly, solution in a resistive oil medium. Addressing the problem of electrochemistry under two of these environmental factors, namely elevated temperatures and presence of a resistive carrier medium, constitutes a major theme of this thesis.

Since ZDTPs are normally operative under typical engine conditions, a major goal of this thesis was the development of an elevated variable temperature voltammetric apparatus for use with resistive solvents. The potential applications of this novel technique which permits the measurement of variable temperature steady state voltammetry is considered in depth. A further aim of this work was to investigate the use of atomic force microscopy as a means of studying the filming action of ZDTPs. Film formation processes are significant in the role of such compounds as anti-wear agents.

In §1.2 we begin by discussing lubricant composition prior to a survey of oil additives presented in §1.3. We then turn our attention more specifically to ZDTPs with a detailed account of the functions and modes of action of these additives in §1.4. An overview of the techniques employed in the study of ZDTPs reported in the literature to date is given in §1.5. Literature reports of electrochemical investigation of ZDTPs are considered in greater depth in §1.6. The theme of electrochemical studies undertaken during the present work is introduced in §1.7. Consideration is given to the steps taken to model engine conditions, namely the high temperature and resistive solvent issues addressed as part of this work, in §1.8. We conclude the chapter with an overview of the work to be presented in this thesis in §1.9.

1.2 Lubricant composition

The lubricant of an automotive engine fulfils a number of important functions. First, it protects the engine components from the effects of considerable friction and wear as moving parts of the engine come into contact during operation. Secondly, the lubricant serves to keep the surface of the engine clean and minimises the effects of rusting and corrosion thereby maintaining the engine components in the shape required for operation. Thirdly, the engine lubricant serves as the primary medium for engine cooling and is also instrumental in the sealing of engine components thereby preventing the leakage of combustion gases. In order to perform these functions effectively, the lubricant should have a number of important properties. Since the oil is required to perform these functions under a wide variety of temperatures and operating conditions, for example, different load conditions arising from city or high speed driving, it must remain fluid ideally maintaining the correct physical properties for optimum performance. Furthermore, the lubricant should be stable over the length of time between oil change intervals even in the presence of water and acidic combustion products [1,2].

These requirements cannot be met by mineral or synthetic oils alone. Thus the addition of chemical additives is necessary to improve the performance of the lubricant. Engine oils typically consist of a base oil comprised of a high quality solvent-refined mineral or synthetic oil. The basestock fluid is then supplemented with 5 to 25% of additives by mass in order to achieve the properties and functions detailed above [1,2,3]. A detailed survey of lubricant additives classified according to function is presented in §1.3. Table 1.1 shows a typical lubricant composition.

Function	**Additive type**	**Concentration, % by mass**
Friction and Wear	Viscosity Index Improver	0-6
	Anti-Wear Agent	0.5-2
	Friction Modifier	0-2
	Rust/Corrosion Inhibitor	0-1
Contamination and Cleanliness	Anti-oxidant	0-1
	Detergent	1-10
	Ashless Dispersant	2-9
Maintaining Fluid Properties	Pour Point Depressant	0-0.5
	Anti-foamant	0-0.001
Base oil (mineral and/or synthetic)		75-95

Table 1.1: Typical composition of oil lubricants (from ref. 1)

1.3 Lubricant additives

1.3.1 Friction and wear control

Minimisation of friction and wear are desirable as a means of improving fuel economy and to ensure long term durability of the engine.

1.3.1.1 Viscosity index improvers

Surfaces of rubbing components are lubricated by a film of oil which separates the surfaces. The viscosity of the oil is important in determining the efficiency with a higher viscosity oil providing greater wear protection. However this is counteracted by high friction which results in poor fuel economy. Thus an oil is used with viscosity that optimises these two factors. However, the engine consists of a number of components of differing dynamic loading and velocity cycles. Thus there is no single optimum viscosity for an engine. Furthermore the engine operates over a significant temperature range from a start-up temperature of -20 ^{0}C to a typical piston temperature of 350 ^{0}C. Over such a temperature range the viscosity characteristics of the oil change markedly. A measure of the variation of viscosity with temperature is provided by the viscosity index in which a high viscosity index denotes a lower sensitivity to temperature change therefore indicating increased performance efficiency over high and low temperatures. Viscosity index improvers are added to the oil in order to reduce the temperature sensitivity. These comprise polymers with molecular weights ranging from 10, 000 to 1, 000, 000. The polymer is swollen by the lubricant in solution and increases in volume which occur at higher temperatures have a thickening effect on the engine oil. By careful selection of the polymers added, the frictional efficiency and wear protection of the lubricant can be optimised over the wide range of temperatures and load cycles found in the engine. Typical viscosity index improvers include olefin co-polymers, polymethacrylates and hydrogenated styrene butadiene co-polymers [1,2].

1.3.1.2 Anti-wear agents

Wear refers to the loss of metal from engine components. It is generally caused by metal-to-metal contact and will ultimately result in engine malfunction. Contact between sliding surfaces in the working engine is unavoidable during the operating cycle, particularly during starting-up, stopping and running-in. Thus anti-wear additives are essential to control wear to an acceptable level. ZDTPs are used almost entirely for this purpose. They function by forming a film on the engine components under the working conditions of the engine. A more detailed account of the anti-wear action of ZDTPs is presented in §1.4.1 [1,2].

1.3.1.3 Friction modifiers

Frictional properties of the lubricant influence overall friction losses in both engine and transmission systems. Friction modifying additives are added to the lubricant as a means of reducing friction and associated surface wear. Typical friction modifiers include a variety of esters, amides and metal soaps. These have been observed to reduce boundary friction by up to 30% in simple laboratory tests and to provide fuel economy benefits of up to 4% [1,3].

1.3.1.4 Rust/corrosion inhibitors

Corrosion of engine components occurs via acid reaction with oxides of the metal surface. Acidic products originate from incomplete fuel combustion or oxidation of the base lubricant. Corrosion can cause seizure of engine components and accelerate wear on sliding surfaces. In addition, corrosion products, in particular oxide particles, can cause abrasive wear elsewhere in the engine. Corrosion can be minimised by the neutralisation of acidic products prior to contact with the metal surface. This is achieved using dispersant and detergent additives as described in §1.3.2.2 and 1.3.2.3 respectively. In addition, corrosion inhibitors are added to the oil. These function by forming a strongly adsorbed passivating film on the metal surface thereby making it impervious to attack. Typical corrosion inhibitors include ethoxylated alcohols and phenols and neutral metal sulphonates [1,2,3].

1.3.2 Contamination control and cleanliness

At the high temperatures under which the engine is operative, the oil is subject to severe oxidation and thermal degradation leading to accumulation of insoluble material. The original molecular structure is broken down and products polymerise forming gums and lacquer deposits on engine surfaces. In certain parts of the engine, the oil is exposed to combustion products containing hydrocarbon radicals and nitrogen oxides which cause severe oxidation of the engine oil and the formation of carbonaceous deposits [1,3].

1.3.2.1 Anti-oxidants

Anti-oxidants prevent the deterioration associated with oxygen attack on the base oil. Hydrocarbon oxidation occurs via radical chain reaction leading to the production of hydroperoxides. These inhibitors function either by free radical removal or by interaction with the peroxides involved in oxidation mechanisms. The most widely used anti-oxidant additives are ZDTPs. A more detailed account of their anti-oxidant activity is presented in §1.4.2. A variety of hindered phenol and amine compounds are also used as anti-oxidants [2,3].

1.3.2.2 Ashless dispersants

Ashless dispersants are instrumental in the neutralisation of combustion acids and in the removal of contaminant particles from the lubricant. Insoluble material which accumulates in the oil as a result of thermal degradation and oxidation is ultimately removed from the engine by the oil filter. For effective removal, the contaminants should be maintained in solution. Ashless dispersants typically comprise a polar head for attachment to contaminant particles together with a solubilising high molecular weight hydrocarbon tail. A typical ashless dispersant is polyisobutene succinic acid polyamide [1,2,3].

1.3.2.3 Detergents

Detergents comprise a polar head and solubilising hydrocarbon tail similar to the ashless dispersant additives described in §1.3.2.2 and as such are also instrumental in the neutralisation of acidic species and suspension of insoluble material. In addition, detergent additives are effective in the removal of carbonaceous deposits that form on the engine components as a result of oil degradation. Accumulation of such deposits can cause deviation from design geometry leading to, in extreme cases, piston seizure. Detergents are composed of a metal carbonate species (K, Na, Mg, Ca, Li and Ba) attached to a surfactant tail comprising either sulphonate, alkyl phenate or alkyl salicylate groups [1,2,3].

1.3.3 Fluid properties

1.3.3.1 Pour point depressants

Pour-point depressants maintain the flow characteristics of the lubricant in the presence of paraffin wax which crystallises from the mineral oil. This is achieved by adsorption of the pour-point depressant onto the wax surface with subsequent reduction of the amount of oil in the crystal. This serves to reduce the volume of the wax crystal thereby permitting lubricant flow. Typical pour-point depressants include polymethacrylate and alkylated phenol compounds [2,3].

1.3.3.2 Anti-foamants

Foam formation on the surface of the lubricant is a hazard as oil and air are mixed in the working engine. Silicone oil is added to the lubricant as an anti-foam additive. Silicone oil is essentially insoluble in mineral oil and globules of silicone on a microscopic scale keep the oil film around the air bubbles sufficiently thick so as to facilitate rapid oil drainage with consequent collapse of the foam [3].

1.4 ZDTPs

We noted the dual activity of ZDTP species as both anti-wear and anti-oxidant agents in §1.3. The chemical structure of ZDTP is shown in Figure 1.1. The importance of these additives is exemplified by the large quantity of research pertaining to ZDTP investigation which has been reported in the literature. Research is driven by the commercial and environmental implications of improving engine performance. Specific areas of investigation are summarised in §1.4.1 to 1.4.4. An overview of the techniques used in the study of ZDTPs is presented in §1.5.

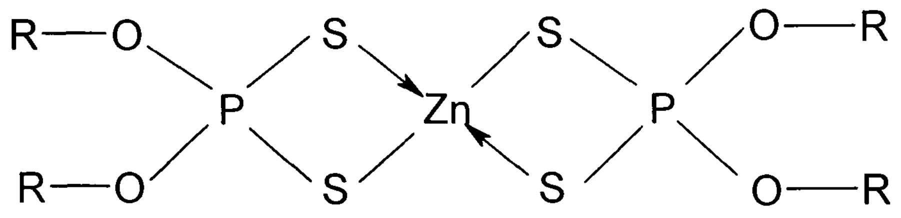

Figure 1.1: Chemical structure of ZDTP

1.4.1 Anti-wear behaviour

ZDTP species have been included in lubricant formulations as anti-wear additives for over 30 years. It is known that in the absence of such additives the more highly stressed areas of the engine, such as the cam/follower and the piston/ring/cylinder, can fail prematurely as a result of catastrophic wear [4]. The necessity of ZDTP additives is therefore apparent. In spite of research into alternative anti-wear agents, no other compound has been found to equal their effectiveness [4].

The need to enhance lubricant performance has resulted in considerable research into the anti-wear mechanism of ZDTPs. Despite this, the precise mechanism of the anti-wear process remains undetermined. This can be attributed to two factors. First, the complexity of the ZDTP reaction mechanisms and secondly, the multidisciplinary nature of the anti-wear process [4,5]. It is widely thought that ZDTPs function by forming a protective surface film on the engine components under boundary lubricant conditions. In view of this, a large number of studies have been undertaken focussing on the analysis of film structure and correlation to wear behaviour or load bearing performance. Data obtained and subsequent wear mechanisms inferred are, however, both inconclusive and inconsistent [6,7,8,9,10,11,12,13,14,15,16]. A brief review of the literature pertaining to ZDTP anti-wear behaviour follows.

A number of studies have suggested that wear films comprise polymeric pyrophosphato-zinc materials formed via thermal degradation of the parent molecule. In 1967, Dickert and Rowe investigated the decomposition of iso-propyl ZDTP at 155 °C [6]. They postulated that the resulting film comprised a glass like solid with a polymeric dithiopyrophosphato structure. A subsequent study by Harrison and Kikabhai investigated the decomposition of ethyl and iso-propyl ZDTPs at 250 °C [7]. These workers proposed a similar film composition but with alkene elimination from alkoxy groups and a lower sulphur content to yield a non-carbonaceous polymeric monothiopyrophosphato-zinc material. A study by Harrison and Brown using external reflection FTIR, ^{31}P MAS NMR and SEM to analyse steel surfaces heated in ZDTP solution suggested that film composition was temperature dependant [8]. Film formation was not apparent at 150 ^{0}C. At 200 ^{0}C, a weakly adhering, uniform film composed of zinc monothiopyrophosphate was observed. Films formed at 260 ^{0}C were non-uniform and composed of alkylmonothiopyrophosphates and zinc polyphosphates.

In contrast, a study by Glaeser et al using in-situ scanning Auger spectroscopy in conjunction with running sliding contact experiments on steel surfaces in ZDTP solution suggested that the resulting film was composed of a chemisorbed iron sulphide-iron oxide layer [9]. Such findings are consistent with investigations by Godfrey [10] and Baldwin [11]. Watkins et al proposed a physisorbed zinc phosphate layer together with an iron sulphide layer formed by reaction of sulphur from the thiophosphate groups with the oxidised steel surface of the engine [12]. These workers suggested that the phosphate layer is easily removed and it is the sulphide layer which serves as the anti-wear film.

More recently, a number of workers have concluded that boundary lubricant layers comprise amorphous polyphosphates. Martin et al used EXAFS to study ZDTP films formed under typical wear conditions and concluded that amorphous, inorganic long chain polyphosphates containing iron cations were present [13]. Willermet et al agreed with these findings following a study of wear films generated in a cam tappet contact using reflectance-absorbance infrared, XPS and Auger spectroscopies [14]. However, zinc or magnesium were proposed as the cationic species in this instance. A further study by Willermet et al used ex-situ infrared spectroscopy to investigate films prepared on steel surfaces under frictional conditions. These workers suggested that wear film structure comprised both long and short chain phosphate species [17]. Formation was postulated to follow a thermooxidative mechanism as opposed to the thermal decomposition pathway proposed by previous workers.

The confusion in this area is evident. Such diverse findings result from the complexity of the film formation process and varying experimental conditions which reflects the extreme sensitivity of ZDTP action to temperature and pressure.

1.4.2 Anti-oxidant behaviour

Hydrocarbon oxidation proceeds via a series of well known, mainly free radical steps to form oxygen-containing species which include peroxy radicals, hydroperoxides, acids, alcohols and water [18,19]. Of these, peroxy radical and hydroperoxide species are most detrimental to engine wear. Peroxy radicals contribute to engine wear by acceleration of the hydrocarbon oxidation process. Hydroperoxides are a source of peroxy radicals. Furthermore literature reports suggest that hydroperoxides contribute to the wear process via direct attack on engine surfaces [20]. The significance of hydroperoxides in engine wear has been demonstrated by Habeeb and Stover during motored and fired engine tests [20] and Rounds during four ball studies [21]. During both investigations, wear was measured in the presence of a known amount of hydroperoxide. Both studies correlated extent of engine wear with hydroperoxide concentration. ZDTPs can potentially react with any of the products of hydrocarbon oxidation but react most readily with peroxy radical and hydroperoxide species.

ZDTPs have two roles of anti-oxidant activity. First they act as chain-breaking radical scavengers by reaction with peroxy radicals [22]. Secondly, they function as preventative anti-oxidants via the decomposition of hydroperoxides [22]. The anti-oxidant behaviour of ZDTP is complex and a large number of studies have focussed on elucidating the processes involved. A brief survey of the pertinent literature follows.

Ohkatsu et al report a kinetic study of the decomposition of cumene hydroperoxide by isobutyl ZDTP at 70 ^{0}C in chlorobenzene [5]. These workers noted the formation of zinc sulphate and sulphuric acid. They suggested that ZDTP reacted with hydroperoxide to form sulphuric acid which upon further reaction with ZDTP yielded zinc sulphate. These workers hypothesised that the reaction of ZDTP with sulphuric acid was critical in the overall decomposition process.

Bridgewater et al conducted a kinetic study of cumene hydroperoxide decomposition using a variety of ZDTP compounds in decane at temperatures in the range 90 ^{0}C to 150 ^{0}C [23]. These workers proposed the formation of thiolic acid via ZDTP decomposition at elevated temperatures which served as the key hydroperoxide decomposing species. However, this investigation was aimed at inferring rate determining steps with hydroperoxide present in excess. Such conditions may not be representative of a typical lubricant oxidation process.

Colclough et al proposed a mixture of strong-oxy acids to be the reaction products of ZDTP with peroxy radical and hydroperoxide species [24]. These workers postulated that such species are subsequently involved in the catalytic decomposition of ZDTP.

Paddy et al report a kinetic study of cumene hydroperoxide decomposition using a hydroperoxide:ZDTP ratio of 3:1 at 30 °C in a hydrocarbon solvent [25]. The reaction was monitored using Raman and ^{31}P NMR Spectroscopy. These workers proposed the formation of a cluster compound $[(Bu^nO)_2PS_2]_6Zn_4O$ and a disulphide species, with subsequent oxidation of the cluster compound to produce disulphide, trisulphide, and tetrasulphide compounds.

Korcek et al used engine degradation studies combined with a peroxy radical titration technique to study the anti-oxidant mechanism of ZDTP [26]. These workers suggested that ZDTP reacts with hydroperoxides to yield more active anti-oxidant species.

We note that as for the ZDTP anti-wear process, anti-oxidant behaviour is poorly understood. The range of mechanisms postulated reflects complexity of the reaction pathway and variation of environmental conditions.

1.4.3 Inter-relationship between anti-wear and anti-oxidant behaviour

In addition to the separate study of ZDTP anti-oxidant and anti-wear activities, research has focussed on the inter-relationship between these two functions. Clearly a thorough understanding of the link between anti-wear and anti-oxidant behaviour is necessary to achieve an appropriate combination of ZDTPs to perform optimum engine protection.

Willermet et al report wear tests using n-octyl-ZDTP in a commercial base oil in the presence and absence of peroxy radicals [27,28]. These workers suggested that the anti-oxidant reactions of ZDTP reduce its effectiveness as an anti-wear additive. They postulated the formation of a disulphide product which functions as a less effective anti-wear agent than the parent compound.

More recently, it was proposed by the same group that oxidation reactions of ZDTP are fundamental to anti-wear activity [16]. Their studies compared wear measurements in air, in an inert atmosphere and under inert conditions with added hydroperoxide. Wear was noted to be significantly decreased in systems in which oxidation was allowed to take place. Willermet et al proposed formation of the anti-wear film via a thermooxidative mechanism. It was suggested that the anti-oxidant reactions of ZDTP formed a mixture of phosphates, thiophosphates together with their esters and water which function as pre-cursors for inorganic film formation.

1.4.4 Interaction of ZDTP with other lubricant additives

We noted in §1.3 that a typical lubricant formulation is comprised of numerous additive species in addition to ZDTP. Interaction between different compounds is probable particularly at the high temperatures generated between the moving metal surfaces of a working engine [29]. An understanding of the interaction of ZDTP with other lubricant additives is required for the accurate elucidation of mechanistic action.

Harrison and Kikabhai describe a proton and ^{31}P NMR study of ethyl and isoproyl ZDTPs in chloroform and toluene solutions in the presence of nitrogen-donor molecules which serve as models for dispersant additives [30]. These workers report complexation of the ZDTP species by the nitrogen containing compounds as evidenced by shifts in the NMR signals obtained.

The effects of metallic detergents on the anti-wear and anti-oxidant properties of ZDTPs have been studied by Yamada et al using a variety of methods [31]. These workers concluded that the anti-oxidant properties of ZDTP, as evaluated in the thin film oxygen uptake test, significantly deteriorated in the presence of over-based calcium detergents. The authors suggest that the formation of acidic products during ZDTP oxidative degradation contributes to anti-oxidant activity. Thus, presence of overbased detergents neutralise acidic products thereby retarding anti-oxidant activity. Wear tests also indicated that metallic detergents hindered the anti-wear properties of ZDTP. This was attributed to competitive adsorption of detergents on the metal surface.

Barcroft and Park investigated the structure of ZDTP wear films formed on heated metal surfaces in the presence of a variety of oil additive species via microprobe analysis [29]. These workers found that rate of film formation, film thickness, morphology and composition were unaffected by the addition of a typical viscosity index improver. In contrast, the authors report that rate of formation and film thickness were substantially reduced in the presence of a typical dispersant additive although film composition remained unaltered. Typical anti-rust inhibitor and detergent additives were observed to decrease rate of film formation. In addition, the incorporation of substantial amounts of calcium within the film structure was noted. These workers concluded that even in multi-additive systems, the ZDTP retains its ability to form anti-wear films on metal surfaces.

1.5 Techniques implemented in the study of ZDTPs

A variety of techniques have been implemented for the study of ZDTP mechanistic action. We note that for the accurate elucidation of ZDTP processes, the application of typical engine conditions is desirable. Due to practical considerations, in-situ experiments performed under the high temperature and pressure conditions of a working engine environment are generally confined to the physical measurement of wear between sliding surfaces.

Anti-oxidant studies have principally been limited to kinetic studies of ZDTP and hydroperoxide/peroxy radical reaction. Elevated temperatures have been utilised for the evaluation of kinetic data but in general studies have not been performed under in-situ conditions.

Measurements of anti-wear behaviour relating to film composition and film formation processes have frequently been performed under ex-situ conditions. However, more recently extension of these techniques to the in-situ study of film formation processes has been reported.

A brief overview of chemical techniques implemented in the study of ZDTP anti-wear and anti-oxidant activity follows. The information such methods have afforded is demonstrated. Electrochemical investigations are reviewed in greater depth in §1.6.

1.5.1 Nuclear magnetic resonance

Proton and ^{31}P Nuclear Magnetic Resonance (NMR) have been used for the characterisation of ZDTP reactions in solution. Harrison et al report a proton and ^{31}P NMR study of ZDTP dimerisation in chloroform, toluene and hydrocarbon solvents [32]. These workers correlated the degree of ZDTP association with the nature of the alkyl substituent group and solvent polarity. Burn et al utilised ^{31}P NMR in a study of the hydrolysis reactions undergone by a variety of ZDTP compounds in 1,2-dimethoxyethane [33,34]. The authors report formation of phosphoric acid along with several by-products and show hydrolysis rates to be independent of the ZDTP alkyl substituent. Paddy et al used ^{31}P NMR to monitor the products formed during reaction of ZDTP with cumene hydroperoxide for a variety of alkyl substituent groups during the study described in §1.4.2 [25]. The formation of a number of sulphide species was reported as detailed previously.

Solid state NMR has also been applied to the study of ZDTPs. Harrison and Brown describe the use of ex-situ solid state ^{31}P NMR for the analysis of wear films formed on stainless steel surfaces at elevated temperatures as detailed previously in §1.4.1 [8]. These workers noted a variation in film composition with temperature.

1.5.2 Infrared and raman spectroscopies

Infrared (IR) spectroscopy has been used to provide information as to the composition and structure of ZDTP surface films. Until recently this technique has been limited to the study of ZDTP films under ex-situ conditions. Willermet et al report an IR spectroscopy study of isopropyl ZDTP films prepared using a cam/tappet tribometer with a removable friction disc [17]. These workers proposed that wear films were predominantly composed of amorphous orthophosphate and pyrophosphate species. Harrison et al utilised IR in conjunction with the ex-situ ^{31}P MAS NMR study of ZDTP films previously noted [8].

More recently, Westerfield and Agnew have implemented IR spectroscopy in conjunction with a diamond anvil cell to observe boundary layers in situ at high temperatures and pressures [35]. During a study of a commercial ZDTP additive, these workers postulated film formation to be triggered by pressure increases associated with boundary lubrication in addition to temperature effects.

Paddy et al describe application of Raman spectroscopy to the kinetic study of ZDTP oxidation by cumene hydroperoxide during the study previously noted in §1.4.2 [25].

1.5.3 X-ray photoelectron spectroscopy

Bell et al describe ex-situ X-ray photoelectron spectroscopy (XPS) as a means of characterising films formed by Bu^n-ZDTP on iron surfaces under frictional conditions [36]. XPS depth-profiling studies indicated that the film was composed of a layer structure which changed with depth. The main constituent of the film approximated to a phosphate structure with varying amounts of organic material and sulphides and oxides of iron and zinc. Rhodes and Stair used XPS to characterise films formed from a commercial ZDTP blend in a hydrocarbon lubricant on stainless steel surfaces at elevated temperatures [37]. These workers suggested a model for anti-wear activity based on a sulphur containing species.

In-situ XPS and Auger Spectroscopy in conjunction with sliding contact experiments have been reported by Glaesar et al as a means of characterising wear films formed by a commercial ZDTP at elevated temperature and pressure [9]. These workers proposed a chemisorbed iron sulphide-iron oxide layer as the boundary lubricating medium as detailed previously in §1.4.1.

1.5.4 X-ray absorption spectroscopy

Fuller et al have applied X-ray absorption near edge structure (XANES) spectroscopy to the analysis of wear films formed from a variety of ZDTP compounds on steel substrates at different temperatures and pressures [38]. These workers concluded that films were composed of a mixture of short chain and long chain polyphosphate compounds where relative amounts were dependant on temperature. Sulphur content was found to decrease with increasing temperature. The application of extended X-ray absorption fine structure (EXAFS) to ZDTP investigation has been demonstrated by Martin et al during a study of friction-induced ZDTP films to reveal a locally ordered glass structure [13].

1.5.5 Scanning electron microscopy, electron microprobe analysis and mass spectrometry

Bell et al describe application of scanning electron microscopy (SEM), electron microprobe analysis (EMPA) and secondary ion mass spectrometry (SIMS) for the analysis of surface films in conjunction with the XPS study described previously in §1.5.3 [36]. These techniques indicated the presence of a polyphosphate structure for Bu^n-ZDTP films formed under frictional conditions.

Rounds implemented SEM during a study of steel surfaces subjected to wear conditions using different concentrations of hydroperoxide and a commercially blended ZDTP as described previously in §1.4.2 [21]. The ZDTP additive appeared to reduce surface wear by increasing the threshold hydroperoxide concentration necessary for engine degradation to occur.

1.6 Previous electrochemical studies of ZDTPs

Electrochemical techniques have featured infrequently in reported investigations of ZDTP activity. A detailed review of the literature pertaining to electrochemical studies of ZDTP activity follows.

Shafiqul Alam et al report a differential-pulse polarographic study of isopropyl-ZDTP during an investigation aimed at introducing this technique for the quantitative analysis of ZDTPs in oil samples [39]. Their investigation was conducted in DMF solution containing 0.1 M NEt_4ClO_4 as supporting electrolyte. These workers reported a peak at –0.9 V versus a silver-silver chloride reference which was assigned to the reduction of Zn^{2+} to Zn metal at the mercury electrode. Since this investigation was concerned with the assay of ZDTP in solution, these workers restricted their study to this peak at varying ZDTP concentration. Detail concerning electrochemical mechanism of ZDTP behaviour is not presented.

A subsequent d.c. polarographic study of isobutyl-ZDTP in ethanolic solution containing 0.1 M $NaClO_4$ as electrolyte was reported by Hutchings et al [40]. These workers noted the reduction of Zn^{2+} to Zn metal at –1.05 V versus silver-silver chloride. Additional peaks at –0.2 V and +0.1 V were attributed to formation of mercury(II) complexes formed via interaction of the electrode with the DTP anion as previously reported by Bond et al [41]. Oxidation of the complex was not investigated due to the potential limitations of the mercury electrode. Furthermore, no detailed information was presented concerning ZDTP reduction.

Blankespoor reports a more detailed study of ZDTP redox activity using cyclic voltammetry [42]. This investigation focussed on both ethyl and isopropyl-ZDTP complexes in acetonitrile solution containing 0.1 M $LiClO_4$ as electrolyte at a glassy carbon electrode. Both compounds were oxidised at +1.5 V versus SCE with oxidation waves revealing chemical irreversibility over a wide range of scan rates. Using a plot of peak potential versus the square root of scan rate, the process was identified as being diffusion controlled. Electroreduction of both ZDTP complexes revealed peaks at –0.64 V and –1.24 V versus SCE. The peak at –1.24 V was assigned to the reduction of a disulphide product formed during the oxidation process. This assignment assumed the loss of ZDTP ligands during electrooxidation followed by rapid dimerisation consistent with the irreversible nature of the oxidation process. Assignment of the peak was made by comparison with an independent cyclic voltammogram obtained for the corresponding disulphide in each case. No assignment was made for the peak at –0.64 V.

A subsequent investigation by Stezeryanskii et al using cyclic voltammetric and chronopotentiometric techniques aimed to elucidate the electrooxidation mechanism of ZDTP in greater detail [43]. These workers used iso-octyl-ZDTP in DMF solution containing 0.1 M $NaBF_4$ as supporting electrolyte. The investigation was carried out using a glassy carbon electrode substrate. Irreversible oxidation of the complex was observed at +0.81 V versus Ag-AgCl. The irreversible nature of the reaction was ascribed to rapid dimerisation of sulphide ligands following the reduction process. These workers suggest the overall electron transfer process comprises a one electron oxidation. In contrast to the work of Blankespoor, these workers report that the oxidation of ZDTP is kinetically hindered. This assignment was made on the basis of cyclic voltammetric and chronopotentiometric studies where $I_{pc}/c\upsilon^{1/2}$ shows a decrease with potential scan rate and $I\tau^{1/2}$ is seen to decrease with current density respectively. I and I_{pc} denote current and peak current values respectively, c corresponds to concentration of the electroactive species, υ represents scan rate and τ denotes the transition time during chronopotentiometric investigation. ZDTP dissociation is suggested to be the preceding chemical reaction.

1.7 Introduction to ZDTP studies undertaken in the present work

We have noted that the mechanistic action of ZDTPs in their capacity as both anti-wear and anti-oxidant agents is ill-defined. This is despite considerable research aimed at elucidating ZDTP activity and can be attributed to the complexity of the reaction processes and the varying experimental conditions employed. Previous studies have encompassed a wide variety of techniques. However, electrochemical methods as a tool for the study of ZDTPs have been poorly exploited.

During this study we seek to investigate the information that electrochemical analysis can contribute to this field. We have noted the importance of conducting investigations under typical engine conditions. As part of this thesis, we consider voltammetry in resistive media which serve as suitable models for oil. In addition, we describe development of an elevated temperature voltammetric apparatus for use in conjunction with resistive solvent media. A consideration of voltammetry in resistive media and at elevated temperatures is presented in §1.8.

1.8 Modelling the engine environment

1.8.1 Working in resistive solvents

Electrochemical cells require sufficient conductivity so as to enable the unhindered passage of current through the solution. Electrochemical investigations have generally been confined to a small range of conductive solvents. In addition, supporting electrolytes are generally added to electrolytic solutions to ensure sufficient conductivity as detailed in Chapter 2. Solutions composed of resistive solvents or solutions in which supporting electrolyte is absent will suffer from ohmic distortion.

Ohmic distortion is proportional to the amount of current passed through the solution as defined by Ohm's law (Equation 1.1):

$$E=iR_{soln}. \tag{1.1}$$

Steady state voltammograms recorded for an electrochemically reversible process under conditions of significant ohmic drop will appear "drawn out". Wave shape analysis via a plot of E versus $\log(I_{lim}/I-1)$ will yield a value greatly in excess of the theoretical 59.1/n mV figure predicted at 25 ^{0}C as described in §2.5.3. Cyclic voltammetry of a reversible process under conditions of ohmic distortion will exhibit increased peak-to-peak separation exceeding the theoretically predicted 59.1 mV at 25 ^{0}C [44].

Ohmic drop can be kept to a minimum by reduction of the distance between working and reference electrodes. More recently, the literature has seen the emergence of microelectrodes as a means of overcoming ohmic distortion. Since the current passing through the cell is necessarily low, ohmic distortion is greatly reduced. Microelectrodes have been exploited for voltammetry in resistive solvents and using conventional solvents in the absence of supporting electrolyte.

Voltammetry in a range of resistive solvents has been reported using microelectrodes. Measurements in aromatic hydrocarbons such as benzene [45,46,47], chlorobenzene [45], and toluene [48,49,50] can be made routinely with the use of conventional electrolytes. For example, Bond et al report voltammetry of ferrocene in both toluene [48] and benzene [46] with $NHex_4ClO_4$ as supporting electrolyte using a 5 μm diameter platinum microelectrode. These researchers investigated the effects of ferrocene:supporting electrolyte ratios on the current-voltage response. Their results indicated that decreased substrate:electrolyte support ratios yielded increasingly "drawn out" waves arising from ohmic distortion. Typically support ratios in excess of 100 produced reversible Nernstian behaviour. This investigation demonstrates that despite the reduced susceptibility of microelectrodes to ohmic distortion, it does ultimately limit tolerance to a resistive solution.

Voltammetry in more resistive aliphatic hydrocarbon solvents presents a more significant challenge. Murray et al report voltammetry of ferrocene in heptane using a mixture of a fatty acid and fatty base as supporting electrolyte [51].

Very recently, Farrington and Slater have reported cyclic voltammetry directly in oil with $LiClO_4$ as supporting electrolyte [52]. This was achieved using a novel electrode assembly comprising a disposable gold microelectrode of 5 μm diameter and adjacent silver pseudo reference wire which minimised electrode separation to 5 μm. Characterisation of this novel electrode system was carried out using ferrocene. Wave shape analysis of the steady state wave obtained at 25 ^{0}C yielded a value of 60 mV indicative of a diffusion limited process without ohmic distortion. Voltammetry of an amine anti-oxidant was carried out to demonstrate the applicability of this technique as an oil degradation sensor. This investigation represents the first published voltammetric work undertaken in oil and demonstrates that voltammetry in highly resistive media is possible with the application of microelectrodes and with minimal separation between working and reference electrodes.

Microelectrode voltammetry using conventional solvents in the absence of supporting electrolyte has also been the subject of considerable investigation [53,54]. Development of theory to account for the absence of electrolyte taking into account double layer effects and migration of the electroactive species has been extensive [48,55,56].

Investigation of voltammetry in toluene has constituted some of the work undertaken in this thesis. To this end, microelectrode techniques were implemented as a means of overcoming ohmic distortion. A general introduction to the use and theory of microelectrodes is given in Chapter 2. Experimental details pertaining to the use of microelectrodes during this work are presented in Chapter 3. The elevated temperature apparatus developed as part of this thesis was aimed for use with resistive solvents which serve as models for oil. For this reason, design incorporated microdisc working electrodes and minimisation of the distance between reference and working electrodes.

1.8.2 Working at elevated temperatures

Previous electrochemical studies have frequently incorporated the use of elevated temperatures during investigations aiming to mimic the conditions of commercially viable processes. Studies are generally confined, however, to one temperature. Amongst the most frequently reported investigations are those using molten salt electrolytes. Molten salt mixtures have a variety of applications. They show promise as reaction media for the electrolytic extraction of metals [57] such as magnesium [58] and zinc [59,60]. These materials are also significant as electrolytes in rechargeable batteries and fuel cells [57]. Accurate elucidation of processes at elevated temperatures, typical of operational conditions in both these instances, is required as a means of improving efficiency.

Castrillejo et al report the electrochemical study of iron in the $ZnCl_2$ – 2NaCl molten salt. This mixture shows potential as a source of zinc metal [59,60]. The electrochemical behaviour of iron is significant in this case since it is contained as an impurity in zinc ores. Their investigation used linear sweep voltammetry and chronoamperometry as a means of studying the electrodeposition of iron from the melt at a range of different electrode substrate materials. Experiments were carried out at a temperature of 450 ^{0}C with the melt located in a Pyrex crucible inside a furnace.

Literature examples also include application of microdisc electrodes to elevated temperature studies. Yaegar et al implemented microelectrodes during a study comparing perfluoro-ethylene-1,2-bis-phosphonic acid and phosphonic acid as electrolytes in H_2/O_2 fuel cells [61]. Their investigation used chronoamperometry at platinum microelectrodes to obtain oxygen diffusion coefficients in both polymer electrolyte materials. Oxygen diffusivity is considered an important contributory factor to fuel cell performance [62]. Temperatures of up to 200 ^{0}C were used as a means of simulating typical fuel cell operating conditions.

Less routine are investigations incorporating a variable temperature strategy. Over a variable temperature regime, the rate and equilibrium constants of electron transfer processes vary to provide a useful handle on the characterisation of reaction mechanisms. As part of this thesis, we introduce a novel experimental approach to allow steady state microelectrode voltammetry at elevated and variable temperatures.

The apparatus was aimed for the study of ZDTP compounds and as such was designed with the typical operating conditions of the engine in mind. First, the apparatus is required to operate at temperatures typical of engine conditions. Work undertaken during this thesis was performed at temperatures of up to 100 ^{0}C. Temperatures were limited by volatility of the solvents used. The apparatus is designed for use at temperatures up to 200 ^{0}C with the application of less volatile hydrocarbon solvents. Secondly, design incorporated microdisc electrodes for use with resistive solvents as models for oil as outlined in §1.8.1. A detailed account of apparatus design and construction is presented in Chapter 4. Application of the apparatus to Bu^n-ZDTP is described in Chapter 9.

A demonstration of the applications of the novel elevated variable temperature steady state technique is given in Chapter 5. These include, first, the determination of diffusion coefficients at variable temperatures in the case of simple one electron transfer processes to yield activation parameters for diffusion and Stokes-Einstein radii and secondly, the accessing of rapid kinetic processes.

1.9 Overview of work presented in this thesis

In summary, the work undertaken during this thesis can be broadly divided into three sections.

First we are concerned with the development of voltammetric techniques relevant to the modelling of engine environments. A novel elevated temperature microelectrode apparatus has been developed for the study of voltammetric processes in resistive solvents. A detailed account of apparatus design and construction is presented in Chapter 4. An elevated temperature microelectrode apparatus has applications in addition to the study of resistive solvents. A demonstration of the applications of this technique in a variety of chemical scenarios is described in Chapter 5.

A demonstration of this novel experimental approach as a method for the evaluation of diffusion coefficients at varying temperatures is presented. Values obtained for *N,N,N′N′*-tetramethyl-p-phenylenediamine and tris(4-bromophenyl)amine were used to determine activation parameters for diffusion of the species in solution. The variation of diffusion with temperature was used to estimate effective radii for each compound via the Stokes-Einstein relationship. Variation of diffusion coefficient with temperature was also compared to the theoretically predicted relationship according to Wilke-Chang theory. Correlation of the results obtained for each of these two theories was linked to diffusional behaviour of each species in solution according to a "slip" or "stick" model.

Application of the technique to the study of rapid kinetic processes is described. Both ortho-bromonitrobenzene and 9-chloroanthracene are reduced via an ECE mechanistic scheme where halide bond cleavage constitutes the chemical step. In both instances, kinetic study of the bond cleavage process is hampered by rapid reaction of the intermediate chemical species. Microelectrode voltammetry at varying temperatures permits the "outrunning" of bond cleavage kinetics to give an n_{eff} of less than 2 from which rate constants can be evaluated. Arrhenius plots were used to determine the energy and entropy of activation for halide bond cleavage in both compounds.

Secondly this thesis seeks to assess the potential of electrochemical methods as an analytical tool for the study of ZDTP mechanistic action in their capacity as both anti-oxidant and anti-wear lubricant additives. The compound Bu^n-ZDTP has been used throughout this work as a typical ZDTP additive. A comprehensive study of Bu^n-ZDTP redox activity under standard electrochemical conditions using N,N-dimethylformamide (DMF) as solvent is presented in Chapter 6. Cyclic voltammetry of Bu^n-ZDTP at two different electrode substrate materials is compared. At both electrode surfaces, Bu^n-ZDTP is oxidised via an irreversible 2 electron process. Bu^n-ZDTP reduction proceeds via nucleation of zinc at the electrode surface. Differences in hostility to zinc deposition between the two surface materials are noted. The application of rotating disc electrode voltammetry to the determination of Bu^n-ZDTP diffusion in DMF solution is described. A detailed study of the zinc deposition process using chronoamperometric techniques is presented in Chapter 7. Current-time responses were modelled in terms of theoretical descriptions of nuclear growth to determine the zinc nucleation mechanism.

Preliminary studies of Bu^n-ZDTP redox activity under conditions more typical of an engine environment are presented in Chapter 9. Application of the novel microelectrode apparatus to an elevated temperature study of Bu^n-ZDTP is described. Voltammetric investigations in toluene, a resistive solvent which serves as a convenient model for oil, are discussed.

Finally, we describe the first application of atomic force microscopy to the study of Bu^n-ZDTP filming action in Chapter 8. Ex-situ studies were carried out in conjunction with cyclic and RDE voltammetry as a means of directly observing zinc deposits formed during Bu^n-ZDTP reduction.

References

[1] J. C. Bell, Engine Lubricants, Engine Tribology (Ed. C. M. Taylor), 1993, Elsevier, Ch9

[2] J. W. Crawford, Chemicals for the Automotive Industry, 1990, The Royal Society of Chemistry

[3] A. Cairns, R. Haycock, Automotive Lubricants Reference Book, Chapter 2, Mechanical Engineering Publications Ltd., 1996

[4] H. Spedding, R. C. Watkins, Tribology Int., 1982, **15**, 2, 9

[5] Y. Ohkatsu, K. Kikkawa, T. Osa, Bull. Chem. Soc. Jap., 1978, **51**, 12, 3606

[6] J.J. Dickert, C. N. Rowe, J. Org. Chem, 1967, **32**, 647

[7] P. G. Harrison, T. Kikabhai, Wear, 1987, **116**, 25

[8] P. G. Harrison, P. Brown, Wear, 1991, **148**, 123

[9] W. A. Glaeser, D. Baer, M. Engelhardt, Wear, 1993, **162-164**, 132

[10] D. Godfrey, ASLE Trans., 1962, **5**, 57

[11] B. A. Baldwin, ASLE Trans., 1976, **19**, 335

[12] R. C. Watkins, Tribology Intern., 1982, **12**, 1, 13

[13] J. M. Martin, M. Belin, J. L. Mansot, H. Dexpert, P. Lagarde, ASLE Trans., 1985, **29**, 4, 253

[14] P. A. Willermet, J. M. Pieprzak, D. P. Dailey, R. O. Carter III, N. E. Lindsay, L. P. Haack, J. E. deVries, ASLE J. O. T., 1991, **113**, 1, 38

[15] P. A. Willermet, D. P. Dailey, R. O. Carter III, P. J. Schmitz, W. Zhu, J. C. Bell, D. Park, Tribology Intern., **28**, 3, 165

[16] P. A. Willermet, D. P. Dailey, R. O. Carter III, P. J. Schmitz, W. Zhu, Tribology Intern., 1995, **28**, 3, 177

[17] P. A. Willermet, R. O. Carter III, E. N. Boulos, Tribology Int., 1992, **25**, 6, 371

[18] R. K. Jenson.,S. Korcek, L. R. Mahoney, M. Zinbo, J. Am. Chem. Soc., 1979, **100**, 7574

[19] A. J. Burn, Oxidation of Organic Compounds 1, **75**, Advances in Chemistry Series, (ed. R. F. Gould), ACS, Washington DC, 1968.

[20] J. J. Habeeb, W. H. Stover, ASLE Trans., 1987, **30**, 4. 419

[21] F. Rounds, Tribology Trans., 1993, **36**, 2, 297

[22] L. Margielewski, S. Plaza, The Analyst, 1992, **17**, 207

[23] A. J. Bridgewater, J. R. Dever, M. D. Sexton, J. Chem. Soc. Perkin II, 1980, 1006

[24] T. Colclough, Ind. Eng. Chem. Res., 1987, **26**, 1888

[25] J. L. Paddy, N. C. J. Lee, D. N. Waters, W. Trott, Tribology Trans., 1990, **33**, 1, 15

[26] S. Korcek, L. R. Mahoney, M. D. Johnson, W. O. Siegl, SAE paper 810014, 1981

[27] P. A. Willermet, L. R. Mahoney, C. M. Haas, ASLE Trans., 1979, **22**, 4, 301

[28] P. A. Willermet, S. K. Kandah, ASLE Trans., 1984, **27**, 1, 67

[29] F. T. Barcroft, D. Park, Wear, 1986, **108**, 213

[30] P. G. Harrison, T. Kikabhai, J. Chem. Soc Dalton Trans., 1987, 807

[31] Y. Yamada, J. Igarashi, K. Inque, Lubrication Eng., 1991, **48**, 6, 511

[32] P. G. Harrison, P. Brown, M. J. Hynes, J. M. Kiely, J. McManus, J. Chem Research (S), 1991, 174

[33] A. J. Burn, I. Gosney, P. S. G. Tan, J. P. Wastle, J. Chem Soc. Perkin Trans. 2, 1992, 1725

[34] A. J. Burn, I. Gosney, C. P. Warrens, J. P. Wastle, J. Chem Soc. Perkin Trans. 2, 1995, 265

[35] C. Westerfield, S. Agnew, Wear, 1995, **181-183**, 805

---

[36] J. C. Bell, K. M. Delargy, A. M. Seeney, Wear Particles, Elsevier, 1992

[37] K. L. Rhodes, P. C. Stair, J. Vac. Sci. Technol., A, 1988, **6**, 3, 971

[38] M. F. Fuller, Z. Yin, M. Kasrai, G. M. Bancroft, E. S. Yamaguchi, P. R. Ryason, P. A. Willermet, K. H. Tan, Tribology Int., 1997, **30**, 4, 305

[39] A. M. Shafiqul Alam, J. M. Martin, Ph. Kapsa, Analytica Chemica Acta, 1979, **107**, 391

[40] M. J. Hutchings, G. J. Moody, J. D. R. Thomas, The Analyst, 1987, **112**, 601

[41] A. M. Bond, A. T. Casey, J. R. Thackerey, J. Electrochem. Soc., 1973, **120**, 1502

[42] R. L. Blankespoor, Inorg. Chem., 1985, **24**, 1126

[43] E. A. Stezeryanskii, K. I. Litovchenko, V. S. Kublanovsky, J. Electroanal. Chem., 1995, **390**, 143

[44] A. M. Bond, The Analyst, 1994, **119**, 11, R1-R21

[45] R. Lines, V. D. Parker, Acta Chemica Scandinavica, B, 1977, **31**, 369

[46] A. M. Bond, T. F. Mann, Electrochim Acta, 1987, **32**, 873

[47] S. Nakabayashi, A. Fujishima, K. Honda, J. Electroanal. Chem., 1980, **111**, 392

[48] A. M. Bond, J. B. Cooper, J. Electroanal. Chem, 1991, **315**, 143

[49] C. Amatore, F. Plüger, Organometallics, 1990, **9**, 2276

[50] T. J. Cardwell, J. H. Santos, A. M. Bond, Analytica Chemica Acta, 1997, **340**, 169

[51] L. Geng, A. G, Ewing, J. C. Jernigan, R. W. Murray, Anal. Chem., 1986, **58**, 852

[52] A. M. Farrington, J. M. Slater, The Analyst, 1997, **122**, 593

[53] A. M. Bond, M. Fleischmann, J. Robinson, J. Electroanal. Chem., 1984, **168**, 299

[54] C. Amatore, M. R. Deakin, R. M. Wightman. J. Electroanal. Chem, 1987, **225**, 49

[55] J. B. Cooper, A. M. Bond, K. B. Oldham, J. Electroanal. Chem., 1992, **331**, 877

[56] K. B. Oldham, J. Electroanal. Chem., 1988, **250**, 1

[57] G. Picard, V. Villard, D. Ferry, J. M. Hicter, Y. Bertaud, Molten Salts, The Electrochemical Society Softbound Proccedings, **90**, 17, 550

[58] D. Schuzhen, P. Dudley, D. Inman, J. Electroanal. Chem., 1982, 142, 215

[59] Y. Castrillejo, A. M. Martinez, M. Vega, P. Sanchez Batabero, J. Applied Electrochem., 1996, 1279

[60] Y. Castrillejo, A. M. Martinez, M. Vega, E. Barrado, G. Picard, J. Electroanal. Chem.,1995, **397**, 139

[61] K. Kanamura, A. Tanaka, D. Gervasio, V. Kennedy, R. Adzic, E. B. Yaegar, D. Burton, R. Guneratne, J. Electrochem. Soc, 1996, **143**, 9, 2765

[62] E. Yaegar, M. Razaq, D. Gervasio, A. Razaq, D. Tryk, J. Serb. Chem. Soc., 1992, **57**, 819

Chapter 2

Theory

2.1 Introduction

In this chapter, an overview of the experimental techniques used during the course of this work is presented including a consideration of the theory behind and applications of each technique. Since much of the work reported in this thesis utilises electrochemical methods, we begin in §2.2 with a brief introduction to the controlling factors of electron transfer processes before considering mass transport in greater depth. In §2.3 we move onto general experimental requirements for an electrochemical investigation. The techniques utilised during this work are then considered in detail. Cyclic voltammetry, rotating disc electrode voltammetry, chronoamperometry and microdisc electrode voltammetry are considered in §2.4, 2.5, 2.6 and 2.7 respectively. We conclude the chapter with a review of the surface imaging technique atomic force microscopy in §2.8.

2.2 Nature of electron transfer

A simple electron transfer process in which species O is reduced to form species R is denoted in Equation 2.1:

$$O + ne^- \rightarrow R. \tag{2.1}$$

This reaction is, in general, composed of three steps, including transport of reactant to the electrode surface and removal of products in addition to the electron transfer step itself. The electrode reaction can be represented thus:

$$O_{bulk} \xrightarrow[\ ]{\substack{mass\\transport}} O_{electrode} \tag{2.2}$$

$$O_{electrode} \xrightarrow[\ ]{\substack{electron\\transfer}} R_{electrode} \tag{2.3}$$

$$R_{electrode} \xrightarrow[\ ]{\substack{mass\\transport}} R_{bulk}. \tag{2.4}$$

In many instances, the electrode reaction is more complex comprising coupled chemical reactions in addition to the possibility of adsorption, desorption and phase formation of the species involved. The current obtained in an electron transfer process can therefore be limited by any of the following factors.

1. Mass transport of reactants to the electrode surface.
2. Kinetics of the electron transfer process.
3. Coupled chemical reactions to the electron transfer step.

We now consider the forms of mass transport which control rate at which reactant is delivered to the electrode surface.

2.2.1 Mass transport

Three mechanisms exist by which reactant species are transported from bulk solution to the electrode surface and conversely by which products may be removed from the electrode surface into bulk solution. These are diffusion, migration and convection.

2.2.1.1 Diffusion

Diffusion is defined as the transport of mass under the influence of a concentration gradient. This process is therefore, by necessity, in operation as any electrochemical change occurs at a surface. As material undergoes reaction at an electrode, its concentration decreases relative to the bulk concentration and additional material will diffuse down the concentration gradient to the electrode surface.

Fick showed experimentally that diffusion was proportional to a concentration gradient, embodied in Fick's first law (Equation 2.5) [1]:

$$J = -D\frac{\partial c}{\partial x} \tag{2.5}$$

where J is the flux of material to the electrode surface in mol cm^{-2} s^{-1}, D is the diffusion coefficient and c corresponds to the concentration of the species of interest.

Diffusion alters the concentration gradient with time and Fick's second law describes the time dependence of the concentration of a species [2]. This is derived in the following way. Assuming diffusion occurs only in the x direction, and A is a cross-sectional area as defined in Figure 2.1, change in concentration at a location x is given by the difference in flux into and out of an element of width *dx*. Rate of entry at *x* and rate of leaving at *x*+*dx* are given by Equations 2.6 and 2.7 respectively:

$$\text{rate} = -DA\frac{\partial c}{\partial x} \tag{2.6}$$

$$\text{rate} = -\mathrm{DA}\left(\frac{\partial c}{\partial x} + \frac{\partial^2 c}{\partial x^2}\mathrm{dx}\right). \tag{2.7}$$

Subtraction of these two rates gives the rate of accumulation:

$$\text{rate} = -\mathrm{DA}\frac{\partial c}{\partial x} - \left[-\mathrm{DA}\left(\frac{\partial c}{\partial x} + \frac{\partial^2 c}{\partial x^2}\mathrm{dx}\right)\right] = +\mathrm{DA}\frac{\partial^2 c}{\partial x^2}\mathrm{dx}. \tag{2.8}$$

Division of the rate of accumulation by the volume of the considered area, Adx, yields Fick's second law:

$$\frac{\partial c}{\partial t} = D\frac{\partial^2 c}{\partial x^2}. \tag{2.9}$$

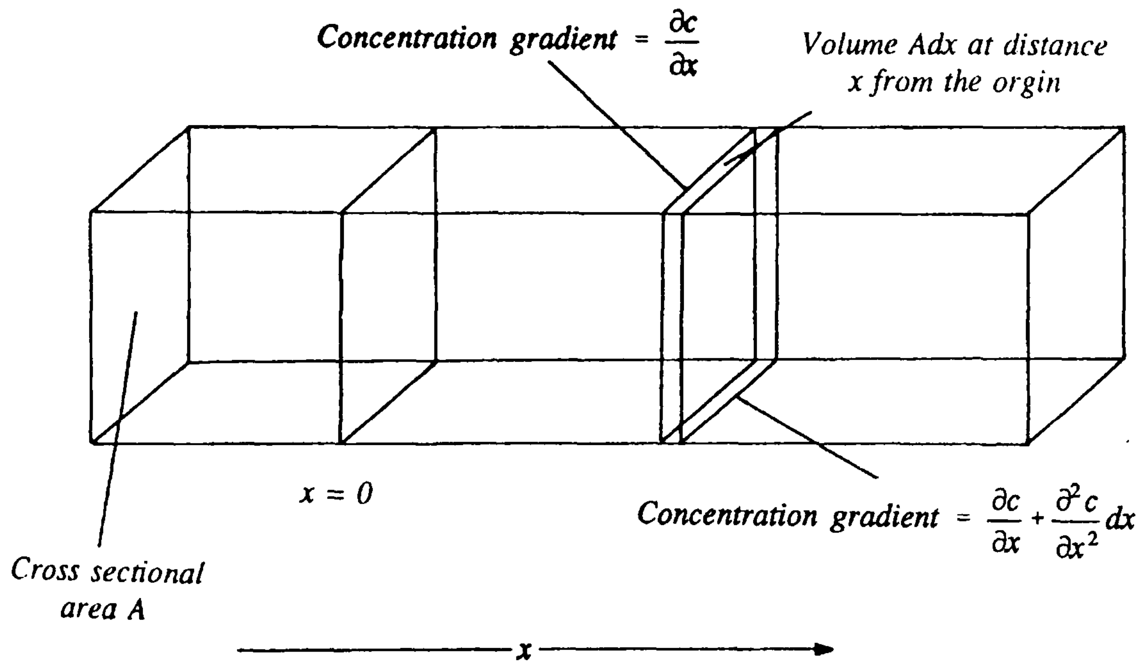

Figure 2.1: Volume element of length ∂x and cross-sectional area A for the derivation of Fick's second law in the case of planar diffusion

---

2.2.1.2 Migration

Migration is the movement of charged species under an electric potential gradient and is the mechanism by which charge passes through the solution to balance the passage of current through the external circuit. If the local potential φ varies in a direction x, then there will be an electrostatic force which acts upon a charged species which is opposed by viscous forces. This results in the species having velocity ν as denoted by Equation 2.10:

$$\nu = -\frac{z\mu}{|z|}\frac{\partial \phi}{\partial x} \tag{2.10}$$

in which μ is the mobility of the species with charge number z [3]. $|z|$ denotes the absolute value of the charge. Thus, the charge is reduced to unity in each case but direction of movement remains significant.

In general, the current produced by migration can be largely ignored since addition of supporting electrolyte, which serves to reduce migration of the electroactive species, is common experimental procedure. This occurs since the ions of the supporting electrolyte distribute themselves throughout the solution so as to nullify any potential gradients which are present, although current is still carried by the electroactive species. In the absence of supporting electrolyte, the migration flux is found to equal that of the diffusive flux, hence total current obtained is twice that of the supported case [4]. It has been shown that a 33-fold excess of supporting electrolyte is necessary to reduce the migratory component to 1% of the diffusive component [5].

2.2.1.3 Convection

Convection involves the transport of material via the mechanical motion of the solution. This may either be as a result of a density gradient, termed natural convection, or due to specific movement of the solution or electrode, eg via stirring or flowing of the electrolyte through a cell, which gives rise to forced convection. Two experimental approaches can be employed. Experiments can take the form of an unstirred solution over a short timescale, typically a matter of seconds, to eliminate both forced and natural convection. Alternatively, experiments can be performed employing forced convection applied in a controlled and quantifiable manner, such as in the case of the rotating disc electrode. In this way, the contribution of convection to the limiting current can be determined.

To describe the transport of material to the electrode surface as a result of forced convection, the flux of a species in one direction is dependant on solution velocity in that direction (Equation 2.11):

$$J = cv_x . \tag{2.11}$$

Thus to quantify the influence of forced convection, the flow regime of the solution must be known.

A detailed treatment of the hydrodynamics and solution of the convective-diffusion equation for the rotating disc electrode is presented in §2.5.1 and 2.5.2 respectively.

2.3 Experimental design for electroanalytical investigations

Electroanalytical investigations utilise an electrochemical cell as a means of investigating electron transfer processes. The cell is composed of reference and working electrodes with a measured potential difference between the two. By varying the voltage at the working electrode with respect to the reference electrode, a current will be obtained when oxidation or reduction of the electroactive species under investigation occurs.

Electrochemical techniques encompass a wide variety of procedures in which different parameters associated with the cell are varied and the effect on other parameters monitored. Such techniques can provide a range of information concerning the nature of the electron transfer process. Specific techniques utilised during the course of this work are considered later in this chapter. Consideration is now given to individual components within the experimental design.

2.3.1 Working electrode

The working electrode forms the surface at which the electrode reaction takes place. A number of different working electrode configurations are employed as a matter of course. They include flat, spherical and microelectrodes. Hydrodynamic working electrodes, such as the rotating disc electrode, are also frequently employed. Mass transport controls for each electrode configuration are well documented. Since electrodes are under different mass transport regimes, the type of information obtained for each electrode will vary. Electrodes used during this study are documented later in this chapter.

2.3.2 Reference electrode

The reference electrode consists of an ideal non-polarisable material with a well-defined redox couple which serves as the standard to which the working surface is connected and thereby the potential monitored against. Practically a reference electrode should be easily and reproducibly prepared and maintained, stable over time and usable under a wide variety of conditions. Reference electrodes commonly in use for aqueous systems include the saturated calomel and silver-silver chloride reference electrodes which both have well-defined potentials. The calomel reference electrode consists of a Hg/Hg_2Cl_2 emulsion immersed in a saturated aqueous KCl solution. The use of saturated aqueous KCl as the electrolyte allows the electrode to be conveniently used with the minimum of preparation whilst ensuring that a constant chloride concentration is maintained. The standard half-cell reaction which serves as the reference is

$$Hg_2Cl_2(s) + 2e^- \rightarrow 2Cl^-(aq) + 2Hg(l) \quad (2.12)$$

which occurs at a standard potential of +0.244 V at 25 ^{0}C [6]. The Ag-AgCl electrode is composed of a silver wire coated with silver chloride immersed in aqueous KCl solution. The standard half-cell reaction in this instance is denoted in Equation 2.13 which occurs at a standard potential of +0.205 V using 3.5 M KCl solution at 25 ^{0}C [6].

$$AgCl(s) + e^- \rightarrow Ag(s) + Cl^-(aq) \quad (2.13)$$

Pseudo-reference electrodes, such as silver and platinum, are also used frequently in organic solvents. However, these reference materials have potential couples which are less well-defined. Furthermore, the chemical nature of the redox couples which serve to stabilise the electrode potential is not always clear.

Inaccuracy can occur in the use of reference electrodes as a result of ohmic drop. When an external potential E_{appl} is applied to the cell, the working electrode shifts to a potential E relative to the reference which is equivalent to E_{appl} minus a contribution from ohmic distortion (iR_s) as shown in Equation 2.14:

$$E = E_{appl} - iR_s. \quad (2.14)$$

In instances where solution resistance is negligible, E can be taken as equal to E_{appl}.

For cases of low ohmic resistance, such as when passing small currents or in solutions of high conductivity, the actual potential at the working electrode can be approximated to the applied potential and a two electrode system can be used. For solutions in which ohmic resistance is high, such as when passing large currents or when using organic solvents of low conductivity, the applied voltage will not be equivalent to the potential of the working electrode. In this instance, it is preferable to use a three electrode system incorporating a counter electrode. In this case, current is passed between the working and counter electrodes with negligible current flow through the reference electrode.

2.3.3 Counter electrode

As noted previously, the counter electrode serves to complete the electrochemical cell so that current is passed to the working electrode without affecting the potential of the reference electrode. Composition of the counter electrode is not critical since its electrochemical properties do not affect the working electrode. However, it is generally composed of a substance that will not form products during the electrochemical process which will interfere with the reaction at the working electrode.

2.3.4 Control and measurement of potential

Experiments incorporating conventional sized working electrodes generally use a potentiostat for the measurement of current across the working-counter electrode pair and control of potential between the reference and working electrodes. The circuit of a typical potentiostat design is shown in Figure 2.2.

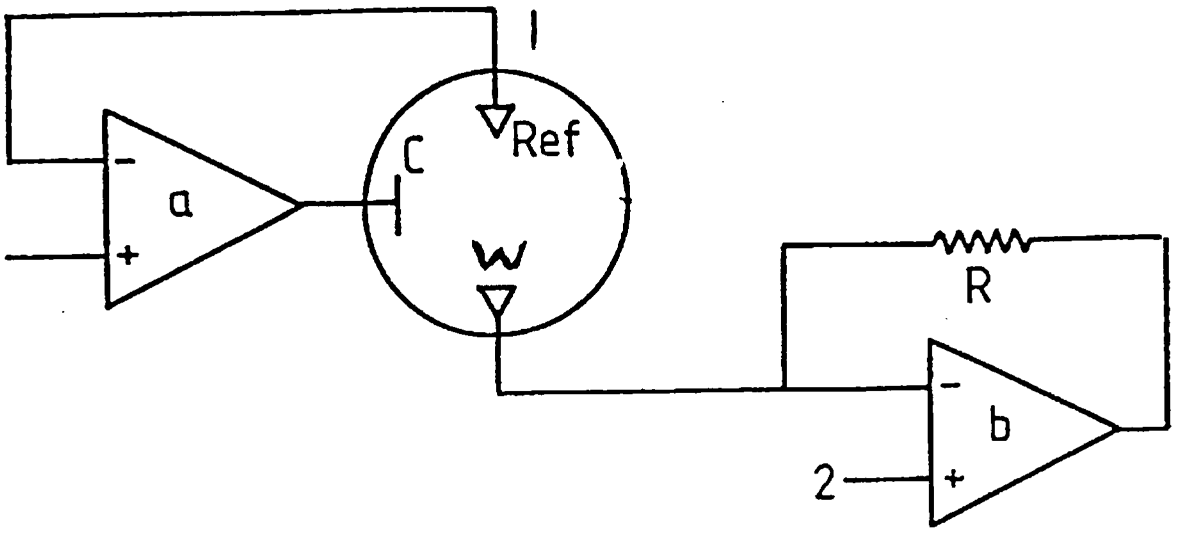

Figure 2.2: Circuit of a typical potentiostat

The potentiostat functions in the following way. The operational amplifier circuit, labelled *a* in Figure 2.2 functions as a voltage follower. This maintains the reference electrode at the desired potential, input into the circuit at point 1, while passing the bulk of the current through the counter electrode. A further operational amplifier labelled *b* in Figure 2.2 acts as a "current to voltage" converter to enable measurement of currents at the working electrode. Voltage is maintained at a potential which is input into the circuit at point 2, measurement of flowing currents then occurs as the voltage drops across a known resistor R.

Experiments using microelectrodes utilise a picoammeter as a means of measuring and controlling potential. Basic circuit design is similar to the potentiostat as shown in Figure 2.2. However, resistor R in the current-voltage converter *b*, which allows for the measurement of currents obtained at the working electrode, has a much higher resistance in comparison to the potentiostat. This allows for a more sensitive measure of the small currents, typically as low as 10^{-10} A, obtained at microelectrodes.

2.3.5 Supporting electrolyte

A supporting electrolyte is added to the solution in order to ensure solutions are sufficiently conductive thereby reducing ohmic loss, to reduce the thickness of the double layer and to provide a constant electric potential throughout the solution so as to eliminate electric migration effects. Practical considerations require the electrolyte to be soluble in the solvent to be used, inert so as not to have electrochemical signals which obscure signals of interest and to have a suitably wide potential window. In the case of organic solvents, utilised during the course of this work, tetraalkylammonium salts are frequently used due to their solubility in organic media and because they are less prone to reduction than alkali metal salts, widely used in aqueous solutions. Furthermore, R_4N^+ salts do not form tight ion pairs with anions. The most common choices of anion are ClO_4^-, BF_4^-, PF_6^-, BPh_4^-. These compounds are favoured since the delocalised charge aids their solubility in organic solvents, they are not prone to ion pairing and because they are not readily oxidised or reduced at electrodes [7].

2.4 Cyclic voltammetry

The technique of cyclic voltammetry involves application of a triangular wave potential to the cell as shown in Figure 2.3. As the cell potential is swept linearly with time, the current is recorded as a function of potential. Sweep rates can be varied and practically normally lie in the range 10 mV s^{-1} to 10 V s^{-1} for conventional sized electrodes with scan speeds of up to 10^6 V s^{-1} possible using microelectrodes. The increased response time which can be achieved with microelectrodes is explained in §2.7.1.2. Greater sweep rates introduce experimental difficulties such as double layer charging and ohmic drop which restrict their application.

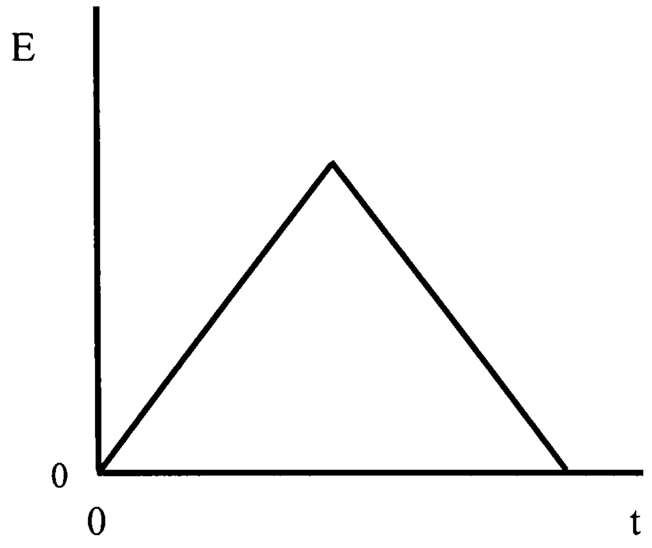

Figure 2.3: Triangular wave potential applied to the cell during cyclic voltammetry

A typical cyclic voltammogram showing the characteristic peak shape obtained for a simple electrochemically reversible process is shown in Figure 2.4.a. Electrochemical reversibility implies that both oxidised and reduced forms of the electroactive species are in equilibrium at the electrode surface. If the cell is in equilibrium, then the potential at the working electrode will be given by the Nernst equation [8]:

$$E = E^{\theta} + \frac{RT}{nF} \ln\left(\frac{[O]_0}{[R]_0}\right) \tag{2.15}$$

where E^{θ} is the standard electrode potential for the couple O and R, E is the equilibrium potential and $[O]_0$ and $[R]_0$ represent the surface concentrations of O and R respectively. If the potential of the working electrode is altered, equilibrium can only be restablished if the surface concentrations of O and R take up the new values as dictated by the Nernst relationship. This implies that the flow of current occurs through the cell as the potential is changed in order to maintain equilibrium at the electrode surface. The interchange between O and R at the electrode surface is controlled by two factors. First, the rate of mass transfer of O and R to the electrode and secondly, the electron transfer kinetics of the reaction. For the electrochemically reversible case, electrode kinetics are much faster than the rate of mass transfer to the electrode surface. Rate of mass transport is therefore the dominant control on voltammogram shape. The peak shape can be qualitatively explained by consideration of the reaction between O and R denoted in Equation 2.1, assuming this to be electrochemically reversible. No current flows in the region where species O is stable. Upon reaching the potential of the reversible couple O/R, current increases as O is reduced to form R. However, the current reaches a maximum since the rate of consumption of O is limited by transport to the surface from the bulk solution. The current then begins to decline since depletion of O from the electrode region reduces the flux to the electrode surface. Since electrochemical reversibility assumes the process to be also chemically reversible, a similar peak is observed upon reversal of the scan as R is reoxidised to form O.

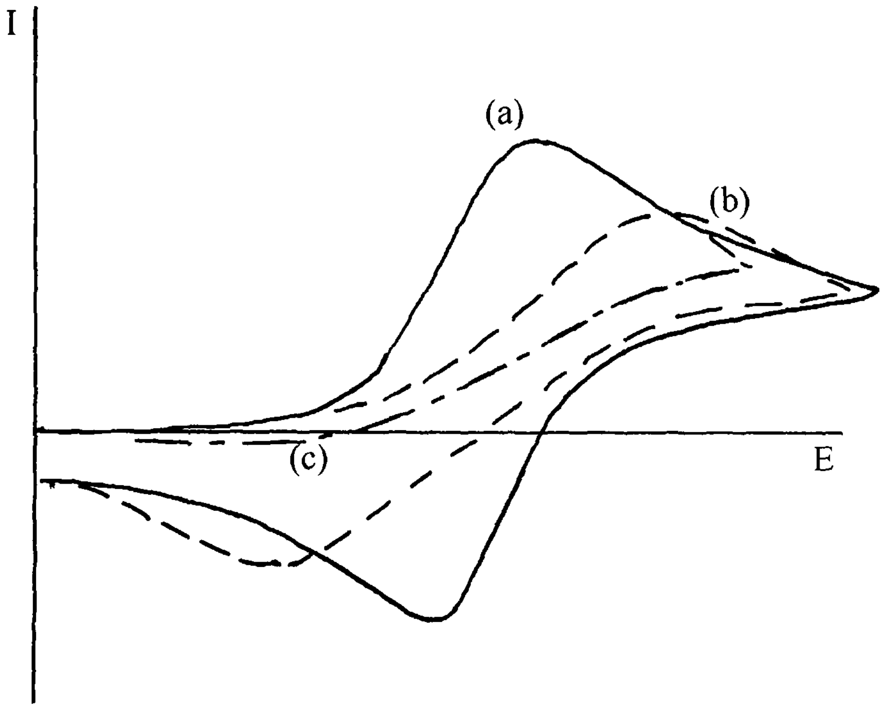

Figure 2.4: Cyclic voltammograms showing the characteristic peak shape for (a) electrochemically reversible (b) electrochemically irreversible and (c) chemically irreversible electron transfer processes

For the electrochemically irreversible case, the redox reaction is limited by electron transfer kinetics. The high kinetic barrier to the reaction is surmounted by applying an overpotential, η, which supplies the additional energy required for reaction to occur. A typical cyclic voltammogram obtained for an electrochemically irreversible process is shown in Figure 2.4.b. Both forward and reverse peaks are observed but peaks appear broader and there is greater peak separation.

For a chemically irreversible process, the reverse reaction is limited by subsequent chemical reaction of species R formed in the initial forward reaction. A cyclic voltammogram obtained for a chemically irreversible process is shown in Figure 2.4.c. The forward scan appears approximately identical to that obtained for the reversible case above, but the peak in the reverse scan is absent.

In addition to the extreme cases of irreversibility defined above, instances of intermediate behaviour between the reversible and irreversible cases are also observed and can be identified using cyclic voltammetry.

2.4.1 Applications of cyclic voltammetry

In principle, cyclic voltammograms can be used for the quantitative analysis of electron transfer processes. Solution of the diffusion equations for an electrochemically reversible process has been carried out [9]. However, for a time-dependant boundary condition, this is relatively complex. In addition, practical complications occur with the contribution of capacitative charging currents and ohmic distortion preventing accurate current determination. More frequently, cyclic voltammetry has found use in the determination of more qualitative data. Potentials at which electron transfer processes occur are readily obtained from cyclic voltammetry. Moreover, variation of the peak current with scan rate can provide a useful diagnostic test as to whether a process is diffusion controlled.

Cyclic voltammetry has also proved to be a useful tool in providing qualitative information concerning electrochemical mechanisms. Voltammogram shape is a useful diagnostic indication of the presence of coupled chemical reactions, complicating reaction kinetics and presence of complicating physical processes such as adsorption of a product. Examples of the chemically irreversible case, which has a following coupled chemical reaction, and the electrochemically irreversible case, with complicating reaction kinetics, have been described above.

2.5 Rotating disc electrode voltammetry

A rotating disc electrode allows voltammetry to be performed under steady state conditions. As in the case of cyclic voltammetry, current is recorded as a function of applied voltage. However, in this instance, a steady state regime is achieved by using the electrode to stir the solution so that a continuous supply of electrolytic material is presented to the electrode surface so as to remove the time dependence of the measurement.

The electrode consists of a disc of the working electrode material set within a non-conducting sheath so that the electrode and sheath are flush to ensure that only the face of the electrode is exposed to electrolytic solution. The electrode is rotated normal to the electrode surface. As the electrode rotates, adjacent solution is pulled along by viscous drag and thrown away from the axis of rotation by the centrifugal force. The expelled solution is replaced by flow normal to the electrode surface. The solution flow at a rotating disc electrode is depicted in Figure 2.5. This experimental protocol means that currents are enhanced as a result of the forced convection. Moreover, the technique provides a defined and reproducible experimental regime in which mass transport can be varied and controlled over a wide range. Typically scan rates in the range 1-5 mV s^{-1} are used to ensure that a steady state regime is maintained throughout the experiment.

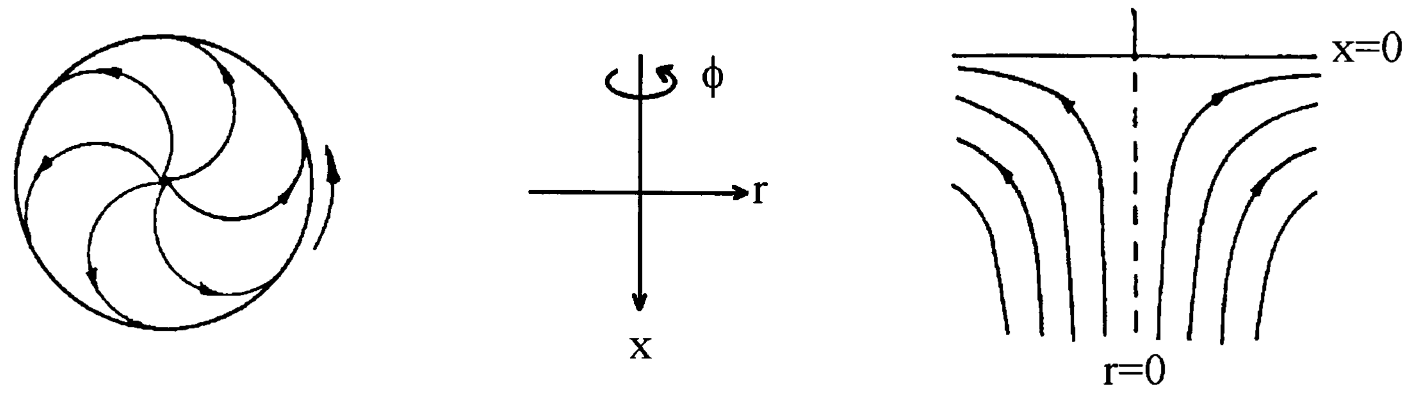

(a) (b)

Figure 2.5: Schematic representation of solution flow at a rotating disc electrode viewed (a) below and (b) sideways to the electrode surface

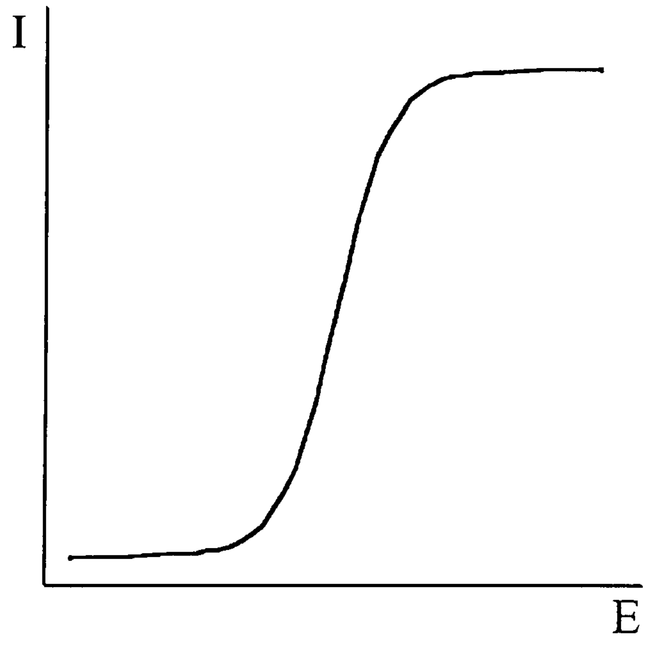

Figure 2.6: Typical steady state response obtained during RDE voltammetry

A typical steady state voltammogram obtained is shown in Figure 2.6. For an electrochemically reversible reaction, voltammogram shape can be explained with reference to the reaction considered previously in Equation 2.1. As the potential is scanned, no current is observed to flow in the region when O is stable prior to the potential of the O/R couple. However, upon reaching the potential at which reduction of O occurs, the current is observed to rise exponentially. As the potential is scanned further, the current ultimately reaches a plateau. This is the transport limited current where the maximum amount of material which can be brought to the electrode surface at the rate of forced convection employed is reached. The limiting current is thus dependant on the amount of convection in the solution, which is controlled by the rotation speed.

2.5.1 Hydrodynamics of a rotating disc electrode

The quantitative description of the flow profile depicted in Figure 2.7 is necessary if the current obtained at a rotating disc electrode is to be separated into its convective and diffusive components. Hydrodynamic equations can be defined in which the velocity profile, v, is expressed in cylindrical space in terms of the co-ordinates x, r, and ϕ as depicted in Figure 2.5. For cylindrical co-ordinates, the velocity profile v is:

$$v = \mu_1 v_r + \mu_2 v_x + \mu_3 v_\phi \tag{2.16}$$

where μ_1, μ_2, μ_3 are unit vectors in the direction of positive change for x, r, and ϕ at a given point [10]. The situation at the rotating disc electrode is complex since μ_1 and μ_3 have directions that depend on the position of the point. Treatment of this problem by von Karman and Cochran yielded values for the velocities of the flow along each of the three co-ordinates as follows [11,12]:

$$V_\phi = \mathrm{r}\varpi\theta(\mathrm{x}/\mathrm{x}_{\mathrm{Hy}}) \tag{2.17}$$

$$V_r = r\varpi R(x/x_{Hy}) \tag{2.18}$$

$$V_x = (\varpi \nu)^{1/2} X(x/x_{Hy}) \tag{2.19}$$

where

$$x_{Hy} = \left(\frac{\nu}{\varpi}\right)^{1/2}. \tag{2.20}$$

ϖ corresponds to the rotation speed in Hz, υ is the solution kinematic viscosity in cm^2 s^{-1}, and θ, R and X are functions of x/x_{Hy}. x_{Hy} is the hydrodynamic boundary layer thickness parameter which approximates to the thickness of the layer induced to rotate by the disc.

The flow profile of each of the velocity components, V_ϕ, V_r and V_x as a function of distance from the electrode surface where x=0 is shown in Figure 2.7. The spinning fluid velocity function, θ, is unity at the electrode surface where, as the disc spins, the solution next to the disc spins round with it. As distance x from the disc increases, the spinning motion is gradually quenched so that solution velocity decreases to 0. The spinning motion also induces radial flow away from the disc. The function R increases to a maximum when $x=x_{Hy}$ as solution is flung away from the disc centrifugally. Solution is replaced by a constant stream which flows towards the disc. As in the case of the spinning fluid velocity, the radial component decreases to 0 with distance from the surface due to quenching by the flow of fresh solution to the electrode surface. The function X, representing flow of solution normal to the disc, is 0 at the electrode surface. The normal component increases with distance from the electrode surface as the effects of slowing by the radial component at the hydrodynamic boundary layer lessen. X reaches a limiting value at distances greater than the value of $x=x_{Hy}$.

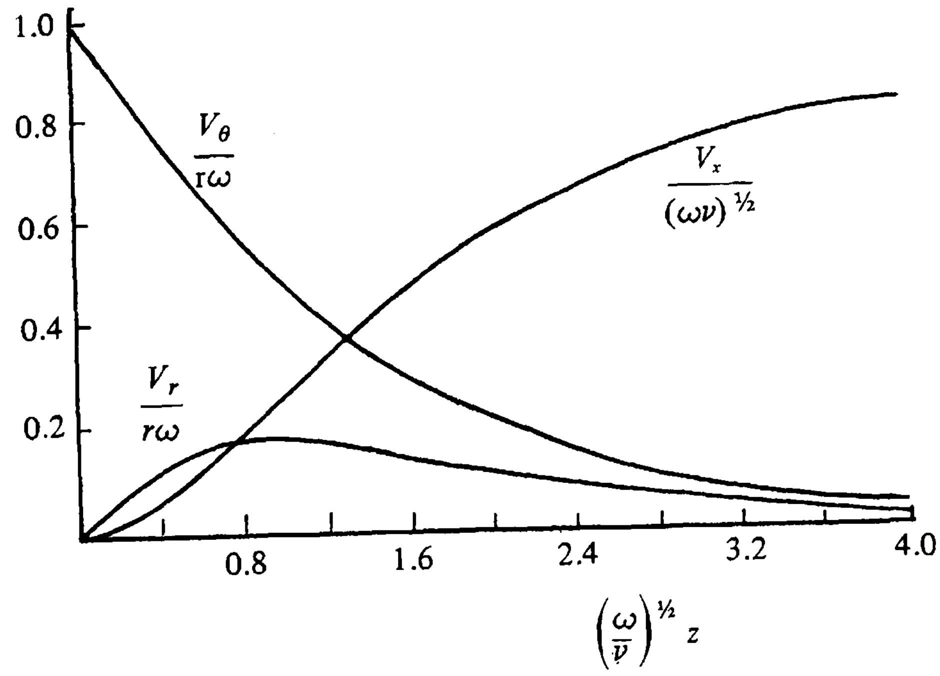

Figure 2.7: Dimensionless representation of velocity components as a function of distance from the electrode surface.

2.5.2 Transport to a rotating disc electrode

The full convective-diffusion equation at a rotating disc electrode may be expressed in cylindrical polar co-ordinates thus:

$$\frac{\partial c}{\partial t}=D\left(\frac{\partial^2 c}{\partial x^2}+\frac{\partial^2 c}{\partial r^2}+\frac{1}{r}\frac{\partial c}{\partial r}+\frac{1}{r^2}\frac{\partial^2 c}{\partial \phi^2}\right)-\left(V_r\frac{\partial c}{\partial r}+\frac{V_\phi}{r}\frac{\partial c}{\partial \phi}+V_x\frac{\partial c}{\partial x}\right). \qquad (2.21)$$

This can be simplified by the following considerations.

1. The system is totally symmetrical about the centre of the disc. This means that c is not a function of ϕ and therefore all $\partial c/\partial\phi$ and $\partial 2c/\partial\phi 2$ must be zero.
2. Provided the radius of the interface is small compared to that of the disc, Vx will be independent of r. This results in a uniform supply of material to the disc so that $\partial c/\partial r = \partial 2c/\partial r2 = 0$
3. For steady state measurements, $\partial c/\partial t = 0$.

This leads to considerable simplification of the convective-diffusion equation yielding:

$$v_x\left(\frac{\partial c}{\partial x}\right)=D\frac{\partial^2 c}{\partial x^2}. \qquad (2.22)$$

The value of the velocity component calculated for v_x can then be substituted into this equation which upon rearrangement gives:

$$\frac{\partial^2 c}{\partial x^2}=\frac{-x^2}{B}\frac{\partial c}{\partial x} \qquad (2.23)$$

in which $B = D\omega^{-3/2}v^{1/2}/1.28$. By integrating Equation 2.23 we obtain:

$$\frac{\partial c}{\partial x}=\left(\frac{\partial c}{\partial x}\right)_{x=0}\exp\left(\frac{-x^3}{3B}\right). \qquad (2.24)$$

Integrating once more yields:

$$\int_0^{c^*}dc=\left(\frac{\partial c}{\partial x}\right)_{x=0}\int_0^{\infty}\exp\left(\frac{-x^3}{3B}\right)dx. \qquad (2.25)$$

Thus:

$$c^*=\left(\frac{\partial c}{\partial x}\right)_{x=0}2.2394\left(\frac{3D\varpi^{-3}v^{1/2}}{1.28}\right)^{1/3}. \qquad (2.26)$$

The current corresponds to the flux of electroactive species to the electrode surface, that is:

$$I=nFAD\left(\frac{\partial c}{\partial x}\right)_{x=0}. \qquad (2.27)$$

Combining Equations 2.26 and 2.27 gives the Levich equation which describes the dependence of the limiting current on mass transport in terms of both diffusive and convective components where convection is dependant on rotation speed [13]:

$$I_{\text{lim}} = 1.554nFAD^{2/3}\nu^{-1/6}\omega^{1/2}c_{\infty}. \qquad (2.28)$$

This applies to the mass transport limited condition with no kinetic or mechanistic complications.

2.5.3 Applications of rotating disc electrode voltammetry

Since the convective-diffusion equations have been rigorously solved for a rotating disc electrode, the acquisition of quantitative data is readily possible using this technique. First, values for diffusion coefficients can be obtained by monitoring limiting current dependence on rotation speed using the Levich equation.

Secondly, analysis of steady state current/voltage waveshapes forms the basis of a diagnostic test for electrochemical reversibility. For a reversible couple, wave-shape is described by Equation 2.29 [14]:

$$E = E_{1/2} + \frac{RT}{nF}\ln\frac{I_{\text{lim}} - I}{I} \qquad (2.29)$$

where the symbols take their usual meanings. This equation predicts a wave that rises from baseline to diffusion-controlled region over a narrow potential range centred on $E_{1/2}$. For a reversible one electron process, a plot of E versus $\log(I_{\text{lim}}/I-1)$ for a series of points sampled along the wave will be linear with a slope of 59.1 mV at 25 ^{0}C. For a reversible 2 electron process, a steeper wave shape is anticipated and a plot of E versus $\log(I_{\text{lim}}/I-1)$ yields a slope of 28 mV at 25 ^{0}C. In contrast, for an electrochemically irreversible process, where coupled electrode kinetics limit the reversibility of the electron transfer step, a plot with slope significantly in excess of the value for a reversible reaction is obtained. This occurs since an overpotential is required to surmount the high kinetic barrier to the reaction. Thus, increased potentials will be necessary to achieve the same current as observed during sampling of the reversible wave. Correspondingly, waves appear more “drawn out”.

Thirdly, for reactions with coupled chemical reactions or complicating reaction kinetics, the magnitude of the current will be affected by these processes. Hence, this technique has frequently found use during mechanistic studies.

2.6 Chronoamperometry

Chronoamperometry is a potential step experiment in which current is recorded as a function of time. Practically the experiment is performed by stepping the potential applied to a cell from an initial value, E1, prior to the onset of an electrochemical process with negligible current flow to a final value, E2, beyond the half wave potential of the electrochemical process to be studied. The potential step profile during a chronoamperometric experiment is given in Figure 2.8.a with the typical current-time response obtained shown in Figure 2.8.b. For an electrochemically reversible reaction, the response obtained can be explained with reference to the reaction considered previously in Equation 2.1. As the current is stepped beyond the half-wave potential, O present in the vicinity of the electrode is reduced to form R giving rise to the current spike seen initially in Figure 2.8.b. With the depletion of O close to the electrode, a concentration gradient is produced with a resultant net flux of O to, and subsequent reduction at, the electrode surface. The concentration gradient decreases with time as the zone of O depletion near to the electrode increases. Thus, the flux of O to the electrode surface also decreases. This accounts for the "tail-off" of current with time as observed in Figure 2.8.b. Ultimately an approximately constant value is reached due to the onset of natural convection. The current-time response therefore levels out to a plateau with a current greater than zero.

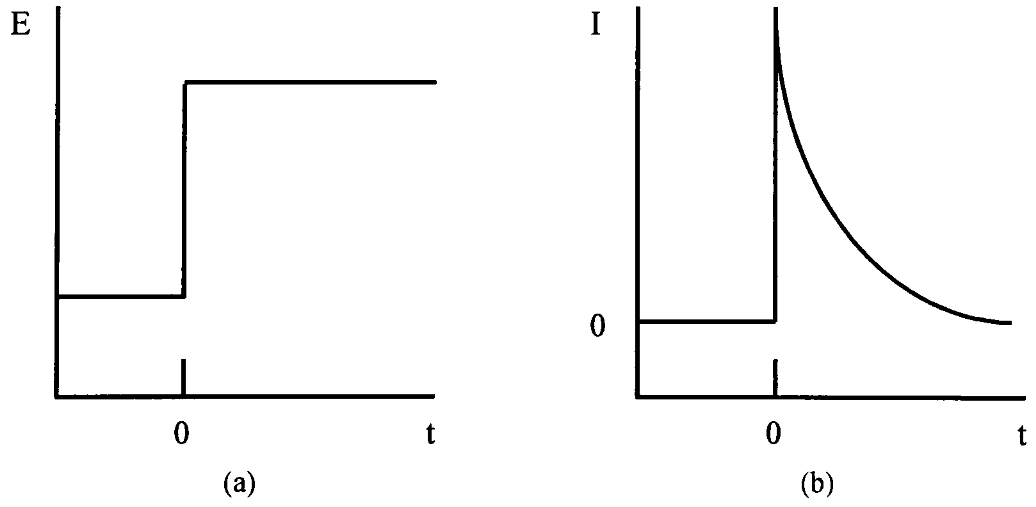

Figure 2.8: (a) Potential step profile and (b) typical current time response for a chronoamperometric experiment

2.6.1 Applications of chronoamperometry

For an electrochemically reversible system, chronoamperometry provides a method of determining diffusion coefficients. Diffusion limited current to a planar electrode was derived by Cottrell in 1902 (Equation 2.30) [15] and verified experimentally by Koltoff and Laitinen [16]:

$$I = nFAC^{\infty}\sqrt{\frac{D}{\pi t}}. \tag{2.30}$$

Hence a plot of I versus $t^{-1/2}$ will give a straight line with slope $nFAC^{\infty}(D/\pi)^{1/2}$ from which the value of D can be derived. However in practice this slope may deviate from linearity. At short timescales, this may occur due to a capacitative current caused by charging of the double layer which is superimposed onto the current response to give an additional spike initially in the current-time transient. At long time periods, the onset of natural convection will become significant in the transient obtained. For chronoamperometry performed using microelectrodes, the onset of radial diffusion over the timescale of the experiment will also cause deviation from the Cottrell relationship.

Chronoamperometic techniques can also be used to probe electrochemical processes in addition to the simple reversible case described above. This is possible since the current-time response obtained will reflect the influence of chemical steps in the electrochemical process in addition to electron transfer steps. A number of workers have elucidated the transient shape and current functions for a range of complex electrochemical mechanisms thus allowing for the determination of electron-transfer kinetic parameters [17].

Chronoamperometry is also a useful tool in the identification of phase formation processes which occur during an electrochemical reaction. The shape of the current-time response obtained is indicative of the nature of the phase formation process.

2.7 Microdisc voltammetry

Microelectrodes are defined as electrodes which have at least one dimension of the order of 0.1 to 25 μm [18]. They have been constructed in a number of different geometries including inlaid discs, cylinders, hemispheres and bands [18]. The present discussion will be confined to microdisc electrodes since these are by far the most common geometry reported in the literature and because these were used exclusively during the course of this work.

2.7.1 Characteristics of microdisc electrodes

The small size of these electrodes gives rise to a number of unique properties in comparison to their macroelectrode counterparts, namely increased mass transport, faster response time and reduced ohmic distortion.

2.7.1.1 Mass transport

First we compare the mass transport characteristics of conventional sized and microdisc electrodes. Over the timescale of an experiment, the diffusion layer which forms as the reaction proceeds at a macroelectrode is always small in comparison to the electrode dimensions. Thus mass transport, under conditions where convection is negligible, is dominated by diffusion normal to the electrode surface. In contrast, the diffusion layer at a microdisc becomes comparable in size to the electrode after a very short time period. When this happens, radial diffusion to the electrode surface becomes significant. A comparison of the diffusion regimes at macro- and microdisc electrodes is depicted in Figure 2.9.

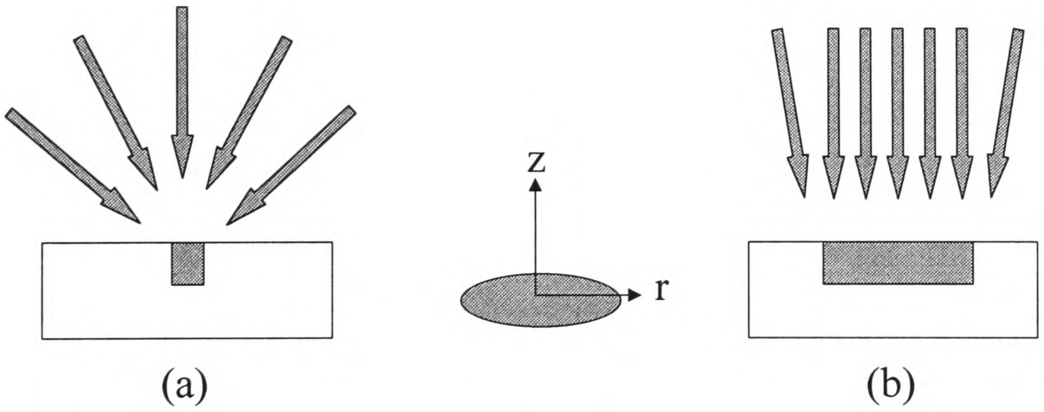

Figure 2.9: Diffusion regimes for (a) microdisc and (b) macro electrodes

Over very short experimental timescales, when the diffusion layer is still very thin, the electrode behaves as if it were a macroelectrode. For example, cyclic voltammograms consist of the characteristic peak shape obtained at macroelectrodes. However at longer timescales, when the diffusion layer is large in comparison to electrode size, mass transport to the electrode is correspondingly large resulting in a steady state regime.

Theoretical treatments of mass transport to a microdisc electrode must take into account radial diffusion. The diffusion equation for a microdisc electrode including both the co-ordinate normal to the electrode surface, z, and the radial distance, r, as shown in

Figure 2.9, is:

$$\frac{\partial c}{\partial t} = D\left(\frac{\partial^2 c}{\partial r^2} + \frac{1}{r}\frac{\partial c}{\partial r} + \frac{\partial^2 c}{\partial z^2}\right). \tag{2.31}$$

A closed form solution of this equation is not possible. However, Soos and Ligane showed that Equation 2.32 provided satisfactory agreement with experimental diffusion controlled currents [19]:

$$I = nFAC^{\infty}\left(\frac{1}{\sqrt{\pi D t}} + \frac{b}{r^0}\right) \tag{2.32}$$

where n corresponds to the number of electrons transferred during the electrode process, F is the Faraday Constant, C^{∞} is the bulk concentration of the species being electrolysed, D refers to the diffusion coefficient, r^0 corresponds to the electrode radius and b is an empirical constant (equivalent to 1 for a spherical electrode). At short times or large electrodes, $\sqrt{\pi Dt}$ is less than r^0 and the current drops as $1/\sqrt{t}$. Over increasing timescales where $\sqrt{\pi Dt}$ is greater than r^0, the current becomes time-independent correlating to the onset of radial diffusion.

This solution was further modified by Heinze who tested Equation 2.32 using digital simulation techniques [20]. He found that b was not quite constant and ranged from 1 at short times to $4/\pi$ over long timescales. The steady state diffusion current is therefore given by Equation 2.33:

$$I = 4nFC^{\infty}Dr^0. \tag{2.33}$$

2.7.1.2 Faster response times

The second important feature of microdisc electrodes is the faster response times which can be accessed in comparison to conventional sized electrodes. The significance of capacitative charging currents in reduced accuracy during cyclic voltammetry at fast scan rates and the appearance of a current charging spike in chronoamperometric experiments has been described. Such problems arise since the surface of the electrode behaves like a capacitor and when a change in potential is applied to the electrode, a charging current is produced due to the movement of ions to and from the electrode. Since magnitude of the current will depend on the size of the capacitor, which in this case is the electrode area, the contribution from the charging current will be greatly reduced at a microdisc electrode. In addition the charging current decays much more quickly than at conventional electrodes. The accessible timescale of experiments is therefore greatly increased at a microdisc electrode.

2.7.1.3 Reduced ohmic distortion

The third important characteristic of microdisc electrodes is their reduced susceptibility to ohmic distortion in comparison to macroelectrodes. Ohmic distortion can be expressed in terms of the product of current and solution resistance. Since with the implementation of microelectrodes current passing through the cell is very low, typically of the order of nA, the problems of ohmic distortion are greatly reduced.

2.7.2 Uses of microdisc electrodes

The characteristics of microdisc electrodes are reflected in the areas in which they have found application. Since a steady state regime is reached over a short timescale, the use of microdiscs has extended the range of steady state techniques and has facilitated the recording of steady state data quickly and easily. Steady state curves can be used to determine diffusion coefficients and can provide information concerning reversibility of a process as described for rotating disc steady state voltammetry in §2.5.3.

As a result of the decreased influence of ohmic distortion on microdisc electrodes, the range of media in which electrochemical experiments are possible has been greatly extended. Microdiscs have frequently found use in the observation of voltammetry in resistive solvents and in conventional solvents in the absence of supporting electrolytes. For example, well defined current voltage curves have been recorded in heptane and oils. An account of the use of microdiscs in this field is presented in §1.8.1. Microdiscs have also facilitated electrochemical investigation into more "exotic" media such as the solid and gas phases in which ohmic drop poses significant problems. For example, in the solid phase, Wooster et al have carried out a study on poly(ether) polymers as both films deposited on the electrode surface and with the electrode embedded in a bulk sample of polymer. These compounds are used in the formation of polymer electrolytes [21]. Such materials exhibit low conductivity but voltammetric studies have been possible due to the reduced ohmic distortion at microdisc electrodes. In the gas phase, Fleischmann et al have demonstrated the carbon electrode as an electrochemical detector for a range of organic compounds in gas-phase chromatography [22,23]. This procedure further demonstrates the applicability of microdisc electrodes to electrochemical measurements in resistive media.

The decreased response time has resulted in the application of microdisc electrodes to the study of fast electrode reactions without distortion from ohmic drop and charging current. For example, current transients below a millisecond can be observed and voltammograms at scan rates above 10^6 V s^{-1} can be recorded [24,25,26].

Microdisc electrodes have also been exploited for use principally as a result of their small physical size. One such area where microdiscs have found wide usage is in the study of physiological processes where the miniaturisation of electrodes has facilitated electrochemical measurements in biological samples with minimum disruption to tissues. Many such studies have been reported in the literature illustrating how widely microdiscs have been used in this field. For example, Crespi reports the use of carbon-fibre microdisc electrodes in the determination of the oxidation potential of carboxylic acids present in rat brain slices [27]. As electrode fabrication techniques have become increasingly sophisticated, recent years have seen the implementation of microelectrodes with tips small enough to enable processes in individual cells to be monitored. For example, Hardingham et al have used microdisc electrodes to investigate reactions in individual neurones [28].

Microdisc voltammetry has been utilised during the course of this work as a means of probing electrochemical reactions in resistive solutions. Since the high temperature electrochemical apparatus, designed and constructed during the course of this work, was designed for application to resistive solvents, this apparatus also incorporated the use of microdisc electrodes.

2.8 Surface studies using atomic force microscopy

2.8.1 Scanning probe microscopy

Scanning probe microscopy is the general label given to the family of techniques which involve rastering a tip of atomic resolution across a sample to derive spatially resolved information based on a physical characteristic of the surface displaying heterogeneity. All scanning probe microscope (SPM) techniques are descendants of the scanning tunnelling microscope (STM) conceived by Binnig and et al in 1981 [29] and implemented with atomic resolution by the same workers in 1982 [30]. The STM experiment is based upon the spatial variation in quantum-mechanical tunnelling of electrons between a sharp tip and conducting sample. Electron tunnelling occurs when the tip and sample are sufficiently close so that their wavefunctions overlap, generally within a few angstroms of one another, and is maintained by a bias potential between the two. Since size of the tunnelling current is strongly distance dependant [31], it provides a mechanism by which surface topography can be mapped. Information can be obtained in either of two ways. During constant current mode, the tip-sample distance can be monitored as the tip is drawn across the sample at constant tunnelling current. Vertical movement of the tip provides a direct measure of surface topography. Tip movement is controlled using piezoceramics, the expansion and contraction of which can be controlled with sub-angstrom precision. Constant height mode involves measurement of the magnitude of tunnelling current as the tip is scanned at fixed tip-sample separation. Schematic representations of constant current and constant height operation are shown in Figures 2.10.a and b respectively.

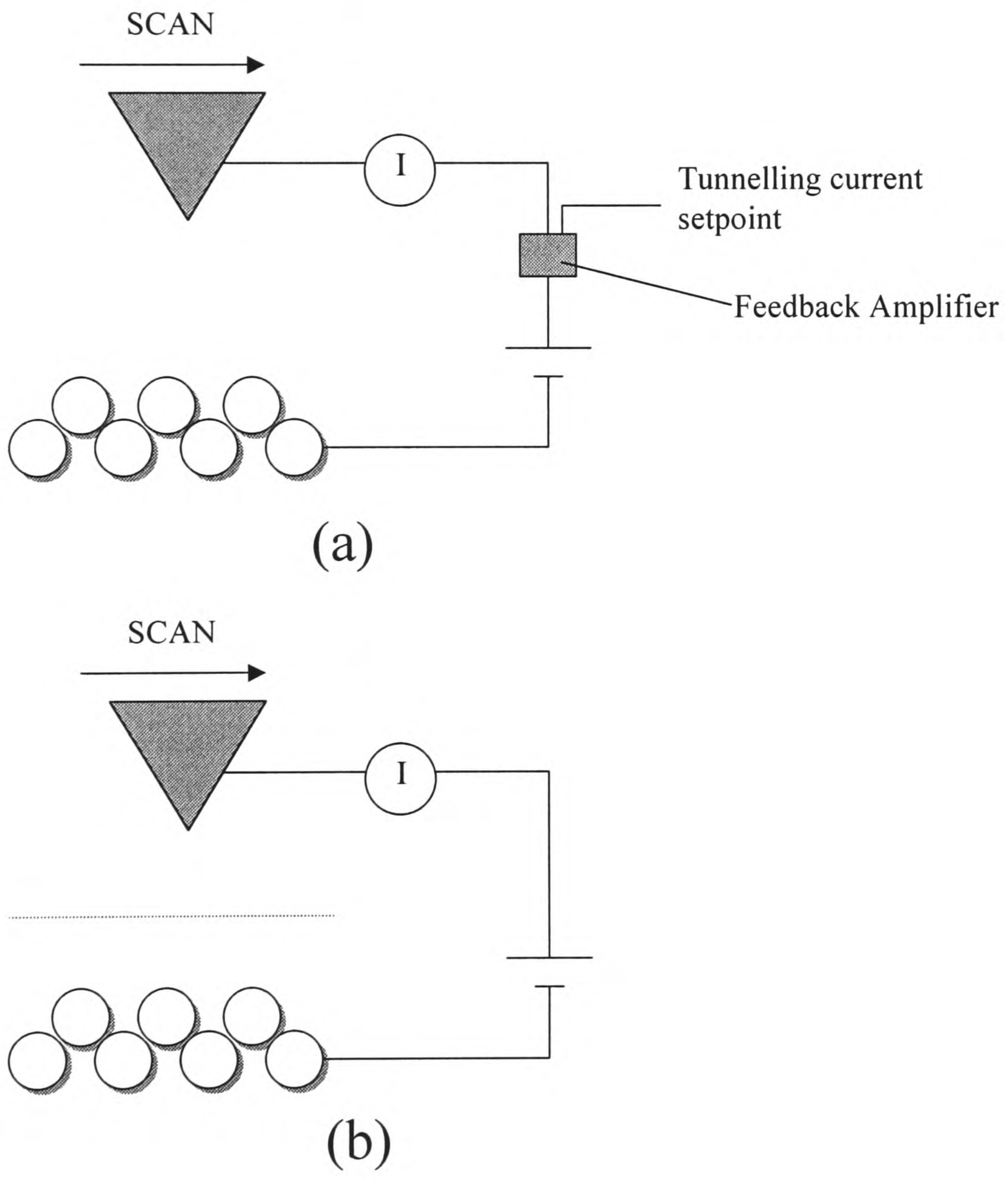

Figure 2.10: Schematic representation of STM operation in (a) constant current mode where vertical movement of the tip correlates to surface topography and (b) constant height mode where variations in tunnelling current are used to image the sample surface

The range of SPM techniques was extended in 1986 with the development of the atomic force microscope (AFM) which uses tip-surface force interactions as a means of probing the sample surface. The AFM was used during the course of this work and is described in detail in the following section. Since the inception of the STM and AFM, a wide range of variant techniques have been developed which are based on the measurement of forces or tunnelling currents as a means of obtaining surface information A brief introduction to some of the SPM techniques commonly in use as a demonstration of the wide range of methods now available, including a comparison of operational details and information which can be obtained, is presented in Table 2.1.

SPM technique	**Operational Details**	**Lateral Resolution**	**Applications**	**Ref.**
Scanning Tunnelling Microscopy	Tunnelling currents between tip and sample are used to image the sample either at constant height or at constant force with feedback control.	nm	Conducting and semi-conducting samples	29,30
Contact Atomic Force Microscopy	Short-range repulsive forces between tip and sample are used to image the sample by measuring deflections of a scanning probe with known effective spring constant at constant height or as part of a feedback control system which adjusts tip-sample separation to maintain a constant force.	nm	Hard samples, both insulating and conducting	32,33
Atomic Force Microscopy Force Modulation	The scanning probe is modulated at very low frequency ca. 5 kHz with amplitude 0.5-1 nm during normal contact AFM imaging.	nm	As above, force modulation allows enhanced contrast topographic images to be obtained.	34
Non-contact Atomic Force Microscopy Low amplitude resonance	Long-range attractive forces between tip and sample are used to image the sample with a tip-sample separation of 0.1-10 nm. The cantilever is vibrated at 5-500 kHz with amplitude 0.2-10 nm. Changes in resonant frequency as a result of tip-surface force interactions are measured and can be used as part of a feedback control system to maintain a constant resonant frequency via adjustment of sample-tip separation.	Low	Soft samples which are less likely to be damaged using this technique since forces exerted by the tip on the sample are minimised in contrast to contact Atomic Force Microscopy.	35
Non-contact Atomic Force Microscopy High amplitude resonance	As above with oscillation of the cantilever at 50-500 kHz and amplitude 10-100 nm.	Low	Very soft and poorly adhered samples since tip-sample force interactions are minimised further in comparison to contact Atomic Force Microscopy	32

Tapping Mode Atomic Force Microscopy	The scanning probe is vibrated at a frequency of 50,000-500,000 Hz with amplitude up to 20 nm. Tip-sample force interactions affect the vibrational amplitude which can be monitored and used as part of a feedback control system which adjusts tip-sample separation to maintain constant vibrational amplitude.	nm	Soft samples since tip-sample interactions are reduced in comparison to contact mode Atomic Force Microscopy	36
Frictional Force Microscopy	In addition to forces normal to the surface, lateral forces are measured by detecting induced torsion mode deflections of the cantilever using a 4-segment PSD during scanning.	nm	Tribological investigations	37
Magnetic Force Microscopy	Using a magnetic tip, magnetic interaction of the tip and sample occur when the tip is within 1-50 nm of the sample. Magnetic interaction is monitored by measurement of changes in cantilever resonant frequency as described for non-contact Atomic Force Microscopy above.	10-100 nm	Spatial variation of magnetic domains, eg in recording media	38
Electrostatic Force Microscopy	An ac bias is applied between the tip and an electrode behind the sample which causes an oscillating charge on the electrode and tip with a resulting tip-electrode force. As the sample is scanned, changes in the phase of this oscillating force occur which are indicative of the sign of the surface charge.	Low	Real space imaging of electrical charge distribution on a surface such as domains and domain walls in ferroelectric materials	39
Chemical Force Microscopy	Chemically functionalised tips are used as the scanning probe. Reactions between tip and surface are used as a means of mapping the surface in terms of chemical structure.	10 nm	Probing chemical bond energies and mapping the spatial arrangement of functional groups.	40
Capacitance Microscopy	A metallised cantilever is used to scan the sample. Changes in capacitance are measured and used as part of a feedback control system which adjusts tip-sample separation to maintain constant capacitance.	25 nm	Real space imaging of surface dielectric properties	41

Scanning Electrochemical Microscopy	Using an ultramicroelectrode as the scanning tip, faradaic currents which arise from reduction or oxidation of the surface species as the tip rasters the sample are measured.	10 nm	Used to provide chemical information on a surface, such as mapping of the local concentration of an electroactive species in addition to topographic imaging	42,43
Scanning Micropipette Microscopy	The probe comprises an electrolyte filled micropipette. As the probe scans the surface, changes in tip-sample conduction are monitored and used as part of a feedback control system which adjusts tip-sample separation to maintain constant conductance	200 nm	Insulating samples in electrolytic solutions	44
Scanning Near Field Acoustic Microscopy	A quartz tuning fork is used as an oscillator driven at resonance with one leg serving as the probe tip. Changes in oscillation amplitude or frequency as the tip rasters the surface are measured and used as part of a feedback control system which adjusts tip-sample separation to maintain constant oscillation.	1 µm	Both conducting and non-conducting samples	45

Table 2.1: Overview of SPM techniques

2.8.2 The atomic force microscope (AFM)

In contrast to the STM, the AFM senses forces between the scanning probe and the sample to produce an image of the sample topography. As in the case of the STM where tunnelling current is dependant on tip-sample separation, the AFM utilises the relationship between force and distance as a means of mapping the surface. Since this does not require either the tip or sample to be conducting, the range of samples which can be investigated has been greatly extended to include insulating materials. The technique was introduced by Binnig and co-workers in 1986 [32] who subsequently reported atomic resolution in 1987 [46].

2.8.2.1 AFM instrumentation

A schematic diagram of the AFM instrumentation is depicted in Figure 2.11. In general, the experiment comprises a scanning probe together with a means of probe detection and a sample mounted on a piezoceramic to allow sample movement with respect to the probe. This instrumentation is coupled with electronics to facilitate feedback and sample scanning together with computer automation. Specific requirements of individual components within the AFM instrumentation are now considered.

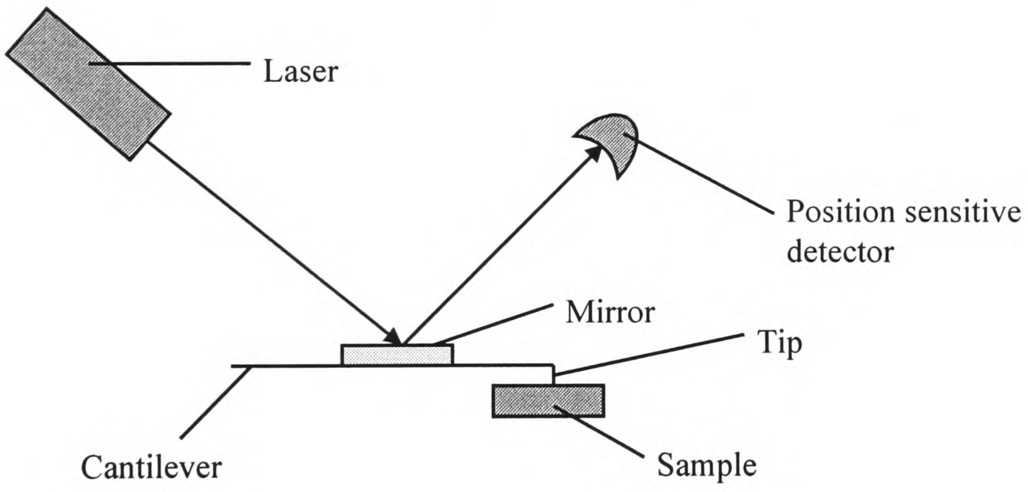

Figure 2.11: Schematic representation of AFM instrumentation

The force sensor of an AFM consists of a scanning tip attached to a cantilever beam which behaves as a weak spring and deflects under the influence of interactions with forces from the sample surface. The force sensor is required to have several properties. First, we consider requirements of the cantilever. The cantilever should have a sufficiently small spring constant to allow detection of small forces. In addition, the resonant frequency of the cantilever spring should be sufficiently high so as to minimise sensitivity to low frequency mechanical vibrations [32]. To achieve this, cantilevers are generally microfabricated via photolithographic techniques from pure silicon, silicon oxide or silicon nitride [47]. Fabrication in this manner allows lateral and thickness dimensions of 100 μm and 1 μm to be achieved respectively which ensures spring constants in the range 0.1-1 N m^{-1} and resonant frequencies of 10-100 kHz. Secondly, we consider requirements of the tip. Scanning tips are required to be sharp with small effective radius of curvature to ensure atomic resolution [48]. This has been achieved using pyramidal and conical tips integrated onto silicon nitride and silicon oxide cantilevers [47]. Furthermore, tip opening angles should be as small as possible to enable penetration into troughs on the sample surface. Opening angles have been improved with the advent of microfabricated AFM tips [49]. Scanning probes used during this thesis comprised microfabricated silicon nitride cantilevers with integrated pyramidal tips.

Cantilever deflections can be monitored with high sensitivity in a number of ways. Techniques which have been utilised include electron tunnelling, in which tunnelling from the cantilever to an adjacent STM tip was used as a means of recording cantilever movement [32]. Capacitance detection has also been used in which a counter electrode positioned adjacent to the cantilever measures changes in distance which occur as the cantilever undergoes deflection [50]. In recent years, the most frequently used method, and the one used in this instance, is laser beam detection implemented initially by Meyer and Amer [51]. In this method, cantilever displacement is measured by detection of a laser beam reflected from a mirror mounted on the near side of the cantilever as schematically illustrated in Figure 2.11. Laser deflection is recorded by means of a position sensitive detector comprised of photo-active segments. During imaging, the sample is moved beneath the tip as opposed to movement of the delicate tip mount. To achieve this, the sample is mounted on a piezoceramic stage which allows movement of the sample beneath the tip. It also allows movement of the sample up and down as required during constant force imaging mode.

2.8.2.2 Imaging modes of the AFM

Different imaging modes in atomic force microscopy arise according to how the scanning tip is positioned and moved with respect to the sample. AFM experiments can be classified as to whether they are operating in the repulsive or attractive force regime of the sample. The variation of force with distance from a surface is depicted in Figure 2.12.

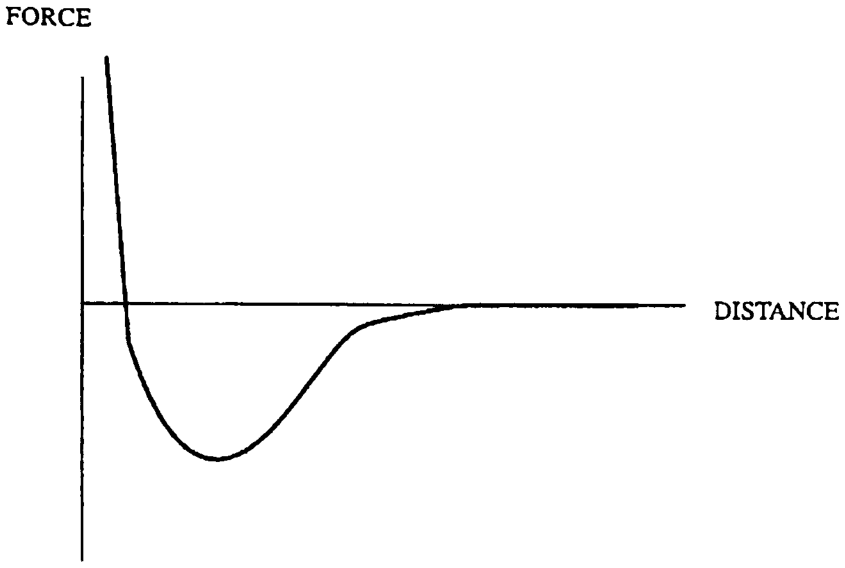

Figure 2.12: Variation of force with distance from a sample surface during AFM experiments

Experiments performed in contact mode operate in the repulsive regime of the sample in Figure 2.12. Upon interaction of the tip with such repulsive forces, the cantilever is distorted away from the sample. As in the case of the STM, two imaging methods are possible. Constant force microscopy is analogous to constant current mode in the STM. In this method, the deflector signal is kept constant by means of a feedback circuit which controls the motion of the piezoceramic stage, in order to maintain a constant tip-sample separation. The output signal of the feedback loop is used to produce a surface map. The AFM can also be operated without feedback control analogous to constant height mode in the STM. In this case, deflections in the cantilever beam which occur with changes in tip-sample separation as the sample is scanned at a fixed height position form the basis of surface mapping. Schematic representations of constant force and constant height operation are shown in Figures 2.13.a and b respectively.

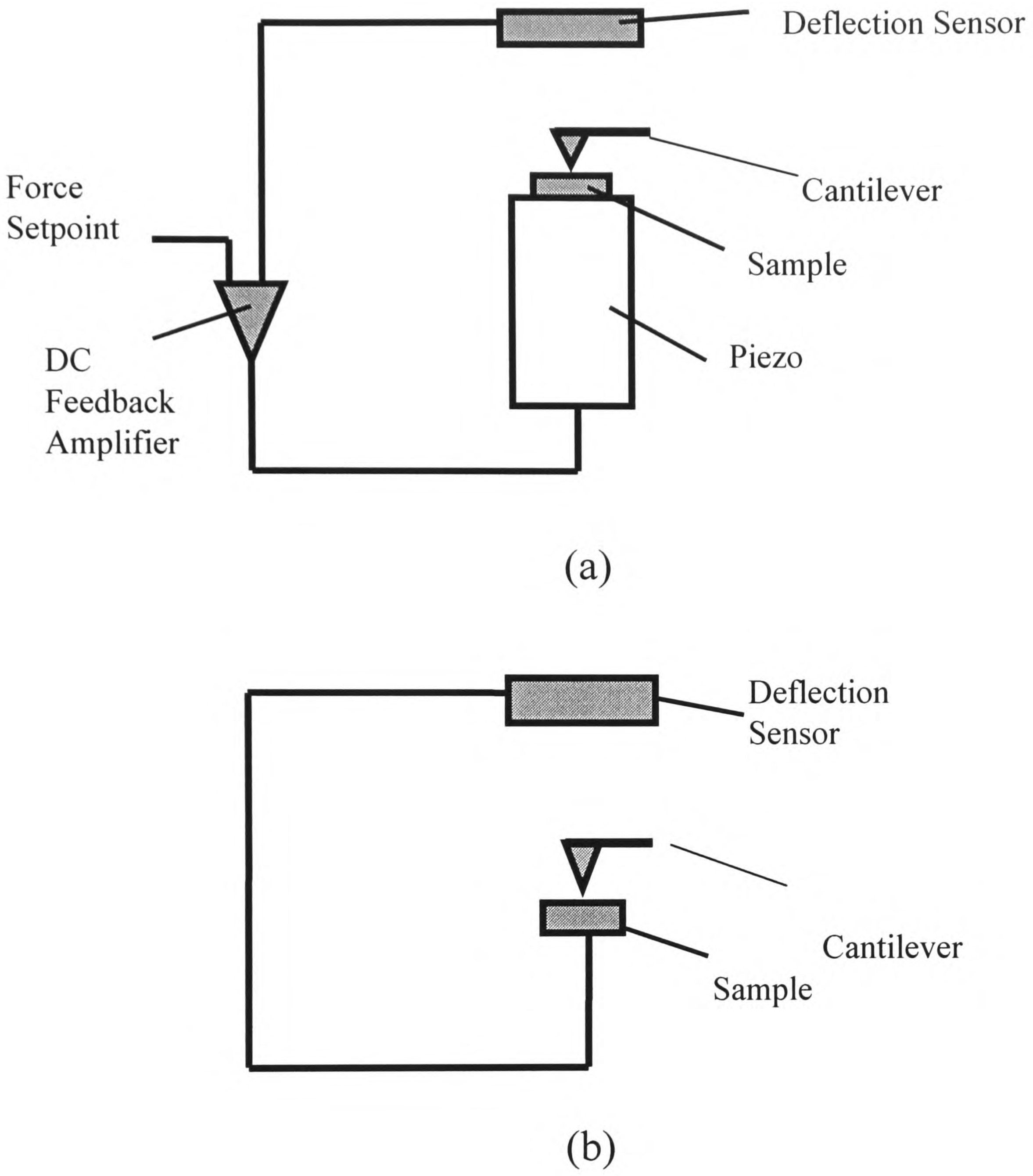

Figure 2.13: Schematic representation of AFM operation in (a) constant force mode where constant tip-sample separation is maintained via feedback to produce the sample image and (b) constant height mode where variations in force are used to image the sample surface

AFM imaging is based on Pauli and nuclear repulsion. However, additional forces also influence the nature of the tip-sample interaction as described in §2.8.2.3.B. Long range forces also operate during contact mode AFM operation as described in §2.8.2.3.A but these are less influential than their short range counterparts. Using contact AFM operation, atomic-scale lateral resolution has been demonstrated for a wide variety of materials with measurement of forces in the range 10^{-3} to 10^{-9} N [52].

Contact AFM experiments can also be classified as to whether they employ a static or a modulated tip. In conventional AFM operation described above, forces between the tip and sample are measured according to deflection of a static cantilever. Less widely used is modulated AFM imaging in which the cantilever is vibrated in a plane perpendicular to the sample surface. This is generally achieved by mounting the cantilever on an ac driven piezoelectric ceramic. During the scan, tip-sample separation is adjusted by means of a feedback loop to maintain a constant force as in conventional AFM operation. Modulation amplitude, however, remains constant throughout the scan. Ratio of modulation amplitude to cantilever deflection provides enhanced contrast for samples in which surface hardness varies.

During non-contact mode, the tip is poised above the sample. The tip responds to long range attractive forces which cause the cantilever to bend down towards the surface. During non-contact AFM operation, the cantilever is vibrated using an ac driven piezoceramic mounted at the base of the cantilever as for force modulated atomic force microscopy. Changes in resonant frequency which occur as a result of tip-surface force interactions are measured and used as part of a feedback control system in which the sample-tip separation is adjusted in order to maintain constant resonant frequency. Long range forces responsible for tip-sample interaction include van der Waals interactions, electrostatic forces in the case of charged surfaces and in some instances, capillary attraction. Such forces are present at low tip-sample separations during contact mode operation but do not contribute to image contrast on an atomic scale to a large extent since the magnitude of long range forces is considerably lower than that of short range forces. Such forces are, however, dominant at tip-separations between 10-100 nm. Relative magnitude of long and short range forces accounts for the different mode of detection in comparison to contact AFM operation, with changes in tip resonant frequency at a vibrating cantilever providing a more sensitive measure of force interaction.

Of these two techniques, contact mode is the most widely employed. However, non-contact mode has emerged as a suitable method for the imaging of soft samples which are readily damaged by the tip during contact mode imaging [53].

All experiments performed during the course of this work employed a non-modulated cantilever operated in contact mode.

2.8.2.3 Forces in atomic force microscopy

Despite the widespread use of the AFM as an imaging technique, there is still much to be learnt about the nature of the sample-tip force interaction. An understanding of such forces is crucial if fundamental theoretical models to describe the AFM are to be devised. Sample-tip interaction is complex and several factors need to be considered.

1. The number of atoms that have an influence on the measurement depends upon the nature of the interaction.
2. Some forces are not simply two-bodied but many-bodied.
3. Environmental influence must be taken into account since van der Waals forces will be significantly different in gases, liquids and solids.

There are many sources of sample-tip interaction. Consideration is now given to the nature of forces which operate as the tip scans the surface.

A Long range forces

Van der Waals interactions are the principle source of tip-sample interaction for non-contact AFM operation. Electrostatic and capillary forces can also be significant in the tip-sample interaction under certain conditions. As described previously, van der Waals and electrostatic forces are present during short range contact AFM operation but are less significant than repulsive forces. Capillary attractions are, however, significant during contact mode and prevent the imaging of hygroscopic substances in air as described below.

Van der Waals forces

Van der Waals forces are attractive long range forces which occur between materials as a result of dipole-dipole, dipole-induced dipole and dispersion forces. For point charges, under most circumstances, van der Waals forces decay with a $1/r^7$ dependence on distance although dispersion forces show a $1/r^8$ dependence at distances greater than 100 Å due to relativistic effects. However, for a spherical body (approximating to the geometry of the AFM tip) adjacent to a plane surface, van der Waals forces decay with $1/r^2$ dependence on distance.

Furthermore, van der Waals forces are strongly dependant on tip geometry, tip and sample composition and environment. In a vacuum, van der Waals forces are always attractive. In a liquid environment, if tip and sample are composed of the same material, van der Waals forces are attractive, independent of the surrounding medium. If tip and sample are composed of different materials, van der Waals forces vary according to the immersion medium and can become repulsive in the case of polar media [54]. Thus by choice of an appropriate immersion medium, van der Waals forces can be reduced during contact AFM imaging. In this way, fluctuations which could be introduced as a result of such interactions are removed leading to enhanced resolution of the technique.

Van der Waals forces are the sole source of long range force interactions for neutral and non-magnetic samples and tips in an environment in which capillary interactions do not occur such as under ultra high vacuum (UHV) or in liquids. They are exploited during non-contact force microscopy as described in Table 2.1 in which the reduced load on the sample makes this a suitable technique for the non-destructive imaging of delicate, soft samples such as biological material.

Electrostatic forces

Electrostatic Coulomb forces are a further source of long range interaction. Such forces, which arise as a result of interaction between electrically charged bodies, decay as the square of the separation of the point charges as defined by Coulomb's Law (Equation 2.34) in which r is the separation between two charges q_1 and q_2 and ε_0 is the vacuum permittivity ($8.854\times10^{-12}\,J^{-1}\,C^{-2}\,m^{-1}$) [55]:

$$F = \frac{q_1 q_2}{4\pi\varepsilon_0 r^2}. \qquad (2.34)$$

This force has been used as the basis of the AFM variant electrostatic force microscopy, implemented to deduce charge separation across a surface as described in Table 2.1.

Capillary forces

The sharp tip of the AFM probe in the vicinity of a planar surface acts as a site at which capillary condensation by water vapour in air can occur. The surface tension of the resulting meniscus results in an attractive force by pulling the tip towards the sample. For a tip of radius 1000 Å, a force of around 9×10^{-8} N as a result of capillary attraction has been estimated [56]. Capillary forces therefore increase cumulative attractive forces measured during non-contact AFM imaging and decrease repulsive forces measured during contact AFM operation since capillary attractive forces will equilibrate repulsive forces. Effects of capillary condensation can be eliminated by operation of the AFM under UHV or in liquid environments.

B Short range forces

Short range forces dominate the tip-sample interaction up to a separation distance of around 10 nm. Pauli and nuclear repulsion are the short range forces which form the basis of AFM imaging in contact mode. However, other short range forces also contribute to the tip-sample interaction. These are considered in turn below.

Pauli and nuclear repulsion

Electrostatic forces arise when particles of like charge come into close proximity. Nuclear and pauli repulsion result from interaction between positively charged nuclei and negatively charged electron clouds respectively. Such repulsive forces hinder the tip from penetrating the sample.

Physisorption and chemisorption

Bonds can be formed between the tip and sample which give rise to an additional attractive force at the surface. This phenomenon has been utilised in the AFM variant chemical force microscopy which probes reactions between the surface and a chemically modified tip as described in Table 2.1.

Friction

This is the lateral force which acts on the tip during scanning of the surface. This force forms the basis of the AFM variant frictional force microscopy as described in Table 2.1.

Elasticity and plastic deformation

Elastic deformations can affect AFM image contrast as, for example, in the case of layered materials such as graphite. Molecular dynamics calculations have shown that strong plastic deformations can occur for some tip-sample arrangements often leading to complete collapse of the original tip and sample geometries [57].

2.8.2.4 Description of the tip sample contact

While there is no unified theory concerning AFM operation, a number of theoretical techniques have been used to describe the tip-sample interaction at an atomic level.

A Empirical potentials

The interaction of an AFM tip with a surface involves a many-bodied interaction. For N identical atoms, interaction of the tip with the surface can be described by a potential function, ϕ, which takes into account each of the many-bodied contributions as defined in Equation 2.35:

$$\phi(1,\ldots,N)=\sum_{i} v_1(i)+\sum_{i<j} v_2(i,j)+\sum_{i<j<k} v_3(i,j,k)+\ldots v_N(1,\ldots N). \qquad (2.35)$$

The single particle interaction, v_1, describes interaction of the tip with external fields, v_2 is the normal pair potential, v_3 describes the three-bodied interaction, and so on. Similarly, i represents the sum of the external fields interacting with the tip, j, k, etc. denote each of the particles influencing the AFM tip. Empirical expressions have previously been derived for the pair potential, v_2, the most familiar of which is the Lennard-Jones (6,12) potential [58]. This expression is given in Equation 2.36 and shown graphically as a plot of potential versus internuclear separation in Figure 2.14:

$$v_2(r)=4\varepsilon\left[\left(\frac{\sigma}{r}\right)^{12}-\left(\frac{\sigma}{r}\right)^{6}\right]. \qquad (2.36)$$

r refers to the internuclear separation between the two entities, ε corresponds to the depth of the graph shown in Figure 2.14 ie. the maximum attractive force between the two species and σ denotes the internuclear separation where $v_2=0$.

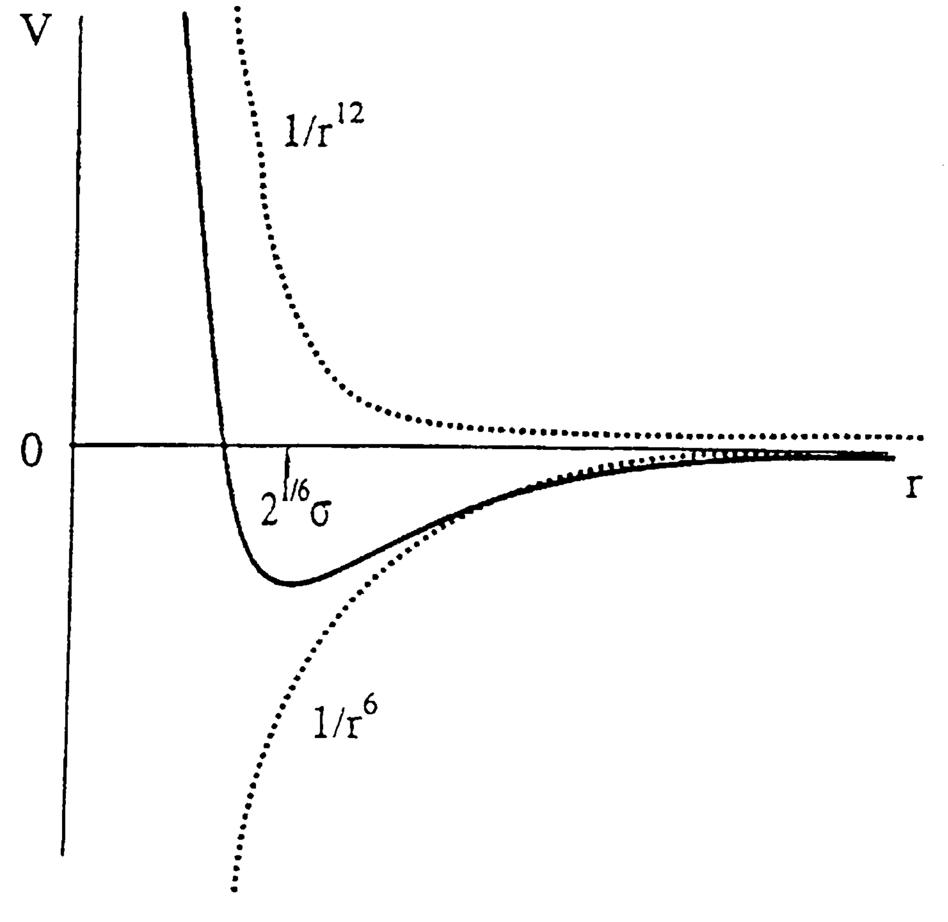

Figure 2.14: The Lennard-Jones (6,12) potential

Although this expression describes the two-bodied interaction reasonably well, it is not suitable as a model for the tip-surface interaction which is many-bodied. An improvement to the empirical approach can be made by taking the three-bodied interaction into account [59] but this treatment of AFM interaction remains approximate.

B Molecular dynamics

Molecular dynamics have been utilised as a means of simulating sample-tip interactions. For example, this approach has been used to visualise how AFM interactions modify the atomic structure of both sample and tip [60,61]. Although useful, these models are limited by small time scale computations and poor potential approximations.

C Ab initio calculations

The ab initio approach to providing a model for tip-sample interaction involves calculation of electron densities using quantum mechanics. Calculations are based on density functional theory introduced by Hohenberg and Kohn [62] which has been applied to tip-sample interactions using the Kohn-Sham equations on the basis of a repeated slab model in which sample and tip are treated as arrays of identical atoms [63].

2.8.3 Previous applications of the AFM

Since its inception, the applications of atomic force microscopy have been wide-ranging encompassing the fields of chemistry, physics, materials science and biology. Examples which illustrate some of the diverse areas in which the AFM has found use now follow.

2.8.3.1 Semi-conductors

The AFM has been implemented in the electronics industry with the investigation of semi-conductor materials. AFM investigations have been useful in providing structural information as well characterising growing or corroding films or multilayers. For example, Koinuma and Uosaki report surface studies of GaAs using the AFM. In view of the applications of this material as a semi-conductor in various electronic devices and solar cells, their studies focussed on monitoring changes in surface structure of n-GaAs(100) [64] and p-GaAs (100) [65] at different potentials and comparing illuminated and dark conditions. Investigations were conducted in aqueous HCl. In this environment, Koinuma and Uosaki noted that the n-GaAs(100) surface was smoothed at positive potentials under illumination. On p-GaAs (100), uniform structures were observed to appear on the surface at open circuit potential or when a positive current flowed. This was ascribed to anodic dissolution of the p-GaAs surface in HCl which proceeds most selectively at the (111) face. Thus, there appears to be a flow of anodic current at open circuit which is compensated by cathodic photocurrent.

2.8.3.2 Biological samples

The AFM has been utilised in the study of biological molecules. To facilitate imaging, molecules are adsorbed onto a solid surface. During the study of biological molecules, problems can arise due to the large capillary forces which occur between the tip and these typically hygroscopic substances. Reduction of such forces can be achieved by imaging the sample in a fluid environment. Alternatively samples can be imaged in air with the AFM operated in non-contact or tapping mode. For example, structure within single strands of DNA and fine structure on tobacco mosaic virus have been observed. This was achieved using the non-contact imaging mode with the substrates immobilised onto mica surfaces [66].

The study of biological systems has demonstrated the value of the AFM in the observation of dynamic processes. For the study of in vivo processes, AFM investigations are performed under liquids to mimic cell conditions. Höberle et al utilised the AFM in an investigation of the dynamic events following injection of a virus into a single cell [67]. Cell events were monitored over a period of 2 days to observe intracell activity and changes to the cell wall. Hansma has implemented the AFM as a means of observing DNA replication providing useful information concerning molecular shape during this process [68].

2.8.3.3 Chemical investigations

The advent of the AFM with its ability to observe individual molecules, internal molecular structure and to observe processes such as adsorption, deposition and diffusion at a molecular level presents the potential for understanding factors controlling reactivity. Many surface techniques such as in-situ Infrared, UV, ESR and Raman spectroscopy provide valuable information but results obtained are limited by the fact that they are averaged over the entire surface. In contrast, the AFM can be used as a means of obtaining site specific information on a real timescale with atomic resolution.

The AFM has been employed in electrochemical investigations in order to elucidate processes occurring at the solid/liquid interface. Deposition processes have been the focus of many AFM studies. For example, the underpotential deposition (UPD) of metals on surfaces has received much attention. UPD deposition occurs when mono or sub monolayers of a metal are deposited onto a surface at potentials positive of bulk deposition. UPD studies have focussed on a wide range of deposits and substrate materials [69]. One of the first systems to be studied using the AFM was the deposition of copper on the Au (111) surface which revealed an $(\sqrt{3}\times\sqrt{3})R30^0$ adlattice during the UPD process [70]. Since this study was reported, very many UPD systems have been investigated using this technique, as reviewed in the literature [69]. Deposition studies using the AFM have also focussed on metal bulk deposition as a means of studying metal texture and growth on surfaces ranging from highly oriented pyrolytic graphite to semi-conductor materials [69]. The AFM has also been utilised during investigations of alloy formation. Czerwinski et al report the electrocrystallisation of iron-zinc alloys from a sulphate electrolyte with an Sn^{2+} additive [71]. Atomic force microscopy revealed the formation of hexagonal columnar crystals with (002) planes of η-phase aligned perpendicular to the growth direction.

Dissolution and corrosion have also been the focus of considerable investigation using the AFM. One such example is the corrosion of stainless steel studied separately by Fan and Bard [72] and Miyasaka and Ogawa [73] which showed that corrosion was initiated at defects and edges. A second study reported by Booth et al examined the dissolution of the enteric drug polymer hydroxypropyl methylcellulose phthalate [74]. This investigation compared dissolution rates at varying pH by monitoring mean changes in the position of the sample surface as a function of time in order to assess the efficiency of drug dissolution.

The AFM has also been utilised to observe species immobilised onto a surface. Examples range from the adsorption of atoms and small molecules on surfaces to the observation of large polymeric molecules. Investigations of atom adsorption include numerous studies of ionic halides adsorbed on metal surfaces [69], such as layers of iodine on Pt(110) and Pt(100) surfaces [75,76]. An AFM study of the molecule benzene, including the observation of internal molecular structure, has been reported by Hallmark and Chiang [77]. Problems can be experienced when imaging a single molecule due to surface diffusion of species over the surface. In this case, this was overcome by deposition of a packed monolayer onto the surface. Diffusion was therefore restricted by steric interactions with neighbouring molecules. Large polymeric molecules observed using the AFM include Langmuir-Blodgett (LB) monolayers which comprise densely packed ordered films composed of molecules consisting of aliphatic chains bound to polar heads. For example, Garneas et al report the observation of packing and structure within LB multilayers [78].

2.8.4 Application of the AFM to nanotribology

Recent years have seen the emergence of the AFM as a useful tool in nanotribological investigations as a means of providing information concerning surface friction, adhesion, lubrication and wear on an atomic scale [79,80]. Tribological investigations which have been undertaken on a macroscopic level have yielded information on physical aspects of lubrication such as dependence of friction on load. Such observations, however, fail to explain tribological behaviour on an atomic scale and therefore limited conclusions concerning the fundamental nature of lubrication can be drawn. In contrast, a sharp AFM tip can simulate a single asperity contact with the sample thus probing lubrication at a fundamental level.

The AFM and the modified AFM technique, the frictional force microscope (FFM), have been widely used in nanotribology. As described in Table 2.1, this technique simultaneously measures lateral forces on the sample in addition to forces normal to the sample surface by detection of induced torsional deflections of the cantilever. The AFM has been utilised to image surfaces during investigation of the tribological properties of surfaces in contact, providing valuable information such as characterisation of surface roughness [81,82]. The AFM has also been used for the topographic imaging of surfaces subjected to wear as a result of an applied load from the tip. Xiao et al report a study of siloxanes on mica under different load conditions produced by a sharp silicon nitride tip [83]. Under low load conditions, a lattice-resolved image is observed reflecting the ordered nature of the siloxane film on the mica surface. As the load is increased, periodicity of the image increases to resemble that of the mica substrate as the tip penetrates the film and moves closer to the surface. Upon reduction of the load, recovery of the ordered siloxane structure does not occur, instead a permanent wear scar remains. Such investigation can be used to identify critical loads which can be tolerated by lubricant layers.

In addition to providing purely topographic information, both the AFM and FFM have been used to measure a number of mechanical properties at the surface interface. The FFM has been used to map friction across surfaces. Such investigations have been carried out both on unlubricated surfaces, as a means of identifying the wear and frictional processes which act on the sample, and during studies of lubricant films.

Studies involve application of a measured load to the scanning tip from which the resulting frictional effect produced at the surface is monitored. Mate et al report a study of friction on a highly oriented pyrolytic graphite surface and correlated friction with surface topography [37]. Numerous studies of LB and self-assembled monolayer (SAM) films have been reported in the literature. Such films are widely used to model lubricants since they form densely packed ordered layers on surfaces. Meyer et al report FFM studies of cadmium-arachidate LB films deposited on silver bromide [84] and silicon surfaces [85]. In both instances, friction was found to be lower on the lubricated surface as opposed to exposed substrate. A comparison of LB films formed from normal and fluorinated hydrocarbons was also carried out by the same group. Their FFM investigation revealed friction to be a factor of 4 lower on the normal hydrocarbon versus the fluorinated film [86]. In addition to serving as model lubricant layers, LB and SAM films are currently being investigated as potential lubricant layers in microdevices [87].

The AFM can be used for measurements of surface mechanical strength by the evaluation of scratch depth following application of various loads to the surface. In this way, surface resistance to scratching and wear can be assessed on micro to nanoscales [88]. The evaluation of the mechanical integrity of lubricating films has also been performed using this technique [88]. Mechanical strength can be assessed on micro to picoscales by monitoring cantilever deflection as a function of sample travelling distance after the sample and tip come into contact. Cantilever deflection will be smaller for a soft sample where the cantilever indents the surface. Bhushan and Koinkar have used such measurements to show that hardness and therefore wear resistance of silicon surfaces is increased by ion implantation [89].

Thin-film thickness determination with nanometer lateral resolution is also possible using the AFM [90]. Lubricant thickness is obtained by measuring the tip-sample force as it approaches, contacts and pushes through the film to ultimately reach the substrate. From the different forces recorded, film thickness can be assessed.

Measurements of surface elasticity are possible using force modulated AFM operation in which the cantilever is modulated at very low frequency during normal contact AFM imaging as described in Table 2.1. During the scan, tip-sample separation is adjusted by means of a feedback loop to maintain a constant force. Modulation amplitude, however, remains constant throughout the scan. For the same applied force, cantilever deflection is dependant on sample elasticity. Thus, the ratio of modulation amplitude to cantilever deflection serves as a measure of surface elasticity [34]. This technique was used by Overney et al who studied the correlation between friction and elastic properties of normal and fluorinated LB films on a Si (100) surface [91,92]. They observed that fluorinated films had lower elasticity and higher friction in comparison to normal hydrocarbon films. This was attributed to the larger contact area for the softer fluorinated film in comparison to an equivalent load on the harder hydrocarbon film which in turn leads to higher frictional force.

At present the application of the AFM and FFM to the field of nanotribology is in its infancy. The majority of investigations which have been undertaken to date demonstrate the potential of the AFM and FFM in addressing tribological problems. However, many of the studies reported in the literature incorporate the study of model systems in ideal environments such as UHV. Extension of this technique to actual tribological situations involving real lubricating films has received limited attention.

References

[1] A. Fick, Philosophical Magazine, 1855, **10**, 30

[2] A. Fick, Poggendorfs Annalen der Physic and Chemie, 1855, **94**, 59

[3] K. B. Oldham, C. G. Zoski, Comprehensive Chemical Kinetics, 1986, Eds. C. H. Bamford, R. G. Compton, **26**, 93

[4] K. B. Oldham, C. G. Zoski, Comprehensive Chemical Kinetics, 1986, Eds. C. H. Bamford, R. G. Compton, **26**, 113

[5] K. B. Oldham, C. G. Zoski, Comprehensive Chemical Kinetics, 1986, Eds. C. H. Bamford, R. G. Compton, **26**, 122

[6] P. H. Rieger, Electrochemistry, 1994, Chapman and Hall, p32

[7] P. H. Rieger, Electrochemistry, 1994, Chapman and Hall, p170

[8] A. J. Bard, A. J. Faulkner, Electrochemical Methods, 1980, Wiley, p91

[9] R. S. Nicholson, I. Shain, Anal. Chem., 1964, **36**, 706

[10] A. J. Bard, A. J. Faulkner, Electrochemical Methods, 1980, Wiley, p285

[11] T. von Karman, Z. Angew, Mat. Mech. I., **1921**, 233

[12] W. G. Cochran, Proc. Cambridge Philos. Soc. Matt. Phys. Sci., 1934, **30**, 365

[13] V. G. Levich, Physiochemical Hydrodynamics, 1962, Prentice-Hall, Englewood Cliffs, p45

[14] A. J. Bard, A. J. Faulkner, Electrochemical Methods, 1980, Wiley, p160

[15] F.G. Cottrell, Z. Physik, Chem., 1902, **42**, 385

[16] H. A. Laitinen, I. M. Kolthoff, J. Am. Chem. Soc., 1939, **61**, 3344

[17] P. H. Rieger, Electrochemistry, Chapman and Hall, New York, USA, p287

[18] G. Denault, Chemistry and Industry, 16 September 1996, 678

[19] Z. G. Soos, P. J. Lingane, J. Phys. Chem., 1964, **68**, 3821

[20] J. Heinze, J. Electroanal. Chem., 1981, **124**, 73

[21] M. L Wooster,. H. Longmire, M. Zhang,. F. Watanabe, Murray R. W., Anal. Chem., 1992, **64**, 1132

[22] R. Brina, S. Pons, M. Fleichmann, J. Electroanal. Chem, 1988, **244**, 81

[23] J. Ghoroghchian, F. Sarfarazi, T. Dibble, J. Cassidy, J. J. Smith, A. Russell, G. Dunmore, M. Fleichmann, S. Pons, Anal. Chem. 1986, **58**, 2278

[24] G. Denault, M. V. Mirkin, A. J. Bard, J. Electroanal. Chem, 1991, **308**, 27

[25] J. O. Howell, R. M. Wightman, Anal. Chem., 1984, **56**, 524

[26] J. O. Howell, J. M. Goncalves, C. Amatore, L. Klasinc, R. M. Wightman, J. K. Kochi, J. Am. Chem. Soc., 1984, **106**, 3968

[27] F. Crespi, Biosensors and Bioelectronics, 1990, **11**, 8, 743

[28] N. R. Hardingham, A. U. Larkham, Journal of Physiology, 1998, **507**, 1, 249

[29] G. Binnig, H. Roher, C. Gerber, E. Wiebel, E. Appl. Phys. Lett., 1982, **40**, 178

[30] G. Binnig, H. Roher, Ch. Gerber, E. Wiebel, E. Appl. Phys. Lett., 1983, **50**, 120

[31] R. Wiesendanger, H. J. Güntherodt (Eds.), Scanning Tunnelling Microscopy 1, Springer Series in Surface Science 28, Springer-Verlag, Berlin, 1992

[32] G. Binnig, C. F. Quate, Ch. Gerber, Phys. Rev. Lett., 1986, **56**, 930

[33] Y. Sugawara, T. Ishizaka, S. Morita, J. Vac., Sci. Tech., 1991, **9**, 2, 1092

[34] P. Maivald, H. J. Butt, S. A. C. Gould, C. B. Prater, B. Drake, J. A. Gurley, V. B. Elings, P. K. Hansma, Nanotechnology, 1991, **2**. 103

[35] Topometrix Technical Report, AFM Imaging Modes, 1993, Topometrix, Santa Clara, CA, USA

[36] Hansma P. K., Appl. Phys. Lett., 1994, **64**, 2454

[37] C. M. Mate, G. M. McClelland, R. Erlandsson, S. Chiang, Phys. Rev. Lett., 1987, **59**, 1942

[38] Y. Martin, H.K. Wickramasinghe, Appl. Phys. Lett., 1987, **50**, 1455

[39] Y. Martin, D. W. Abraham, H.K. Wickramasinghe, Appl. Phys. Lett., 1988, **53**, 1103

[40] C. M. Lieber, M. S. Wrighton, C. D. Frisbie, A. Noy, L. F. Roznyai, Science, 1994, **265**, 2071

[41] R. C. Barrett, C. F. Quate, J. Appl. Phys., 1991, **70**, 2725

[42] A. J. Bard, F.-R. F.Fan, M. V. Mirkin, Electroanalytical Chemistry, A. J. Bard Ed., Marcel Dekker, New York, 1994, **18**, 243

[43] A. J. Bard, F.-R. F.Fan, D. T. Pierce, P. R. Unwin, D. O. Wipf, F. Zhou, Science, 1991, **245**, 68

[44] P. K. Hansma, B. Drake, O. Marti. S. A. C. Gould, C. B. Prater, Science, 1989, **243**, 641

[45] P. Guethner, U. Ch. Fischer, K. Dransfield, Appl. Phys. B, **48**, 89

[46] G. Binnig, Ch. Gerber, E. Stoll, T. R. Albrecht, C. F. Quate, Europhys. Lett., 1987, **3**, 1281

[47] T. R. Albrecht, S. Akamine, T. E. Carver, C. F. Quate, J. Vac. Sci. Technol. A, 1990, **8**, 3386

[48] F. F. Abraham, I. P. Batra, S. Ciraci, Phys. Rev. Lett., 1988, **60**, 1314

[49] O. Wolter, T. Bayer, J. Greschner, J. Vac. Sci. Technol. B, 1991, **9**, 1353

[50] T.Goddenhenrich, H. T. Lemke, U. Hartmann, C. Heidel, J. Vac. Sci. Technol. A, 1990, **8**, 383

[51] G.Meyer, N. M. Amer, Appl. Phys. Lett., 1988, **53**, 1045

[52] R. Wiesendanger, Scanning Probe Microscopy and Spectroscopy: methods and applications, 1994, Cambridge University Press, p229

[53] E. A. G. Chernoff, D. A. Chernoff, K. Kjoller, Molecular Biology of the Cell, 1992, **3**, 55, P.A.227

[54] R. Wiesendanger, Scanning Probe Microscopy and Spectroscopy: methods and applications, 1994, Cambridge University Press, p245

[55] P. W. Atkins, Physical Chemistry, 1987, Oxford University Press, UK, p254

[56] J. N. Isrealachvili, Intermolecular and Surface Forces, 1995, Academic Press, NY.

[57] U. Landman, W. D. Luedtke, A. Nitzan, Surf. Sci., 1989, **209**, L177

[58] J. E. Lennard-Jones, Trans. Faraday. Soc., 1932, **24**, 332

[59] F. H. Stillinger, T. A. Weber, Phys. Rev. B., 1985, **31**, 5262

[60] U. Landman, W. D. Luedtke, N. A. Burnham, R. J. Colton, Science, 1990, **248**, 454

[61] U. Landman, W. D. Luedtke, J. Vac. Sci., Technol. A, 1991, **9**, 414

[62] P. Hohenberg, W. Kohn, Phys. Rev. B., 1964, **140**, 1133

[63] W. Kohn, L.J.Sham, Phys. Rev.A., 1965, **139**, 949

[64] M. Koinuma, K. Uosaki, J Vac. Sci. Technol B, 1994, **12**, 1543

[65] M. Koinuma, K. Uosaki, Surface Science, 1994, **311**, L737

[66] D. Anselmetti, R. Lüthi, E. Meyer, T. Richmond, M. Dreier, J. E. Frommer, H. J. Güntherodt, Nanotechnology, 1994, **5**, 2, 87

[67] W. Höberle, J. K. H. Hörber, F. Ohnesorge, D. P. E. Smith, G. Binnig, Ultramicroscopy, 1991, **42-44**, 1161

[68] P. K. Hansma, J. Vac. Sci. Technol. B., 1994, **12**, 1465

[69] A. A Gewirth, B. K. Niece, Chem. Rev., 1997, **97**, 1129

[70] S. Manne, P. K. Hansma, J. Massie, V. B. Elings, A. A. Gewirth, Science, 1991, **251**,183

[71] F. Czerwinski, K. Kondo, J. A. Szpunar, J. Electrochem. Soc., 1997, **144**, 2, 481

[72] F. R. F. Fan, A.J.Bard, J. Electrochem. Soc., 1989, **136**, 166

[73] A. Miyasaka, H. Ogawa, Corros. Sci., 1990, **31**, 99

[74] J. Booth, DPhil thesis, University of Oxford, 1996

[75] I. Villegas, M. J. Weaver, J. Electroanal. Chem., 1994, **73**, 846

[76] W. L. Desimone, J. J. Breen, Langmuir, 1995, **11**, 4428

[77] V. W, Hallmark, S. Chiang, Surf. Sci., 1993, **286**, 190

[78] J. Garnaes, D. K. Schwartz, R. Viswanathan, J. A. N. Zasadzinski, Nature, 1992, **357**, 54

[79] B. Bhushan, J. N. Israelachvili, U. Landman, Nature, 1995, **374**, 607

[80] B. Bhushan, Langmuir, 1996, **12**, 4481

[81] A. Majumdar, B. Bhushan, ASME J, Tribology, 1990, **112**, 205

[82] A. Majumdar, B. Bhushan, ASME J, Tribology, 1991, **113**, 1

[83] X.-d. Xiao, G.-y. Liu, D. H. Charych, M. Salmeron, Langmuir, 1995, **11**, 1600

[84] E. Meyer, L. Howald, R. Overney, D. Brodbeck, R. Lüthi, H. Haefke, J. Frommer, H.-J. Güntherodt, Ultramicroscopy, 1992, **42-44**, 274

[85] E. Meyer, L. Howald, R. Overney, D. Brodbeck, R. Lüthi, H. Haefke, J. Frommer, H.-J. Güntherodt, Phys. Rev. Lett., 1992, **69**, 1777

[86] R. M. Overney, E. Meyer, J. Frommer, D. Brodbeck, R. Lüthi, L. Howald, H.-J. Güntherodt, M. Fujihara, H. Takano, Y. Gotoh, Nature, 1992, **359**, 133

[87] B. Bhushan, J. N. Israelachvili, U. Landman, Nature, 1995, **374**, 607

[88] B. Bhushan, J. Ruan, ASME J.Tribology, 1994, **116**, 389

[89] B. Bhushan, V. N. Koinkar, J. Appl. Phys., 1994, **75**, 5741

[90] C. M. Mate, M. R. Lorenz, V. J. Novotny, J. Chem. Phys., 1989, **90**, 7550

[91] R. M. Overney, E. Meyer, J. Frommer, H. J. Güntherodt, Langmuir, 1994, **10**, 1281

[92] R. M. Overney, D. P. Leta, Tribol. Lett, 1995, **1**, 247

Chapter 3

Experimental protocol

3.1 Introduction

The purpose of this chapter is to describe the standard experimental techniques employed during the course of the work undertaken in this thesis. The novel elevated temperature microelectrode apparatus developed as part of this thesis is described in a later chapter. The experimental features of microdisc voltammetry, cyclic voltammetry, rotating disc electrode voltammetry, chronoamperometry and atomic force microscopy are considered in §3.2, 3.3, 3.4 , 3.5 and 3.6 respectively. Methods of data analysis are given in §3.7. Solution preparation is described in §3.8. The chapter concludes with a detailed survey of the source and purity of solvents; electrochemical reagents and supporting electrolytes; and other chemicals used during this research in §3.9 as tabulated in Tables 3.2, 3.3 and 3.4 respectively.

3.2 Microdisc voltammetry

3.2.1 Cell configuration

Two types of steady state microelectrode experiments were implemented during the course of this work. First, microelectrodes were incorporated for use in the high temperature apparatus developed as part of this thesis. Since this piece of apparatus was designed for use with resistive solvents, microdisc electrodes were included as part of the experimental design due to their decreased susceptibility to ohmic distortion as described in §2.7.1.3. The cell configuration of this novel piece of apparatus is described in Chapter 4.

Microelectrode experiments were also performed at ambient temperatures using the electrochemical cell shown in Figure 3.1.

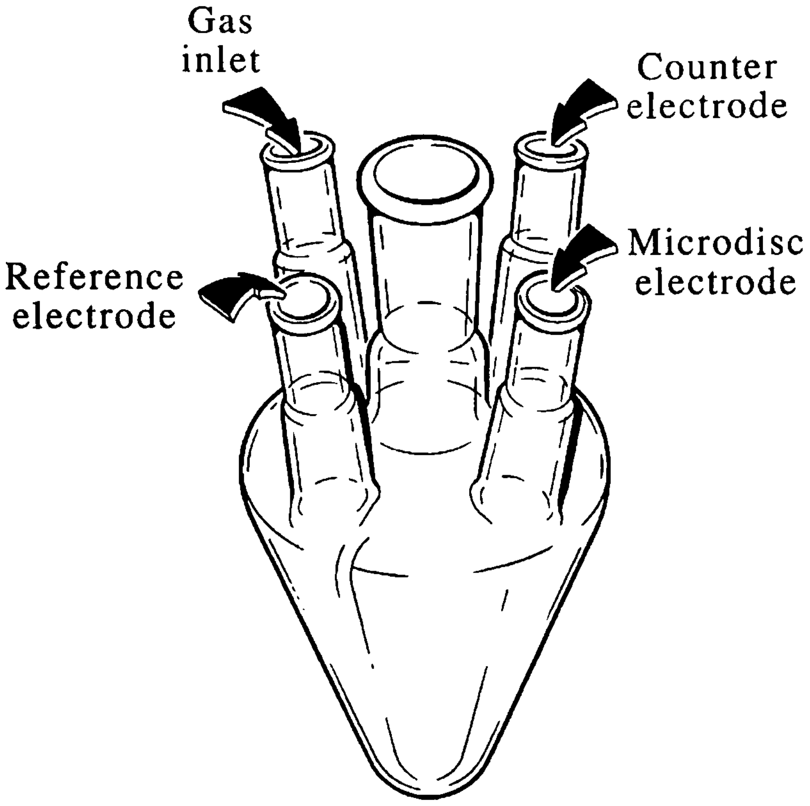

Figure 3.1: Electrochemical cell for microelectrode experiments at ambient temperature

The cell consisted of a closed vessel containing 1 large inlet and 4 small inlet arms. The reference electrode comprised a saturated calomel electrode (SCE). The counter electrode was composed of a platinum mesh so as to give a large surface area. The reference, working and counter electrodes were each placed in one of the small inlet arms and the gap between electrodes and glass apparatus sealed using parafilm. The fourth small inlet arm allowed for a pipette to be placed into the solution to facilitate deoxygenation of the solution with argon gas. All solutions were deoxygenated for 30 minutes prior to each experiment. While voltammograms were recorded, the pipette was removed and positioned above the solution in order to maintain a steady flow of argon over the solution. In this way, voltammograms could be obtained in the absence of oxygen and with the minimum amount of noise.

We attribute an accuracy of ± 50 mV to $E_{1/2}$ values measured using this experimental procedure. Limiting current values are accurate to ± 4%.

3.2.2 Microdisc electrodes

Platinum microdisc electrodes of nominal diameters ranging from 5 μm to 100 μm were fabricated in collaboration with Dr. Barry Coles of the Physical and Theoretical Chemistry Laboratory of Oxford University. Wolaston (silver clad platinum) wire was used for the fabrication procedure with initial pre-treatment of the wire with concentrated nitric acid to remove the silver coating. A short length of platinum wire of the required diameter was heated inside a length of soda glass capillary using a hand torch. The application of sufficient heat caused the glass to soften until it collapsed onto the platinum wire to form a seal. Soda glass was chosen as the medium to house the platinum wire rather than harder borosilicate glasses, first, due to the closer match in linear expansion coefficient for platinum and soda glass over the range of temperatures from ambient to glass melting [1]. Values of linear expansion coefficients for the three materials at room temperature are reported in Table 3.1 [2,3]. This is an important consideration since electrodes are formed at the glass melting temperature and cool to room temperature. As the electrode cools, the glass surround and platinum metal are required to contract at the same rate so as not to put strain onto the glass to metal seal [1]. Furthermore the microdisc electrodes were intended for use in conjunction with the high temperature apparatus. With such similar expansion coefficients, the platinum wire and glass surround expanded to the same extent during elevated temperature application. Thus microdisc electrodes did not become protruded from the glass surface or recessed. Secondly, it was observed that soda glass "wetted" the platinum more effectively than borosilicate glass to produce a better seal.

Substrate	**Linear Expansion Coefficient (K^{-1})**	**Reference**
Borosilicate Glass	3.3×10^{-6}	2
Soda glass	9.0×10^{-6}	2
Platinum	9.0×10^{-6}	3

Table 3.1: Linear expansion coefficients of platinum and soda glass used in the construction of microdisc electrodes in comparison with Pyrex

Following their fabrication, the electrodes were ground on a diamond wheel to expose the cross section of the embedded wire. Electrodes were then polished in order to obtain a flat surface. The polishing procedure incorporated aqueous alumina slurries [4]. Grades of 9 μm and 3 μm were used initially applied directly to a glass surface. These were followed by 1 μm and 0.3 μm grades supported on a soft nap (PSU-S) lapping pad (Kemet International Ltd., Maidstone, Kent). Electrodes were sonicated in ethanol between each stage to ensure complete removal of all alumina particles before proceeding with the smaller grit size. The electrode was wiped with a cloth soaked in ethanol prior to use.

Electrodes were electrochemically calibrated at 25 ^{0}C in a 1 mM ferrocene solution in acetonitrile containing 0.1 mM tetrabutylammonium perchlorate (NBu_4ClO_4) as supporting electrolyte. This procedure performed two functions. First it served as a means of checking the electrode was functioning correctly. In addition, the procedure provided an accurate value for the electrode diameter. Ferrocene is used to perform the electrochemical calibration since it has a well established diffusion coefficient of $2.3x10^{-5}$ cm^2 s^{-1} in this medium and undergoes a simple one electron, electrochemically reversible electron transfer with no complicating reaction kinetics [5]. From the limiting current obtained, the diameter of the electrode was calculated using the expression for the diffusion limited current at a microdisc electrode given previously in Equation 2.33. Electrode diameters calibrated in this way were found to agree with nominal electrode diameters to within 10%.

The electrode was repolished prior to each experiment using a 0.3 μm alumina slurry supported on a soft nap lapping pad and the electrode electrochemically recalibrated to allow for any changes in diameter resulting from the polishing procedure.

3.2.3 Electronics

Experiments were performed using a linear sweep potential scan generator attached to a picoammeter (Oxford Electrodes) which permitted measurement of the very small currents associated with microdisc electrodes. The picoammeter was controlled by a model 486 PC with 66 MHz clock speed using a data acquisition program written by Dr. Barry Coles of the Physical and Theoretical Chemistry Laboratory of Oxford University. The program allowed for scan rates in the range 5 mV s^{-1} to 1 V s^{-1}. Scan rates of 10 mV s^{-1} were used in conjunction with microdisc experiments to ensure a steady state regime was maintained. The same computer program was used to record current/voltage curves. Analysis of the results obtained in computerised format was performed using a data analysis program written by Mr. John Alden of the Physical and Theoretical Chemistry Laboratory. This program allowed for the measurement of limiting currents and half wave potentials. In addition, wave shape analysis of steady state current-voltage curves could be carried out.

3.3 Cyclic voltammetry

3.3.1 Cell configuration

The electrochemical cell and conditions described previously in §3.2.1 for microdisc investigation at ambient temperature were employed during cyclic voltammetric experiments.

We attribute an accuracy of ± 50 mV to peak potential values measured during cyclic voltammetric investigations.

3.3.2 Working electrodes

Glassy carbon and platinum working electrodes were used during cyclic voltammetric experiments. The glassy carbon electrode comprised a commercial electrode obtained from Bioanalytical Systems Ltd (West Lafayette, Indiana, USA). It was composed of a glassy carbon disc, approximately 3 mm in diameter, mounted within a 6 mm diameter insulating annular sheath with electrode and insulating surfaces flush. A piece of brass at the top of the electrode served as a point of external electrical contact. Electrical connection between the brass contact and glassy carbon disc was achieved via a piece of wire running the length of the electrode.

The platinum working electrode was manufactured by the workshops of the Physical and Theoretical Chemistry Laboratory of Oxford University. It consisted of a platinum disc of 4 mm in diameter set within a 1 cm thick Teflon annular sheath with the platinum and Teflon surfaces flush. As in the case of the glassy carbon electrode, a piece of brass served as the external electrical contact with connection between the external contact and platinum disc achieved via a wire running inside the electrode.

Electrodes were polished initially with successively smaller grades of organic based diamond lapping spray of grit size 25 μm, 14 μm, 8 μm, 6 μm, 3 μm, 1 μm, 0.25 μm and 0.1 μm (Kemet International, Kent, UK) supported on soft nap (PSU-S) lapping pads (Kemet International, Kent, UK). Electrodes were rinsed in ethanol between each stage to ensure complete removal of all diamond particles before proceeding with the smaller grit size. Prior to the recording of each voltammogram, the electrode was repolished using 0.1 μm diamond lapping compound supported on a soft nap lapping pad and the electrode wiped with a cloth soaked in ethanol to remove all traces of lapping compound present. Precise electrode dimensions were determined using a travelling microscope to an accuracy of ± 0.01 mm.

3.3.3 Electronics

Experiments were performed using a linear potential scan generator (Oxford Electrodes, Oxford, UK) which allowed current-voltage characteristics to be measured at scan rates in the range 1 to 2000 mV s^{-1}. Typically scan rates of 20 to 500 mV s^{-1} were employed during cyclic voltammetric experiments. Voltammograms were recorded using a Lloyd Instruments (Southampton, UK) PL3 chart recorder. Potentials and currents were checked independently using a digital voltmeter (Cirkit Ltd., Broxbourne, Herts, UK), capable of resolution to 0.1 mV.

3.3.4 Cyclic voltammetry in conjunction with ex-situ atomic force microscopy

Electrodes for use in conjunction with ex-situ atomic force microscopy were fabricated by the workshops of the Physical and Theoretical Chemistry Laboratory at Oxford University. A schematic diagram of electrode construction is shown in Figure 3.2. Electrodes comprised a disc of glassy carbon (supplied by Bioanalytical Systems Ltd., West Lafayette, Indiana, USA) or platinum metal (supplied by Goodfellows Ltd., UK) embedded in a Teflon disc of 15 mm diameter and 1 cm thickness. With such dimensions this part of the electrode was small enough to be placed under the atomic force microscope. A wire was attached to the electroactive part of the electrode and exited the side of the Teflon disc as shown in Figure 3.2 for connection to the potentiostat. Electrodes were polished prior to use via the procedure outlined in §3.3.2.

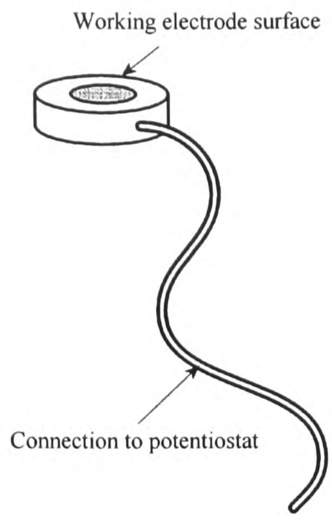

Figure 3.2: Cyclic voltammetry electrode for use in conjunction with atomic force microscopy

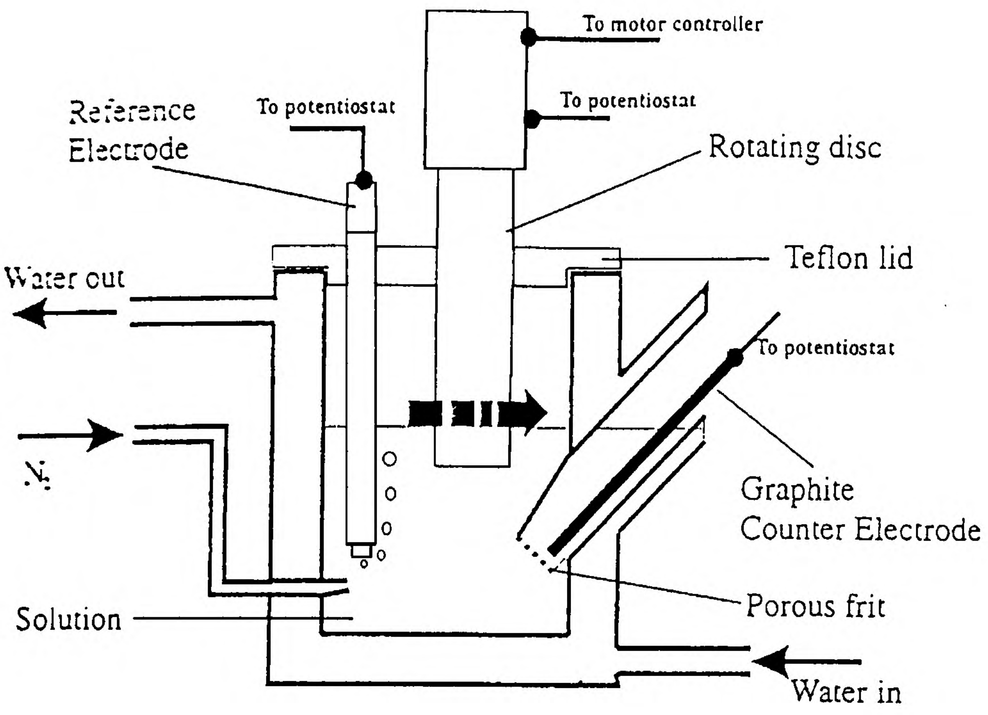

Figure 3.3: Electrochemical cell for RDE experiments

3.4 Rotating disc electrode voltammetry

3.4.1 Cell configuration

All rotating disc electrode (RDE) voltammetric experiments were performed in a purpose made vessel as illustrated in Figure 3.3. The vessel comprised a double walled glass configuration with 4 inlet arms. Two inlets reached the inside of the cell. The larger of these allowed the graphite counter electrode to be positioned into the solution. A frit at the base of the inlet arm ensured that counter products were kept separate from the electroactive solution. The second smaller arm permitted attachment of the cell to a supply of argon gas to facilitate deoxygenation of the solution. Solutions were degassed for 30 minutes prior to, and during, each experiment. The two remaining inlet arms on either side of the cell were connected to the space between the inner and outer cell walls. These allowed a flow of water to be circulated around the apparatus, with the aid of an electric pump, as a means of regulating solution temperature to 25 ^{0}C ± 0.5 ^{0}C. The top of the cell was covered by a Teflon lid in order to minimise solution evaporation. A hole in the covering lid allowed the RDE to be placed into the solution. A second hole supported the saturated calomel reference electrode. Overall capacity of the vessel was in the order of 250 cm^3 and the diameter of the cell allowed for a distance in excess of 1 cm between the RDE and the cell walls thereby ensuring that hydrodynamic flow to the electrode was not perturbed.

The RDE was rotated perpendicular to the face of the disc at angular frequencies between 5 and 30 Hz, stable to ± 0.05 Hz. Angular frequency was maintained by a motor and motor controller employing proportional feedback. Electrical contact was made to the rotating disc via a metal screw thread attached to the mercury motor head.

We attribute an accuracy of ± 50 mV to $E_{1/2}$ values measured using this experimental procedure. Limiting current values are accurate to ± 4%.

3.4.2 Rotating disc electrodes

Glassy carbon and platinum RDEs were employed during rotating disc investigations. Electrode structure comprised a 3 mm glassy carbon disc (supplied by Bioanalytical Systems Ltd., West Lafayette, Indiana, USA) or a 7 mm platinum disc (supplied by Goodfellows Ltd., UK) set within a 2 cm diameter Teflon sheath with electrode and Teflon surfaces flush. The Teflon sheath was attached to a brass head which served first as a means by which the electrode could be attached to the mercury motor via an inset screw thread and second as a point of electrical contact between the rotating disc and motor. Connection between the external contact and working electrode surface was achieved via a wire running inside the electrode.

The polishing procedure and determination of precise electrode dimensions were as for electrodes used during cyclic voltammetric investigation previously detailed in §3.3.2.

3.4.3 Electronics

Electronic equipment utilised for RDE experiments was identical to that used for cyclic voltammetric experiments as described in §3.3.3. Current-voltage curves were recorded at scan rates of 2-5 mV s^{-1}.

3.4.4 Rotating disc electrode voltammetry in conjunction with ex-situ atomic force microscopy

Electrodes used for cyclic voltammetry in conjunction with ex-situ atomic force microscopy described in §3.3.4 also formed the basis of RDE imaging experiments. For use with the rotating disc apparatus, the electrode was held inside a Teflon tube 2 cm in diameter with a section cut away at the top in which the Teflon disc could be placed. The Teflon holder had a brass head for attachment to the rotating disc motor. Electrical contact was made from the electrode surface to the brass head of the Teflon holder via the wire embedded in the side of the Teflon disc. As this exited the electrode, it was pushed into a groove along the side of the large Teflon holder and wound around a brass screw at the head to ensure contact was made. A schematic diagram of the electrode and holder for the rotating disc apparatus is shown in Figure 3.4. The electrode polishing procedure was as previously detailed in §3.3.2.

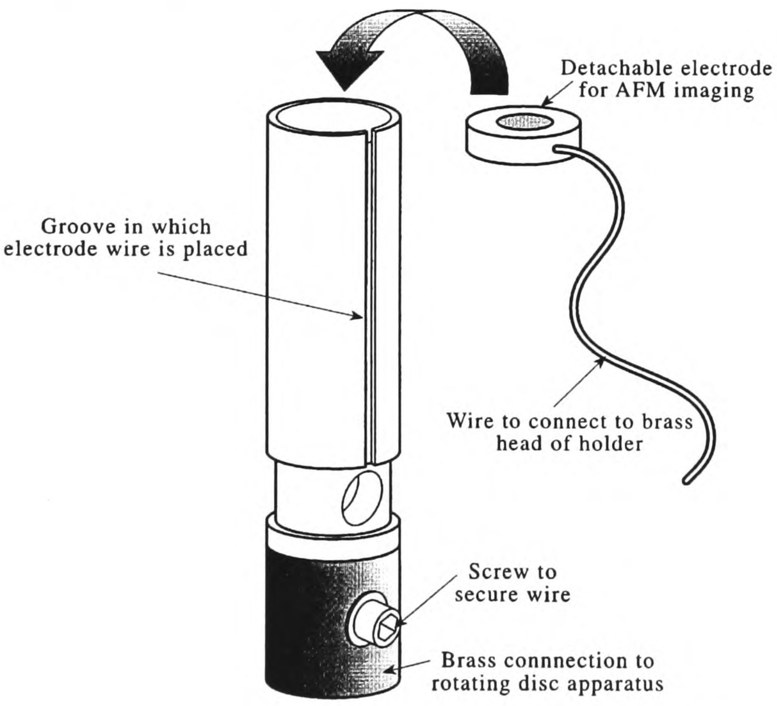

Figure 3.4: The RDE and holder for use in conjunction with ex-situ atomic force microscopy

3.5 Chronoamperometry

3.5.1 Cell configuration

Cell configuration was identical to that used for microelectrode voltammetry at ambient temperatures as described in §3.2.1.

3.5.2 Working electrodes

Chronoamperometry was carried out using both glassy carbon and platinum working electrodes. The glassy carbon electrode was identical to that used for cyclic voltammetric experiments as described in §3.3.2. The platinum electrode comprised a platinum disc of 1 mm diameter set within a 1 cm thick Teflon sheath manufactured by the workshops of the Physical and Theoretical Chemistry Laboratory of Oxford University. The electrode polishing procedure and determination of electrode dimensions were also as previously outlined in §3.3.2.

3.5.3 Electronics

Transient waves were recorded using an Ecochemie General Purpose Electroanalytical System Model PGSTAT20 (Ecochemie BV, Utrecht, The Netherlands). This commercial system allowed chronoamperometric experiments to be performed with the application of a pre-set sequence of up to 9 potential steps in the range 0-6 V. Analysis of data obtained in computerised format to obtain current-time transient maxima and minima was also possible using this system.

3.6 Atomic force microscopy

3.6.1 The AFM

The AFM employed during this research was a Topometrix TMX 2000 Discoverer (Topometrix, Santa Clara, CA, USA) controlled by a model 486 PC with 66 MHz clock speed and 1 GB hard disc capacity. Data storage capacity was augmented by 100 MB capacity floppy discs in conjunction with a portable Zipdrive (Iomega Corp., USA) and 500 MB DC6525 data cartridge tape (3M, UK).

During the work undertaken in this thesis, the AFM was run in feedback mode in which cantilever deflection was used to control the motion of the z-piezo ceramic on which the sample was mounted. In this way, constant tip-sample separation was maintained throughout the scan. Cantilever deflection was measured optically using a laser beam and photo-detector. This was accomplished by directing a laser beam, with wavelength 670 nm and power 3 mW, onto the back of the cantilever. The beam was then deflected onto a position sensitive detector (PSD) consisting of 4 photo-active segments. Changes in the distribution of the photocurrent generated across the PSD were used to control the length of the z-piezo ceramic so that a constant tip sample separation was maintained.

Two types of AFM experiment were conducted during the course of this thesis:

1. ex-situ experiments performed in air;
2. in-situ experiments performed under liquids.

For all experiments, the AFM was operated in contact mode using commercial premounted probes (Topometrix, Santa Clara, CA, USA). Model 1520-00 and 1710-00 probes were used during ex-situ and in-situ investigations respectively. Both probe types incorporated a cantilever with spring constant 0.032 Nm^{-1}. Tips were fabricated from silicon nitride in both cases. In addition, model 1710-00 probes used during in-situ work were coated with a layer of insulating material except for the small exposed area of the tip.

3.6.2 Ex-situ atomic force microscopy

Ex-situ AFM experiments were conducted in conjunction with cyclic and RDE voltammetry. Electrode construction and experimental details for cyclic and RDE voltammetric experiments are described in §3.3.4 and §3.4.4 respectively . Experiments were performed by recording a voltammetric wave at the AFM electrode. The potential was then held at a voltage beyond the half-wave potential of the process under study to prevent stripping of material from the electrode surface. The AFM electrode was disconnected from the potentiostat, and removed from the Teflon holder in the case of RDE experiments, to enable the electrode surface to be imaged in air.

3.6.3 In-situ atomic force microscopy

In-situ electrochemical AFM experiments were performed using a novel electrochemical cell. The cell contained reference and counter electrodes in addition to the working electrode sample. Electrodes were connected to a potentiostat to enable the electrochemical reaction to be performed inside the AFM cell immediately prior to the recording of an AFM image. Cell design was based on the commercial Topometrix electrochemical AFM cell (Topometrix, Santa Clara, CA, USA).

3.7 Data analysis

Data analysis was frequently performed on computer using an IBM compatible PC. A model 486 was used with 33 MHz clock speed run under MS-Windows. Microsoft excel was used to manipulate data in a graphical form.

3.8 Solvents and solution preparation

Experiments conducted during the course of this thesis used acetonitrile (Fisons), N,N-dimethylformamide (DMF) (Aldrich), toluene (Aldrich) and water as solvents. Aqueous solutions used UHQ water with a measured resistivity of 18 MΩ cm^{-1} achieved using an Elgastat water purifier (High Wycombe, Bucks, UK). The supporting electrolyte comprised 0.1 M potassium chloride. Acetonitrile, DMF and toluene solvents were dried prior to use by passage through an alumina column [6] with the dried solvent run directly into the reaction vessel under a stream of argon gas in order to exclude moisture as much as possible. In addition, toluene was further dried by stirring with phosphorous pentoxide for 1 hour prior to use [6]. Tetrabutylammonium perchlorate (NBu_4ClO_4) was used as the background supporting electrolyte for all experiments using acetonitrile and N,N-dimethylformamide. Tetrahexylammonium hexafluorophosphate ($NHex_4PF_6$) was used as the supporting electrolyte for experiments in which toluene served as the solvent medium. This was prepared according to literature methods as described below [7].

Preparation of $NHex_4PF_6$

Tetrahexylammonium bromide (Hex_4NBr) (50 g) was dissolved in a mixture of water and ethanol. An excess of potassium hexafluorophosphate (KPF_6) (25 g) was dissolved in a minimum quantity of ethanol. The Hex_4NBr solution was then added dropwise to the KPF_6 solution with stirring to form a white suspension. The white solid formed was filtered off under vacuum and recrystallised from ethanol three times. The resultant white crystals of $NHex_4PF_6$ were stored under vacuum. A 90% yield was obtained.

Chemicals were weighed using a Unimatic CL 41 electronic balance capable of resolution to ± 0.1 mg. An ultrasonic bath (Semat Scientific, St. Albans, UK) was used to dissolve material where necessary. Solutions were deoxygenated with argon or nitrogen gas for a minimum of 30 minutes prior to use.

3.9 Chemicals

Comprehensive lists of solvents; electrochemical reagents and supporting electrolytes; and other chemicals used during the course of this work are given in Tables 3.2, 3.3 and 3.4 respectively.

Solvent	**Supplier**	**Grade/Purity**
Acetonitrile	Fisons	>99.99%
N,N-dimethylformamide	Aldrich	99.9% HPLC
Ethanol	BDH	99.5%
Toluene	Aldrich	99.8% HPLC

Table 3.2: Solvents

Chemical	**Source**	**Grade/Purity**
Ortho-Bromonitrobenzene	Aldrich	98%
9-Chloroanthracene	Lancaster	97%
Ferrocene	Aldrich	99%
Potassium hexafluorophosphate	Aldrich	98%
Potassium chloride	Aldrich	99%
Tetrabutylammonium perchlorate	Fluka	>99%
Tetrahexylammonium bromide	Fluka	>99%
N,N,N,N,-Tetramethyl-p-phenylenediamine	Aldrich	98%
Tris-(4-bromophenyl)amine	Aldrich	99%
Zinc n-dibutyldithiophosphate	Thornton Research Centre, Shell UK Ltd.	99.5%

Table 3.3: Electrochemical reagents and supporting electrolytes

Chemical	Supplier	Grade/Purity
Alumina drying agent	Aldrich	Activated, neutral, Brockmann 1, STD Grade Ca. 150 mesh
Alumina micropolish (0.3-9 μm particle size)	Buehler	Deagglomerated alpha alumina
Argon gas	BOC	Pureshield
Diamond lapping compound (0.1-25 μm particle size)	Kemet Int.	
Nitrogen gas	BOC	Oxygen free
Platinum sheet metal	Goodfellow	99.95%
Phosphorus pentoxide	Fluka	Purum
Platinum gauze	Goodfellow	99.95%
Silver wire	Goodfellow	99.95%

Table 3.4: Other chemicals

References

[1] J. F. Partridge, Glass-to-Metal Seals, The Society of Glass Technology, Sheffield, 1949

[2] J. H. Moore, C. C. Davis, M. A. Coplan, S. C.Greer, Building Scientific Apparatus, Addison-Wesley, Redwood City, California, USA, 1989, Chapter 2

[3] C.R.C. Handbook of Chemistry and Physics (55th Edition), CRC Press, Cleveland, Ohio, USA, 1974, D-152

[4] T. J. Cardwell, J. Mocak, J. H. Santos, A. M. Bond, The Analyst, 1996, **121**, 3, 357

[5] P. Sharp, Electrochimica Acta, 1983, **28**, 301

[6] D. D. Perrin, W. L. F. Armarego, Purification of Laboratory Chemicals, Pergamon Press, 1988

[7] J. H. Santos, A. M. Bond, J. Mocak, T. J. Cardwell, Anal. Chem., 1994, **66**, 1925

Chapter 4

Development of a variable temperature microelectrode apparatus

4.1 Introduction

This chapter describes the novel voltammetric apparatus, constructed as part of this thesis, which had the specific aims of being used at variable temperature and with resistive solvents. Experimental requirements of the apparatus are initially outlined in §4.2. A detailed description of construction and experimental characterisation as divided into individual components within the apparatus design then follows in §4.3 to 4.6.

4.2 Apparatus design

As defined in the introduction, the apparatus was designed for use with resistive solvents and at variable elevated temperatures. We first consider requirements of the apparatus for use in conjunction with resistive solvents. Since work in aprotic media is hampered by ohmic drop, the design required incorporation of microdisc working electrodes and minimisation of distance between reference and working electrodes. Secondly, we consider requirements of the apparatus in relation to elevated temperatures. The construction was required to be robust. We aimed to construct an apparatus which was suitable for use at temperatures of up to 200 ^{0}C. In addition, for ease of manipulation during an experiment, the design had to allow for quick and easy temperature control in which the temperature could be ramped to successively higher values. Furthermore, the electrolytic solution had to be maintained at an accurate and stable temperature during the measurement of voltammetric data.

To achieve these requirements, the apparatus design consisted of a tube-like heated cell into which a microelectrode was inserted so as to be positioned close to a reference electrode. Temperature control consisted of a heating wire wrapped around the electrode controlled by a temperature control system. The tube-like construction allowed for easy and accurate heating of the solution within. However, the confined volume of the cell necessitated the implementation of a flow system to ensure a fresh supply of electrolytic solution was maintained to the electrode surface and to facilitate removal of waste products. Furthermore, the flow system was required to deliver electrolytic solution to the electrode surface in a quantifiable and easily controlled manner. Finally, experimental design comprised a computer control system for the control and measurement of voltammetric parameters during the experimental procedure.

A detailed description of the apparatus as divided into the four main components, namely the heated voltammetric cell, temperature control system, flow system and computer control system now follows in §4.3, 4.4. 4.5 and 4.6 respectively. In addition, experimental characterisation of the apparatus in terms of stability of the temperature control system, and effects of flow on solution temperature stability and limiting current is described in the appropriate sections.

4.3 Heated voltammetric cell

The heated voltammetric unit of the experimental apparatus consisted of a Pyrex (borosilicate) glass tube 20 cm in length and 0.7 cm in diameter with electrodes positioned at one end. Such a structure allowed rapid and accurate heating of the small volume of solution contained within. Since Pyrex softens at temperatures in excess of 500 ^{0}C [1], fabrication of the cell from this material ensured its use in the temperature range required. A diagram of the heated cell is shown in Figure 4.1.

The apparatus incorporated the use of microdisc electrodes as a means of overcoming the ohmic resistance experienced in resistive media as described in §1.8.1. Fabrication of microdisc electrodes is described in §3.2.2. Microdiscs were sealed into one end of the heated unit by means of silicone rubber tubing as shown in Figure 4.1. The reference electrode comprised a platinum wire positioned inside the heated unit close to the microdisc electrode as in Figure 4.1. The platinum wire was placed inside the heated unit via a Pyrex arm on the side of the tube. The wire was soldered to a brass cap at the top of the arm which served as an external electrical contact. The counter electrode consisted of a platinum coil inside which the microdisc electrode was positioned to be located as close as possible to the reference electrode. In this way distance between working and reference electrodes was minimised to 2 mm so as to reduce ohmic distortion. Positioning of the counter electrode downstream of the working electrode ensured that unwanted counter products were removed without contact with the working electrode by flow of the solution to waste. As in the case of the reference electrode, external electrical contact was made by passing the end of the platinum coil into a small side arm and soldering to a brass cap.

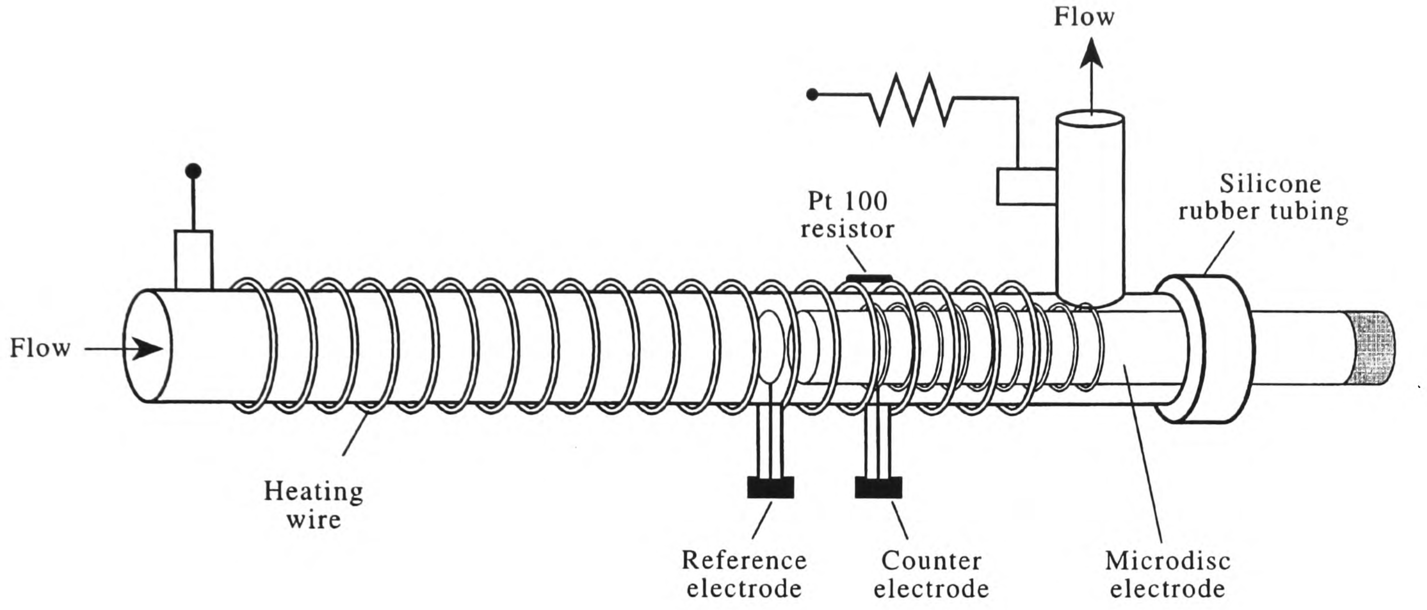

Figure 4.1: The heated voltammetric cell of the elevated temperature microelectrode apparatus

4.4 Temperature control

Heat was supplied to the voltammetric unit by means of heating wire coiled around the glass tube. The heating wire comprised manganin wire insulated with an epoxy laquar (supplied by Johnson Matthey, Reading, Berks, UK). Heating wire was bonded to the Pyrex unit using epoxy varnish (supplied by Gittings and Hill Ltd., Birmingham, UK). The manganin wire is stable up to temperatures in the region of 300 ^{0}C after which it begins to oxidise. The epoxy insulating coating and varnish are stable up to temperatures of approximately 200 ^{0}C.

Two successive systems were employed to control the temperature of the apparatus. The first consisted of a feedback control system whilst the second comprised a Proportional-Integral-Differential (PID) control system. These two systems are considered in §4.4.1 and 4.4.2 respectively. Electronics were fabricated by the Physical and Theoretical Chemistry Laboratory Electronics Department. Insulation of the heated voltammetric cell and characterisation of solution temperature in relation to the set-point is described in §4.4.3.

4.4.1 Feedback temperature control system

In the initial feedback control system, the temperature sensor consisted of a ceramic thermocouple located adjacent to the heating wire. This had an accuracy of ± 3 ^{0}C. The thermocouple was connected to a temperature controller (supplied by the Electronics Department of the Physical and Chemistry Laboratory, Oxford University) which was in turn connected to the heater via a transformer. In addition, both the controller and heating unit were connected to a mains power supply. To reach a desired temperature, a set-point temperature was entered into the temperature controller. Input of power to the heating unit was regulated by the controller via the transformer. This was done by comparison of the pre-set temperature and the temperature measured by the thermocouple. At measured temperatures lower than the set-point, the temperature controller maintained the transformer "on" to enable a continuous input of power to the heating unit. Upon reaching the required set-point, further power input to the heater was prevented by switching off the transformer.

Since power input was switched off only when the heater reached the set-point, the heating unit continued to heat up for a few seconds after this with the result that the set-point temperature was exceeded. With the power input switched off, the heater then began to cool and the temperature dropped below the desired set-point. At this point, the controller switched the transformer on once more to allow power input to resume. It was therefore found that temperature stability with this system was poor with considerable temperature oscillation around the set-point. Such fluctuations were found to increase with temperature. Stability of the heater temperature at various set-point temperatures is tabulated in Table 4.1.

Set-point instability using this temperature controller together with thermocouple inaccuracy led to measurement errors of approximately ±3.6 ^{0}C at 30 ^{0}C increasing to ±5.3 ^{0}C at 95 ^{0}C. The PID control system was implemented to address these problems as described in the following section.

Set-Point Temperature (⁰C)	Temperature accuracy (±⁰C)
30	0.6
40	0.7
50	1.0
60	1.0
70	1.4
80	1.7
90	2.0
95	2.3

Table 4.1: Set-point temperature stability using the feedback temperature control system

---

4.4.2 PID temperature control system

The temperature sensor of the PID temperature control system comprised a platinum Pt100 resistor located adjacent to the heating wire. The resistance measured was directly proportional to temperature with an accuracy of ± 0.1 ^{0}C. Temperature control was performed using a PID controller (an Autotune Temperature Controller, Model CAL3200, supplied by CAL Controls Ltd., Hitchin, Herts., UK). This delivered power to the heater in the form of pulses using a transformer which was turned on for a defined period within a set time scale. Power input to the heating unit could be varied by altering the pulse length within the same set time scale. Pulse length, therefore power input required, was determined according to the error between the pre-set temperature and the actual temperature measured by the Pt100 sensor. As the set-point was approached, pulse length was shortened to slow down the rate of heating in order to avoid temperature over-shoot. Upon reaching the required set-point, the pulse length required to maintain the temperature was calculated. This is shown diagrammatically in Figure 4.2.

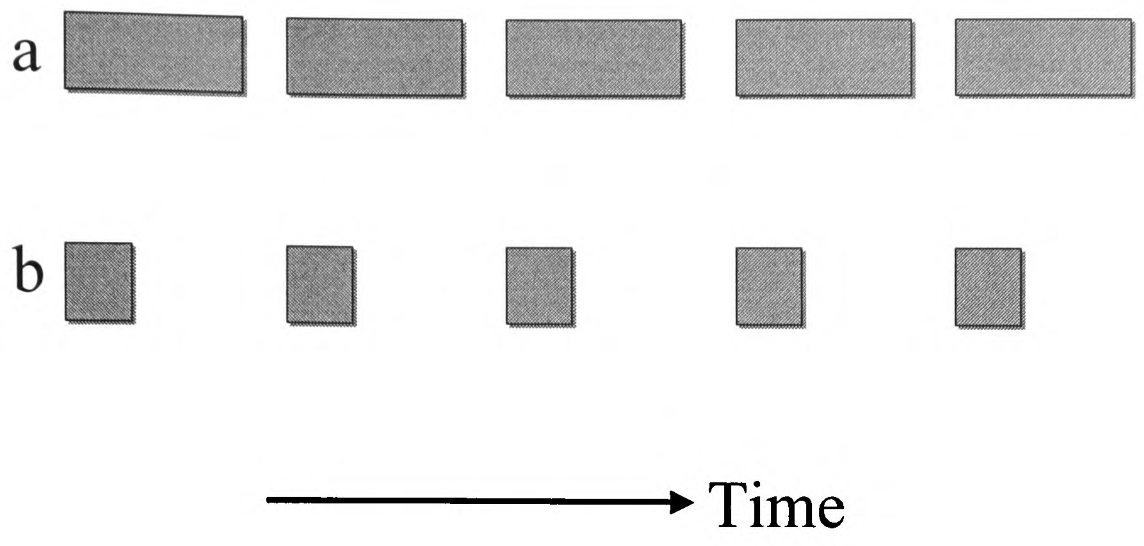

Figure 4.2: Diagrammatic representation of power input to the heating unit via the PID temperature control system showing pulse length a) at the onset of heating to the set-point temperature and b) as the set-point temperature is approached.

A diagram of the circuit is included in Appendix A. The PID temperature control system was observed to have a higher degree of temperature stability than the feedback temperature control system employed previously. Stability of the heater temperature using the PID temperature control system at various set-point temperatures is tabulated in Table 4.2. Overall error limits of the system including set-point instability coupled with sensor inaccuracy were ±0.2 °C at 30 °C rising to ±0.4 °C at 95 °C.

Set Point Temperature (°C)	**Temperature Accuracy (±°C)**
30	0.1
40	0.1
50	0.1
60	0.1
70	0.2
80	0.2
90	0.2
95	0.3

Table 4.2: Set-point temperature stability using the PID temperature control system

4.4.3 Characterisation of solution temperature

With an acceptable level of temperature accuracy and stability achieved for the heated voltammetric unit using the PID temperature control system, attention was directed toward solution temperature stability inside the cell at the site of the working electrode. To prevent loss of heat to the surroundings, the heated unit was surrounded by a double layer of 'Armiflax' material, a substance generally used for pipe-lagging, which served for insulation. Experiments were undertaken to investigate whether the insulation maintained the solution at the same temperature as measured by the Pt100 temperature sensor and therefore defined by the temperature control system.

A Pt100 resistor, identical to that used as the temperature sensor, was placed inside the heated voltammetric cell at the position of the working electrode. This was connected to a digital voltmeter (supplied by Cirkit Ltd., Broxbourne, Herts, UK) which enabled a value for the resistance to be determined which could be directly correlated to temperature. The resistor was sealed inside the cell in an identical manner to the working electrode using silicone rubber tubing. Insulation was reassembled around the cell and the cell filled with water. Since water was used as the solvent in this case, temperatures of up to 95 ^{0}C could be attained prior to the onset of boiling. The temperature controller was ramped to successively higher temperatures up to 95 ^{0}C and the temperature maintained at each value for 15 minute periods. Temperature stability was monitored using the Pt100 resistor located inside the cell for the duration of the 15 minutes. Results obtained are shown in Table 4.3. It can be seen that the position of the working electrode inside the heated cell reaches and maintains the temperature defined by the temperature controller well within a 2% margin of error.

Set-point Temperature (^{0}C)	**Solution Temperature Stability (^{0}C)**
30	0.3
40	0.3
50	0.3
60	0.5
70	0.6
80	0.8
90	1.0
95	1.0

Table 4.3: Solution temperature stability measured over 15 minute periods

This temperature range was adequate for the work undertaken during the course of this thesis, in which temperatures of up to 90 ^{0}C were utilised. Temperatures which could be achieved during experimental work were generally limited by the boiling temperature of the solvents used. Relevant boiling point values for the solvents used during this work, namely acetonitrile, N,N-dimethylformamide (DMF) and water, are shown in Table 4.4 [2].

Solvent	**Boiling Point (^{0}C)**	**Viscosity at 20 ^{0}C (*mPa s^{-1}*)**
Acetonitrile	81.6	0.34
DMF	153.0	0.92
Water	100.0	1.00

Table 4.4: Boiling point and viscosity values of solvents used in the variable temperature voltammetric apparatus

It is anticipated that the apparatus could be utilised at temperatures up to 200 ^{0}C with the application of higher boiling point solvents. This would require prior testing of temperature stability using the procedure outlined above.

4.5 Flow system

During the course of experimental work, a flow of solution was maintained through the heated voltammetric cell. This ensured a fresh supply of electrolytic solution was presented to the electrode surface within the confined volume of the heated cell and also permitted removal of waste products. To enable the flow of solution past the electrodes, a flow system was devised incorporating delivery of solution from a reservoir to the electrodes in a controlled and measurable manner. We first consider how control of flow rate was achieved in §4.5.1 before characterising influence of flow rate on limiting current and temperature stability in §4.5.2 and 4.5.3 respectively. §4.5.4 gives details of the solution reservoir and solution degassing procedures. The overall flow system construction is described in §4.5.5.

4.5.1 Flow rate control

Flow rate was controlled by means of two calibrated capillary tubes, constructed of Pyrex glass, through which the waste solution flowed. The two capillaries were of identical bore-size but different lengths, thus flow rate could be varied through choice of capillary used. In addition, a by-pass tube was present to enable rapid flow of solution through the cell as a means of filling and emptying the cell and also to facilitate bubble removal. Selection of the capillary or by-pass was made using a three-way valve.

Flow rate of each capillary was calibrated in relation to the height difference between outlet tube and reservoir (ΔH). The capillary was calibrated by measuring flow rate of a solvent at different ΔH values. Flow rate was measured by recording the volume of solvent passed through the capillary in a given time period. The resulting calibration plot of flow rate versus ΔH was linear with a gradient characteristic of the capillary, termed the capillary constant. Experimental flow rates could then be calculated from the measured ΔH using Equation 4.1:

$$\text{Flow rate } (\text{cm}^3\,\text{s}^{-1}) = \text{Capillary Constant } (\text{cm}^2\,\text{s}^{-1}) \times \Delta H \text{ (cm)}. \qquad (4.1)$$

Calibration plots for each solvent are shown in Figure 4.3. In all three cases, calibration plots are linear and pass through the origin within a 5% margin of experimental error as depicted by the associated error bars. Errors arise from sources such as height measurement, weighing and time-keeping inaccuracies. Flow rates decrease in the order acetonitrile>DMF>water in line with the viscosities reported in Table 4.4 [2].

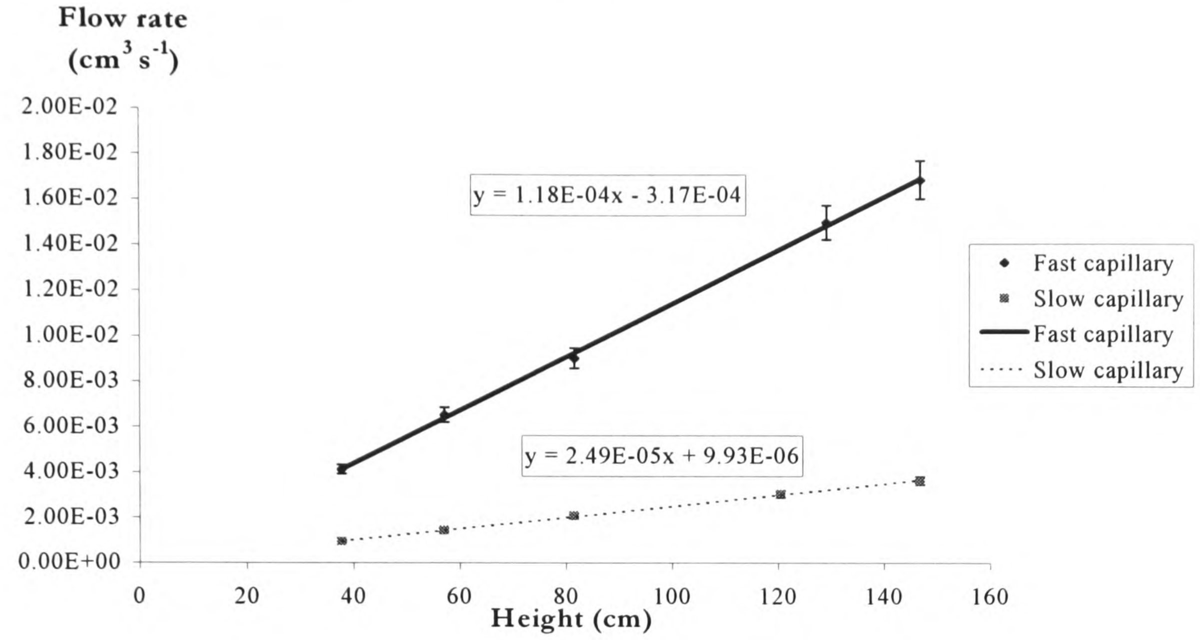

(a)

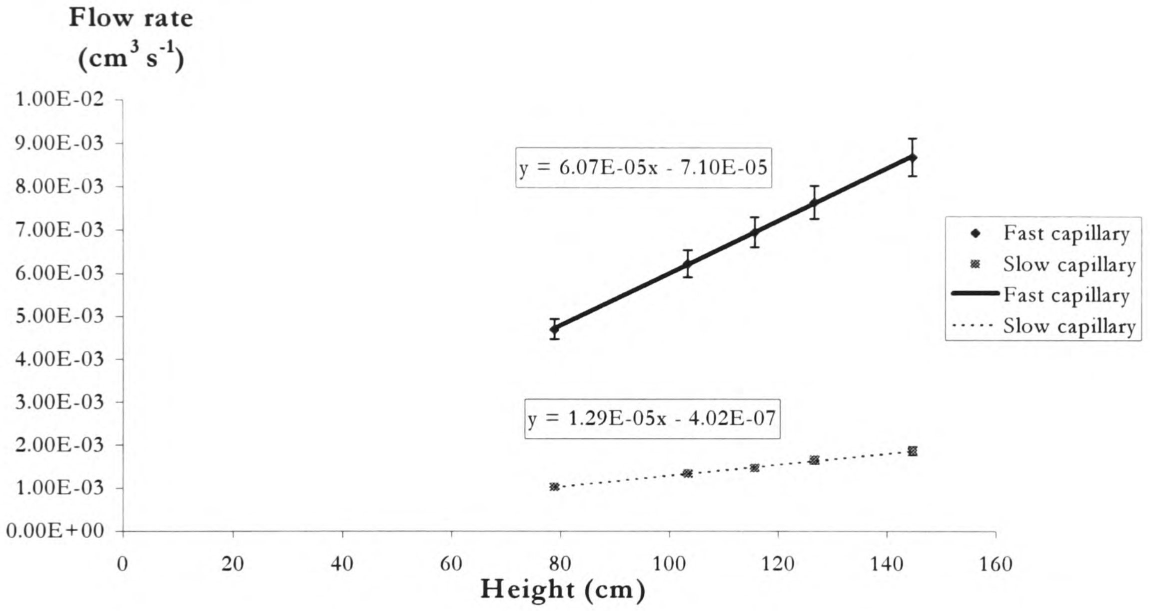

(b)

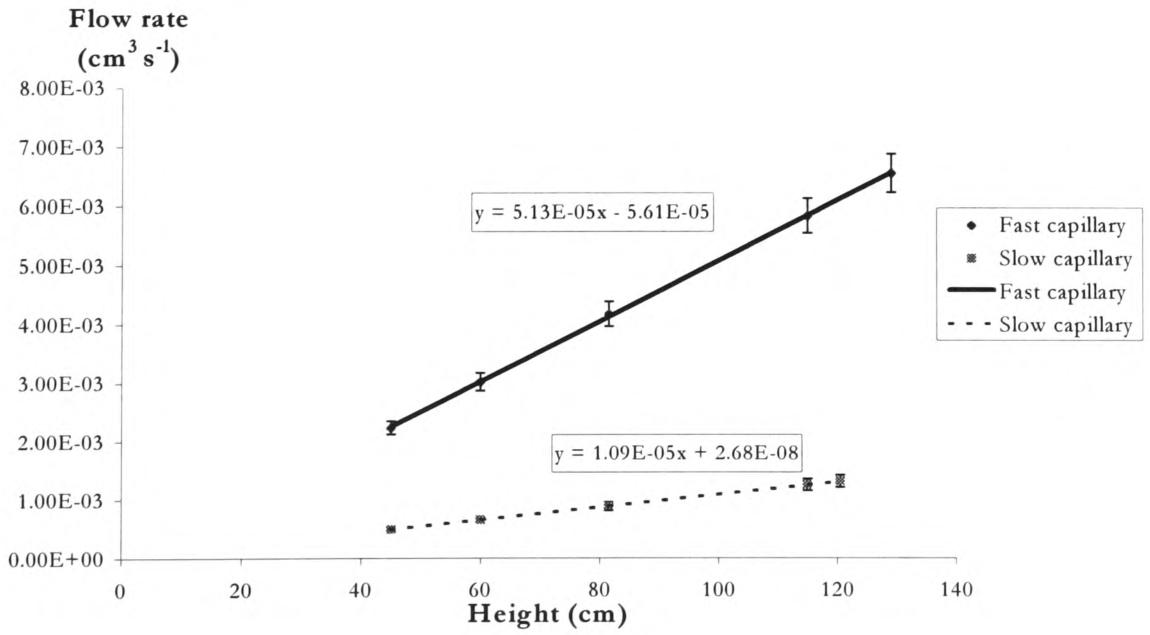

(c)

Figure 4.3: Calibration curves for the flow of (a) acetonitrile (b) DMF and (c) water through the elevated temperature apparatus

4.5.2 Characterisation of flow rate effects on limiting current

Compton et al report enhancement of limiting current at a microdisc electrode in the presence of flow as a result of convective effects [3]. The flow rates implemented were greatly in excess of those used during this investigation. To assess the effects of convection at the slow flow rates employed during this work, we undertook an empirical investigation of limiting current dependance on flow rate.

Investigations were carried out using a microdisc electrode with a nominal diameter of 10 μm. An accurate value for the electrode diameter was determined prior to use via electrochemical calibration using a standard ferrocene solution at 25 ^{0}C. Start/stop flow experiments were carried out in which the working electrode was maintained at a potential in excess of the electrochemical process under study and the current recorded as a function of time as flow rate was successively turned on and off. In this way, the effect of flow on limiting current could be directly observed. A flow rate of 7.21×10^{-3} cm^3 s^{-1} was used which is a little in excess of the typical flow rate employed during elevated temperature investigations. A 1 mM ferrocene/acetonitrile solution containing 0.1 M NBu_4ClO_4 as supporting electrolyte was used as a model system which as we have previously noted in §3.2.2 undergoes a reversible one electron oxidation which is readily and easily measured. The temperature of the heated unit was maintained constant at 25 ^{0}C throughout the experiment. The current-time results obtained are shown in Figure 4.4. There are no appreciable differences in measured current in the presence or absence of flow.

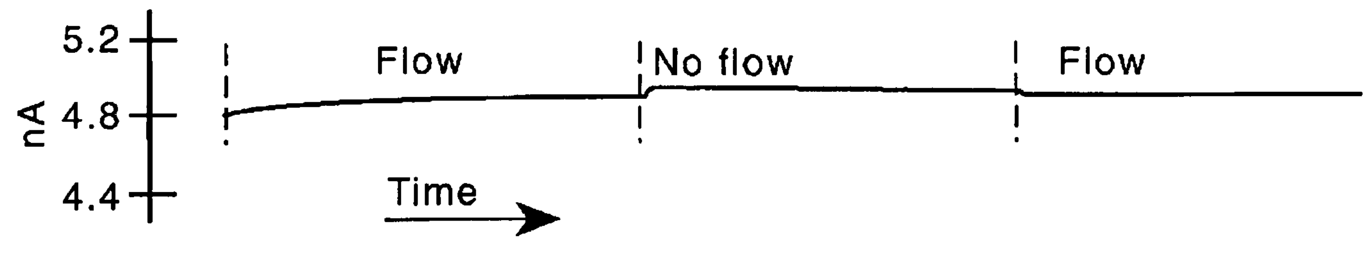

Figure 4.4: Limiting current obtained for the oxidation of 1 mM ferrocene in acetonitrile/0.1 M NBu_4ClO_4 solution in the presence and absence of flow using a flow rate of 7.21×10^{-3} cm^3 s^{-1} at a 10 μm diameter microelectrode, temperature 25 ^{0}C

In a second investigation of flow rate effects on limiting current, current-voltage curves were recorded at a variety of flow rates for a 1 mM ferrocene solution in acetonitrile using the 10 μm microelectrode. Throughout the experiment, temperature was maintained at a constant value of 25 ^{0}C. Flow rates ranged between 1.05×10^{-2} cm^3 s^{-1} and 1.62×10^{-3} cm^3 s^{-1}. Five current-voltage curves were recorded for each flow rate and an average value obtained. Average limiting currents obtained at each flow rate are tabulated in Table 4.5.

Flow rate (cm^3 s^{-1})	Average limiting current (A)
1.050×10^{-2}	4.83×10^{-9}
8.44×10^{-3}	4.81×10^{-9}
6.14×10^{-3}	4.78×10^{-9}
5.38×10^{-3}	4.80×10^{-9}
4.44×10^{-3}	4.80×10^{-9}
4.33×10^{-3}	4.75×10^{-9}
3.17×10^{-3}	4.77×10^{-9}
3.10×10^{-3}	4.83×10^{-9}
2.30×10^{-3}	4.81×10^{-9}
1.62×10^{-3}	4.80×10^{-9}

Table 4.5: Average limiting currents obtained at varying flow rates for ferrocene (1 mM) with NBu_4ClO_4 (0.1 M) in acetonitrile at a 10 μm diameter microelectrode

---

A plot of average limiting current as a function of flow rate is shown in Figure 4.5. There are no appreciable trends in the graph obtained, in contrast random scatter of the points is observed. Furthermore, limiting currents lie within a 1% margin of experimental error. This is well within the experimental error that would be expected to arise from measurement and instrumentation sources. Limiting currents can therefore be assumed to be essentially identical. In addition, an average value of 4.74×10^{-9} A was obtained for the limiting current in the absence of flow. This is virtually identical to the values obtained under flowing conditions tabulated above.

Electrode diameters of 10 μm or smaller were used exclusively during the course of this work and for these it was concluded that flow rates were sufficiently slow as to not to enhance limiting current via forced convection. Larger electrode diameters are more susceptible to the effects of forced convection than their smaller counterparts since their larger diffusion layers will overlap more effectively with the region of flowing solution. The use of electrodes with diameters in excess of 10 μm would require further monitoring of flow rate effects on limiting current using the procedures outlined above.

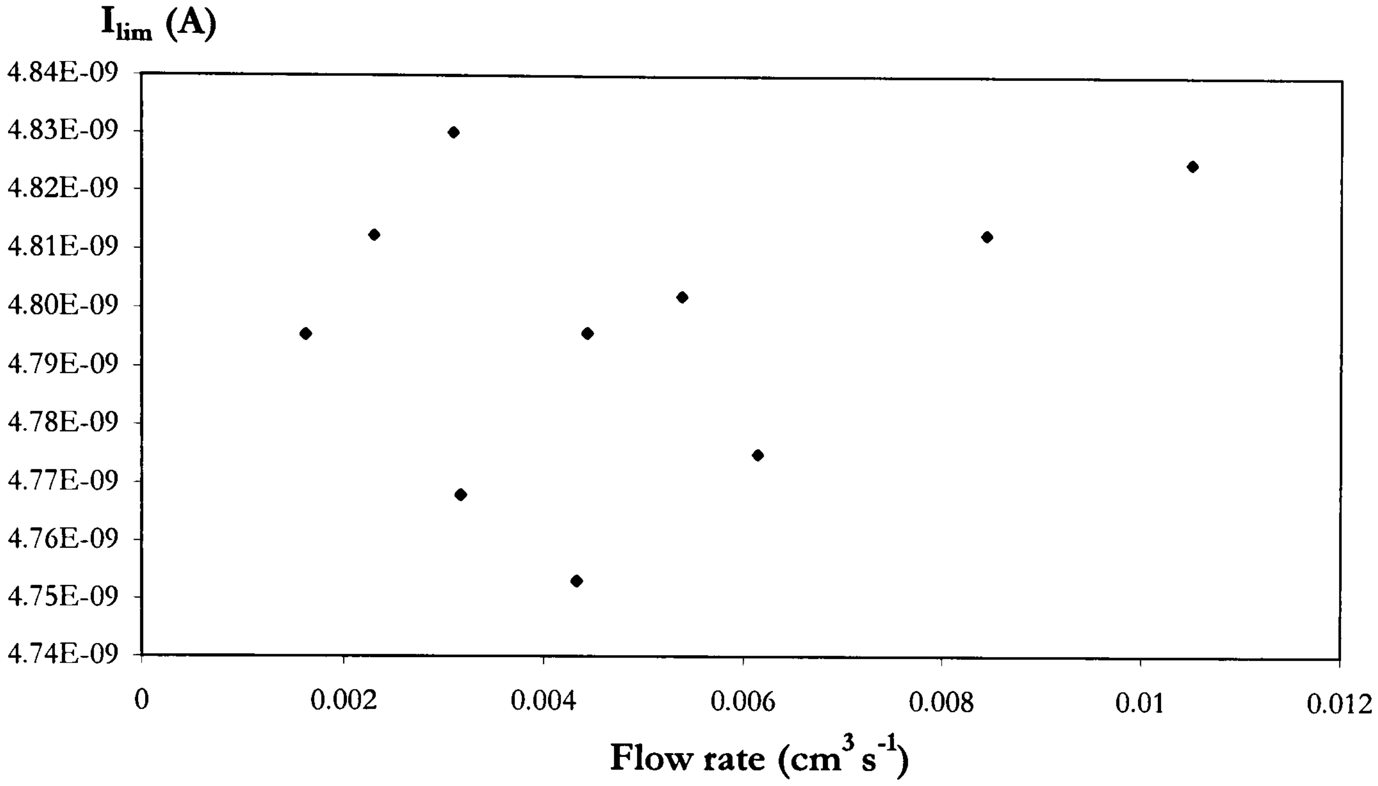

Figure 4.5: Limiting current as a function of flow rate for the oxidation of 1 mM ferrocene in acetonitrile/0.1 M NBu_4ClO_4 solution using a 10 μm microelectrode at a temperature of 25 °C

4.5.3 Characterisation of flow rate effects on temperature stability

Characterisation of flow rate effects on solution temperature stability at the site of the working electrode was carried out using the procedure defined in §4.4.4. In this case, temperature stability was recorded over 15 minute time periods for various temperatures at 3 different flow rates. Solution temperature stabilities observed for each of the flow rates are shown in Table 4.6.

At flow rates of 4.3×10^{-3} and 7.54×10^{-3} $cm^3\ s^{-1}$, there was no significant difference in temperature instability observed. Temperature was maintained at stable values throughout, fluctuating by a maximum of ±1.2 °C at 95 °C. For the fastest flow rate investigated, significantly increased temperature instability was apparent. Furthermore, solution temperatures measured at this flow rate were invariably lower than the set-point temperature. This suggests that solution flow through the heated voltammetric unit was too fast to allow an equilibrium temperature value to be reached. With this in mind, elevated temperature work was carried out at flow rates typically of the order 5×10^{-3} cm^3 s^{-1}. In this way, a constant supply of fresh electrolytic solution was presented to the electrode surface without increased temperature instability or, as observed in the previous section, enhancement of limiting current due to forced convection.

Set Point Temperature (°C)	**Flow rate (cm^3 s^{-1})**		
	4.20×10^{-3}	**7.54×10^{-3}**	**9.70×10^{-3}**
30	0.3	0.3	0.4
40	0.4	0.3	1.3
50	0.3	0.5	2.7
60	0.5	0.5	3.0
70	0.7	0.6	3.5
80	0.9	1.0	3.3
90	1.1	1.1	4.2
95	1.1	1.2	4.3

Table 4.6: Comparison of solution temperature stability (± °C) measured over 15 minute time periods for different flow rates

---

4.5.4 Solution reservoir and pre-treatment

Solution was delivered to the heated voltammetric unit via gravity flow from a 500 cm^3 glass reservoir. The reservoir comprised a round-bottomed vessel with 1 large inlet and 2 small inlet arms. The bottom of the cell contained a glass exit tube through which solution flowed to reach the voltammetric cell. One of the small inlet arms contained a pipette connected to a supply of argon gas thereby facilitating solution deoxygenation. Argon gas was bubbled through the solution for 30 minutes prior to use and throughout the experimental procedure in order to exclude the presence of oxygen. The gap between the pipette and inlet arm was sealed using parafilm. In addition, solutions were heated during the degassing procedure to a temperature of 40 °C using a heating mantle placed around the reservoir. This procedure served to remove dissolved gas present in the solution which at higher temperatures became less soluble in the solution yielding gas bubbles. In this way, the formation of bubbles in the flow cell during elevated temperature work was avoided. Bubbles in the vicinity of the working electrode form an area of high electrical resistance thus preventing the measurement of voltammetric data. A thermometer was placed into the remaining small inlet arm to facilitate measurement of solution temperature. As in the case of the pipette, the thermometer was sealed into the inlet arm using parafilm.

4.5.5 Flow system construction

The flow system was composed principally of glass where possible and Teflon tubing where greater flexibility was required. This was necessary to prevent the ingress of oxygen into the solution as it flowed to the heated voltammetric cell. The flow system between the reservoir and heating unit incorporated a length of glass tubing connected to a 20 cm length of Teflon which was then joined to the voltammetric cell. The remainder of the flow system comprised a length of Teflon tubing running from the heating unit to the glass capillary system. After exiting the capillary system, solution flowed through a length of Teflon tubing to a glass tip where it dripped into a waste receptacle. Connections were made using silicone rubber tubing. Since silicone rubber tubing is permeable to oxygen, connections upstream of the electrode were jacketed with plastic bags filled with a positive pressure of nitrogen to exclude oxygen. Sealing of downstream connections within a nitrogen atmosphere was not necessary since ingress of oxygen into used solution at these points did not affect voltammetric reactions. The length of Teflon tube upstream of the heating cell was also jacketed using a nitrogen filled plastic bag to prevent the possible ingress of oxygen. A schematic diagram of the flow system is given in Figure 4.6.

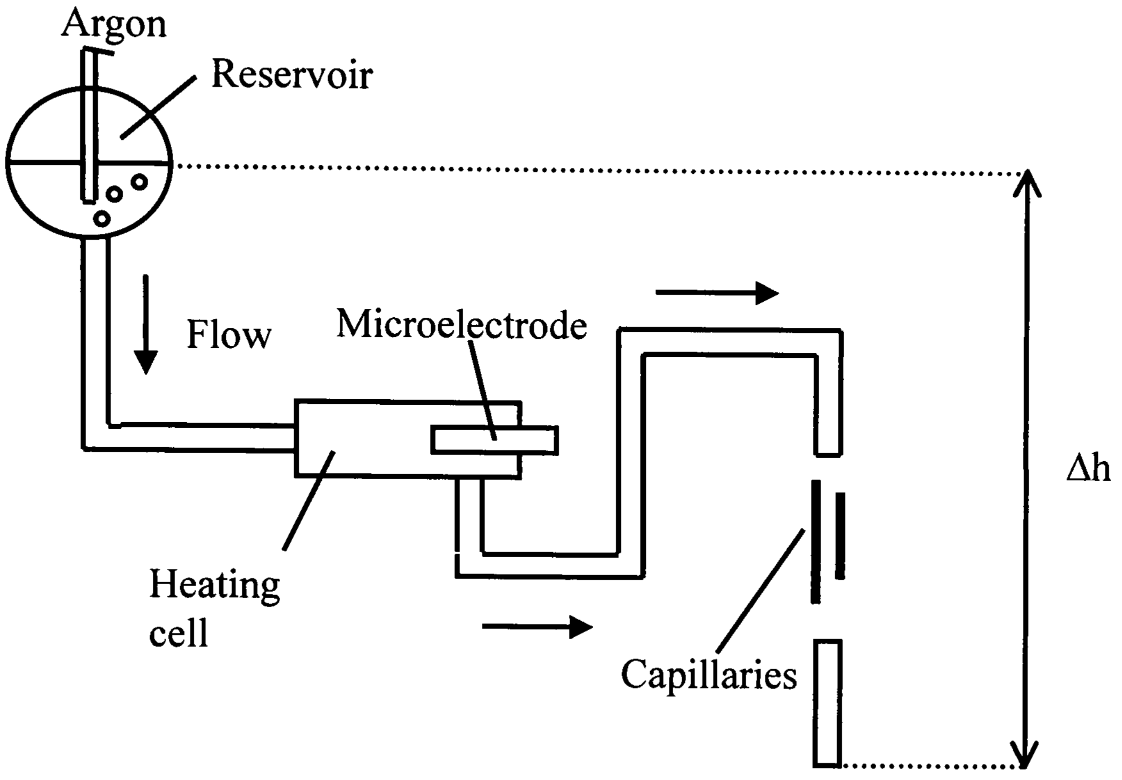

Figure 4.6: Schematic representation of the gravity flow system for the elevated temperature microelectrode apparatus

4.6 Computer control system

Linear sweep functions and current measurement were performed using a linear sweep potential scan generator attached to a picoammeter. This was controlled by a model 486 personal computer with 66 MHz clock speed using data acquisition software written by Dr. Barry Coles of the Physical and Theoretical Chemistry Laboratory of Oxford University. The program allowed for linear sweep scan rates in the range 5 mV s^{-1} to 1 V s^{-1} and acquisition of the resulting current-voltage curves obtained. Scan rates of 10 mV s^{-1} were used in conjunction with the heated voltammetric apparatus to ensure a steady state regime at the microdisc electrodes was maintained. Analysis of data obtained in computerised format was performed using a data analysis program written by Mr. John Alden of the Physical and Theoretical Chemistry Laboratory. This permitted measurement of limiting currents and half wave potentials. In addition, analysis of the steady-state current-voltage curves in terms of the diagnostic test for electrochemical reversibility as outlined in §2.5.3 was also possible.

4.7 Summary

A novel variable temperature electrochemical apparatus has been described for the measurement of voltammetric data in resistive media at elevated temperatures. The structure of the apparatus allows for temperatures of up to 200 ^{0}C to be attained. However, in the course of work undertaken during this thesis, temperatures were limited by the boiling points of the solvents used. The highest temperature practically achieved using this experimental set-up was 95 ^{0}C.

The apparatus structure consisted of a heated Pyrex voltammetric unit containing reference, counter and microdisc working electrodes; a temperature control system comprising heating wire, insulation and associated electronics designed to heat the unit in a rapid and controllable manner and maintain the set-point temperature at a stable value; a flow system to allow a continuous supply of solution to the working electrode in a quantifiable and easily controlled manner; and a computer system for the control of voltammetric parameters and the measurement and analysis of data.

Characterisation of the apparatus at temperatures of up to 95 ^{0}C is described in terms of stability of the temperature control system, solution temperature stability under flowing conditions and the effects of flow rate on limiting current obtained at the microdisc electrode. To be used at temperatures up to 200 ^{0}C, further characterisation of the equipment would be necessary.

We now move on to demonstrate the use of the apparatus as applied to real chemical systems in Chapter 5.

References

[1] J. F. Partridge, Glass-to-Metal Seals, The Society of Glass Technology, Sheffield, 1949

[2] C.R.C. Handbook of Chemistry and Physics (74th Edition), CRC Press, Cleveland, Ohio, USA, 1993, 8-55

[3] J. Booth, R. G. Compton, J. A. Cooper, R. A. W. Dryfe, A. C. Fisher, C. L. Davies, M. K. Walters, J. Phys. Chem., 1995, **99**, 10942

Chapter 5

Application of the variable temperature microelectrode apparatus

5.1 Introduction

The novel variable temperature steady state microelectrode technique developed as part of this thesis has a variety of applications. Over a variable temperature regime, the rate and equilibrium constants of reactions vary to provide a useful handle on the characterisation of chemical processes. During the present chapter we demonstrate the potential of this technique as applied to the determination of diffusion coefficients at variable temperatures in the case of simple one electron transfer processes during studies of *N,N,N′,N′*-tetramethyl-p-phenylenediamine and tris(4-bromophenyl)amine in §5.2 and 5.3 respectively. The variation in diffusion coefficient with temperature was subsequently used in the calculation of activation parameters for diffusion and Stokes-Einstein radii. We also demonstrate the potential of this novel technique as a method of accessing rapid kinetic processes at variable temperatures to derive activation parameters during investigations of ortho-bromonitrobenzene and 9-chloroanthracene halide bond cleavage in §5.4 and 5.5 respectively. Areas in which this apparatus has significant advantages over previously applied techniques are highlighted.

5.2 *N,N,N′,N′*-Tetramethyl-p-phenylenediamine (TMPD)

5.2.1 TMPD oxidation

(TMPD) shown in Figure 5.1, undergoes a reversible one electron oxidation to form the radical cation, as denoted in Equation 5.1:

$$\text{TMPD} \rightarrow \text{TMPD}^{+\cdot} + e^{-}. \qquad (5.1)$$

The one electron oxidation process has been demonstrated in a range of solvents including acetonitrile [1,2,3,4,5], water [6,7,8] and chloroform [50]. For the purpose of this work, we consider the oxidation of TMPD in both acetonitrile and water. A review of the literature pertaining to TMPD oxidation in these two solvents is presented.

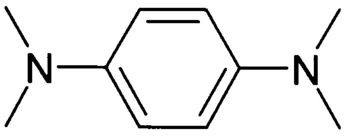

Figure 5.1: Structure of TMPD

The nature of the TMPD reversible one electron oxidation in acetonitrile solution has been demonstrated by Fernàndez and Zon using cyclic voltammetry during studies carried out with a platinum working electrode using a range of supporting electrolytes [1,2]. Voltammograms showed anodic and cathodic peak currents to be equal with a peak separation of circa 60 mV at 20 ^{0}C characteristic of a reversible one electron process. A further study by the same group used potentiometric titration at 20 ^{0}C to interrogate the oxidation of TMPD in acetonitrile at a platinum electrode with 0.1 M $NaClO_4$ as supporting electrolyte [3]. A plot of $\log I/(I_{lim}-I)$ versus E gave a slope of 57 mV consistent with a reversible one electron charge transfer process.

Reversible one electron transfer processes have also been observed by other workers during cyclic voltammetric studies of TMPD in acetonitrile solution with 0.1 M $NHex_4ClO_4$ as supporting electrolyte [4,5].

The existence of a second oxidation peak at a more positive peak potential has been noted during cyclic voltammetric studies described above [3,4,5]. This is assigned to a second one electron transfer to yield the dication. However, cyclic voltammetric studies report that the two oxidation waves occur at well separated potentials and for the purpose of this work, we consider only the first reversible one oxidation process. Thus, steady state scans were stopped prior to the onset of the second oxidation wave.

One electron oxidation of TMPD to form the radical cation has also been observed using water as the solvent species. A well-defined reversible one electron oxidation has been observed over most of the aqueous pH range by Adams et al [6,7]. These workers also described the use of EPR to confirm the presence of the radical cation following the oxidation process. Friend and Roberts report a study of TMPD oxidation in aqueous solution conducted over a range of pH values containing acetate buffers maintained at a constant ionic strength of 1.0 M using a platinum microelectrode

[8]. A plot of $\log I/(I_{\lim}-I)$ was linear with a slope in the region of 60 mV indicative of a one electron oxidation process at 20 ^{0}C. The above investigations also noted the presence of a second oxidation process but, as in the case of acetonitrile, first and second charge transfer reactions were observed to occur at well separated peak potentials. Thus, the second oxidation process was not significant during the investigation reported below.

5.2.2 Application of the elevated temperature apparatus to the study of TMPD

We used the elevated temperature electrochemical cell as a means of obtaining diffusion coefficients at variable temperatures in two different solvents, acetonitrile and water. From these, activation parameters for diffusion were calculated. Variation of diffusion coefficient with temperature was compared to the theoretical Wilke-Chang relationship. Variable temperature data was also used to calculate a value for the effective radius of TMPD via the Stokes-Einstein relationship. The value obtained was compared with previously reported literature values and an alternative value calculated by us using the Nemesis computer simulation. A description of the Nemesis package is given in the appropriate section.

We have shown oxidation of TMPD in acetonitrile solution to be a well established experimental system. Elevated temperature work has previously been reported including the determination of activation parameters for diffusion and determination of effective radii. Calculation of effective radii for TMPD in acetonitrile is also reported via alternative methods. Recourse to previously published work is made in the appropriate section of the experimental work which now follows. Such previous work serves as a useful validation of our results.

Our study of TMPD oxidation in water represents, as far as we are aware, the first variable temperature study of TMPD in this solvent system. The activation parameters for diffusion together with effective radii extracted from the data obtained are the first, as far as we know, with water as the solvent species. Furthermore, from the data obtained in acetonitrile and water, a comparison was possible in terms of solvent characteristics between the two systems.

5.2.3 Experimental determination of diffusion coefficients at elevated temperatures in acetonitrile

During our study, steady-state current-voltage voltammograms were recorded for a 1 mM solution of TMPD in acetonitrile containing 0.1 M NBu_4ClO_4 as supporting electrolyte. Steady state waves were obtained at temperatures ranging between 25 and 60 ^{0}C using a 5 μm diameter microelectrode. An accurate value for the electrode diameter was obtained prior to use via electrochemical calibration at 25 ^{0}C using a standard ferrocene solution.

A single wave corresponding to the oxidation of TMPD was observed at a half-wave potential ($E_{1/2}$) of +0.2 V versus the platinum pseudo reference electrode. A representative voltammogram for the oxidation of TMPD in acetonitrile obtained at 23.5 ^{0}C is shown in Figure 5.2. The $E_{1/2}$ value obtained is in good agreement with the formal peak potential of +0.278 V versus the ferrocene/ferrocenium (Fc/Fc^+) couple reported by Zon and Fernández [1]. This value was obtained from the mean of anodic and cathodic peak potentials of cyclic voltammograms recorded at 25 ^{0}C using 0.1 M $NaClO_4$ as supporting electrolyte. It also correlates well with further formal peak potential values derived by these workers using the same technique. Values of +0.095 V and +0.010 V versus SCE were obtained using 0.1 M NEt_4BF_4 and 0.1 M $NaClO_4$ electrolytes respectively at 0 ^{0}C [2]. A value of +0.004 V versus SCE was recorded by Zon et al using potentiometric titration at 20 ^{0}C with 0.4 M $NaClO_4$ as electrolyte [3]. There is also good correlation with E_p values obtained during the cyclic voltammetric studies described previously of +0.100 V [4] and +0.138 V [5] versus SCE.

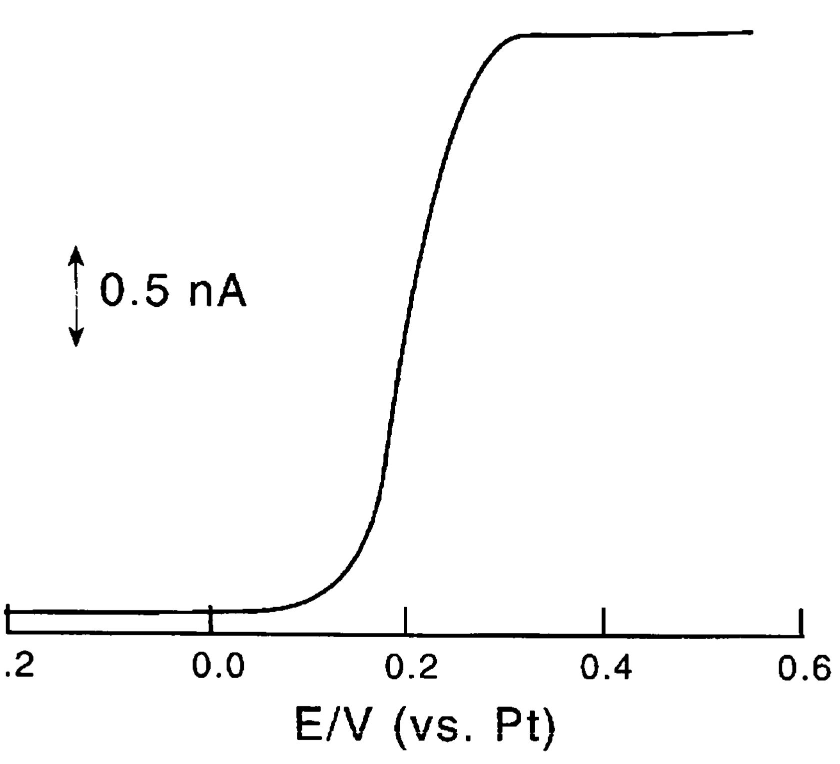

Figure 5.2: Steady state voltammogram for oxidation of 1 mM TMPD in acetonitrile/0.1 NBu_4ClO_4 solution recorded using a 5 μm diameter platinum microelectrode at 23.5 °C, scan rate 10 mV s^{-1}.

Limiting currents obtained at each temperature are given in Table 5.1. For each temperature, 5 current-voltage curves were recorded and an average value obtained. Limiting currents were used to derive diffusion coefficients at each temperature using the theoretical expression for the transport limited current at a microelectrode previously defined in Equation 2.33. Diffusion coefficients calculated in this way are recorded in Table 5.1.

Temperature (°C)	**I_{lim} (A)**	**D (cm^2 s^{-1})**
23.5	2.92×10^{-9}	$2.39\times10^{-5} \pm 0.9\times10^{-6}$
30	3.19×10^{-9}	$2.61\times10^{-5} \pm 1.0\times10^{-6}$
40	3.62×10^{-9}	$2.96\times10^{-5} \pm 1.2\times10^{-6}$
50	4.07×10^{-9}	$3.33\times10^{-5} \pm 1.3\times10^{-6}$
60	4.56×10^{-9}	$3.73\times10^{-5} \pm 1.5\times10^{-6}$

Table 5.1: Limiting currents and diffusion coefficients obtained for oxidation of 1 mM TMPD in acetonitrile/0.1 M NBu_4ClO_4 solution using a 5 μm diameter electrode at temperatures ranging from 23.5 to 60 °C

The value of D obtained at 23.5 ^{0}C is in good agreement with previously reported literature values. A value of $2.81\text{x}10^{-5}$ cm^2 s^{-1} was reported for the diffusion of TMPD in acetonitrile by Fernández and Zon [1]. This value was obtained via chronoamperometric techniques using 0.1 M $NaClO_4$ as supporting electrolyte at 25 ^{0}C. The same authors derived values of $2.27\text{x}10^{-5}$ and $2.32\text{x}10^{-5}$ cm^2 s^{-1} with 0.1 M Et_4NClO_4 and 0.1 M $NaClO_4$ as electrolytes respectively using the same technique at 0 ^{0}C [2]. Diffusion coefficients have also been determined by the same group for TMPD in acetonitrile solution with various supporting electrolytes using microelectrode chronoamperometry [9]. Values obtained at 25 ^{0}C with 0.1 M $NHex_4ClO_4$ and 0.1 M $NaClO_4$ were $1.96\text{x}10^{-5}$ and $2.46\text{x}10^{-5}$ cm^2 s^{-1} respectively.

5.2.4 Estimation of diffusion coefficients using Wilke-Chang theory

The Wilke-Chang relationship has been developed as a means of estimating diffusion of species in solution [10]. It is an extension of the qualitative conclusions of the Stokes-Einstein relationship [13,14] that temperature and the inverse of solution viscosity contribute to the rate of diffusion of a species in solution. Extension of the theory to incorporate the effects of solvent and solution properties was made by empirical observation of a wide range of experimental data. Wilke and Chang concluded that the following correlation could be used to estimate values of diffusion coefficients in solution:

$$D = 7.4\text{x}10^{-8}\frac{(\chi M)^{1/2}T}{\nu V^{0.6}} \qquad (5.2)$$

in which M is the molecular weight of the solvent and V is the molal volume of the solute at normal boiling point estimated for complex molecules by atomic contributions as defined by La Bas [11]. A list of some atomic volume contributions together with volume deductions necessary for cyclic and aromatic structures are given in Tables 5.2 and 5.3 respectively. χ is the association parameter introduced to define the molecular weight of the solvent with respect to the diffusion process. This is equal to 2.6 in the case of water and 1 in the case of non-associated solvents.

Atom	Atomic volume
Bromine	27.0
Carbon	14.8
Chlorine: Terminal as in R-Cl	21.6
Medial as in R-CHCl-R	24.6
Hydrogen	3.7
Iodine	37.0
Nitrogen: except as noted below	15.6
in primary amines	10.5
in secondary amines	12.0
Oxygen: doubly bonded	7.4
In aldehydes and ketones	7.4
In methyl esters	9.1
In methyl ethers	9.9
In higher ethers and esters	11.0
In acids	12.0
In union with S, P, N	8.3
Phosphorus	27.0
Sulphur	25.6
Zinc	20.4

Table 5.2: Atomic contributions for the calculation of molal volumes as defined by La Bas

Cyclic/aromatic structure	Volume deduction
3-membered ring	6.0
4-membered ring	8.5
5-membered ring	11.5
6-membered ring	15.0
Naphthalene	30.0
Anthracene	47.5

Table 5.3: Volume deductions necessary for cyclic and aromatic structures during calculation of molal volumes as defined by La Bas

For most of the systems studied during development of the empirical equation above, a correlation to within 10% of the experimentally determined diffusion coefficient was observed. However, Wilke and Chang also concluded that the diffusion process is extremely complex and since a more rigorous treatment of solute-solvent interactions would be desirable, the correlation may be less accurate in some instances.

Using the Wilke-Chang method for estimation of diffusion coefficients, a value of 1.51×10^{-5} cm^2 s^{-1} is anticipated for diffusion of TMPD in acetonitrile at 25 ^{0}C. This deviates from the experimentally determined value considerably. Possible causes for this deviation are considered later in this chapter in §5.2.11.

5.2.5 Determination of activation parameters for diffusion

A chemical reaction, such as electron transfer in solution, is a rate controlled process where the rate is described by the Arrhenius relationship [18] shown in Equation 5.3:

$$k = Ae^{\frac{-E_a}{RT}}. \tag{5.3}$$

E_a denotes the activation energy and is regarded as the energy barrier that reacting particles are required to overcome in order for reaction to occur and A is referred to as the pre-exponential factor. This equation can be justified in general terms by collision theory which correlates the $-E_a/RT$ term to the probability that the collision carries enough energy for reaction to occur and A defines the frequency of collisions. More sophisticated theories can be invoked to describe this relationship. Recourse to activated complex theory will be made in §5.4.8. The Arrhenius relationship can also be written in the form shown in Equation 5.4:

$$\ln k = \ln A - \frac{E_a}{RT}. \tag{5.4}$$

Thus a plot of ln k versus 1/T will yield a straight line from which E_a and A can be extrapolated.

A chemical reaction can be viewed as movement of a particle B from a site in atom A to a site in atom C as denoted in Figure 5.3. By analogy, diffusion of species in solution as illustrated in Figure 5.4, in which a molecule moves to another site within the solvent system, can also be regarded as an Arrhenius process. A plot of ln D versus 1/T can therefore be used to obtain the E_a for diffusion in the same way as for a reaction process as has been described above.

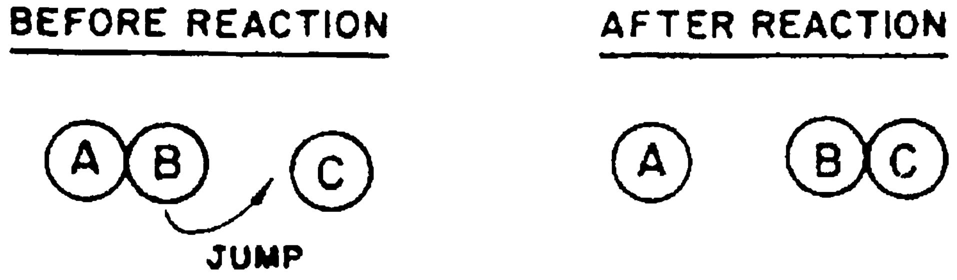

Figure 5.3: Representation of a three-atom chemical reaction AB+C→A+BC viewed as the jump of atom B from atom A to atom C

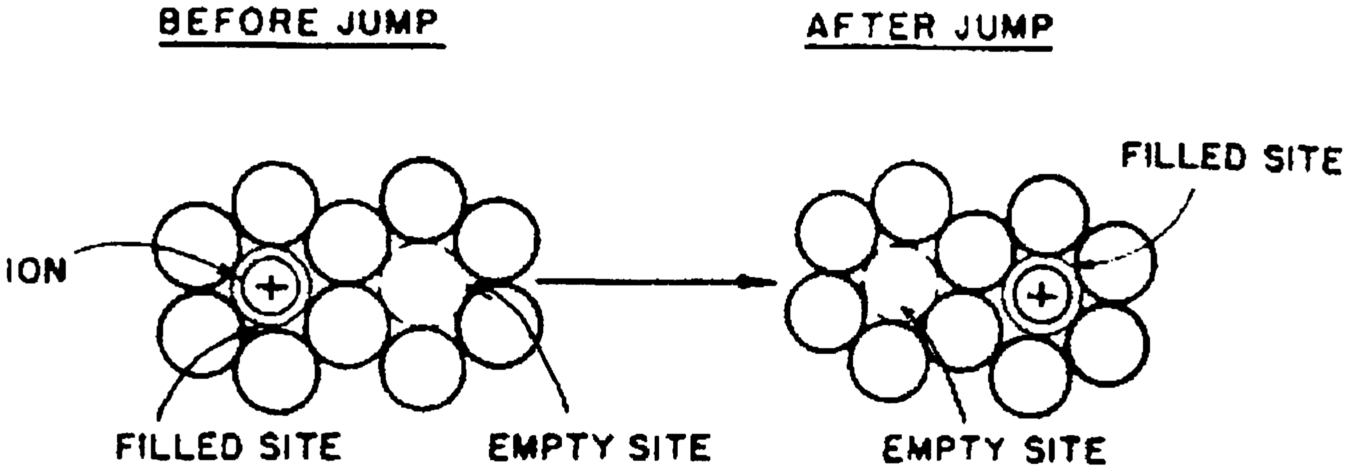

Figure 5.4: Representation of diffusion of a species in solution

---

Values of D at different temperatures given in Table 5.1 were used to construct an Arrhenius plot for the diffusion of TMPD in acetonitrile as shown in Figure 5.5. From this E_a was determined to be 9.98 ±0.8 kJ mol^{-1}. As far as we know, this value represents the first determination of activation energy for diffusion of TMPD in this solvent/supporting electrolyte system. However, values determined in acetonitrile with 0.1 M $NaClO_4$ as electrolyte have been reported by Fernández and Zon. These workers used chronocoulometry to derive values of D at temperatures ranging from –9 to +25 ^{0}C which gave an E_a of approximately 10 kJ mol^{-1} [2]. A value of approximately 11 kJ mol^{-1} was obtained by the same group using chronoamperometry at temperatures ranging between –10 and +20 ^{0}C [12]. These values are similar to those derived during our study since the energy required to move solvent molecules aside during diffusion of a molecular species can be viewed as the energetically consuming process. The effect of the nature of the supporting electrolyte species appears to be negligible at the concentrations used during these investigations.

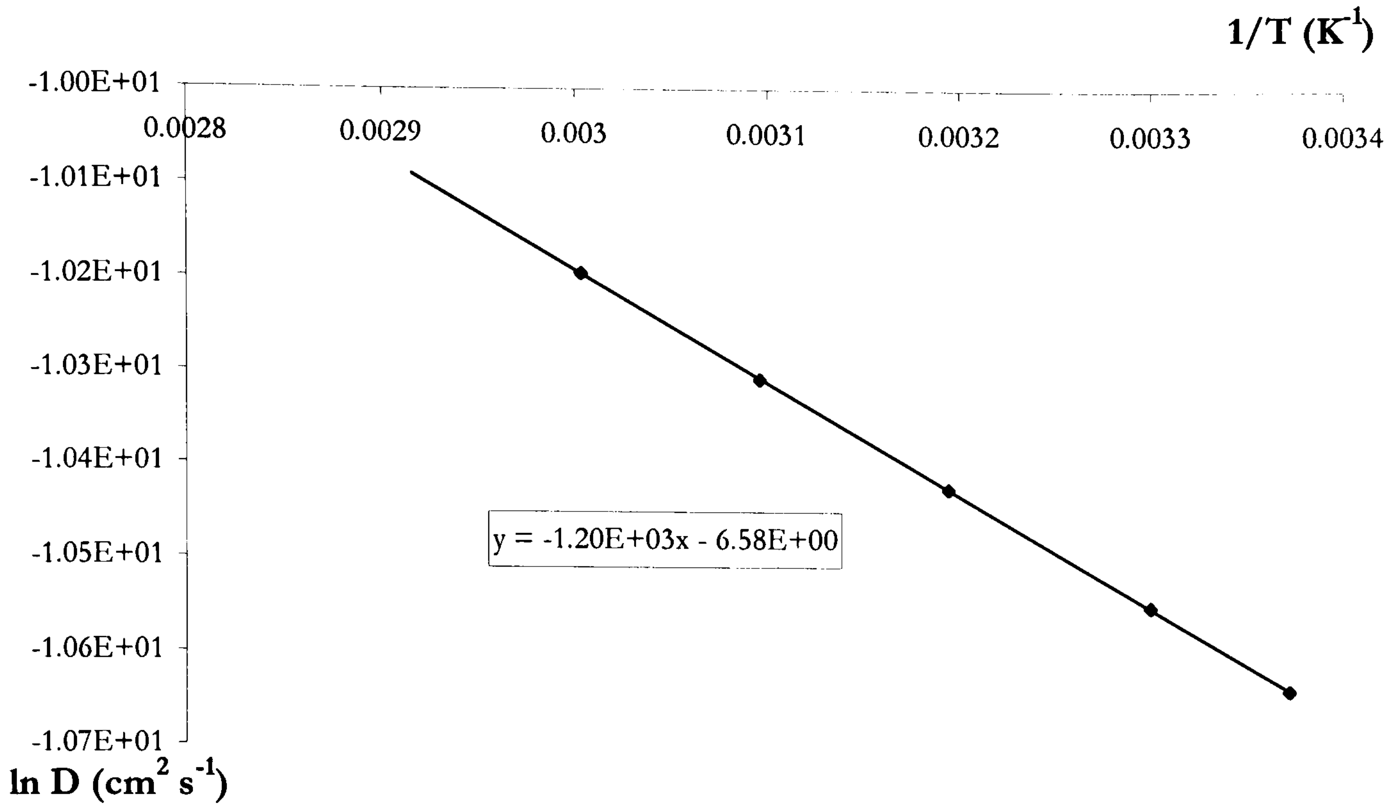

Figure 5.5: ln D versus 1/T for TMPD in acetonitrile/0.1 M NBu_4ClO_4 solution

5.2.6 Comparison of variable temperature data with Wilke-Chang relationship

The Wilke-Chang correlation was introduced in §5.2.4 as a method by which diffusion coefficients of species in solution can be estimated. The relationship can be used in this instance to theoretically predict the correlation of D with temperature. A plot of D versus T/υ will have a slope which corresponds to:

$$\text{slope} = 7.4\text{x}10^{-8}\,\frac{(\chi M)^{1/2}}{V^{0.6}}. \tag{5.5}$$

Values of ν for acetonitrile at each temperature were extrapolated from a plot of viscosity versus temperature (shown in Figure 5.6) with values obtained from a literature source as tabulated in Table 5.4 [15]. D versus T/ν for TMPD in acetonitrile is shown in Figure 5.7.

Temperature (^{0}C)	Viscosity (mPa s^{-1})
295	0.369
323	0.284
348	0.234

Table 5.4: Variation of viscosity with temperature for acetonitrile

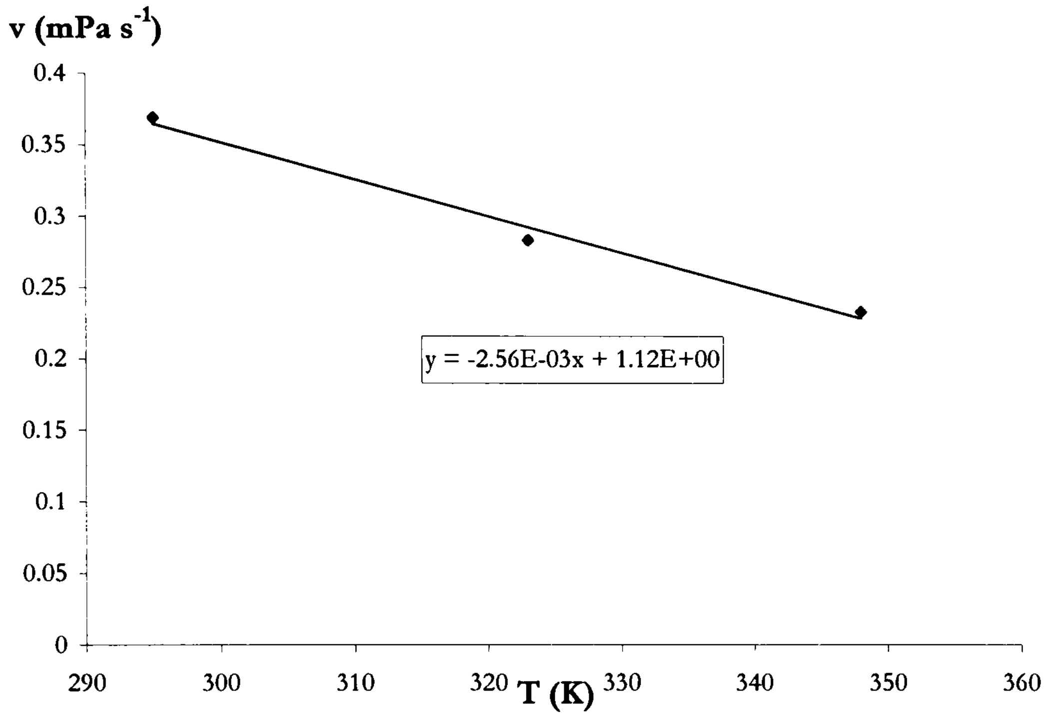

Figure 5.6: Plot of viscosity versus temperature for acetonitrile

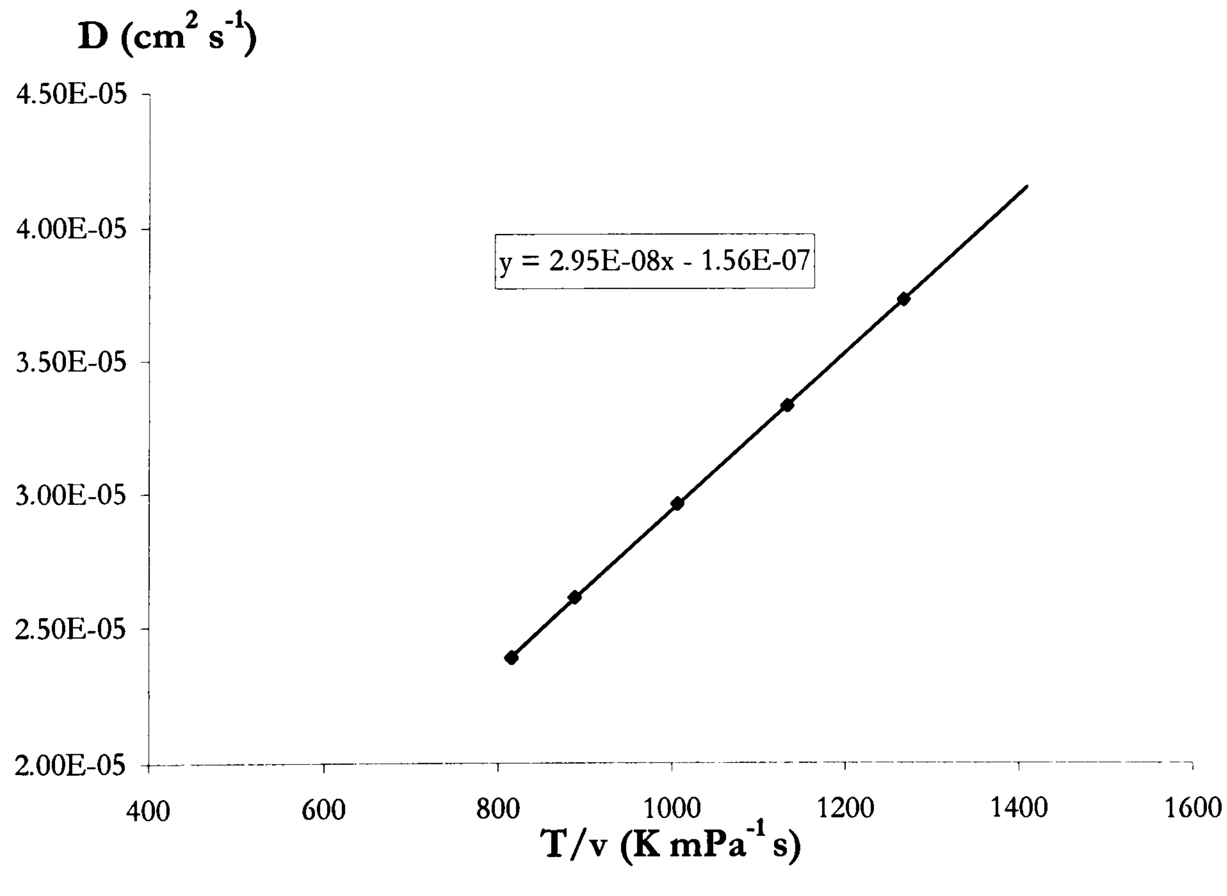

Figure 5.7: D versus T/υ for TMPD in acetonitrile/0.1 M NBu_4ClO_4 solution

The experimentally derived slope for D versus T/υ is $2.95\text{x}10^{-8}$ 10^{-4} K^{-1} N s^{-2}. The slope expected according to the Wilke-Chang equation is $1.88\text{x}10^{-8}$ 10^{-4} K^{-1} N s^{-2}. As in the case of the experimental and Wilke-Chang values of D at room temperature, there is considerable discrepancy between the two. Possible reasons for this are considered later in this chapter in §5.2.11.

5.2.7 Calculation of effective radius

The Stokes-Einstein relationship relates the solution viscosity to the diffusion coefficient as defined in Equation 5.6 [14]:

$$D = \frac{kT}{w\pi va} \qquad (5.6)$$

in which k is the Boltzmann constant, v corresponds to solution viscosity, a defines the molecular radius and w corresponds to a constant dependant on the behaviour of the diffusing particle. Two boundary conditions exist for diffusion of a species in solution as defined by Stokes. If a species diffusing in solution is approximated by a sphere with velocity u, "stick" behaviour occurs when the fluid velocity at the surface of the sphere is taken to equal u everywhere on the surface. Thus, the species is surrounded by a layer of solvent molecules which move with the diffusing molecule. In the "slip" boundary condition, the fluid velocity does not equal u, hence the diffusing species moves independently of the solvent. For "stick" behaviour, a Stokes-Einstein coefficient of 6 is used, and for "slip" behaviour, the coefficient is set equal to 4.

Using the Stokes-Einstein relationship, a value for the effective radius can be extracted from a plot of D versus T/v which will have the slope defined in Equation 5.7:

$$\text{slope} = \frac{k}{w\pi a}. \qquad (5.7)$$

From the plot of D versus T/v shown in Figure 5.7, a value of 0.248 ± 0.02 nm was obtained for the effective radius of TMPD using a value of 6 for the coefficient w in the Stokes-Einstein equation and a value of 0.372 ± 0.02 nm with the numerical coefficient equal to 4. This is in excellent agreement with values reported by Fernández and Zon of 0.25 nm and 0.37 nm using Stokes-Einstein coefficients of 6 and 4 respectively [1]. Their values were calculated by plotting experimental diffusion coefficients evaluated in a range of different solvents via chronocoulometry against the reciprocal of pure solvent viscosity. These workers also calculated effective radii using viscosity values of solvent solutions containing supporting electrolyte. This analysis gave radii of 0.23 nm and 0.34 nm using the coefficients of 6 and 4 respectively. It can be seen that there is an error of up to 10% when the effect of supporting electrolyte on solution viscosity is not taken into account. As far as we know, literature values for the viscosity of our solvent and supporting electrolyte system at elevated temperatures do not exist. Thus our procedure used the pure solvent viscosity value as an approximation of overall solution viscosity.

Kapturziewicz and Jaenicke have calculated theoretical values for the effective radius of TMPD via molecular modelling techniques [17]. A value of 0.34 nm was obtained using a spherical approximation of the TMPD structure where a is calculated from the molar volume. A second value of the effective radius was calculated based upon an ellipsoidal approximation of the TMPD molecule with semi-axes x>y>z. a is calculated using the theoretical relationship of the effective radius to x, y and z where semi-axis distances are measured using crystallographic data. The value of a calculated using this method was 0.406 nm.

We have also calculated a value of a for TMPD using the Nemesis molecular modelling package (Oxford Molecular, UK). The Nemesis calculation is based on the addition of isolated bond lengths for a planar molecular structure. The distance is calculated according to the molecular radius specified by the user. We note that the value obtained serves as an approximation since no account of molecular steric interaction is made. Furthermore, the calculation is limited to a defined molecular axis. For an asymmetric molecule, effective radius will vary according to molecular orientation. The effective radius given by the Stokes-Einstein relationship will be dependant on directionality of the diffusing species. We therefore note the limited nature of this approach but consider it to be a useful approximation of a. The effective radius of TMPD was defined in this instance as the distance from the centre of the benzene ring to the mid-point of the nitrogen attached methyl groups. a calculated via this procedure was 0.335 nm.

Excellent agreement is observed between the theoretical predictions of effective molecular radius, by both Kapturziewicz and Jaenicke and us, and our experimental value in which 4 was used as the Stokes-Einstein coefficient. This suggests that diffusion of TMPD in acetonitrile occurs via a “slip” procedure in which the TMPD molecule moves independently of any solvent species. This is in line with the experimental findings of Fernández and Zon who found an excellent fit of the experimentally determined effective radius with theoretical values using a Stokes-Einstein coefficient of 4 [1].

5.2.8 Experimental determination of diffusion coefficients at elevated temperatures in water

In addition to the study of TMPD oxidation in acetonitrile, steady state voltammograms were recorded for an aqueous solution of 1 mM TMPD with 0.1 M KCl as supporting electrolyte. As in the case of acetonitrile, voltammograms were recorded using a 5 μm diameter microelectrode with an accurate value for the electrode diameter obtained via electrochemical calibration prior to use. The study was conducted over a temperature range from 30 to 80 °C. Higher temperatures are accessible using water as the solvent as defined by the solvent boiling points previously listed in Table 4.4.

The one electron oxidation of TMPD was observed at an $E_{1/2}$ of +0.1 V versus the platinum pseudo reference electrode. A representative voltammogram for the oxidation of TMPD in water obtained at 30 °C is shown in Figure 5.8. The $E_{1/2}$ obtained is in good agreement with values reported by Friend and Roberts which ranged from 0.17 V to 0.09 V versus SCE for pHs varying between 3.9 and 5.3 during the study described previously in §5.2.1 [8].

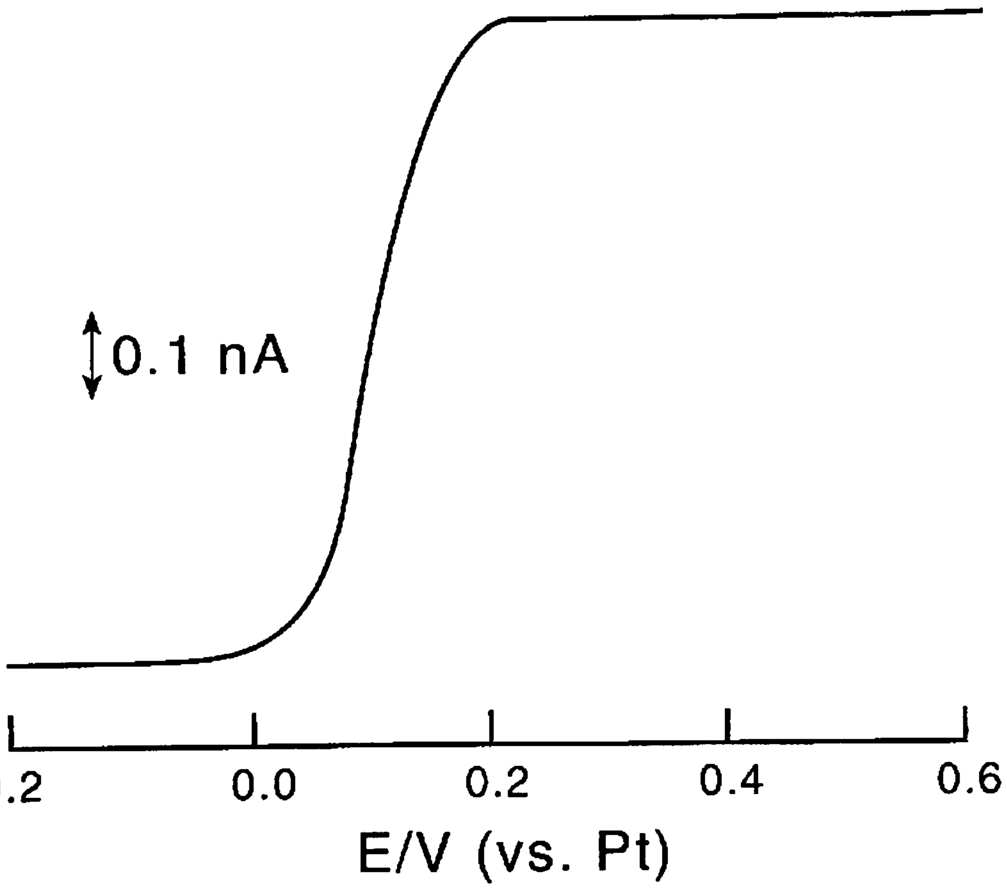

Figure 5.8: Steady state voltammogram for oxidation of 1 mM TMPD in aqueous 0.1 KCl solution recorded using a 5 μm diameter platinum microelectrode at 30 °C, scan rate 10 mV s^{-1}.

Limiting currents obtained at each temperature are given in Table 5.5. Reported I_{lim} values are an average of 5 steady state waves recorded for each temperature. Diffusion coefficients calculated from limiting current values using the theoretical expression for the diffusion limited current at a microdisc electrode previously defined in Equation 2.33 are also recorded in Table 5.5.

Temperature (^{0}C)	I_{lim} (A)	D (cm^2 s^{-1})
30	7.69×10^{-10}	$6.32\times10^{-6} \pm 0.3\times10^{-6}$
40	9.67×10^{-10}	$7.94\times10^{-6} \pm 0.3\times10^{-6}$
50	1.21×10^{-9}	$9.99\times10^{-6} \pm 0.4\times10^{-6}$
60	1.48×10^{-9}	$1.22\times10^{-5} \pm 0.5\times10^{-6}$
70	1.82×10^{-9}	$1.49\times10^{-5} \pm 0.6\times10^{-6}$
80	2.27×10^{-9}	$1.86\times10^{-5} \pm 0.7\times10^{-6}$

Table 5.5: Limiting currents and diffusion coefficients obtained for oxidation of 1 mM TMPD in aqueous 0.1 M KCl solution using a 5 μm diameter electrode at temperatures ranging from 30 to 80 ^{0}C

As far as we are aware, these values represent the first experimentally determined diffusion coefficients for TMPD in water. Using the Wilke Chang method for estimation of diffusion coefficients, a value of $6.99\text{x}10^{-6}$ cm^2 s^{-1} is predicted for the diffusion of TMPD in water at 30 ^{0}C. In contrast to the diffusion of TMPD in acetonitrile, the correlation between the experimental and Wilke-Chang values of D is good. The difference in TMPD diffusional behaviour in acetonitrile and water is considered later in this chapter in §5.2.11.

5.2.9 Experimental determination of activation parameters for diffusion

E_a was determined for the diffusion of TMPD in water using the Arrhenius plot of ln D versus 1/T shown in Figure 5.9. A value of 19.04 ± 1.5 kJ mol^{-1} was obtained. This value is almost twice that observed for diffusion of the same species in acetonitrile. This can be attributed to the increased viscosity of water. Viscosity values of acetonitrile and water have previously been listed in this thesis in Table 4.4. In addition, greater intermolecular force interactions in water may make diffusion in this solvent a more energetically consuming process. The large energy requirement for diffusion of TMPD in water is reflected in the low values of D in comparison to those obtained in acetonitrile.

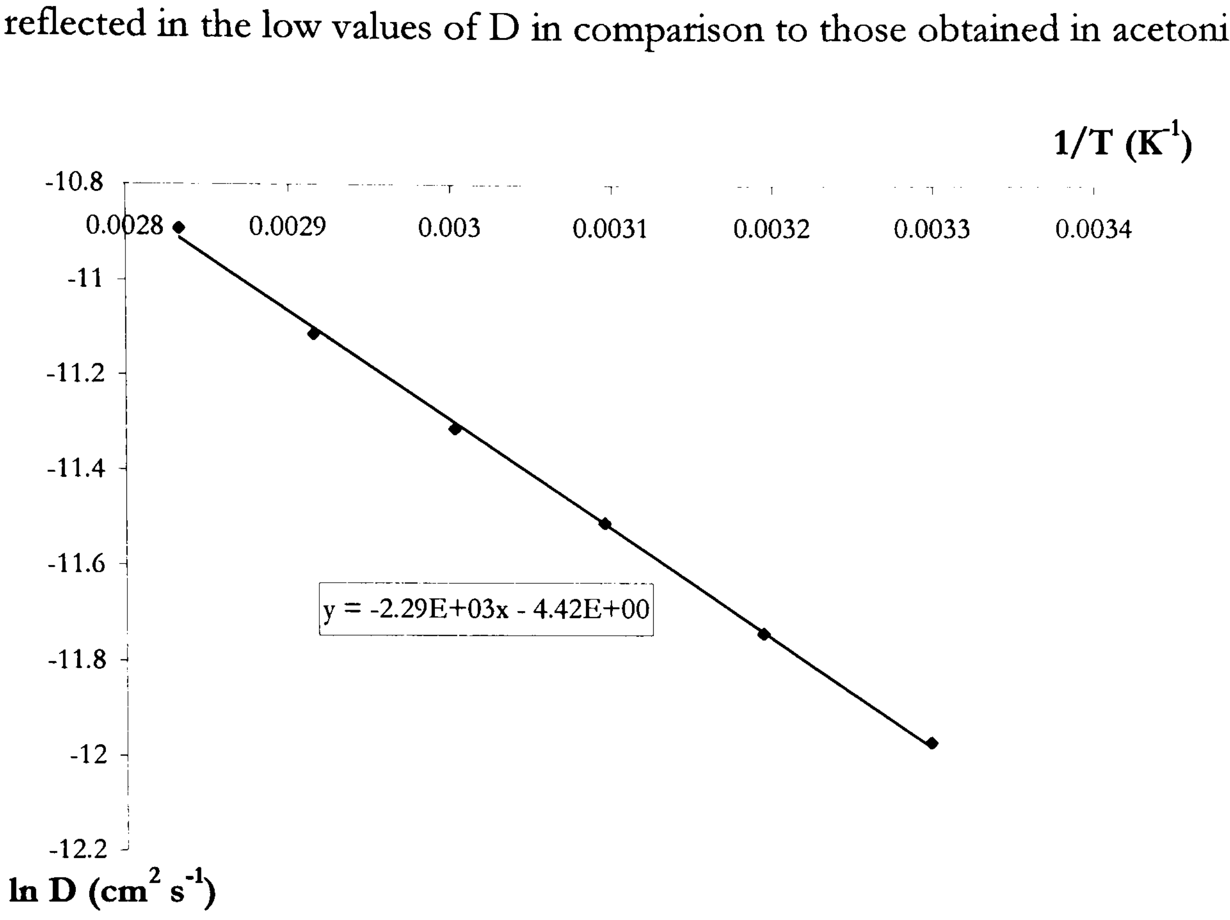

Figure 5.9: ln D versus 1/T for TMPD in aqueous 0.1 M KCl solution

5.2.10 Comparison of variable temperature data with the Wilke-Chang relationship

The theoretically predicted variation of diffusion with temperature for the plot of D versus T/ν was calculated using the Wilke-Chang correlation defined in Equation 5.2. A value of 2.01×10^{-8} 10^{-4} K^{-1} N s^{-2} was obtained. Experimentally determined values of D were plotted versus T/ν (Figure 5.10) using viscosities of water at each temperature obtained from a literature source as tabulated in Table 5.6 [16]. A slope of 1.98×10^{-8} 10^{-4} K^{-1} N s^{-2} is obtained. As for the value of D recorded at room temperature, the correlation of D with temperature was found to be in excellent agreement with Wilke-Chang theory.

Temperature (⁰C)	Viscosity (mPa s-1)
30	0.7977
40	0.6532
50	0.5470
60	0.4665
70	0.4044
80	0.3544

Table 5.6: Variation of viscosity with temperature for water

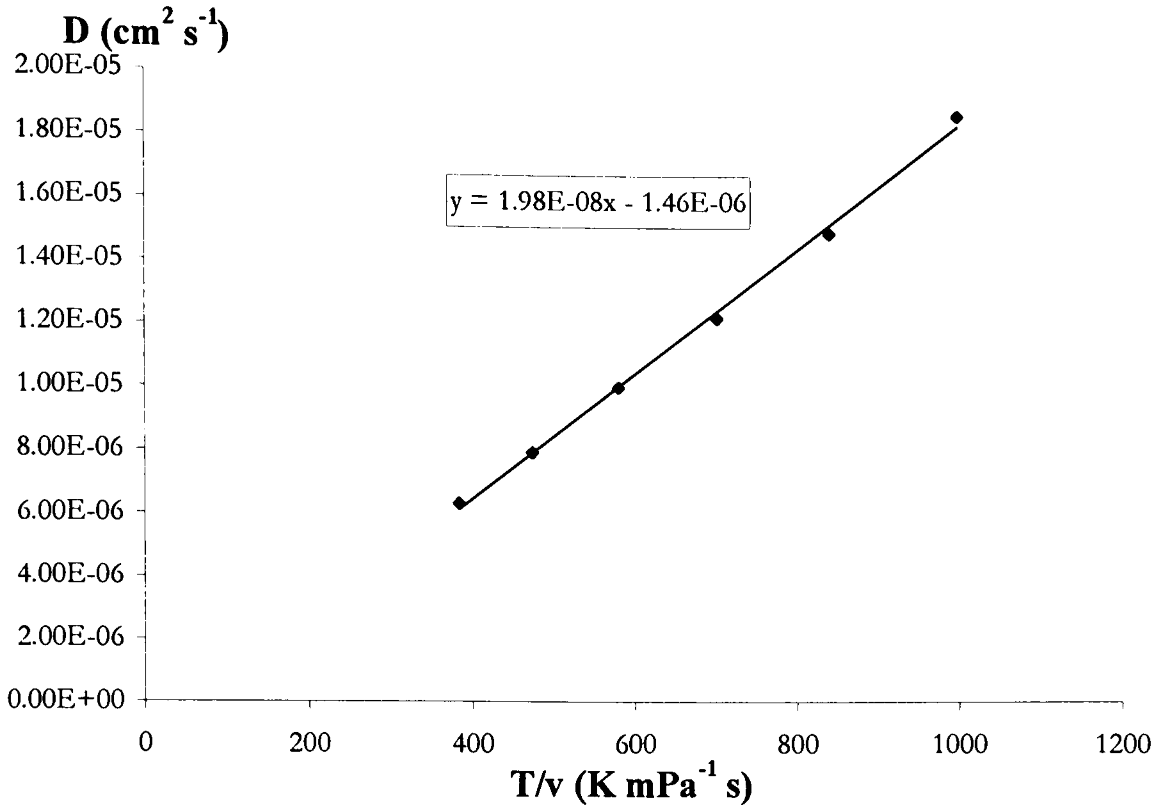

Figure 5.10: D versus T/υ for TMPD in aqueous 0.1 M KCl solution

5.2.11 Calculation of effective radius

The effective radius of TMPD in water was obtained using the Stokes-Einstein equation as described for TMPD in acetonitrile. From the plot of D versus T/ν shown in Figure 5.10, a value of 0.369 ± 0.3 nm was obtained with 6 as the Stokes-Einstein coefficient and a value of 0.554 ± 0.4 nm with the numerical coefficient equal to 4. Good agreement between the experimentally derived effective radius with 6 as the Stokes-Einstein coefficient and theoretical values calculated by Kapturziewicz and Jaenicke via molecular modelling techniques and us via the Nemesis modelling package is observed. This is in direct contrast to the case of TMPD in acetonitrile where a Stokes-Einstein coefficient of 4 was found to provide a better correlation between theoretical and experimentally determined values. Diffusion of TMPD in water can therefore be approximated by "stick" diffusional behaviour where the TMPD molecule diffuses surrounded by a layer of solvent molecules. This contrasts with the "slip" behaviour observed for TMPD diffusion in acetonitrile.

In the case of TMPD in water, we have seen that the "stick" type behaviour predicted by the Stokes-Einstein equation is matched by a good correlation between experimentally determined values of D and those estimated by the Wilke-Chang relationship. In the case of TMPD in acetonitrile, the experimentally determined diffusion coefficient is in excess of that theoretically predicted by the Wilke-Chang equation. It is possible that enhancement of the diffusion coefficient results directly from the "slip" type behaviour. Thus the TMPD can slide past solvent molecules more easily during the diffusion process than the Wilke-Chang correlation predicts.

It is likely that differences between "stick" and "slip" behaviour may arise from different solvation characteristics of the TMPD molecule in water and acetonitrile solution. Typical solute-solvent interactions can be of a non-specific nature such as ion-dipole, dipole-dipole, dipole-induced dipole or of a specific nature such as hydrogen-bonding, acid-base and electron donor-acceptor complexation [19]. We observe that water solvates TMPD more effectively than acetonitrile to produce "stick" type behaviour. The nature of this preferential solvation in the case of water may well arise from the ability of water molecules to hydrogen bond to the TMPD molecule.

5.2.12 Summary

This study demonstrates application of the elevated temperature microelectrode apparatus to the determination of diffusion coefficients at elevated temperatures together with information which such a study can yield. Values of D for TMPD in two solvents, namely acetonitrile and water, at variable temperatures have been obtained. Activation parameters for the diffusion process were calculated in each instance, and diffusion in water was shown to be a more energetically consuming process.

The variation of D with temperature was used to calculate a value for the effective radius of TMPD in both solvents using the Stokes-Einstein equation. The value obtained was compared to literature values and to a value calculated by us using the Nemesis molecular modelling package. An excellent correlation was obtained using a Stokes-Einstein coefficient of 4 in the case of acetonitrile and 6 for water. This suggests diffusion of TMPD can be approximated to "slip" behaviour in acetonitrile. In contrast, diffusion of TMPD in water can be represented by a "stick" mechanism. The difference in behaviour is attributed to the solvation characteristics of TMPD in the two solvents. Greater solute-solvent interaction occurs with TMPD in water possibly due to the ability of water molecules to hydrogen bond to TMPD.

The variation of D with temperature was also compared to that theoretically predicted using the Wilke-Chang relationship. An excellent correlation was found using water as the solvent but the match was poor in the case of acetonitrile. It is concluded that the Wilke-Chang relationship is based on "stick" diffusional behaviour and provides a less accurate estimate of diffusion coefficients in the case of "slip" type processes.

5.3 Tris(4-bromophenyl)amime (TBPA)

5.3.1 TBPA oxidation

TBPA depicted in Figure 5.11 undergoes a reversible one electron oxidation to form the radical cation as shown in Equation 5.8:

$$\mathrm{TBPA} \rightarrow \mathrm{TBPA}^{+\cdot} + e^{-}. \tag{5.8}$$

Evidence for the one electron oxidation process has come from a number of sources. A review of the pertinent literature follows.

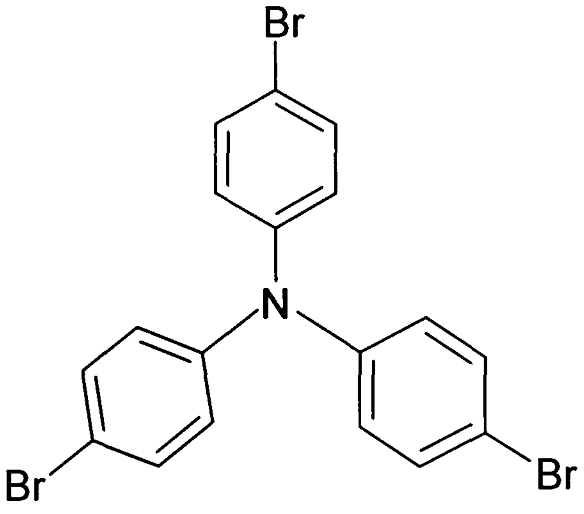

Figure 5.11: Structure of TBPA

Adams et al used cyclic voltammetry to investigate the oxidation of TBPA in acetonitrile solution containing 0.1 M NEt_4ClO_4 as supporting electrolyte [20]. Voltammograms showed a ratio of forward and reverse peak currents equal to one indicative of a reversible one electron process. During the same study, these workers used electron paramagnetic resonance (EPR) spectroscopy to investigate the nature of the oxidation product formed via ex-situ electrolysis under identical solvent/supporting electrolyte conditions. The EPR spectrum obtained for TBPA was inconclusive since line-broadening of the EPR spectra occurred due to the large nuclear quadrupole moment of the bromo isotopes. The EPR spectrum of the oxidation product in the case of tris(4-chlorophenyl)amine, however, revealed the monocation to be present. Formation of the monocation in the case of the chloro derivative is viewed as ample evidence that this is also the product in the case of TBPA. A further study by the same group via cyclic voltammetry, chronoamperometric and chronopotentiometric techniques under identical solvent/electrolyte conditions gave responses characteristic of a simple one electron transfer without complicating chemical processes [21].

Compton and Laing used RDE voltammetry to investigate the oxidation of TBPA in acetonitrile with 0.1 M NBu_4ClO_4 as electrolyte at 25 ^{0}C. A plot of limiting current versus square root of rotation speed indicated Levich type behaviour characteristic of a simple one electron process [22].

The presence of a second oxidation wave has been noted at more positive potentials during the cyclic voltammetric investigations described above [20,21]. This corresponds to an irreversible oxidation process which has not been characterised. For the purpose of this work, only the first oxidation process is considered. Thus, scans are stopped prior to the onset of the second wave.

5.3.2 Application of the elevated temperature apparatus to the study of TBPA

As in the case of TMPD, limiting currents for TBPA oxidation at variable temperatures were recorded using the elevated temperature microelectrode apparatus and used to derive values of D at varying temperatures. From these, activation parameters for the diffusion of TBPA in acetonitrile were calculated. The correlation of D with temperature was compared to the theoretically predicted relationship using Wilke-Chang theory. Data was also used to obtain a value for the effective molecular radius as in the case of TMPD. This was compared to a theoretical value calculated using the Nemesis package. As far as we are aware, this work represents the first reported variable temperature study of TBPA oxidation and experimental determination of the effective radius of TBPA.

5.3.3 Experimental determination of diffusion coefficients

Steady state analysis at variable temperatures was performed on a 1 mM solution of TBPA in acetonitrile solution containing 0.1 M NBu_4ClO_4 as supporting electrolyte. Current-voltage curves were recorded at a 5 μm diameter microelectrode at temperatures ranging between 22 and 60 ^{0}C. An accurate value for the electrode diameter was obtained prior to use via electrochemical calibration at 25 ^{0}C using a standard ferrocene solution.

A single wave corresponding to the oxidation of TBPA was observed at an $E_{1/2}$

of +1.14 V versus the platinum pseudo reference electrode. A representative voltammogram obtained for the oxidation of TBPA at 22 ^{0}C is shown in Figure 5.12. The $E_{1/2}$ obtained is in good agreement with the $E_p/2$ value of +1.05 V versus SCE reported by Adams et al during cyclic voltammetric investigations described previously [20,21]. It is also in agreement with a value measured by Compton et al of +1.12 V versus SCE measured during a channel electrode study of TBPA oxidation in acetonitrile solution containing 0.1 M NBu_4ClO_4 as electrolyte at 25 ^{0}C [23].

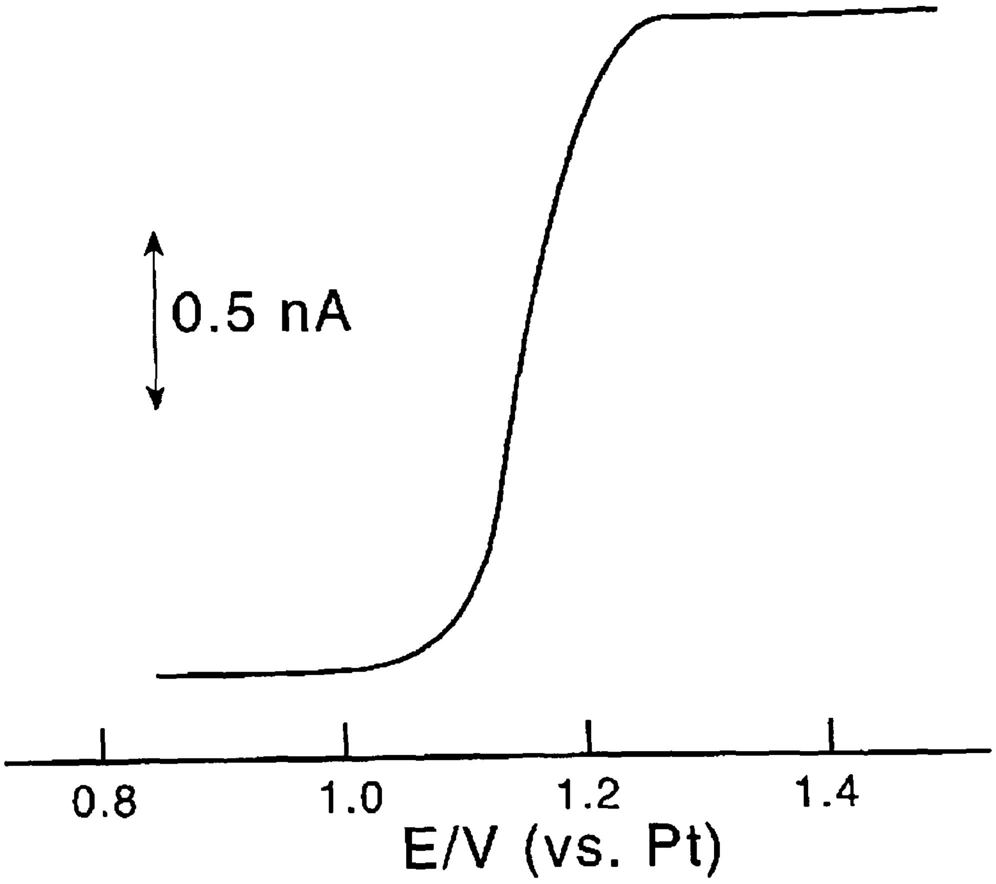

Figure 5.12: Steady state voltammogram for oxidation of 1 mM TBPA in acetonitrile/0.1 M NBu_4ClO_4 solution recorded using a 5 μm diameter platinum microelectrode at 22 ^{0}C, scan rate 10 mV s^{-1}.

Limiting currents obtained at each temperature are given in Table 5.7. Reported I_{lim} values are an average of 5 steady state waves recorded for each temperature. Diffusion coefficients calculated from limiting current values using the theoretical expression for the diffusion limited current at a microdisc electrode previously defined in Equation 2.33 are also recorded in Table 5.7.

Temperature (^{0}C)	**I_{lim} (A)**	**D (cm^2 s^{-1})**
22	1.80×10^{-9}	$1.50\times10^{-5} \pm 0.6\times10^{-6}$
30	2.00×10^{-9}	$1.66\times10^{-5} \pm 0.7\times10^{-6}$
40	2.21×10^{-9}	$1.83\times10^{-5} \pm 0.7\times10^{-6}$
50	2.47×10^{-9}	$2.05\times10^{-5} \pm 0.8\times10^{-6}$
60	2.69×10^{-9}	$2.24\times10^{-5} \pm 0.9\times10^{-6}$

Table 5.7: Limiting currents and diffusion coefficients obtained for oxidation of 1 mM TBPA in acetonitrile/0.1 NBu_4ClO_4 solution using a 5 μm diameter electrode at temperatures ranging from 22 to 60 ^{0}C

The value of D obtained at 22 ^{0}C is in good agreement with previously reported literature values. A value of $1.62\text{x}10^{-5}$ cm^2 s^{-1} was determined by Compton et al from the limiting current obtained for TBPA oxidation at a channel flow electrode at 25 ^{0}C during the study described previously [23]. A value of $1.9\text{x}10^{-5}$ cm^2 s^{-1} was derived by the same group from Levich analysis of data obtained for the oxidation of TBPA at a rotating disc electrode at 25 ^{0}C [22].

Using the Wilke-Chang correlation, a value of $1.11\text{x}10^{-5}$ cm^2 s^{-1} is predicted for the diffusion of TBPA in acetonitrile at 22 ^{0}C. Some deviation in the experimental and estimated values of D is observed although the match is not as poor as that noted previously for TMPD in acetonitrile.

5.3.4 Experimental determination of activation parameters for diffusion

E_a was determined for the diffusion of TBPA in acetonitrile using the Arrhenius plot of ln D versus 1/T shown in Figure 5.13. A value of 8.73 ± 0.7 kJ mol^{-1} was obtained.

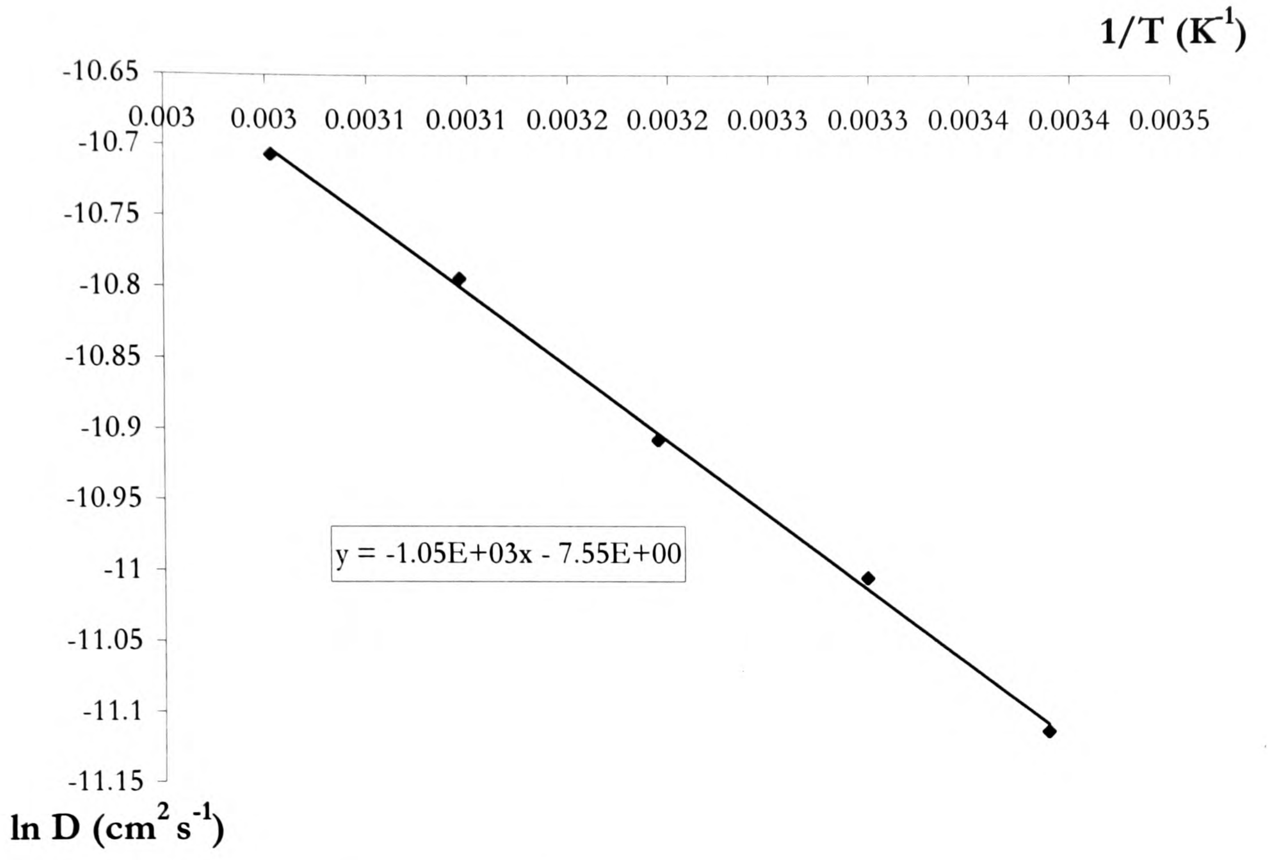

Figure 5.13: ln D versus 1/T for TBPA in acetonitrile/0.1 M NBu_4ClO_4 solution

---

The activation parameters determined here represent, as far as we are aware, the first determined values for TBPA diffusion in acetonitrile. The E_a is similar in magnitude to that derived for diffusion of TMPD in an identical solvent/supporting system in §5.2.5. The activation energy for diffusion of both species in acetonitrile is similar since the energy required to move solvent molecules aside can be viewed as the energetically consuming process. Small variations in magnitude may occur arising from differences in the nature of the diffusing species.

5.3.5 Comparison of variable temperature data with the Wilke-Chang relationship

The theoretically predicted variation of diffusion with temperature for the plot of D versus T/ν was calculated using the Wilke-Chang correlation defined in Equation 5.2 to yield a value of 1.39×10^{-8} 10^{-4} K^{-1} N s^{-2}. Experimentally determined values of D were plotted versus T/ν (Figure 5.14) using viscosities of acetonitrile extrapolated from the plot of viscosity versus temperature shown previously in Figure 5.6. A slope of 1.59×10^{-8} 10^{-4} K^{-1} N s^{-2} is obtained. As for the value of D recorded at room temperature, there is some discrepancy between experimental and Wilke-Chang values although this is not as great as that recorded for TMPD in acetonitrile.

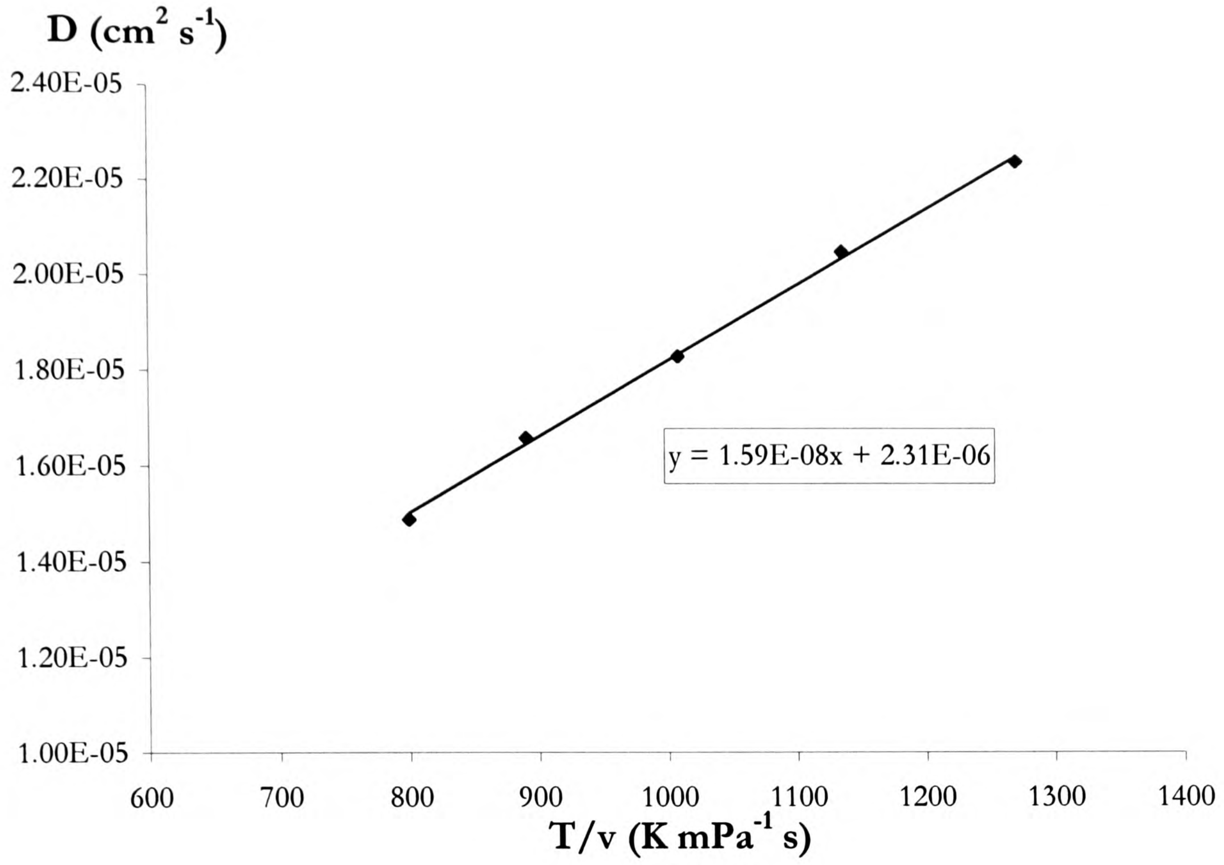

Figure 5.14: D versus T/υ for TBPA in acetonitrile/0.1 M NBu$_4$ClO$_4$ solution

5.3.6 Calculation of effective radius

A value for the effective radius of TBPA was derived from the plot of D versus T/v shown in Figure 5.14 using the Stokes-Einstein relationship defined in Equation 5.6. Values of 0.461 ± 0.03 nm and 0.690 ± 0.05 nm were obtained using Stokes-Einstein constants of 6 and 4 respectively. As far as we are aware, these values represent the first experimentally determined effective molecular radii in the case of TBPA.

Using the Nemesis molecular modelling package, we have estimated a value for the molecular radius of TBPA. For the purpose of the calculation, a was defined as the distance from the central nitrogen to the bromo substituent of one of the phenyl groups. a calculated via this procedure was 0.441 nm. We note good agreement between this and the experimentally determined value obtained using a Stokes-Einstein constant of 6. This suggests that diffusion of TBPA in acetonitrile occurs via a "stick" procedure where the substrate molecule moves in conjunction with a surrounding layer of solvent species. However, in contrast to the case for TMPD in water as described in §5.2.11, "stick" type diffusional behaviour is coupled with a poor correlation between experimentally derived diffusion coefficients and corresponding Wilke-Chang values. This may result from a poor assignment of the diffusional process in this instance reflecting an unreliable estimate of the molecular radius provided by the Nemesis molecular modelling package. In contrast to the TMPD molecule where the addition of individual bonds provides a reasonable estimate of molecular radius, this approach is less reliable in the case of TBPA where more complex steric interactions between bromophenyl substituent groups are ignored.

5.3.7 Summary

Values of D at varying temperatures have been evaluated for TBPA in acetonitrile using the elevated temperature microelectrode apparatus. Activation parameters were calculated for the diffusion process and the value obtained for E_a was shown to be approximately similar to the value obtained for diffusion of TMPD in an identical solvent medium.

A plot of D versus T/ν was used to calculate a value for the effective radius of TBPA. The value obtained represents, as far as we know, the first reported experimental determination of the effective radius for this molecule. The value obtained was compared to a theoretically calculated value using the Nemesis package. A reasonable correlation was observed using a Stokes-Einstein coefficient of 6. This suggests diffusion of TBPA in acetonitrile can be approximated by "stick" behaviour. However, in contrast to the observations of TMPD diffusion both in acetonitrile and water, "stick" diffusion was observed to give a poor correlation with Wilke-Chang theory both in terms of the diffusion coefficient obtained at room temperature and the variation of D with temperature. This may reflect a poor assignment of the diffusional mechanism resulting from an unreliable estimate of the molecular radius provided by the Nemesis molecular modelling package.

5.4 Ortho-bromonitrobenzene (oBNB)

5.4.1 Mechanism of oBNB reduction

A number of studies reported in the literature have sought to elucidate the nature of the reduction process undergone by halonitrobenzene compounds in aprotic solvents. Early work by Adams et al used EPR in conjunction with voltammetry to investigate the products formed during the reduction process for a range of halonitrobenzene compounds [51,52]. Investigations were carried out in DMF solution containing 0.1 M NEt_4ClO_4 as supporting electrolyte using a mercury drop electrode. In the case of the iodonitrobenzenes and oBNB, controlled electrolysis yielded an EPR spectrum identical to that obtained for controlled bulk electrolysis of nitrobenzene. For the iodo compounds, this was observed to proceed via a 2 step process. In the case of oBNB, the 2 step process was obscured since both steps occur at approximately the same potential. For the iodonitrobenzenes, the number of electrons involved in each reduction stage was evaluated by comparison of the two cathodic peak heights as being an initial 2 electron step incorporating halide bond cleavage to yield nitrobenzene followed by a further one electron reduction to form the nitrobenzene anion radical. A similar analysis was not possible in the case of oBNB since reduction steps occur at approximately the same potential, thus differentiation between the two was not possible. However, comparison of peak height in the case of the iodonitrobenzenes as a mean of determining the number of electrons involved in each reduction step is imprecise since peaks were not diffusion controlled. Electrolysis of other halonitrobenzene compounds gave EPR spectra consistent with the halonitrobenzene anion radical. This was ascribed to the formation of more stable anion radicals in these instances which did not readily eject a halide ion.

Similar EPR results were obtained by Fujinaga et al who conducted experiments on a number of halonitrobenzene compounds in DMF solution with 0.1 M NPr_4ClO_4 as supporting electrolyte [53]. These workers noted formation of the nitrobenzene anion radical upon controlled potential electrolysis of oBNB and the iodonitrobenzenes. Other nitrobenzenes were observed to give the anion radical upon electrolysis. Several halonitrobenzene compounds showed formation of the nitrobenzene anion radical upon more exhaustive electrolysis. Ease of formation of the nitrobenzene radical was observed to be related to steric and bond strength considerations within the parent compound.

Hawley et al used chronoamperometry as a more precise method of determining the number of electrons involved in halonitrobenzene reduction. Their investigation focussed on the three isomeric iodonitrobenzenes in DMF solution with 0.1 M NEt_4ClO_4 as supporting electrolyte at a platinum electrode [24]. The reduction of iodonitrobenzenes proceeds via a well-defined 2 step process and the potential was stepped to a value following the second reduction wave. The $It^{1/2}/C$ value was observed to approximate the value obtained for nitrobenzene at short timescales. As the timescale was increased, this value increased to reach a constant value of twice that obtained for nitrobenzene. This was attributed to an overall 2 electron process involving an initial 1 electron step to form the anion radical, subsequent decomposition of the radical via halide loss and hydrogen abstraction to yield nitrobenzene, followed by a second 1 electron step incorporating reduction of nitrobenzene. An overall 2 electron reduction mechanism contrasts with the 3 electron process proposed by Adams et al above. We suggest that the technique used to determine the number of electrons involved in the reduction process in this instance provides a more reliable assessment than that used by Adams et al.

Subsequent investigation by Nelson et al used cyclic voltammetry, chronoamperometry and chronopotentiometry to estimate the number of electrons involved in the first reduction step relative to nitrobenzene for a range of halonitrobenzene compounds in acetonitrile solution with 0.1 M NBu_4ClO_4 as supporting electrolyte [26]. Data obtained confirms an overall 2 electron process for the iodonitrobenzenes and oBNB consistent with a fast two step two electron process as described above which essentially goes to completion on the timescale of the experiment. This is supported by EPR in conjunction with controlled-potential electrolysis which confirms the presence of the nitrobenzene anion radical. Results obtained for other halonitrobenzenes point to an overall 1 electron process consistent with formation of a halonitrobenzene anion radical which is stable on the timescale of the experiment due to a slow rate of halide bond cleavage. This is in agreement with the EPR studies of Adams et al and Fujinaga et al described above who noted the formation of halonitrobenzene anion radicals upon reductive electrolysis with the appearance of nitrobenzene anion radical with more exhaustive electrolysis [51,52,53].

Within the framework of the 2 electron reaction scheme which has been proposed for the reduction of oBNB, a number of distinct mechanistic pathways are possible. The ECE reaction scheme incorporates 1 electron reduction of oBNB to the anion radical, followed by halide bond cleavage and hydrogen abstraction to give nitrobenzene. One electron reduction of nitrobenzene to the nitrobenzene anion radical at the electrode surface completes the overall 2 electron process. The chemical step is the rate determining stage. This reaction scheme is depicted in Equations 5.9.a to d:

$$O_2N\text{-}C_6H_4\text{-}Br + e^- \rightarrow O_2N\text{-}C_6H_4\text{-}Br^{\cdot-} \quad (5.9.a)$$

$$O_2N\text{-}C_6H_4\text{-}Br^{\cdot-} \rightarrow O_2N\text{-}C_6H_4^{\cdot} + Br^- \quad (5.9.b)$$

$$O_2N\text{-}C_6H_4^{\cdot} + SH \rightarrow O_2N\text{-}C_6H_5 + S^{\cdot} \quad (5.9.c)$$

$$O_2N\text{-}C_6H_5 + e\text{-} \rightarrow O_2N\text{-}C_6H_5^{\cdot-} \quad (5.9.d)$$

where the source of hydrogen atoms, denoted HS, can be either the solvent or supporting electrolyte. Nelson et al have investigated the source of hydrogen for the reduction of the three iodonitrobenzenes in acetonitrile containing 0.1 M NBu_4ClO_4 as electrolyte [26]. EPR was used to investigate the nature of the nitrobenzene radical anion formed for controlled potential electrolysis in perdeuterated acetonitrile and in acetonitrile containing deuterium oxide. For the reaction performed in acetonitrile containing deuterium oxide, no change in reaction product was observed. However, deuteronitrobenzene anion radical was identified as the reaction product for the electrolysis performed in the perdeuterated solvent. These results suggest the source of hydrogen atoms in this instance to be the solvent.

The DISP1 mechanism involves 1 electron reduction of oBNB followed by halide bond cleavage and hydrogen abstraction similar as for an ECE type process. The final step in this mechanistic scheme, however, involves disproportionation in solution to regenerate oBNB with the formation of the nitrobenzene anion radical. This mechanism is illustrated by Equations 5.10.a to d:

$$O_2N\text{-}C_6H_4\text{-}Br + e^- \rightarrow O_2N\text{-}C_6H_4\text{-}Br^{\cdot -} \qquad (5.10.a)$$

$$O_2N\text{-}C_6H_4\text{-}Br^{\cdot -} \rightarrow O_2N\text{-}C_6H_4^{\cdot} + Br^- \qquad (5.10.b)$$

$$O_2N\text{-}C_6H_4^{\cdot} + SH \rightarrow O_2N\text{-}C_6H_5 + S^{\cdot} \qquad (5.10.c)$$

$$O_2N\text{-}C_6H_4\text{-}Br^{\cdot -} + O_2N\text{-}C_6H_5 \rightarrow O_2N\text{-}C_6H_4\text{-}Br + O_2N\text{-}C_6H_5^{\cdot -}. \qquad (5.10.d)$$

As for the ECE case, the chemical step is rate determining.

The DISP2 scheme would also account for a 2 electron reduction process. This mechanism can also be described by Equations 5.10.a to d. However, in this instance, the disproportionation process defined by Equation 5.10.d is rate determining.

Compton et al have used hydrodynamic voltammetry at channel microband electrodes [27] as a means of mechanistically discriminating between ECE and DISP processes for oBNB reduction in DMF containing 0.1 M NBu_4ClO_4 as electrolyte [28]. Using this experimental protocol, steady state voltammograms were recorded under different flow rate regimes and at different oBNB concentrations. Limiting currents recorded at each concentration were plotted as a function of flow rate. For steady state techniques, the timescale over which the chemical step of an ECE or DISP reaction can be probed is set by the residence time of the reactant species at the electrode surface. For hydrodynamic techniques, such as the rotating disc electrode or channel flow cell, residence times are smaller due to a decrease in diffusion layer thickness. The diffusion layer can be regarded as the layer adjacent to the electrode surface through which the concentration gradient is linear. Outside of the diffusion layer, species are swept away by the convective motion of the flowing solution. n_{eff} defines the effective number of electrons transferred at steady state normalised to the number of electrons transferred at steady state in the absence of any limiting factors. For an ECE or DISP process at a conventional electrode, where mass transport to the electrode surface is diffusion controlled, n_{eff} values of 2 will typically be obtained where the residence time is greater than the time taken for the chemical step to occur. With a decrease in diffusion layer thickness, there is sufficient time for some of the product from the first electron transfer process to escape from the diffusion layer to give an n_{eff} lower than 2. n_{eff}, will provide a direct measure of the rate of the reaction process. Use of increased flow rates will decrease the diffusion layer further permitting the elucidation of even faster rate constants.

Data obtained at higher flow rates was found to contain information concerning reduction where n_{eff} was less than 2. For the three concentrations, data was modelled as both ECE and DISP1 processes using the backwards implicit finite difference method (BIFD) [29]. For each data set, the rate constant was adjusted systematically to fit the theoretically computed limiting currents to the experimentally observed parameters. For the ECE scheme, modelled values were fitted to experimental data with an approximately constant value of k for all 3 flow rates. For the DISP1 scheme, values of k needed to achieve the optimal agreement showed a systematic variation with concentration of the substrate. Upon assumption of a DISP2 mechanism, systematic variation in k between flow rates increased still further.

Pletcher et al recorded steady state voltammograms for oBNB reduction at gold microdisc electrodes of varying radii in DMF and acetonitrile solutions containing 0.05 M NBu_4BF_4 as supporting electrolyte [30]. Single reduction waves were observed. A plot of I_{lim} versus electrode radius was non-linear reflecting variation in n_{eff} with electrode size. These workers regarded reduction of the solvent radical species formed by hydrogen abstraction to be kinetically significant in the mechanism and analysed their results in terms of an overall ECEE framework. However, these workers present no direct experimental evidence to support their theory. Furthermore, their hypothesis is in direct contrast with data presented by other workers which points to a 2 electron ECE process as described above.

It is therefore possible to conclude from literature sources that reduction of oBNB very likely proceeds via an ECE process. From the ECE mechanistic scheme defined in Equations 5.9.a to d, we note that the chemical step is composed of halide bond cleavage followed by hydrogen abstraction from the solvent. It seems probable that halide bond cleavage is the rate determining step of these two processes since reduction of the solvent radical would become mechanistically significant to give the overall ECEE scheme proposed by Pletcher et al if hydrogen abstraction were the rate controlling stage.

Compton et al report a photoelectrochemical study to determine the rate controlling step during reduction of the related compound pBNB [31]. While the pBNB compound forms a stable halonitrobenzene anion radical under normal electrochemical conditions, halide bond cleavage and subsequent reduction of the anion radical under illuminated conditions occurs to give a reduction process similar to that observed for oBNB in the dark. Photocurrents were recorded for the reduction of pBNB in acetonitrile solution containing 0.1 M NBu_4ClO_4 as electrolyte. The variation in photocurrent with flow rate was monitored. Phototransient experiments in which photocurrents were measured following application of light to the system were also performed. Data was modelled in terms of theory developed for each experimental protocol. An ECEE mechanism was unambiguously discounted. An ECE mechanism was observed to give a better fit than DISP1 but the occurrence of a DISP1 process cannot be completely overruled.

To determine the rate determining stage of the ECE process, experiments were conducted in the presence of different concentrations of added Br^-. Steady state currents were diminished relative to those flowing under corresponding conditions in the absence of Br^-. Kinetic modelling of this effect was consistent with halide cleavage as opposed to hydrogen abstraction as the rate determining chemical step.

5.4.2 Application of microelectrode voltammetry to oBNB reduction

Since the rate determining step during oBNB reduction is unimolecular halide bond cleavage, kinetics of the bond cleavage process can be determined. Kinetic analyses have conventionally been carried out using cyclic voltammetry where the ratio between forward and reverse peaks at different scan rates provides information concerning bond cleavage kinetics. Ratios are correlated to the theoretical working curve for an ECE process from which rate constant values can be extracted. Determination of rate constants via this method for bond cleavage during oBNB reduction is hampered since reduction of nitrobenzene occurs at a more positive potential than that of the parent compound. Reduction of nitrobenzene occurs spontaneously upon formation to render the first electron transfer process irreversible. Kinetic analysis of the oBNB system is possible using steady state techniques.

We have described in §5.4.1 the application of hydrodynamic techniques to the study of rapid 2 electron processes where the decreased residence time of the electroactive species at the electrode surface permits observation of an n_{eff} less than 2. Similarly, microelectrodes provide a means of "outrunning" bond cleavage kinetics since the residence time at the electrode will be necessarily small in comparison to a conventional sized electrode. This will allow the escape of products from the first electron transfer process to give an n_{eff} lower than 2. Residence time will correspondingly decrease with electrode size so that the use of smaller electrode diameters will permit more rapid reactions to be accessed.

5.4.3 Previous kinetic analyses of oBNB

A number of studies reported in the literature have sought to determine the kinetics of oBNB halide bond cleavage via steady state methods. Compton et al used hydrodynamic voltammetry at a channel microband electrode to determine the bond cleavage kinetics of oBNB reduction during the study described previously [28]. A fit of experimentally determined limiting currents to the theoretically computed data for an ECE process yielded a rate constant of 250 s^{-1} for 3 different flow rates at 25 ^{0}C.

The same group have used voltammetry in the presence of power ultrasound at a macroelectrode to record steady state voltammograms for the reduction of oBNB in DMF solution with 0.1 M NBu_4ClO_4 as electrolyte [32]. Values for n_{eff} were obtained for a range of diffusion layer thicknesses from the ratio of the calculated 1 electron process, assuming a literature value for D, to the total limiting current measured. The diffusion layer thickness was varied in each instance by alteration of the distance between electrode and horn tip of the ultrasound transducer. Diffusion layer thickness was measured via calibration with ferrocene. From this a value for the rate constant could be obtained by application of the theoretical expression for n_{eff} for an ECE type process at a uniformly accessible electrode with a planar diffusion layer. A value of 200 ± 50 s^{-1} at 25 ^{0}C was obtained.

Pletcher et al measured a value for the decomposition of oBNB within the framework of their proposed ECEE mechanism during the study described previously [30]. The rate constant was calculated using a variation of a procedure defined by Fleischmann for the determination of rate constants for ECE processes using limiting current data obtained using microelectrodes of variable radii [33]. n_{eff} is plotted versus electrode radius, r^0, and a value for the rate constant extracted from the resulting linear plot. In this instance, the procedure was rewritten for the ECEE process. Values of n_{eff} were obtained from the ratio of the experimentally measured current to the theoretical current for the one electron reduction, calculated assuming the diffusion coefficient of oBNB to be identical to that of nitrobenzene. n_{eff} was converted to a value of X characteristic of the ECEE process and a plot of X versus the radius used to derive a value of k. A value of 2.2 s^{-1} was obtained with acetonitrile as the solvent and 0.2 s^{-1} was obtained using DMF at 25 ^{0}C. These values are not consistent with previously reported figures which may reflect an inappropriate treatment of experimental data as an ECEE type process.

5.4.4 Previous determination of activation parameters for halonitrobenzenes

Kinetic studies of bond cleavage following oBNB reduction have been confined to 25 ^{0}C. To date, activation parameters have not been determined for the halide bond cleavage of this compound.

Parker et al report activation parameters for the halide bond cleavage of a number of halonitrobenzene compounds in DMF solution using 0.1 M NBu_4BF_4 as electrolyte [34]. Activation parameters were obtained using derivative cyclic voltammetry at very fast scan rates, typically in the region of 10 kV s^{-1} [35]. Use of such rapid scan speeds allows the irreversibility of the system to be overcome. Determination of peak currents via conventional cyclic voltammetry is approximate due to the influence of capacitative currents. By contrast, derivative cyclic voltammograms allow the precise determination of peak currents from which accurate rate constant values can be determined [36]. The procedure involves measurement of $\nu_{1/2}$, where $\nu_{1/2}$ is the voltage sweep rate necessary for the current ratio of derivative peaks on forward and backward scans to equal 0.500 [37,38]. For the purposes of their analysis, Parker et al ignored the second charge transfer process and considered their results under the auspices of an EC mechanistic scheme. For such a scheme, the rate constant can be calculated from the value of $v_{1/2}$ using Equation 5.11 [37,38]:

$$k = 906.2v_{1\ 2}/T. \tag{5.11}$$

Using this procedure, values of k were determined at several temperatures. Linear regression analysis was then used to obtain values for the energy (E_a) and entropy ($\Delta S^{\neq}_{298}$) of activation. Activation parameters derived during this investigation are shown in Table 5.8. Activation parameters for halide bond cleavage of oBNB were not reported during this study since reduction of nitrobenzene occurs positive of oBNB as described in §5.4.2.

Anion radical	**E_a (kJ mol^{-1})**	**$\Delta S^{\neq}_{298}$ (J K^{-1} mol^{-1})**	**k (s^{-1})**
Para-iodo	73.2	8.9	7.17
Meta-iodo	76.1	1.8	0.92
Para-bromo	87.4	4.4	0.0014

Table 5.8: Literature values of activation parameters recorded for halonitrobenzene compounds [34]

5.4.5 Application of the variable temperature electrochemical apparatus to the study of oBNB

Using the elevated temperature electrochemical microelectrode apparatus we seek to apply this novel method to a compound which has until now eluded analysis in terms of the determination of activation parameters. Steady state techniques have previously been applied in the derivation of rate constants for oBNB bond cleavage at room temperature. However, such methods have not been utilised to date for the determination of activation parameters for this compound.

We compare the value of the rate constant obtained during this study at room temperature with previously determined literature values. We also use an alternative technique, namely microelectrodes of varying diameters, to derive a value for the rate constant as a means of validating the result obtained. Using the rate constants obtained at elevated temperatures, activation parameters for the halide bond cleavage of oBNB were derived. Results are compared with literature values reported for other halonitrobenzene compounds.

5.4.6 Experimental determination of rate constants for halide bond cleavage of oBNB

During our study, steady state current-voltage voltammograms were recorded for a 1 mM solution of oBNB in DMF containing 0.1 M NBu_4ClO_4 as supporting electrolyte. Waves were obtained at temperatures ranging between 25 and 45 ^{0}C using a 5 μm diameter microelectrode. An accurate value for the electrode diameter was obtained via electrochemical calibration at 25 ^{0}C prior to use. Steady state waves were recorded versus the Fc/Fc^+ couple by addition of a 1 mM concentration of ferrocene to the electrolytic solution to provide a stable reference point to which the reduction potential of oBNB could be compared. In this way, the instabilities inherent in the platinum pseudo reference electrode were overcome. One wave was observed for the reduction of oBNB consistent with reduction of the nitrobenzene product positive of the parent molecule. A representative voltammogram obtained at 25 ^{0}C is shown in Figure 5.15. Reduction of oBNB is observed at an $E_{1/2}$ of –1.38 V versus the Fc/Fc^+couple. This is consistent with the findings of Compton et al [28], Hawley et al [25] and Pletcher et al [30] who report $E_{1/2}$values of –1.05 V, –1.03 V, and –1.06 V versus SCE respectively for the reduction of oBNB in DMF at room temperature during the studies described previously.

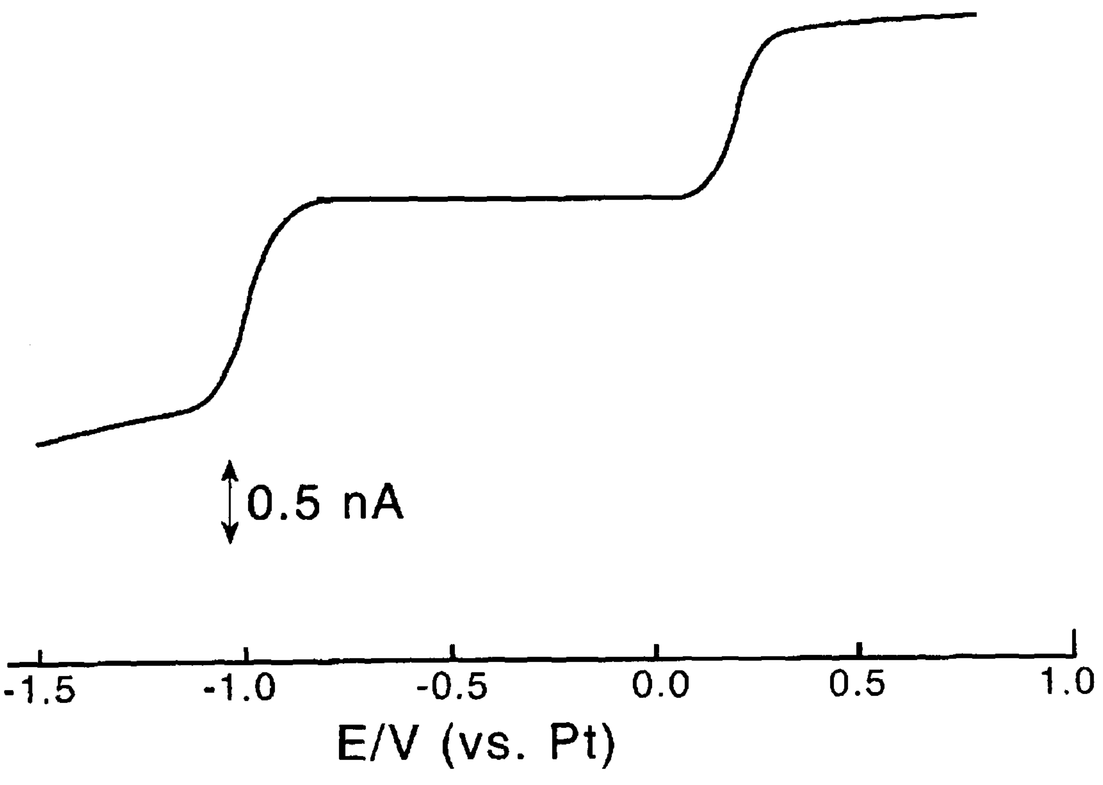

Figure 5.15: Steady state voltammogram for reduction of 1 mM oBNB and oxidation of 1 mM ferrocene in DMF/0.1 M NBu_4ClO_4 solution recorded using a 5 μm diameter platinum microelectrode at 25 ^{0}C, scan rate 10 mV s^{-1}.

Limiting currents obtained for the reduction of oBNB and oxidation of ferrocene in DMF at each temperature are tabulated in Table 5.9. Reported I_{lim} values are an average of 5 steady state waves recorded for each temperature.

Rates for halide bond cleavage at each temperature were obtained by application of theory developed by Fleischmann et al describing the variation of k with n_{eff} for an ECE process at a microdisc electrode [33]. It was shown that the steady state diffusion limited current density at a microdisc of radius r^0_m is identical to that at a sphere of radius $\pi r^0_m/4$. For an ECE reaction where the chemical step is first order and reversible, the diffusion limited current at a spherical electrode with radius r^0_s is given by:

$$I_{lim} = \frac{nFD_A c_A^\infty}{r^0_s}\left[n_1 + \frac{n_2 r^0_s (k/D_B)^{1/2}}{r^0_s (k/D_B)^{1/2}}\right]. \tag{5.12}$$

This can be rearranged to express the effective number of electrons involved in the reaction process:

$$n_{eff} = \frac{n_2 r^0_s (k/D_B)^{1/2}}{1 + r^0_s (k/D_B)^{1/2}} + n_1 . \tag{5.13}$$

For an ECE process where $n_1 = n_2 = 1$, if Δn is defined as:

$$\Delta n = n_{eff} - n_1 , \tag{5.14}$$

Equation 5.13 becomes:

$$\frac{1}{\Delta n} = \left(\frac{D_B}{n_2^2 k}\right)^{1/2} \frac{1}{r^0_s} + \frac{1}{n_2} . \tag{5.15}$$

Using the analogy that a microdisc behaves as if a sphere of radius $\pi r^0_m/4$, the steady state diffusion limited current at a microelectrode can be described by:

$$\frac{1}{\Delta n} = \frac{4}{\pi}\left(\frac{D}{n^2 k}\right)^{1/2} \frac{1}{r^0_m} + \frac{1}{n} \tag{5.16}$$

for the case where all diffusion coefficients are assumed to be equal and since $n_1 = n_2 = n$.

Such a relationship gives a linear dependence between $1/\Delta n$ and $1/r^0_m$ for an ECE process from which a value of k can be extracted. This equation can be applied in this instance to the determination of rate constants from the microelectrode data obtained for oBNB reduction at variable temperatures. For application of the theory, determination of n_{eff} at each temperature is necessary.

n_{eff} is obtained by ratio of the limiting current obtained for the sum of the first and second reduction processes to the current for the first reduction process only. In the case of oBNB, this is not trivial since reduction of nitrobenzene occurs at more positive potentials than the starting material. Thus one wave reflecting the whole ECE reduction process is obtained. Our procedure for the determination of n_{eff} for oBNB reduction at a microelectrode follows.

Values of I_{lim} obtained for ferrocene were used to calculate diffusion coefficients at each temperature using the theoretical expression for limiting current at a microelectrode as defined in Equation 2.33. Values of D obtained via this procedure are given in Table 5.9.

Activation parameters for the diffusion of ferrocene in DMF can be extracted from the Arrhenius plot of ln D versus 1/T shown in Figure 5.16. Using this procedure, E_a was determined to be 14.4 ± 1.2 kJ mol^{-1}. The E_a for diffusion of ferrocene in DMF is significantly higher than the values of 9.98 and 8.73 kJ mol^{-1} reported for diffusion of TMPD and TBPA in acetonitrile in §5.2.5 and 5.3.3 respectively. This reflects the increased viscosity of DMF in comparison to acetonitrile as detailed in Table 4.5.

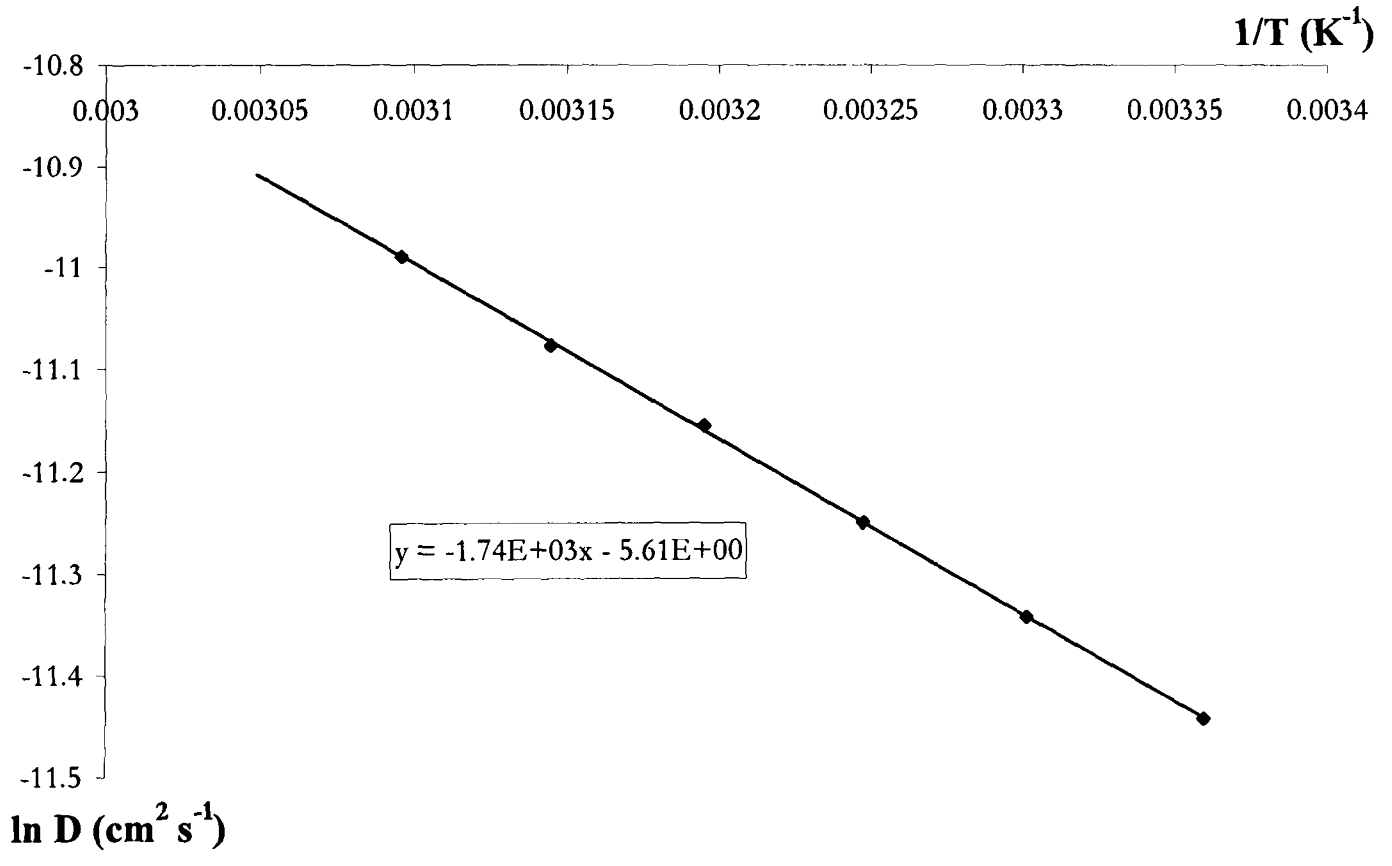

Figure 5.16: ln D versus 1/T for ferrocene in DMF/0.1 M NBu_4ClO_4 solution

We noted previously in §5.3.4 that the dominant control on activation energy required for diffusion of a species in solution is the nature of the solvent. This is because the energy required to move solvent molecules aside can be viewed as the energetically consuming process. The temperature dependence of the diffusion coefficient as reflected by the activation energy in the case of oBNB can therefore be approximated by that of ferrocene. It follows that the slope of ln D versus 1/T for oBNB will be identical to that of ferrocene but a separation between the two plots will be evident reflecting absolute values of D at each temperature. A value of D for oBNB in this solvent system at 25 ^{0}C was obtained from literature sources as 8.8×10^{-6} cm^2 s^{-1} [28]. This value was derived by Compton et al using the steady-state limiting current observed for the two electron reduction of oBNB during channel flow cell experiments. A comparison of D for oBNB and ferrocene at this temperature yields the separation of the two slopes, thus values of D at each temperature can be calculated. Values of D obtained via this procedure are tabulated in Table 5.9. Theoretical limiting currents for the one electron reduction of oBNB calculated using these values of D and the expression for diffusion limited current at a microelectrode are also recorded in Table 5.9.

Values of n_{eff} at each temperature can be directly obtained as the ratio of the experimentally determined current to the theoretically predicted current for the one electron reduction of oBNB. Values of n_{eff} obtained are shown in Table 5.9. n_{eff} shows the correlation with temperature shown in Figure 5.17.

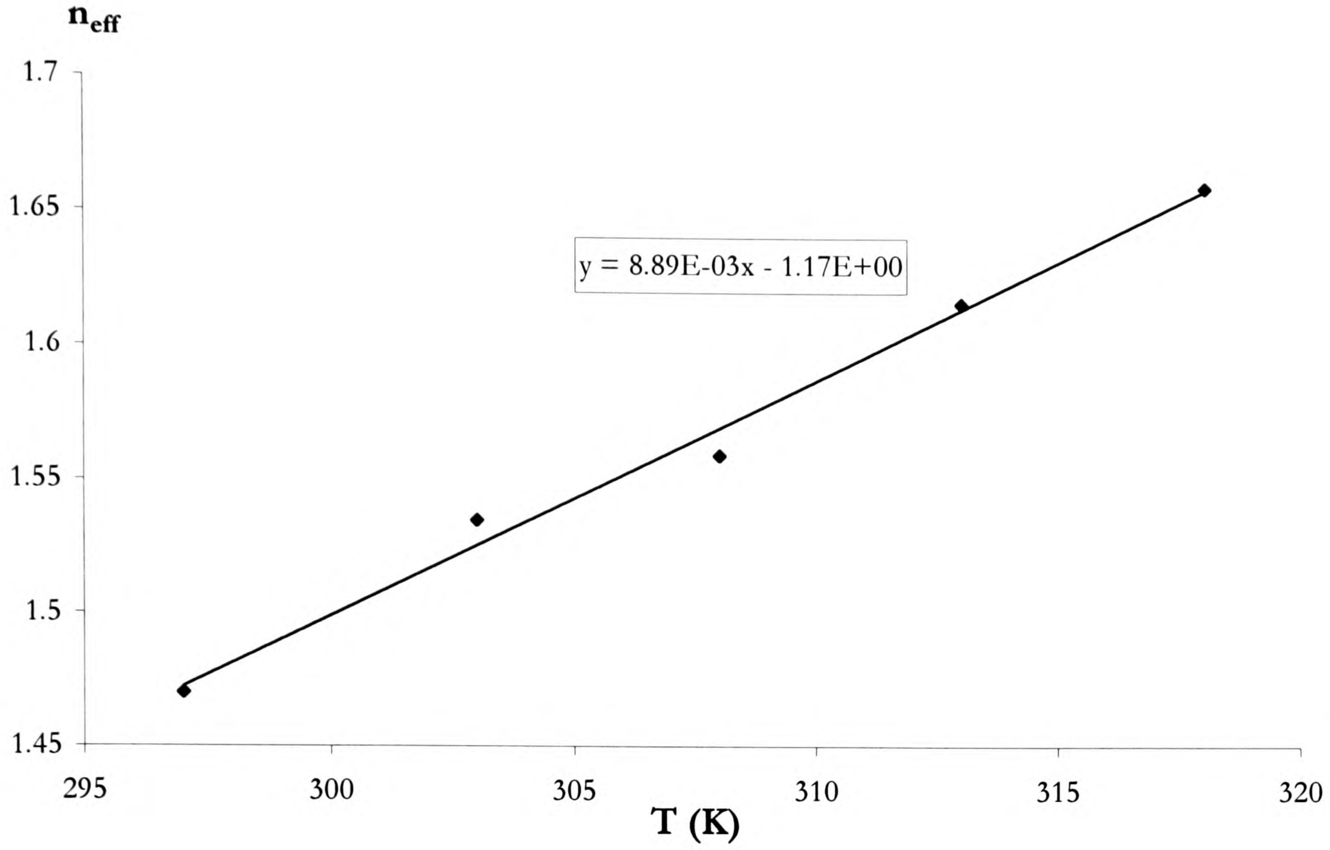

Figure 5.17: n_{eff} versus temperature for reduction of 1 mM oBNB in DMF/0.1 M NBu_4ClO_4 solution at a 5 μm diameter microelectrode

Rate constants for halide bond cleavage of oBNB calculated using Equation 5.12 and experimentally determined n_{eff} values are also shown in Table 5.9. The value of k at room temperature correlates favourably with the literature values of k derived by alternative methods reported in §5.4.3. A value of the rate constant at room temperature was also determined experimentally by us via an alternative method, namely using microelectrodes of varying radii, as described in §5.4.7. This served as a means of validating the rate constant obtained at room temperature using the variable temperature microelectrode apparatus.

5.4.7 Experimental determination of the rate constant at room temperature using microelectrodes of variable radii

Steady state current-voltage voltammograms were recorded for a 1 mM solution of oBNB in DMF containing 0.1 M NBu_4ClO_4 as supporting electrolyte. Waves were obtained using microelectrodes with nominal electrode diameters ranging between 5 and 50 μm. An accurate value was obtained for each electrode prior to use via electrochemical calibration at 25 ^{0}C using a standard ferrocene solution. The temperature of the solution was maintained at 25 ^{0}C throughout. Steady state waves were recorded versus the Fc/Fc^+ couple by addition of a 1 mM concentration of ferrocene to the electrolytic solution as in the case of the variable temperature experiment described above. One wave was observed for the reduction of oBNB at an $E_{1/2}$ of -1.40 V versus Fc/Fc^+ consistent with the findings described previously. Average limiting current values for 5 steady-state waves recorded for each electrode are shown in Table 5.10.

We noted in §5.4.2 that since microelectrodes permit "outrunning" of bond cleavage kinetics due to the decreased residence time of electroactive species at the electrode surface, it follows that n_{eff} will be dependant on electrode size. Using the theory of Fleischmann et al introduced in §5.4.6 and shown in Equation 5.16 to describe the variation of limiting current with electrode radius for an ECE process, a plot of $1/\Delta n$ versus $1/\, r^0_m$ will have the slope shown in Equation 5.17 from which a value for the rate constant can be determined:

$$\text{slope} = \frac{4}{\pi}\left(\frac{D}{n^2 k}\right)^{\frac{1}{2}} . \tag{5.17}$$

Our procedure for the determination of n_{eff} at each electrode diameter was identical to that utilised during the variable temperature experiment. Using the literature value of D for oBNB in an identical solvent medium at 25 ^{0}C, limiting currents for the one electron reduction of oBNB at each electrode diameter were calculated using the theoretical expression for transport limited current at a microdisc electrode. Values of n_{eff} were then obtained from the ratio of the experimentally determined limiting current to the theoretically predicted current for the one electron reduction of oBNB. Figures calculated during this procedure are tabulated in Table 5.10.

Electrode diameter (μ m)	**Experimentally determined I_{lim} (A)**	**Calculated I_{lim} for the one electron reduction of oBNB (A)**	**n_{eff}**
5	$1.36x10^{-9}$	$9.22x10^{-10}$	1.48
10	$3.55x10^{-9}$	$2.10x10^{-9}$	1.69
25	$8.47x10^{-9}$	$4.52x10^{-9}$	1.87
50	$1.98x10^{-8}$	$9.92x10^{-9}$	2.00

Table 5.10: Experimentally determined and calculated parameters for the reduction of 1 mM oBNB in DMF/0.1 M NBu_4ClO_4 solution at microelectrodes of variable diameter at 25 ^{0}C

n_{eff} values were used to construct the plot of $1/\Delta n$ versus $1/r^0_m$ shown in Figure 5.18. From this, the rate constant for halide bond cleavage of oBNB at 25 ^{0}C was determined to be 148 ± 30 s^{-1}. This figure is in good agreement with literature values of k previously reported in §5.4.3 and also the value of k derived at room temperature via the variable temperature apparatus.

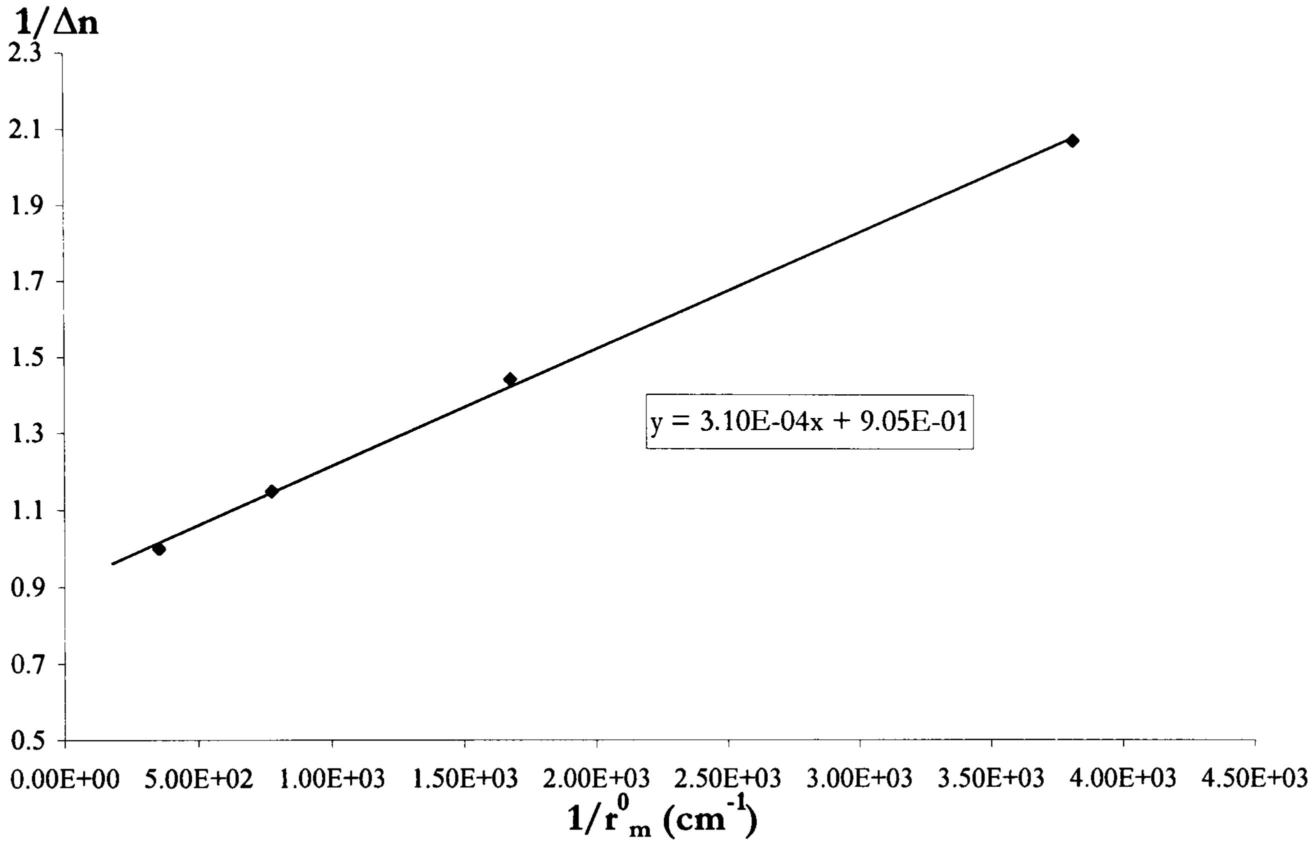

Figure 5.18: $1/\Delta r$ versus $1/r^0_m$ for the reduction of 1 mM oBNB in DMF/0.1 M NBu_4ClO_4 solution at 25 ^{0}C

Correlation of the room temperature value of k determined using the variable temperature apparatus with an independent determination of the rate constant by us, in addition to the correlation observed with previously reported literature values, validates the variable temperature microelectrode apparatus as an effective method for the evaluation of rate constants.

5.4.8 Experimental determination of activation parameters for halide bond cleavage of oBNB

Arrhenius plots of ln k versus 1/T can be used to determine activation parameters for a reaction as previously discussed in §5.2.5. Values of k reported in Table 5.9 were used to construct the plot of ln k versus 1/T shown in Figure 5.19. From this, 71 ± 7 kJ mol^{-1} and $5.83x10^{14}$ s^{-1} were determined for E_a and the pre-exponential factor A of the halide bond cleavage process. We observed in §5.2.5 that the Arrhenius relationship can be described by collision theory. A more complete description of the pre-exponential factor A can be obtained via a more sophisticated treatment using activated complex theory [18]. Here, reaction between 2 molecules A and B is considered to occur through the formation of an activated complex $C^{\neq}$ via an equilibrium process:

$$A + B \leftrightarrow C^{\neq}. \tag{5.18}$$

The rate of reaction is related to the concentration of $C^{\neq}$ which is governed by the equilibrium constant K_p:

$$\Delta G^{\neq}_{298} = -RT \ln K_p \tag{5.19}$$

where $\Delta G^{\neq}_{298}$ defines the free energy change undergone by the reactant species and R the gas constant. This yields an equation of Arrhenius form:

$$k = e^{\frac{-\Delta G^{\neq}_{298}}{RT}}. \tag{5.20}$$

Since:

$$\Delta G^{\neq}_{298} = \Delta H^{\neq}_{298} - T\Delta S^{\neq}_{298} \tag{5.21}$$

where $\Delta H^{\neq}_{298}$ and $\Delta S^{\neq}_{298}$ refer to the energy and entropy of reaction respectively, it follows that:

$$k = Ae^{\frac{-\Delta H^{\neq}_{298}}{RT} + \frac{\Delta S^{\neq}_{298}}{R}}. \tag{5.22}$$

We also need to account for conversion of the activated complex to products. This occurs via a series of complex vibration-like motions of all the atoms where the rate is related to the frequency of vibration defined by ν:

$$\upsilon = \frac{kT}{h} \tag{5.23}$$

in which k corresponds to the Boltzmann constant and h is Planck's constant. Including this term the Arrhenius relationship becomes:

$$\text{rate} = \frac{kT}{h} e^{\frac{-\Delta H^{\neq}_{298}}{RT} + \frac{\Delta S^{\neq}_{298}}{R}}. \tag{5.24}$$

In solution $\Delta H^{\neq}_{298}$ approximates to E_a, so that A is given by:

$$A = \ln\frac{kTe}{h} + \frac{\Delta S^{\neq}_{298}}{R}. \tag{5.25}$$

Using this relationship, the entropy of activation for halide bond cleavage of oBNB was calculated to be +29.4 ± 3 J K^{-1} mol^{-1}. The energy and entropy of activation calculated using this procedure represent the first reported values of these parameters for oBNB bond cleavage.

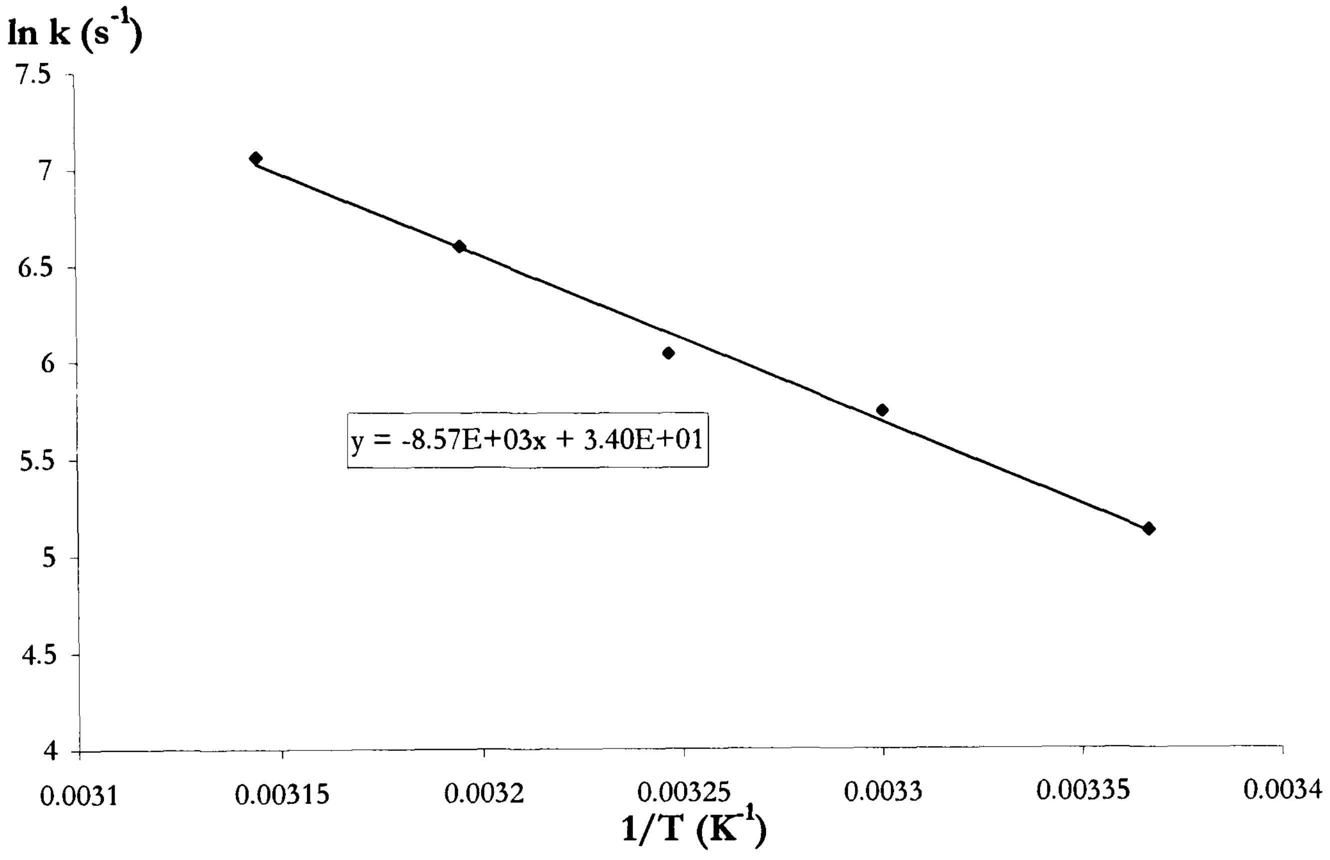

Figure 5.19: ln k versus 1/T for the reduction of 1 mM oBNB in DMF/0.1 M NBu_4ClO_4 solution at a 5 μm diameter microelectrode

Temperature (^0C)	Ferrocene I_{lim} (A)	Ferrocene D ($cm^2\ s^{-1}$)	oBNB I_{lim} (A)	Estimated oBNB D ($cm^2\ s^{-1}$)	Estimated I_{lim} for oBNB one electron reduction (A)	N_{eff}	k (s^{-1})
24.8	$1.10x10^{-9}$	$1.07x10^{-5}\pm0.4x10^{-6}$	$1.334x10^{-9}$	$8.77x10^{-6}$	$9.05x10^{-10}$	1.47	170 ± 20
30	$1.22x10^{-9}$	$1.18x10^{-5}\pm0.5x10^{-6}$	$1.535x10^{-9}$	$9.69x10^{-6}$	$1.00x10^{-9}$	1.54	315 ± 40
35	$1.34x10^{-9}$	$1.30x10^{-5}\pm0.5x10^{-6}$	$1.718x10^{-9}$	$1.06x10^{-5}$	$1.10x10^{-9}$	1.56	423 ± 50
40	$1.47x10^{-9}$	$1.43x10^{-5}\pm0.6x10^{-6}$	$1.944x10^{-9}$	$1.16x10^{-5}$	$1.20x10^{-9}$	1.62	740 ± 90
45	$1.59x10^{-9}$	$1.55x10^{-5}\pm0.6x10^{-6}$	$2.175x10^{-9}$	$1.27x10^{-5}$	$1.31x10^{-9}$	1.66	1175 ± 150

Table 5.9: Experimentally determined and calculated parameters for the reduction of 1 mM oBNB in DMF/0.1 M NBu_4ClO_4 solution using a 5 μm diameter microelectrode at temperatures ranging from 24.8 to 45 ^0C

5.4.9 Comparison of data with literature values derived for other halonitrobenzene compounds

First, the value of the rate constant obtained for halide bond cleavage of oBNB derived during this study was compared to literature values for the pBNB species. Hawley et al report a value of 4×10^{-3} s^{-1} for halide bond cleavage of pBNB in DMF containing 0.1 M NEt_4ClO_4 as electrolyte obtained using chronoamperometric techniques [25]. Parker at al determined a rate constant of 1.4×10^{-3} s^{-1} for the decomposition of the same species in DMF containing 0.1 M NBu_4BF_4 as electrolyte during the study described previously [34]. We note decomposition of the ortho isomer to be significantly faster than for the para compound. This can be attributed to the increased steric hindrance of the ortho structure where the bromo substituent is located immediately adjacent to the nitro group. This results in decreased stability of the anion radical to give a more rapid decomposition process [25].

Secondly, activation parameters of oBNB halide bond cleavage were compared to the values derived by Parker for the halonitrobenzene compounds noted in Table 5.6. The magnitude of activation parameters is dictated by the structure of the transition state. Activation energy defines the amount of energy required to form the transition state. Activation entropy reflects the change in order of the neighbouring solvent molecules during transition state formation. The Hammond-Leffler postulate can be invoked to describe the magnitude of the activation parameters as a reflection of the position of the transition state along the reaction co-ordinate [44]. This states that the interconversion of two states on a reaction pathway with nearly the same energy content will involve only a small amount of structural reorganisation. This principle implies that the transition state of a highly exothermic reaction will appear early on the reaction co-ordinate and resemble reagents. Conversely for a highly endothermic reaction, the transition state will be late and product-like. The position of the transition state will vary with the relative energies of the reagent, transition state and product and will change in a continuous fashion as these energies are perturbed by changes in, for example, structure or solvent.

We note a lower activation energy for the halide bond cleavage of oBNB in comparison to pBNB as reported by Parker in Table 5.6 which suggests a later transition state according to Hammond-Leffler theory. We suggest that the increased steric hindrance of the ortho compound in comparison to the para and meta compounds studied by Parker contributes to a more advanced transition state. A decreased activation energy is also consistent with the increased rate constant observed for decomposition of oBNB in comparison to pBNB as described above. Activation energies for the decomposition of the meta and para-iodonitrobenzene compounds are similar in magnitude to that of oBNB. We attribute this to the decreased halide bond energy of the iodo substituent which in this instance compensates for the magnitude of the steric effect observed for the oBNB and pBNB compounds.

A positive entropy change is observed for the halide bond cleavage of oBNB as reported by Parker for the halonitrobenzene compounds in Table 5.6. This is explained by the charge of the anion radical prior to bond cleavage which is to a large extent localised on the nitro group with appreciable ordering of the solvent in that region of the radical species. The transition state can be viewed as a shifting of negative charge to the halide substituent of the halonitrobenzene anion radical. As this occurs, a less ordered solvent structure is obtained with a corresponding positive entropy change. Similar values of activation entropy obtained for the halonitrobenzene compounds studied by Parker were noted to be a reflection of similar charge distribution in the transition states [34]. In contrast to these values, we note a greater entropy of activation for the halide bond cleavage of oBNB. The increasingly positive entropy of activation in the case of oBNB reflects the later transition state where the increased shifting of negative charge onto the halide substituent results in greater solvent disorder.

5.4.10 Summary

This study demonstrates application of the elevated temperature microelectrode analysis to the determination of kinetic and activation parameters in the case of rapid kinetic processes. This steady state technique has distinct advantages over cyclic voltammetric techniques previously applied in the determination of activation parameters for halonitrobenzene compounds since measurement of rate constants for an irreversible first electron transfer step are possible. The merits of this novel technique are therefore apparent.

The rate constant obtained for the halide bond cleavage of oBNB at 25 ^{0}C was found to agree favourably with previously reported literature values and an alternative value derived during this study using microelectrodes of varying radii. Comparison with literature values for the halide bond cleavage of pBNB showed decomposition of the ortho isomer to be significantly faster than for the para compound. This was attributed to the increased steric hindrance of the ortho structure which correlates to decreased stability of the radical anion.

The first experimentally determined values of energy and entropy of activation for halide bond cleavage of oBNB are reported. Values were compared to activation parameters for other halonitrobenzene compounds reported in the literature. The value of E_a obtained was lower than for pBNB consistent with a faster rate constant. This reflects the increased steric hindrance of the ortho isomer resulting in a later transition state according to the Hammond-Leffler postulate. The entropy of activation was observed to be more positive than for pBNB and meta and para-iodonitrobenzenes. This was attributed to the increased solvent disorder associated with the later transition state.

5.5 9-chloroanthracene (9-ArCl)

5.5.1 Mechanism of 9-ArCl reduction

A number of studies reported in the literature have sought to elucidate the nature of 9-ArCl reduction. Cyclic voltammetric investigation in both acetonitrile and DMF solvents have shown that reduction of 9-ArCl proceeds via a 2 step process. Wipf and Wightman report microelectrode cyclic voltammetry of 9-ArCl in acetonitrile solution containing 0.6 M NEt_4ClO_4 as supporting electrolyte [39]. These workers noted the appearance of 2 reduction waves with the second wave resembling that observed for reduction of anthracene under identical conditions. Similar results were reported by Savéant et al during a microelectrode cyclic voltammetric study in DMF solution containing 0.1 NBu_4BF_4 as supporting electrolyte [40].

However, there is considerable debate as to the nature of the initial reduction step. The rapid scan microelectrode study of Wipf and Wightman previously described suggested an initial irreversible 2 electron process [39]. These workers cite variation in peak current with scan rate as evidence for an initial 2 electron process.

This is consistent with a process in which initial reduction of 9-ArCl is followed by halide bond cleavage to give the anthracenyl radical as denoted in Equations 5.26 and 5.27:

$$ArCl + e^- \rightarrow ArCl^{\cdot -}, \qquad (5.26)$$

$$ArCl^{\cdot -} \rightarrow Ar^{\cdot} + Cl^-. \qquad (5.27)$$

The anthracenyl radical formed in Equation 5.27 undergoes a second electron transfer process to yield anthracene which is subsequently reduced at more negative potentials as evidenced by the second reduction wave:

$$\text{ArH} + e^{-} \rightarrow \text{ArH}^{\cdot-}. \tag{5.28}$$

The nature of the second transfer process was postulated as taking a number of different forms. The anthracenyl radical can undergo a second electron transfer at the electrode surface or in solution within an ECE or DISP mechanistic scheme as denoted in Equations 5.29 and 5.30 respectively:

$$\text{Ar}^{\cdot} + e^{-} \rightarrow \text{Ar}^{-}, \tag{5.29}$$

$$\text{Ar}^{\cdot} + \text{ArCl}^{\cdot-} \rightarrow \text{Ar}^{-} + \text{ArCl}. \tag{5.30}$$

In both cases, formation of the anthracenyl anion radical, $\text{Ar}^{\cdot-}$, is followed by protonation either by the solvent or supporting electrolyte to yield anthracene:

$$\text{Ar}^{-} + \text{H}^{+} \rightarrow \text{ArH}. \tag{5.31}$$

A third alternative involves hydrogen atom abstraction by the anthracenyl radical from the organic solvent:

$$\text{Ar}^{\cdot} + \text{SH} \rightarrow \text{ArH} + \text{S}^{\cdot}. \tag{5.32}$$

The solvent radical formed via this process may then be either reduced at the electrode (Equation 5.33) or in solution (Equation 5.34) if it is reduced at a more positive potential than the parent molecule:

$$\text{S}^{\cdot} + e^{-} \rightarrow \text{S}^{-}, \tag{5.33}$$

$$\text{S}^{\cdot} + \text{ArCl}^{\cdot-} \rightarrow \text{S}^{-} + \text{ArCl}. \tag{5.34}$$

This process will result in the overall transfer of 2 electrons during the initial 9-ArCl reduction stage which is indistinguishable from the ECE and DISP mechanistic schemes described above.

The possibility also exists that decomposition of the solvent radical occurs via a pathway which is insignificant in terms of the overall electron transfer process. For example, dimerisation of 2 solvent radicals or the reduction of solvent radicals at potentials more negative than those of the parent molecule would result in an overall one electron transfer step during the reduction of 9-ArCl to anthracene.

It is clear that reduction of 9-ArCl proceeds via a complex mechanism with the possibility of a number of different decomposition pathways which operate in competition with one another. Furthermore, the significance of each of the reduction pathways is likely to be dependant on the conditions employed. The nature of the competition between these three decomposition processes in acetonitrile, the solvent medium used during the course of this work, has been evaluated by Savéant et al. These workers used deuteration experiments as a means of investigating mechanistic competition [41]. Experiments were carried out in order to determine the amount of deuteration replacing the chloride ion using either 10% D_2O in non-deuterated solvent or 10% H_2O in perdeuterated solvent. 0.1 M $LiClO_4$ was incorporated as supporting electrolyte. It was assumed that water acts as a source of hydrogen ions and the solvent as a source of hydrogen atoms. Amount of deuterium incorporation in each instance revealed relative amounts of hydrogen abstraction and electron transfer respectively. A mathematical analysis was established to derive the competition between each of the three reaction mechanisms in terms of the results obtained. These workers concluded that reduction of 9-ArCl in acetonitrile was dominated by competition between DISP and hydrogen abstraction reactions.

Following cyclic voltammetric investigation of 9-ArCl reduction in DMF containing 0.1 M NBu_4BF_4 as supporting electrolyte, Savéant et al suggested that the initial reduction process comprised an EC mechanism [42]. The number of electrons transferred during the initial reduction step was evaluated by comparison of the peak height with that obtained for the one electron reduction of fluorenone, assuming the diffusion coefficients of these two species to be approximately equal. These workers concluded that the reduction mechanism proceeded via a hydrogen abstraction process where the fate of the solvent radical is insignificant under the experimental conditions employed.

In contrast, during the subsequent rapid scan cyclic voltammetric investigation reported by the same workers under identical solvent/supporting electrolyte conditions described previously, Savéant et al concluded that reduction of 9-ArCl proceeded via an initial 2 electron process [40]. The variation in peak current with scan rate indicated a DISP1 type process. Using an identical procedure, Jaworski et al suggested a DISP1 mechanism for the reduction of 9-ArCl in acetonitrile containing 0.1 M NBu_4ClO_4 as supporting electrolyte [43].

Although reduction of 9-ArCl can occur via the three mechanistic pathways proposed above, we conclude that the actual mechanism of reaction in terms of relative contributions from each reaction path is not well-defined and is likely to be influenced by reaction conditions.

5.5.2 Previous kinetic analyses of 9-ArCl halide bond cleavage

A number of investigations have been reported in the literature aimed at elucidating the halide bond cleavage kinetics of 9-ArCl in acetonitrile. Savéant et al used cyclic voltammetry at scan rates that were sufficiently rapid so as to enable the observation of a reversible wave for the initial electron transfer process [41]. The ratio between forward and reverse waves at varying scan rates permitted determination of the rate constant as being 260 s^{-1} using 0.1 M $LiClO_4$ as electrolyte at 25 ^{0}C. Voltammograms were recorded at a conventional sized mercury electrode. However, implementation of increased scan rates increases the contribution from ohmic and capacitative sources thereby limiting the accuracy of the technique.

Wipf and Wightman used gold and platinum microelectrodes to evaluate a value of the rate constant for the halide bond cleavage of 9-ArCl during the fast scan cyclic voltammetric study described previously [39]. The cleavage rate constant was obtained by fitting experimental cyclic voltammograms obtained over a wide scan range to simulated data with an ECE-DISP1 process assigned under the experimental conditions employed. The value of k determined via this procedure was 200 s^{-1} at 25 ^{0}C.

Jaworski et al used microelectrode cyclic voltammetry to evaluate k for the halide bond cleavage of 9-ArCl in acetonitrile during the study described previously [43]. These workers assigned a DISP1 scheme to the reduction of 9-ArCl. Their analytical procedure incorporated the theoretical variation of cathodic peak potential with scan rate calculated for a DISP1 mechanistic process. Data obtained at different scan rates was fitted to a working curve in which $(F/RT)(E_{pc}-E^0)$ was plotted versus $\log(RT/F)(k/\nu)$, where ν is the scan rate, to yield a value of k. E^0 was determined as the mean potential of forward and reverse peaks as recorded at high scan rates where the process is essentially reversible. The value of k obtained using this procedure was 165 s^{-1} at 22 ^{0}C.

We note the variation in rate constants reported during these investigations which is a reflection of the analytical techniques employed. Rapid scan cyclic voltammetry, particularly at conventional sized electrodes, is hampered by inaccuracy caused by capacitative charging currents and ohmic distortion.

5.5.3 Previous determination of activation parameters for halide bond cleavage of 9-ArCl

Previous determinations of activation parameters for the halide bond cleavage of

9-ArCl are confined to the solvent medium DMF. Savéant et al determined activation parameters for 9-ArCl bond cleavage using 0.1 M NBu_4BF_4 as supporting electrolyte during the study described previously [42]. As noted, these workers assigned an EC mechanism to the reduction of anthracene using cyclic voltammetric techniques. Determination of activation parameters was carried out within the EC mechanistic assignment using double potential step voltammetry (DPS). Further investigation by the same and other workers subsequently reassigned the initial reduction process as a 2 electron step. However, the investigation carried out under the EC mechanistic scheme is valid since rapid step times were utilised. Such conditions allow the complicating reactions of the anthracenyl radical to be "outrun". Reduction of 9-ArCl therefore appears as a reversible one electron process. The DPS procedure involved reversal of the potential at time τ with measurement of the cathodic and anodic currents at times τ and 2τ respectively. $I_{2\tau}/I_\tau$ ratios obtained for several values of τ were fitted to the theoretical working curve of $I_{2\tau}/I_\tau$ versus $k\tau$ from which a value of k was derived. Arrhenius plots were constructed from rate constants determined at 5 temperatures over the range 20 to 60 ^{0}C. From this, values of +57.3 kJ mol^{-1} and –16.73 J K^{-1} mol^{-1} were determined for the energy and entropy of activation respectively. The rate constant obtained at 25 ^{0}C was 158.5 s^{-1}.

Parker et al used derivative cyclic voltammetry to determine activation parameters for the halide bond cleavage of 9-ArCl using 0.1 M NBu_4BF_4 as supporting electrolyte [35]. This technique, previously described in §5.4.4, facilitates accurate measurement of forward and reverse peak current ratios at rapid scan rates. At such rapid scan rates, complicating kinetics of the anthracenyl radical can be "outrun" and the process viewed as a reversible one electron transfer to yield a value for k. Rate constants obtained via this technique at temperatures ranging between 13 and 38 ^{0}C were used to construct Arrhenius plots from which values of +63.6 kJ mol^{-1} and –0.42 J K^{-1} mol^{-1} were obtained for the energy and entropy of activation respectively. The value of k derived at room temperature was 117.4 s^{-1}.

More recently, Savéant et al used the variation of cathodic peak potential during the rapid scan cyclic voltammetric study described previously as a means of evaluating the activation parameters of 9-ArCl bond cleavage [40]. This technique was subsequently implemented by Jaworski et al as described in §5.5.2. Activation parameters were extracted from an Arrhenius plot constructed using rate constants determined for temperatures ranging between 1 and 30 ^{0}C. Values of +46 kJ mol^{-1} and –59 J K^{-1} mol^{-1} were obtained for the activation energy and entropy respectively. The value of k obtained at room temperature was 120.2 s^{-1}.

As for values of k at room temperature, we note a variation in the magnitude of activation parameters obtained which reflects the inaccuracies caused by capacitative charging currents and ohmic distortion with the application of more conventional techniques.

5.5.4 Application of the elevated temperature voltammetric apparatus to the study of 9-ArCl

We have shown in §5.5.1 that due to the rapid nature of the electron transfer reactions undergone by the anthracenyl radical formed as a product of the bond cleavage process, kinetic investigation must by necessity be able to probe bond cleavage processes over a very short time-scale. In §5.4.2 we demonstrated application of the elevated temperature microelectrode apparatus to the determination of activation parameters within an ECE mechanistic scheme in instances where the first electron transfer step is chemically irreversible. We now apply this novel technique to the determination of activation parameters in the case of 9-ArCl bond cleavage, the derivation of which are hampered by the rapid nature of the bond cleavage process and subsequent reaction of the intermediate species formed. In doing so, we demonstrate the advantages of the steady state technique over previously applied methods in the determination of activation parameters which are less prone to the inaccuracies caused by ohmic distortion and capacitative charging currents.

We compare the value of k obtained at room temperature with previously determined literature values. Using rate constants determined at elevated temperatures, activation parameters for the halide bond cleavage of 9-ArCl in acetonitrile are derived. This work represents the first determination of activation parameters for 9-ArCl bond cleavage using a steady state technique and in this solvent system. The energy and entropy of activation were compared to literature values previously derived for this reaction in DMF.

5.5.5 Experimental determination of rate constants for halide bond cleavage of 9-ArCl

Steady state analysis at variable temperatures was performed on a 1 mM solution of 9-ArCl in acetonitrile containing 0.1 M NBu_4ClO_4 as supporting electrolyte using a procedure identical to that outlined in §5.4.6 for oBNB. Waves were obtained at temperatures ranging between 24 and 60 ^{0}C using a 10 μm diameter microelectrode. A representative voltammogram obtained at 24 ^{0}C is shown in Figure 5.20. Two waves corresponding to the reduction of 9-ArCl are observed. The first occurs with $E_{1/2}$ –2.18 V and the second at –2.44 V versus the Fc/Fc^+ couple. This is consistent with the values of –1.78 V and –2.00 V versus SCE recorded by Wipf and Wightman at room temperature during the rapid scan cyclic voltammetric investigation described previously [39].

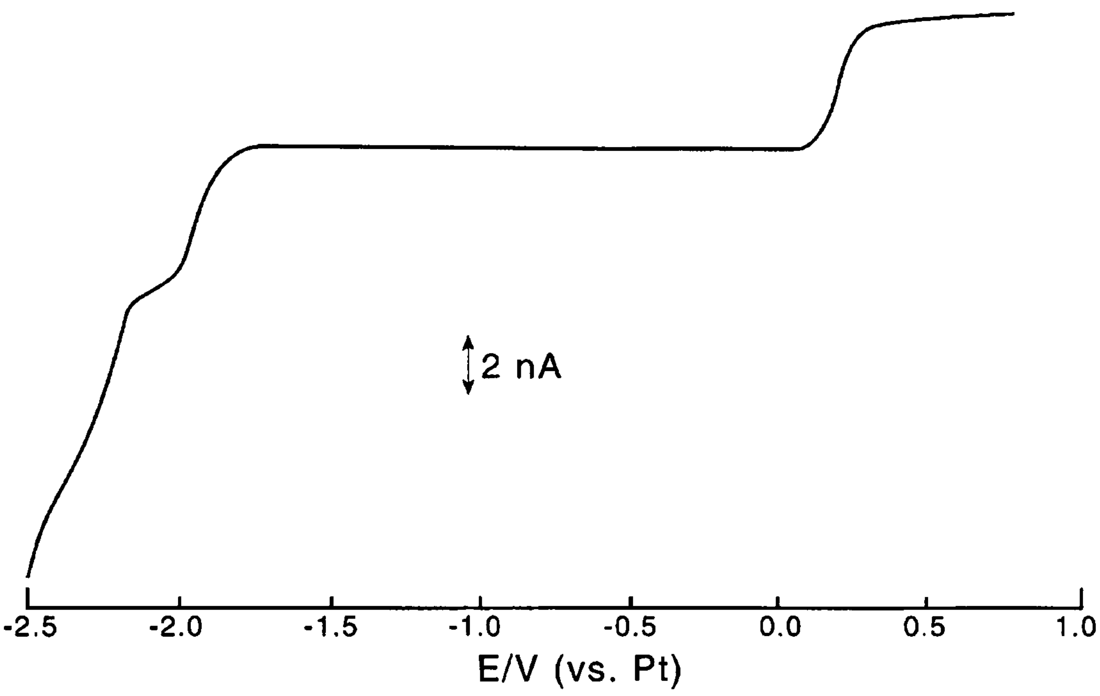

Figure 5.20: Steady state voltammogram for reduction of 1 mM 9-ArCl and oxidation of 1 mM ferrocene in acetonitrile/0.1 M NBu_4ClO_4 solution recorded using a 10 μm diameter platinum microelectrode at 24 ^{0}C, scan rate 10 mV s^{-1}.

Limiting currents obtained for the oxidation of ferrocene and the first reduction process of 9-ArCl at each temperature are tabulated in Table 5.11. Reported I_{lim} values are an average of 5 steady state waves recorded for each temperature. Limiting currents are not recorded for the second 9-ArCl reduction process since this wave occurred at the onset of solvent breakdown which prevented measurement of accurate values.

We noted in §5.5.1 that 9-ArCl reduction does not occur via a well-defined mechanism, rather the reduction process can proceed via a number of reaction pathways. A number of studies suggest that reduction of 9-ArCl proceeds via an initial 2 electron step to form anthracene which is subsequently reduced at more negative potential in a further one electron transfer. However, an initial one electron reduction process to form the anthracene species is also feasible and has been postulated by Savéant et al for the reduction of 9-ArCl in DMF [42]. As the first stage in our analysis, we examined the experimentally determined limiting current in relation to literature and theoretical values of 9-ArCl diffusion in acetonitrile as a means of assessing the number of electrons involved.

As far as we are aware, the only experimentally determined diffusion coefficient for 9-ArCl in acetonitrile has been reported by Wipf and Wightman. This was derived during the rapid scan cyclic voltammetric study of 9-ArCl reduction described previously [39]. Using the height of the irreversible 2 electron wave at slow scan rates and reversible one electron wave at fast scan rates, these workers estimated D to be $1.1\text{x}10^{-5}$ cm^2 s^{-1}. However, since measurement of peak currents was not under diffusion limited conditions, we suggest that this procedure will yield only an approximate value of D. Comparison was made with experimentally determined diffusion coefficients for the related compound anthracene. Since these two molecules differ only by the addition of a chlorine substituent atom, values of D are likely to be similar. Using the diffusion limited current obtained at microelectrodes, Howell and Wightman determined the diffusion coefficient of anthracene in acetonitrile containing 0.6 M NEt_4ClO_4 to be $2\text{x}10^{-5}$ cm^2 s^{-1} at 25 ^{0}C [45]. Using an identical procedure, Amatore and Lefrou determined the diffusion of anthracene to be $1.8\text{x}10^{-5}$ cm^2 s^{-1} in acetonitrile containing 0.6 M NEt_4BF_4 at 25 ^{0}C [46]. The large difference in the experimentally determined values of D at room temperature for 9-ArCl and anthracene is unexpected. The Wilke-Chang correlation has previously been introduced in §5.2.4 as a theoretical basis for the estimation of diffusion coefficients in solution [10]. Wilke-Chang predictions for the diffusion of 9-ArCl and anthracene in acetonitrile are $1.61\text{x}10^{-5}$ and $1.74\text{x}10^{-5}$ $cm^2 s^{-1}$ respectively. By analogy with the close link between the Wilke-Chang and experimentally derived values of D in the case of anthracene, we consider the theoretically predicted value of D to be a more accurate representation of 9-ArCl diffusion in comparison to the experimentally determined value of Wipf and Wightman.

Taking D to equal $1.61\text{x}10^{-5}$ cm^2 s^{-1} at 24 ^{0}C as explained above, the theoretically predicted limiting current for a one electron process was calculated using the expression for the transport limited current at a microelectrode previously defined in Equation 2.33. From this, the effective number of electrons transferred during the first reduction wave at 22 ^{0}C was calculated as 1.59. Since n_{eff} is greater than 1, this suggests an initial 2 electron reduction step. An n_{eff} of 1.59 is obtained in this instance due to the decreased residence time of the intermediate anthracenyl radical species at the microdisc electrode. We conclude that reduction of 9-ArCl proceeds via an irreversible 2 electron reduction process under the conditions employed during this investigation to yield anthracene which is subsequently reduced in a further one electron step. Our assignment of an overall 3 electron reduction process for the reduction of 9-ArCl to the anthracene radical species is consistent with the assignments of Wipf and Wightman [39], Savéant et al [41] and Jaworski et al [43] during the studies of 9-ArCl reduction in acetonitrile described previously.

Kinetic parameters for the reductive cleavage of the halide bond in 9-ArCl at varying temperatures were derived assuming an ECE mechanistic pathway using an identical procedure to that implemented for oBNB in §5.4.6. Diffusion coefficients for ferrocene at each temperature were calculated from the limiting currents obtained for ferrocene oxidation listed in Table 5.11 and used to construct the Arrhenius plot of ln D versus 1/T shown in Figure 5.21. This was used to estimate values of D for 9-ArCl assuming the temperature dependance for diffusion of these two species in acetonitrile to be approximately equal and taking the diffusion coefficient of 9-ArCl as being 1.61×10^{-5} cm^2 s^{-1} at 24 ^{0}C. Diffusion coefficients and the corresponding values of I_{lim} for the one electron reduction of 9-ArCl are reported in Table 5.11. Values of n_{eff}, calculated by ratio of the experimentally determined limiting current to the theoretical current for the one electron reduction, are also listed in Table 5.11. n_{eff} was observed to give the correlation with temperature shown in Figure 5.22. From the values of n_{eff} at each temperature, rate constants were determined using the procedure derived by Fleischmann et al described in §5.4.6 [33].

5.5.6 Experimental determination of activation parameters for halide bond cleavage of 9-ArCl

An Arrhenius plot of ln k versus 1/T, shown in Figure 5.23, was constructed from the values of k reported in Table 5.11. From this, values of +48.7 ± 4 kJ mol^{-1} and $+1.074 \times 10^{11}$ s^{-1} were obtained for E_a and the pre-exponential factor A respectively. From the value of A and using Equation 5.25, the entropy of activation for halide bond cleavage of 9-ArCl was calculated to be −42 ± 4 J K^{-1} mol^{-1}.

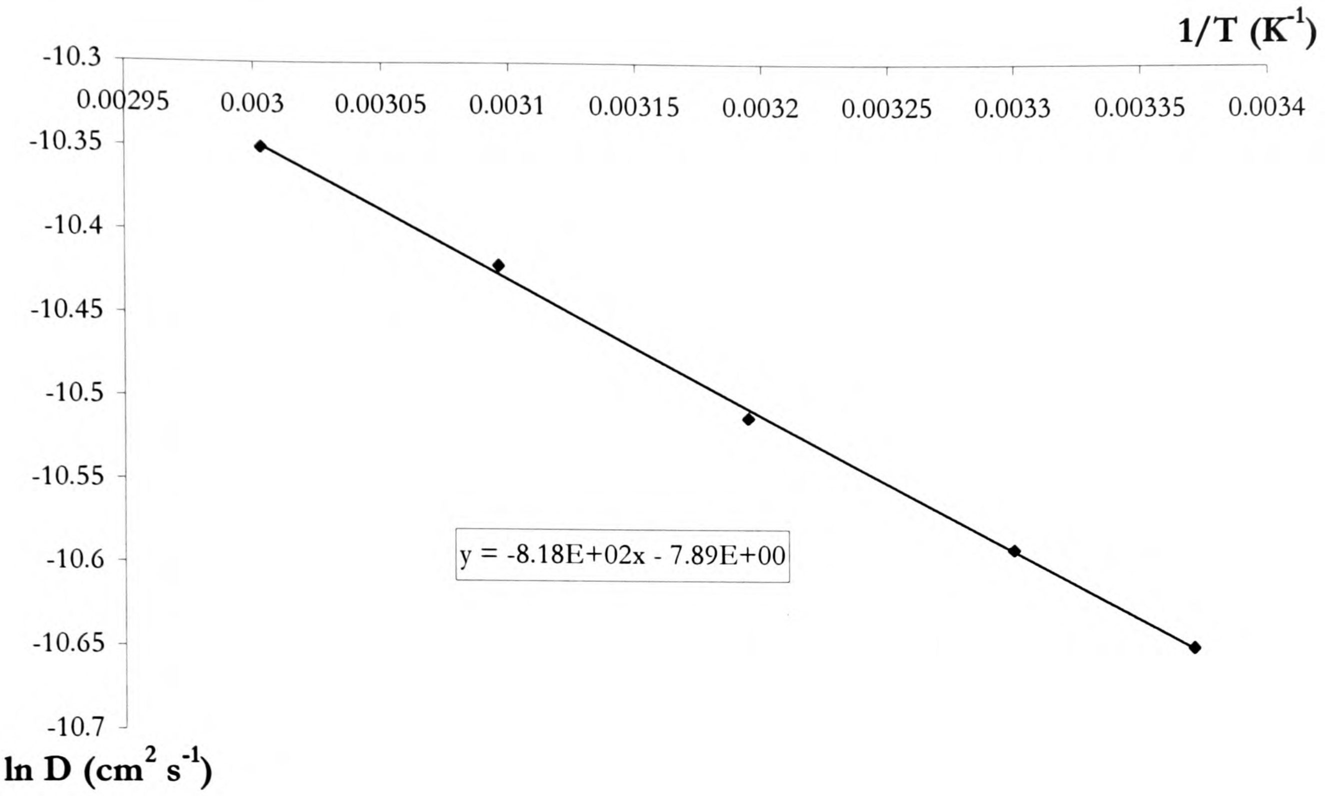

Figure 5.21: ln D versus 1/T for ferrocene in acetonitrile/0.1 M NBu_4ClO_4 solution

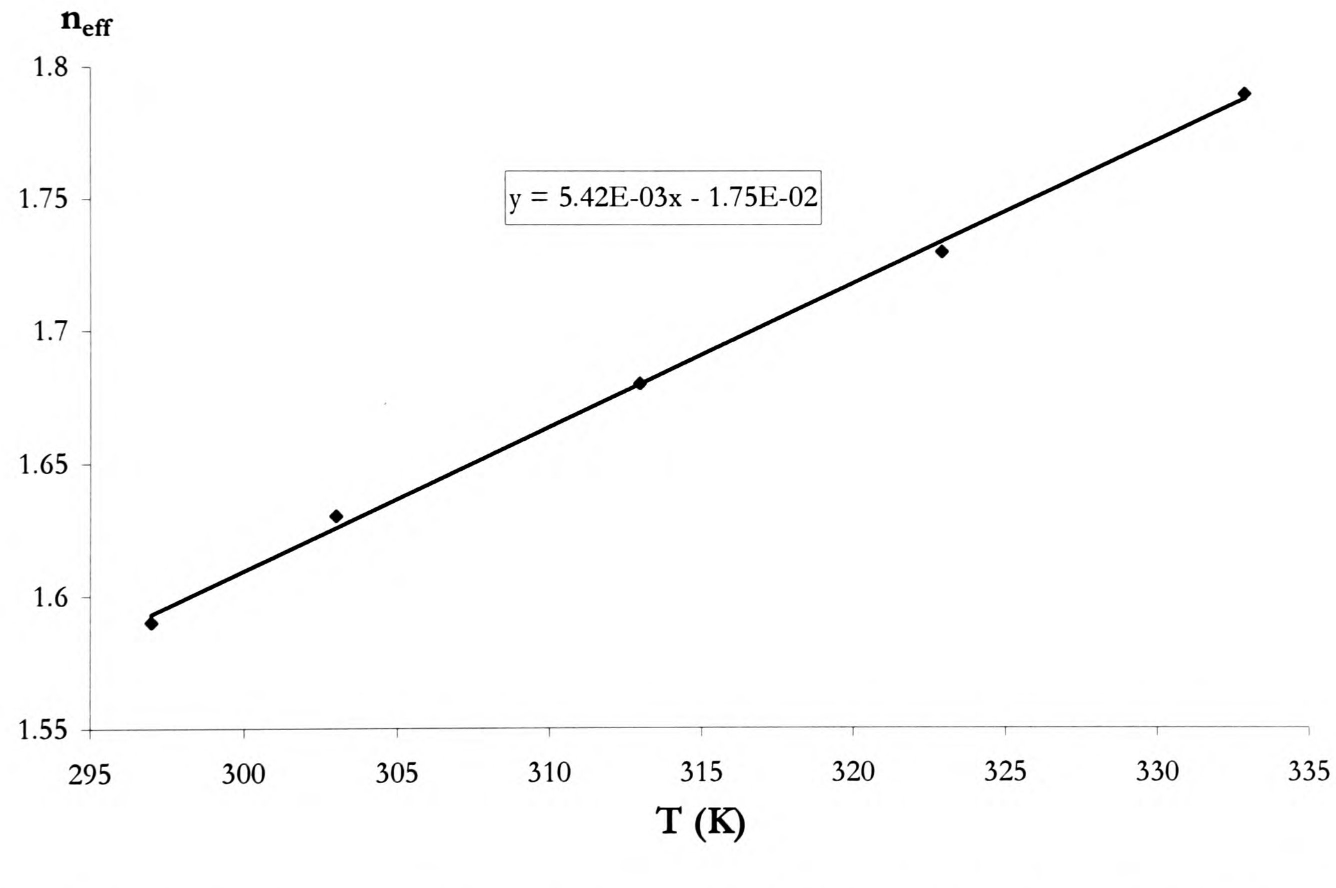

Figure 5.22: n_{eff} versus temperature for reduction of 1 mM 9-ArCl in acetonitrile/0.1 M NBu_4ClO_4 solution at a 10 μm diameter microelectrode

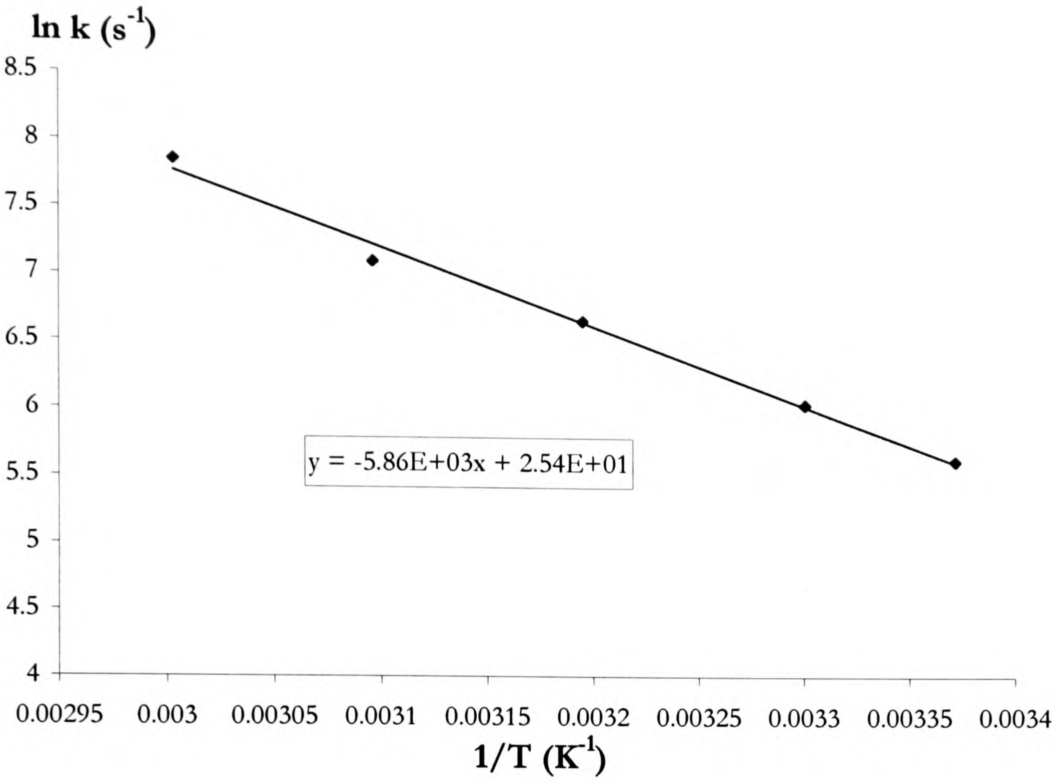

Figure 5.23: ln k versus 1/T for the reduction of 1 mM 9-ArCl in acetonitrile/0.1 M NBu_4ClO_4 solution at a 10 μm diameter microelectrode

Temperature (^{0}C)	Ferrocene I_{lim} (A)	Ferrocene D (cm^2 s^{-1})	9-ArCl I_{lim} (A)	Estimated 9-ArCl D (cm^2 s^{-1})	Estimated I_{lim} for 9-ArCl one electron reduction (A)	n_{eff}	k (s^{-1})
24	$4.33\text{x}10^{-9}$	$2.37\text{x}10^{-5}\pm1.0\text{x}10^{-6}$	$4.24\text{x}10^{-9}$	$1.61\text{x}10^{-5}$	$2.67\text{x}10^{-9}$	1.59	278 ± 35
30	$4.59\text{x}10^{-9}$	$2.51\text{x}10^{-5}\pm1.0\text{x}10^{-6}$	$4.61\text{x}10^{-9}$	$1.71\text{x}10^{-5}$	$2.83\text{x}10^{-9}$	1.63	422 ± 50
40	$4.97\text{x}10^{-9}$	$2.72\text{x}10^{-5}\pm1.1\text{x}10^{-6}$	$5.19\text{x}10^{-9}$	$1.87\text{x}10^{-5}$	$3.09\text{x}10^{-9}$	1.68	781 ± 95
50	$5.44\text{x}10^{-9}$	$2.98\text{x}10^{-5}\pm1.2\text{x}10^{-6}$	$5.80\text{x}10^{-9}$	$2.02\text{x}10^{-5}$	$3.35\text{x}10^{-9}$	1.73	1212 ± 150
60	$5.84\text{x}10^{-9}$	$3.20\text{x}10^{-5}\pm1.3\text{x}10^{-6}$	$6.46\text{x}10^{-9}$	$2.18\text{x}10^{-5}$	$3.61\text{x}10^{-9}$	1.79	2592 ± 310

Table 5.11: Experimentally determined and calculated parameters for the reduction of 1 mM 9-ArCl in acetonitrile/0.1 M NBu_4ClO_4 solution using a 10 μm diameter microelectrode at temperatures ranging from 24 to 60 ^{0}C

5.5.7 Comparison of data with previous literature studies

The value of k at room temperature was observed to be in reasonable agreement with the literature values of k derived by alternative methods reported in §5.5.2. As noted previously, a wide variation in values of k is observed in the literature arising from the nature of the different analytical techniques employed. The consistency observed between the rate constant derived during the present study and literature values suggests the assumption of an ECE type process under the conditions of our investigation is valid.

As far as we are aware, activation parameters for the halide bond cleavage of 9-ArCl in acetonitrile have previously not been reported. Literature values have, however, been reported for 9-ArCl decomposition in DMF as reviewed in §5.5.3. Activation parameters, particularly activation entropy, were observed to vary considerably between the three investigations described. Values of +57.3, +63.6, and +46 kJ mol^{-1} were obtained for E_a by Savéant et al [42], Parker [35] and Savéant et al [40] respectively. Corresponding activation entropies were −16.7, −0.4, and −59.0 J K^{-1} mol^{-1}. Given the wide variation of values reported in DMF, no firm conclusions can be drawn concerning the difference in activation parameters between the two solvent species.

We note that rate constants determined at room temperature during this and previous literature studies in acetonitrile [39,41,43] are consistently higher than those determined in DMF [40,35,42]. From this we infer that there should be a difference in activation parameters for the halide bond cleavage of 9-ArCl in these two solvent systems.

We noted during the discussion of oBNB halide bond cleavage in §5.4.9 that magnitude of activation parameters are dictated by the transition state. Activation energy defines the amount of energy required to form the transition state and activation entropy reflects the change in order of the neighbouring solvent molecules upon transition state formation. In the case of oBNB, discussion focussed on the structure of the reactant species and how this affected activation parameters by alteration of the position of the transition state on the reaction co-ordinate according to the Hammond-Leffler postulate [44]. In this instance, the position of the transition state will be identical in both solvent systems since the same parent molecule structure is under consideration. Instead we need to consider the role of each solvent in transition state stabilisation.

The transition state formed during the halide bond cleavage process can be viewed as a shift of negative charge to the chloride substituent of the chloroanthracene radical anion. The activation energy required to form the transition state can be reduced if the solvent is able to stabilise the localised negative charge. The anion solvating ability of each solvent can be assessed with reference to two separate solvent scales. Swain et al have predicted anionic and cationic solvating ability of various solvents using a statistical analytical procedure incorporating a wide variety of data derived from sources such as IR, ESR, NMR and electronic spectra [47]. Anion-solvating tendency, denoted parameter A, for each solvent is given in numerical form on a scale of 1 to 0 with reference to the compound hexamethylphosphoric acid which, as a poor anion solvator, is taken to be the limiting condition for which A=0. Acetonitrile and DMF exhibit A parameters of 0.37 and 0.30 respectively. Gutmann defines the solvent acceptor number as a dimensionless parameter expressing the acceptor properties of each solvent relative to $SbCl_5$ which is arbitrarily taken to have an acceptor number of 100 [48]. Acceptor numbers were derived using the ^{31}P NMR shifts produced in triethylphosphine oxide by electrophilic solvent interactions which lower electron densities at the P-atoms due to inductive effects. Acetonitrile and DMF are denoted by the acceptor numbers 18.9 and 16.0 respectively.

The correlation between solvating ability of the solvent and rate constant for 9-ArCl bond cleavage reflects the subsequent lowering of the activation energy required to form the transition state. This is in line with findings by Wipf and Wightman [49] and Jaworski et al [43] who investigated the correlation of 9-ArCl bond cleavage rate with solvent solvating ability. Wipf and Wightman used rapid scan cyclic voltammetry at microelectrodes to investigate 9-ArCl halide bond cleavage for a variety of solvent systems at 25 ^{0}C [49]. Values of k were derived using the procedure outlined previously in which experimental voltammograms were fitted to data simulated according to an assumed ECE-DISP1 process. Rate constants showed a linear correlation with solvent solvating ability as defined by the Gutmann acceptor number.

Jaworski et al also used microelectrode cyclic voltammetry to determine rates of 9-ArCl decomposition for a range of solvent systems at 22 ^{0}C [43]. Their analytical procedure incorporated the theoretical variation of the reductive peak potential with scan rate calculated for a DISP1 mechanistic process as described in §5.5.2. Values of k were correlated to the solvent acceptor number as defined by Gutmann.

Since acetonitrile is more effectively able to solvate the transition state, we would anticipate the activation energy for halide bond cleavage of 9-ArCl in acetonitrile to be lower than in DMF. We have noted the wide variation in literature values reported for DMF. Thus no firm conclusions can be drawn by comparison of the activation parameters in the two solvent systems. However, we note that the value of E_a in acetonitrile derived during this study is at the lower end of the values reported for DMF.

By the same reasoning, the negative entropy of activation observed during 9-ArCl halide bond cleavage in both DMF and acetonitrile reflects the increased ordering of solvent molecules around the transition state as solvation of the negatively charged chloride substituent occurs.

Since acetonitrile is able to solvate the transition state more effectively than DMF, we expect the entropy of activation to be more negative in this instance. As for E_a values, a true comparison between the two solvent systems is impractical due to the obvious uncertainties in the data reported for DMF. However, as a general trend, the activation entropy derived during this study for 9-ArCl halide bond cleavage in acetonitrile lies at the more negative end of the data reported for DMF.

5.5.8 Summary

Further to the study of oBNB, this work demonstrates application of the novel elevated temperature microelectrode apparatus to the study of rapid electrode processes. This investigation represents the first determination of rate constants for the 9-ArCl bond cleavage process using a steady state technique. The value of k obtained in acetonitrile at 24 ^{0}C was found to be in good agreement with previously determined literature values.

The first determined values for the energy and entropy of activation for 9-ArCl bond cleavage in acetonitrile were reported. The values obtained were compared to activation parameters reported for the decomposition of 9-ArCl in DMF derived by alternative techniques. Literature values were found to vary considerably, a reflection of the uncertainty in techniques used by previous workers. In general, E_a was found to be lower and $\Delta S^{\neq}_{298}$ more negative in acetonitrile versus DMF. This was attributed to the greater solvating ability of acetonitrile in comparison to DMF which serves to stabilise the negative charge of the transition state. This is in line with the solvation characteristics of these two chemicals as defined by Swain et al and Gutmann. The advantage of this method over previously applied techniques in the determination of activation parameters which are less prone to the inaccuracies caused by ohmic distortion and capacitative charging currents was demonstrated.

5.6 Conclusions

This chapter has described application of the elevated temperature microelectrode apparatus to a number of model chemical systems. Information which can be derived from this experimental system has been demonstrated. Areas in which application of this apparatus has significant advantages over previously applied techniques have been highlighted. Investigations have focussed on the compounds TMPD, TBPA, oBNB and 9-ArCl. Validation of experimentally determined parameters by comparison to literature values and values derived as part of this study via alternative methods has demonstrated the accuracy of this novel technique.

For TMPD and TBPA, the apparatus was used for the evaluation of diffusion coefficients at elevated temperatures. From the values obtained, activation parameters for diffusion of the species in solution were determined. The variation of diffusion with temperature was used to estimate effective radii for each compound via the Stokes-Einstein relationship. Variation of diffusion coefficient with temperature was also compared to the theoretically predicted relationship according to Wilke-Chang theory. Correlation of the results obtained for each of these two theories was linked to diffusional behaviour of each species in solution according to a "slip" or "stick" model. Our value of the effective radius of TMPD determined in acetonitrile was in excellent agreement with a previously reported literature value derived under similar conditions via an alternative method. Correlation to a theoretically determined value reported in the literature and a value calculated by us using the Nemesis molecular modelling package was made assuming a "slip" diffusional process. In contrast, TMPD diffusion in water was approximated by "stick" type behaviour. Correlation of the diffusion mechanism with Wilke-Chang theory suggests that a reliable estimate of the diffusion coefficient is obtained for "stick" behaviour but that the theory is less applicable in instances of "slip" diffusion.

Our value for the effective radius of TBPA represents the first reported value for this compound. The value obtained was observed to be in good agreement with a theoretical value calculated using the Nemesis molecular modelling package assuming "stick" type diffusion. Contrary to TMPD, "stick" diffusion was associated with a poor correlation to Wilke-Chang theory. This was attributed to an unreliable estimate of the molecular radius provided by the Nemesis molecular modelling package.

In the case of oBNB and 9-ArCl, the apparatus was demonstrated to be a viable means of interrogating rapid and/or irreversible kinetic processes. Both compounds undergo reduction via a 2 electron transfer process where halide bond cleavage constitutes an intervening chemical step. Use of microelectrodes permits the "outrunning" of bond cleavage kinetics with the observation of an n_{eff} less than 2. Existing theory for an ECE process was found to be appropriate for the description of both reduction mechanisms and was used to evaluate rate constants at varying temperatures. Arrhenius plots were used to determine the energy and entropy of activation for halide bond cleavage in both compounds. For oBNB, the rate constant obtained at room temperature was in good agreement with literature values. Activation parameters of halide bond cleavage represent the first reported values for this compound. Values obtained were observed to be consistent with activation parameters determined for other halonitrobenzene compounds in line with Hammond-Leffler theory. In the case of 9-ArCl, activation parameters have previously been derived in DMF by a number of workers using cyclic and double potential step voltammetric techniques. Values derived during this investigation in acetonitrile were observed to be in line with those in DMF according to the Hammond-Leffler postulate. The novel steady state method was demonstrated to be a viable method for the determination of activation parameters which are less prone to the inaccuracies caused by ohmic distortion and capacitative charging currents inherent with the application of more conventional techniques.

References

[1] H. Fernández, M. A. Zón, J. Electroanal. Chem., 1992, **332**, 237

[2] H. Fernández, M. A. Zón, J. Electroanal. Chem., 1990, **283**, 251

[3] M. A. Zón, H. Fernández, L. Sereno, J. J. Silber, Electrochimica Acta, 1987, **32**, 1, 71

[4] R. M. Buchanan, G. S. Calabrese, T. J. Sobieralski, M. S. Wrighton, J. Electroanal. Chem., 1983, **153**, 129

[5]. D.L. Jeanmaire, R. P. Van Duyne, J. Electroanal. Chem., 1975, **66**, 235

[6] R. N. Adams, Electrochemistry at Solid Electrodes, Marcel Dekker, New York, 1969, p360

[7] S.V. Tatwawadi, S. Piekarski, M. D. Hawley, R. N. Adams, Chem. Listy, 1967, **61**, 634

[8] J. A. Friend, N. K. Roberts, Aust. J. Chem., 1958, **11**, 104

[9] M. B. Moressi, H. Fernández, J. Electroanal. Chem., 1994, **369**, 153

[10] C. R. Wilke, P. Chang, A. I. Ch. E. Journal, 1955, **1**, no. 2, 263

[11] J. H. Perry, Chemical Engineers Handbook, McGraw-Hill Book Company, Inc., 1950

[12] M. A. Zón, H. Fernández, L. Sereno, J. J. Silber, Electrochimica Acta, 1987, **32**, 12, 1733

[13] J. O'M. Bockris, A. K. N. Reddy, Modern electrochemistry, Plenum Press, New York, 1977, p379

[14] J. P. Hansen, J. R. McDonald, Theory of Simple Liquids, Academic Press, London, 1976, p206

[15] C.R.C. Handbook of Chemistry and Physics (74th Edition), CRC Press, Cleveland, Ohio, USA, 1993, 6-194

[16] C.R.C. Handbook of Chemistry and Physics (74th Edition), CRC Press, Cleveland, Ohio, USA, 1993, 6-10

[17] A. Kapturkiewicz, W. Jaenicke, J. Chem. Soc. Faraday Trans.1, 1997, **83**, 9, 2727

[18] N. Isaacs, Physcial Organic Chemistry, Longman, UK, 1987, p.104

[19] A. Hantzsch, Ber. Dtsch, Chem. Ges., 1922, **55**, 953

[20] E. T. Seo, R. F. Nelson, J. M. Fritsch, L. S. Marcoux, D. W. Leedy, R. N. Adams, J. Am. Chem. Soc., 1966, **88**, 15, 3498

[21] R. F. Nelson, R. N. Adams, J. Am. Chem. Soc., 1968, **90**, 15, 3925

[22] R. G. Compton, M. E. Laing, J. Chem. Soc., Chem. Commun., 1988, 1320

[23] R. L. Wang, K. Y. Tam, F. Marken, R. G. Compton, Electroanalysis, 1997, **9**, 4, 284

[24] J. G. Lawless, D. D. Hawley, J. Electroanal. Chem., 1969, **21**, 365-375

[25] W. C. Danen, T. K. Kensler, J. G. Lawless, M. F. Marcus, M. D. Hawley, J. Phys. Chem., 1969, **73**, 12 4389

[26] R. F. Nelson, A. K. Carpenter, E. T. Seo, J. Electrochem. Soc., 1973, **120**, 206

[27] R. G. Compton, A. C. Fisher, R. G. Wellington, P. J. Dobson, P. A. Leigh, J. Phys. Chem., 1993, **97**, 10410

[28] R. G. Compton, R. G. Wellington, P. J. Dobson, P. A. Leigh, J. Electroanal. Chem., 1994, **370**, 129

[29] R. G. Compton, M. B. G. Pilkington, G. M. Stearn, J. Chem. Soc., Faraday Trans. 1, 1988, **84**, 3155

[30] M. F. Bento, M. J. Medeiros, M. I. Montenegra, C. Beriot, D. Pletcher, J. Electroanal. Chem., 1993, **345**, 273

[31] R. G. Compton, R. A. W. Dryfe, J. Electroanal. Chem., 1994, **375**, 247

[32] R. G. Compton, F. Marken, T. O. Rebbit, J.Chem. Soc., Chem. Commun., 1996, 1017

[33] M. Fleischmann, F. Lasserre, J. Robinson, J. Electroanal. Chem., 1984, **177**, 115

[34] V. D. Parker, Acta Chemica Scandinavica B, 1981, **35**, 655

[35] V. D. Parker, Acta Chemica Scandinavica B, 1981, **35**, 595

[36] E. Ahlberg, E. Svensmark, V. D. Parker, Acta Chemica Scandinavica B, 1980, **34**, 249

[37] E. Ahlberg, V. D. Parker, J. Electroanal. Chem., 1981, **121**, 57

[38] E. Ahlberg, V. D. Parker, J. Electroanal. Chem., 1981, **121**, 73

[39] D. O. Wipf, R. M. Wightman, J. Phys. Chem., 1989, **93**, 4286

[40] C. P.Andrieux, G. Delgado, J. M. Savéant, J. Electroanal. Chem., 1993, **348**, 123

[41] F. M'Halla, J. Pinson, J.M. Savéant, J. Am. Chem. Soc., 1980, **102**, 12, 4120

[42] C. P.Andrieux, J. M. Savéant, D. Zann, Nouveau Journal de Chimie, 1984, **8**, 2, 107

[43] J. S. Jaworski, P. Leszczyñski, J. Tykarski, J. Chem. Research (S), 1995, 510

[44] A. Pross, Adv. Phys. Org. Chem., 1977, **14**, 69

[45] J. O. Howell, R. M. Wightman, Anal. Chem., 1984, **56**, 524

[46] C. Amatore, C. Lefrou, J. Electroanal. Chem., 1992, **324**, 33

[47] C. G. Swain, M. S. Swain, A. L. Powell, S. Alunni, J. Am. Chem. Soc., 1983, **105**, 3, 503

[48] V. Gutmann, Coord. Chem. Rev., 1976, **18**, 225

[49] D. O. Wipf, R. M. Wightman, Anal. Chem., 1990, **62**, 98

[50] G. Cauquis, D. Serve, Anal. Chem., 1972, **44**, 13, 2222

[51] T. Kitagawa, T. P. Layloff, R. N. Adams, Anal. Chem., 1963, **35**, 1086

[52] R. N. Adams, J. Electroanal. Chem., 1964, **8**, 151

[53] T. Fujinaga, Y. Deguchi, K. Umemoto, Bull. Chem. Soc., Japan, 1964, **37**, 82

Chapter 6

Voltammetry of Bu^n-ZDTP

6.1 Introduction

We noted in Chapter 1 that ZDTPs are added to a typical lubricating oil formulation package as an anti-wear and anti-oxidant additive. Redox processes are significant in the activity of this complex as an anti-oxidant agent. Such processes may also contribute to the anti-wear behaviour of the compound. We therefore noted the potential value of electrochemical investigation in the complex problem of elucidation of the nature of anti-oxidant and anti-wear functions. As an assessment of the applications of electrochemical techniques to ZDTP studies and as the first step in ultimately employing these methods in an engine environment, this chapter describes an investigation to establish the nature of the redox processes undergone by this complex under standard electrochemical conditions. We begin with an introduction to the voltammetric investigations undertaken during the course of this work in §6.2. Cyclic and RDE voltammetric studies are considered in §6.3 and 6.4 respectively. We conclude the chapter with a summary of the information obtained in §6.5.

6.2 Introduction to Bu^n-ZDTP voltammetry undertaken in the present work

A detailed review of the literature pertaining to electrochemical investigations of ZDTP compounds has been presented in §1.6 of this thesis. We noted that previously reported voltammetric studies of ZDTPs are few. Furthermore, information is poorly resolved and investigations suggest conflicting assignments of ZDTP redox activity. During the present work we seek to implement a more detailed voltammetric study of ZDTP redox activity than has previously been reported in the literature. Two techniques were employed during the course of our study, namely cyclic and RDE voltammetry. The RDE voltammetry undertaken during the course of this work represents the first reported application of this technique to ZDTP investigation.

The compound Bu^n-ZDTP has been used throughout this work as a typical ZDTP additive. This chapter describes voltammetry of Bu^n-ZDTP under standard electrochemical conditions. Experiments employed DMF as the solvent and used 0.1 M NBu_4ClO_4 as supporting electrolyte. Throughout our investigation, redox activity was investigated at two different electrode substrates, namely platinum and glassy carbon. Cyclic and RDE voltammetric studies are considered in §6.3 and 6.4 respectively.

6.3 Cyclic voltammetry of Bu^n-ZDTP

6.3.1 Experimental

Cyclic voltammetry of Bu^n-ZDTP was performed in DMF solution containing 0.1 M NBu_4ClO_4 as supporting electrolyte at both glassy carbon and platinum electrodes. Glassy carbon and platinum electrodes were used with nominal electrode diameters of 3 and 4 mm respectively. An accurate value for each electrode diameter was obtained using a travelling microscope prior to use. All voltammograms were recorded at a temperature of 25 ^{0}C and under an inert atmosphere of argon versus a SCE reference. A scan rate of 50 mV s^{-1} was typically employed. For variable scan rate experiments, rates ranged between 10 and 100 mV s^{-1} as noted in the text.

Voltammograms were initially recorded using a Bu^n-ZDTP concentration of 1 mM. Results obtained at each of the two electrode substrate materials were compared. Effects of scan speed and Bu^n-ZDTP concentration on voltammetry at each electrode surface were subsequently investigated. Results of multiple scan cyclic voltammetry are also described.

6.3.2 Results and discussion

6.3.2.1 Glassy carbon electrode substrate

A cyclic voltammogram obtained for a 1 mM solution of Bu^n-ZDTP is shown in Figure 6.1. A single peak corresponding to chemically irreversible oxidation of the complex is observed at +0.8 V versus SCE. The chemically irreversible nature and potential of the oxidation wave is in agreement with the results of Stezeryanskii et al who observed oxidation of iso-octyl-ZDTP in DMF solution containing 0.1 M $NaBF_4$ at a potential of +0.81 V versus SCE [1]. Irreversibility of Bu^n-ZDTP oxidation also agrees with the findings of Blankespoor during his investigation of ethyl and iso-propyl-ZDTP oxidation in acetonitrile solution containing 0.1 M $LiClO_4$ as electrolyte [2]. The oxidation signal was recorded over a range of scan rates between 10 and 100 mV s^{-1}. For a diffusion-limited process, without associated mechanistic complication, peak current varies as the square root of scan speed [3]. In this instance, a plot of peak current versus the square root of scan rate gave the linear correlation shown in Figure 6.2. This demonstrates that oxidation of Bu^n-ZDTP is diffusion-limited. This is in agreement with the findings of Blankespoor for reduction of both ethyl and iso-propyl-ZDTP in acetonitrile but conflicts with the cyclic voltammetric and chronopotentiometric study presented by Stezeryanskii et al who suggested kinetic hindrance in the oxidation of iso-octyl-ZDTP in DMF.

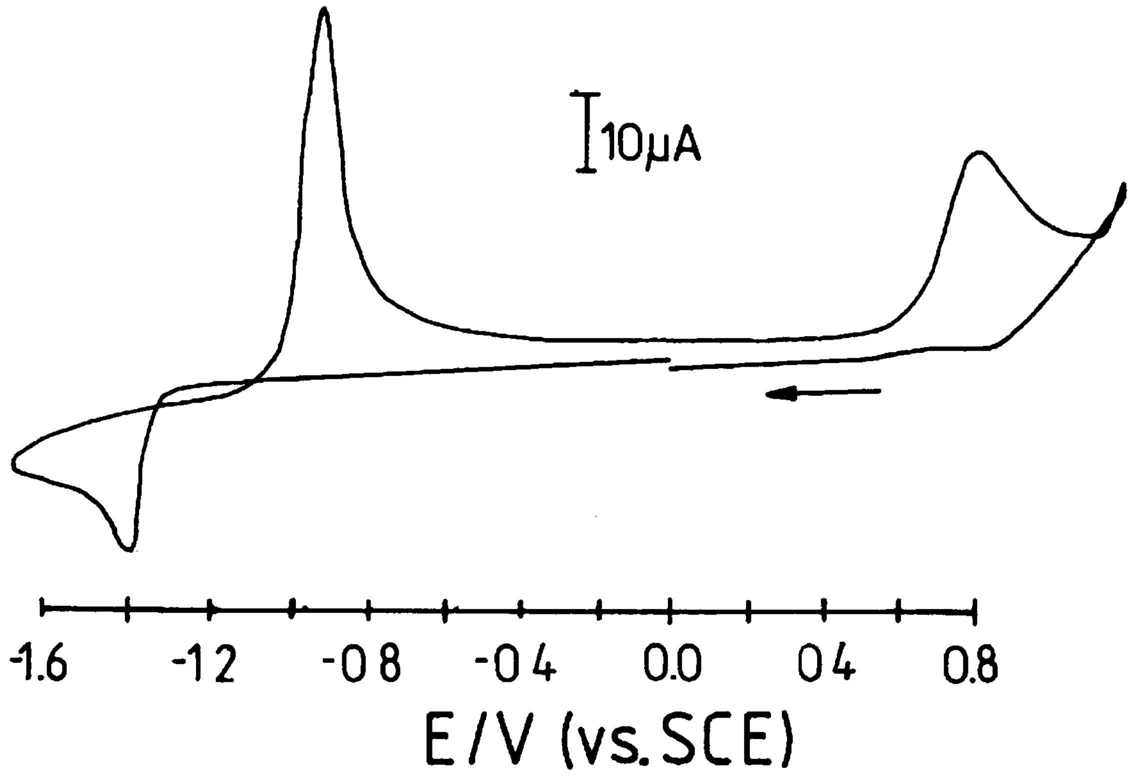

Figure 6.1: Cyclic voltammogram for 1 mM Bu^n-ZDTP in DMF/0.1 NBu_4ClO_4 solution recorded at a 3 mm diameter glassy carbon electrode at 25 °C, scan rate 50 mV s^{-1}.

The reduction of Bu^n-ZDTP at a glassy carbon electrode shows a single wave at –1.42 V versus SCE. The wave obtained is noticeably steeper than that observed for Bu^n-ZDTP oxidation. The appearance of a zinc reduction wave is concurrent with the observations of both Shafiqul Alam et al [4] and Hutchings et al [5] during the polarographic studies described in §1.6. Shafiqul Alam et al report the reduction of isopropyl-ZDTP to zinc metal at –0.9 V versus Ag-AgCl in DMF solution containing 0.1 M NEt_4ClO_4 as electrolyte [4]. Hutchings et al report reduction of isobutyl-ZDTP at –1.05 V versus Ag-AgCl in an ethanolic medium with 0.1 M $NaClO_4$ as electrolyte [5].

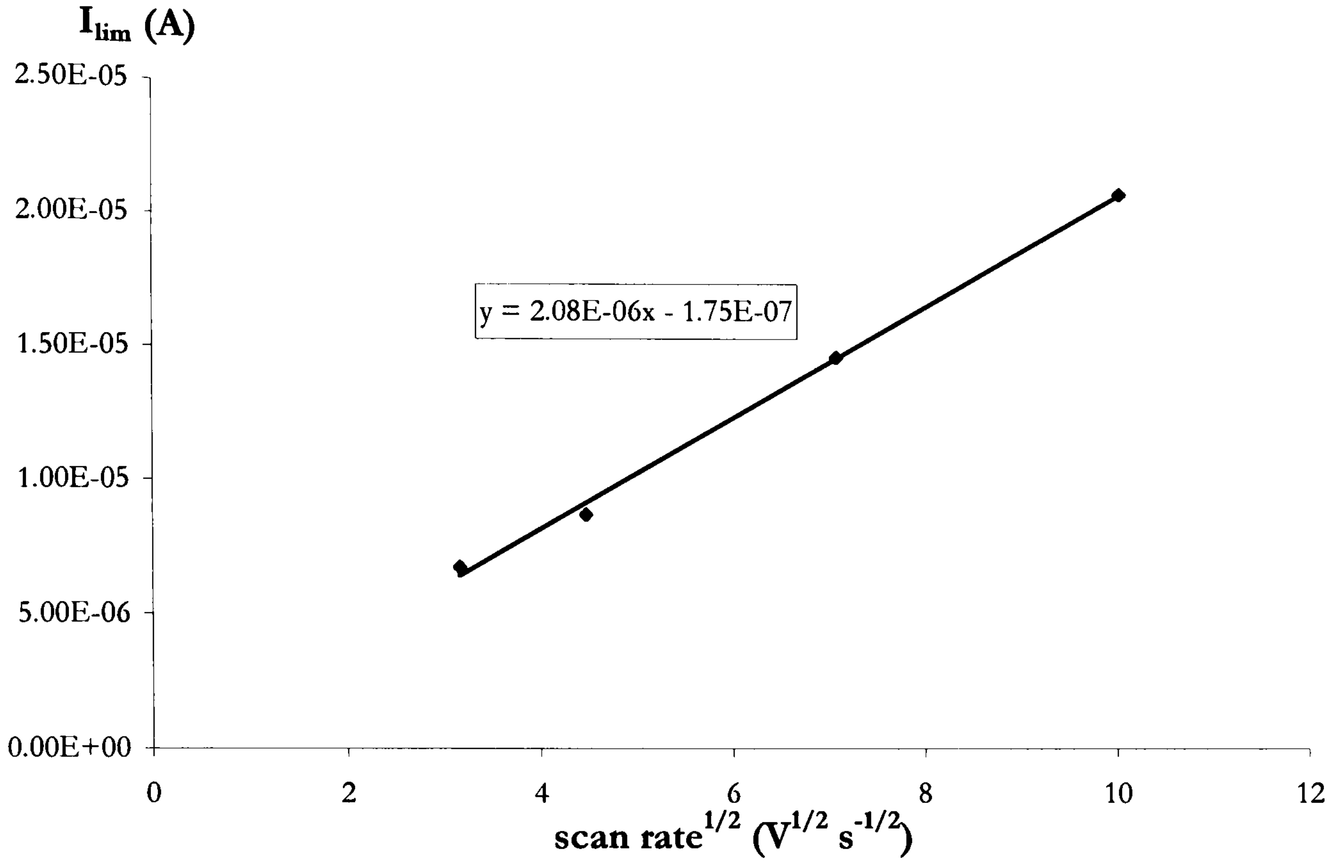

Figure 6.2: Peak current versus square root of scan rate for cyclic voltammetric oxidation of 1 mM Bu^n-ZDTP in DMF/0.1 NBu_4ClO_4 solution recorded at a 3 mm diameter glassy carbon electrode at 25 °C using scan rates between 10 and 100 mV s^{-1}.

Following reversal of scan direction, cross-over is observed between forward and reverse scans. Current-loops are typical of a nucleation controlled process [6]. They arise since deposition of material requires the application of a considerable overpotential in order to initiate nucleation and subsequent growth of a deposit. When the scan direction is reversed, deposition of material continues at the nucleated electrode surface which is less hostile than the bare electrode. Deposition therefore occurs over a greater potential range to yield the observed current-loop. The presence of a steep reduction wave is also concurrent with a nucleated process. This is attributable to the rapid onset of nucleation following the initial deposition of material.

Upon continued scanning in the reverse direction, a sharp peak is visible at –0.92 V versus SCE. This correlates to removal of zinc from the electrode surface once the equilibrium potential of the Zn/Zn^{2+} couple is reached. The characteristic peak shape of a stripping signal results from the rapid current increase due to removal of material as the equilibrium reduction potential is reached. This is followed by an equally rapid current decrease following the complete removal of all deposited material. In this instance, there is some asymmetry in peak shape with the appearance of a “tail” at potentials positive of the stripping signal. We attribute this to the incomplete removal of zinc at the stripping potential with continued oxidation of a small amount of zinc material at more positive potentials.

A number of studies have reported zinc deposition at a glassy carbon electrode surface. However, studies have been largely confined to aqueous media together with one example of zinc deposition from a room temperature molten salt. As far as we know, this investigation represents one of the first reports of zinc deposition on glassy carbon from a non-aqueous solvent medium. A brief review of literature reports concerning zinc deposition at a glassy carbon electrode surface follows.

Sonneveld et al describe an investigation of zinc deposition from an alkaline zincate solution using RDE voltammetry [7]. These workers report zinc nucleation at an overpotential of –1.5 V versus a Hg-HgO reference electrode with subsequent stripping at –1.31 V.

Hussey and Pitner investigated the deposition of electrogenerated Zn^{2+} from the room temperature molten salt aluminium chloride 1-methyl-3-ethylimidazolium chloride using cyclic and RDE voltammetry [8]. These workers noted nucleation of zinc at the electrode surface as evidenced by the presence of a current-loop upon scan reversal. A stripping signal was visible upon reoxidation with noticeable asymmetry due to continued oxidation of material at potentials positive of the equilibrium reduction potential. This is in agreement with observations made during the present study in which continued reoxidation of zinc gives rise to the stripping signal "tail" observed. The origin of this behaviour was not determined. However Hussey and Pitner postulate that a dendritic surface layer may form on top of a more strongly bound compact deposit at the high current densities of the experiment. Reoxidation of different types of surface material correlates to the multiple stripping peaks observed.

6.3.2.2 Calculation of charge during reduction and stripping processes

The charge involved in the reduction and subsequent reoxidation processes was evaluated via integration of peak current in order to assess the efficiency of the stripping mechanism. We note inaccuracy inherent in the procedure due to capacitative charging currents at the electrode surface. An estimate of capacitance at the glassy carbon electrode for this experimental system was made via measurement of the effective current produced by capacitance at different scan speeds. Cyclic voltammograms for a

DMF and 0.1 M NBu_4ClO_4 background solution were recorded at variable scan rates ranging from 500 to 20 mV s^{-1}. The resulting plot of capacitative current versus scan rate is shown in Figure 6.3.

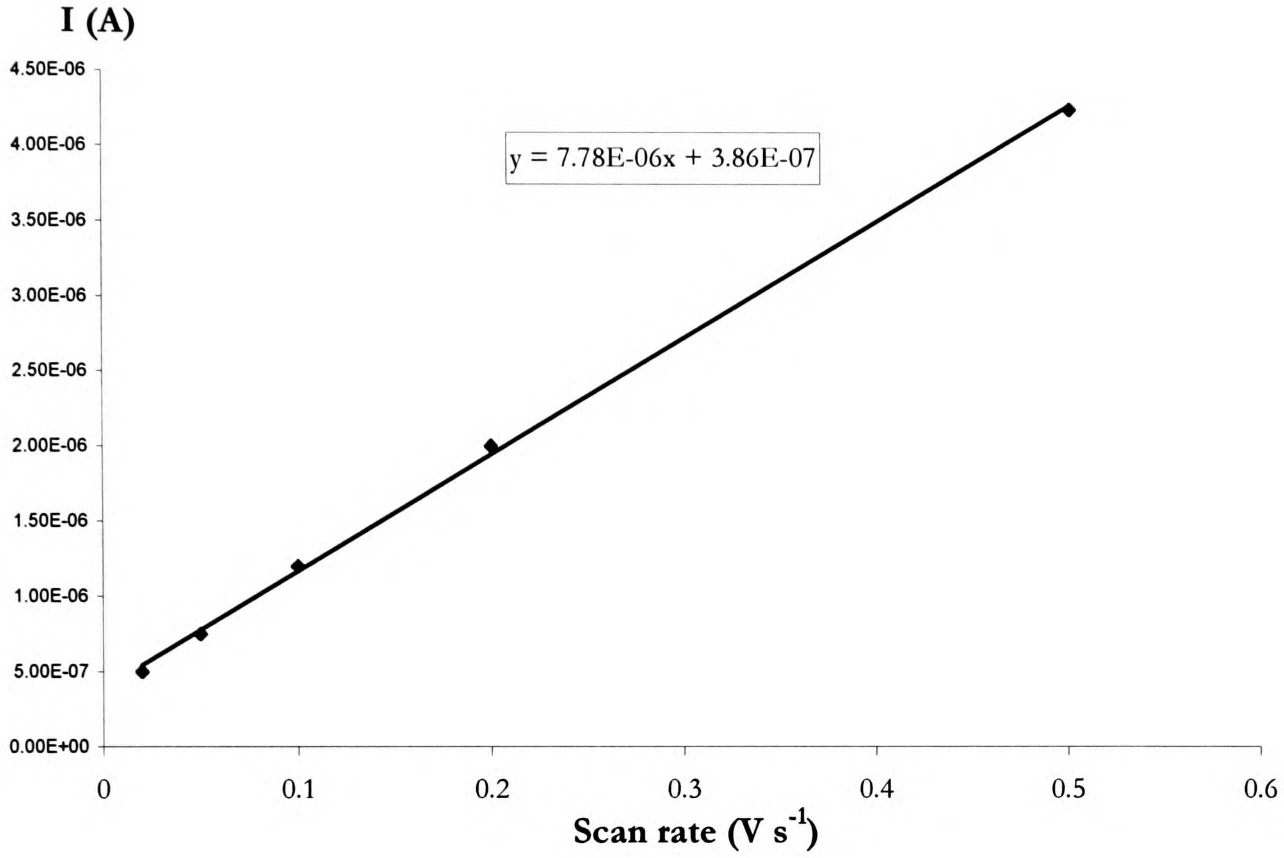

Figure 6.3: Capacitative current versus scan rate for a background solution of DMF and 0.1 M NBu_4ClO_4

Since:

$$C = \frac{q}{V} \tag{6.1}$$

where C corresponds to capacitance, q refers to charge and V denotes potential,

$$C\frac{\partial V}{\partial t} = \frac{\partial q}{\partial t} = I. \tag{6.2}$$

Thus capacitance can be estimated from the plot of current versus scan rate shown in Figure 6.3 as being approximately 7.8 μF. Given that a 3 mm diameter electrode was used during this investigation, this corresponds to a capacitance charge of approximately 110 μF cm^2. However, we note that capacitance will alter upon addition of Bu^n-ZDTP to the solution particularly as deposition of material at the electrode surface occurs.

Since capacitative charging currents increase with scan speed, a cyclic voltammogram recorded at low scan rate, 20 mV s^{-1}, was used to calculate peak areas so as to reduce the capacitative contribution. A ratio of 1.3:1 was obtained for the charges of reduction and subsequent stripping processes. This suggests some inefficiency in the stripping process with incomplete removal of zinc from the electrode surface.

6.3.2.3 Platinum electrode substrate

A cyclic voltammogram obtained for a 1 mM Bu^n-ZDTP solution at the platinum electrode is shown in Figure 6.4. Chemically irreversible oxidation of the complex is observed at +0.81 V versus SCE. Peak potential and chemical irreversibility of the oxidation process correlate with observations made using the glassy carbon electrode. In contrast, the reduction of Bu^n-ZDTP at platinum is noticeably different to that observed on glassy carbon. The characteristic current-loop of an overpotential driven nucleation process is in this instance absent. Furthermore, the single reduction peak ascribed to the reduction of Bu^n-ZDTP on glassy carbon is not apparent. Instead we note a broad reduction wave located in the potential envelope −0.6 to −1.1 V versus SCE together with a small sharp wave at −1.34 V versus SCE. Stripping of material from the electrode surface is visible upon scan reversal. However, a series of stripping peaks are observed at −0.94, −0.17 and +0.1 V versus SCE which lack the intensity and definition of the single stripping peak visible on glassy carbon.

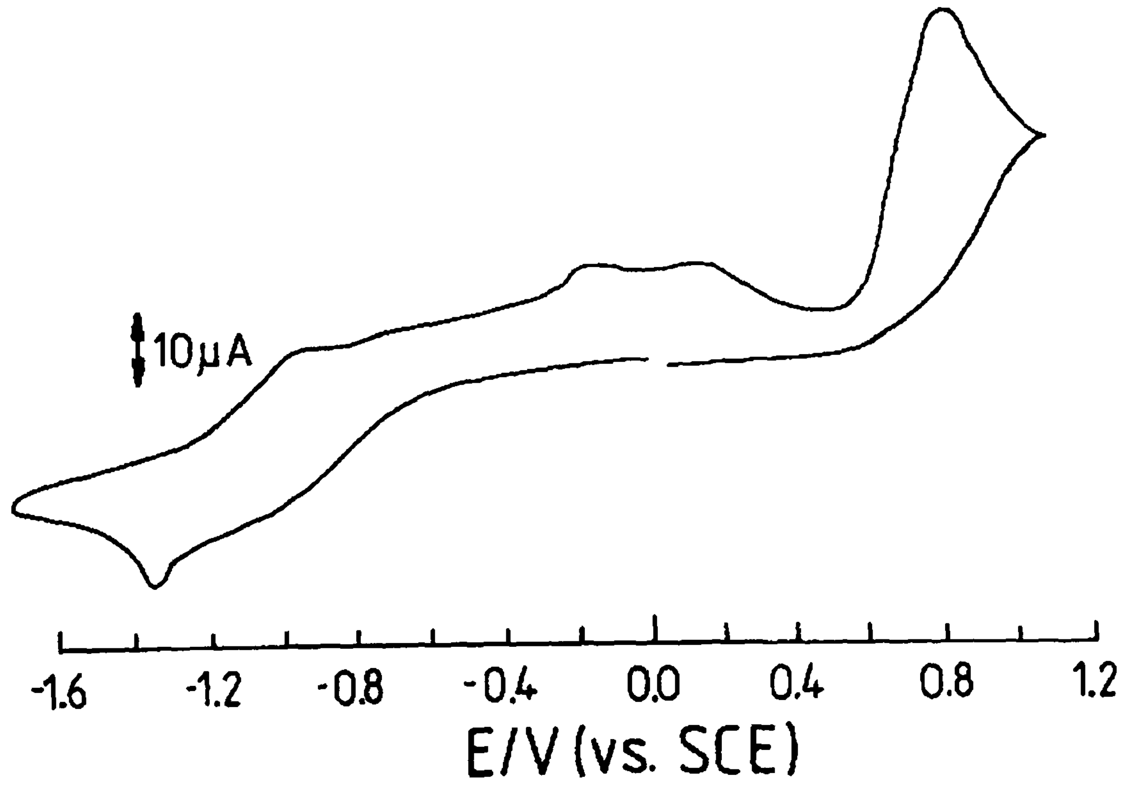

Figure 6.4: Cyclic voltammogram for 1 mM Bu^n-ZDTP in DMF/0.1 NBu_4ClO_4 solution recorded at a 4 mm diameter platinum electrode at 25 °C, scan rate 50 mV s^{-1}.

We first consider the origin of the broad signal observed at −0.6 to −1.1 V versus SCE. Given the broadness of the peak, we suggest that it is unlikely to arise from bulk deposition of material at the platinum surface. It is possible that the peak arises from zinc interaction with the platinum surface prior to the onset of bulk Bu^n-ZDTP deposition. This may either be as a result of zinc-platinum alloy formation or due to underpotential deposition (UPD) of zinc on platinum. UPD refers to the deposition of metal atoms onto a foreign metal substrate material at potentials positive of the thermodynamic reduction potential [9]. Generally speaking, UPD is limited to monolayer coverage although it can extend to two or three monolayers. Deposition of greater amounts leads to the formation of a bulk metal phase with a corresponding shift in peak position to the normal equilibrium potential. The phenomenon is explained by the existence of stronger attractive forces between atoms of the depositing material and foreign atoms of the substrate than between like atoms of the bulk metal [9].

Broadness of the peak in both instances would arise from interaction of zinc with different sites on the polycrystalline platinum surface. Rodriguez and Kuhn used X-ray photoelectron spectroscopy to investigate alloy formation in the zinc-platinum system [10]. During their investigation these workers deposited zinc vapour on platinum surfaces which were subsequently annealed at varying temperatures. The effect of annealing temperature on zinc and platinum binding energies was monitored. These workers concluded that zinc-platinum alloy formation only occurs at temperatures above 400 ^{0}C. Since our investigation was carried out at 25 ^{0}C, alloy formation will not feature in zinc deposition. We therefore attribute the broad peak at −0.6 to −1.1 V to UPD of zinc at the platinum surface.

The theoretical charge associated with the deposition of a monolayer of material was calculated from the atomic radius of zinc using Nicholson's method based on the assumption of a square lattice of material on the electrode surface [11]. For the geometrical area of the electrode used during this investigation, monolayer deposition was calculated as equivalent to 36 μC. For comparison, an estimate of the experimental charge associated with the reduction peak was made by integration of the peak within the potential window −0.6 to −1.1 V. From this, a charge equivalent of 53.6 μC was obtained. However, we note considerable error inherent in this procedure. Our calculation made no account of electrode roughness, as included during calculations of charge for other UPD processes by a number of workers [12]. The contribution from double layer charging was also neglected during this calculation. In addition, the choice of the potential envelope over which current integration is performed is subjective leading to some inaccuracy in the UPD charge obtained. We conclude that the peak observed corresponds to deposition of approximately a monolayer of material and certainly less than two monolayers consistent with a UPD process.

Secondly, we consider the sharp peak located at −1.34 V versus SCE. We note that peak potential is almost identical to that observed for zinc nucleation at the glassy carbon surface. Furthermore, the wave is steep which we have noted to be characteristic of a nucleation driven process. It is probable that the current-loop is masked by the UPD peak. It therefore seems likely that some nucleation of zinc on platinum occurs but that this process is less favourable on platinum in comparison to glassy carbon. The assignment of this peak as a nucleation process is investigated further in §6.3.2.4 to 6.3.2.6 with the application of cyclic voltammetry at variable concentration, variable scan speed and multiple scan cyclic voltammetry respectively.

We now consider stripping of zinc from the platinum surface. We noted the presence of three stripping signals located at peak potentials of −0.94, −0.17 and +0.1 V versus SCE. The signal at −0.94 V occurs at a potential almost identical to the removal of nucleated zinc from the glassy carbon electrode. This further suggests zinc nucleation at the platinum surface. We attribute the remaining stripping peaks to removal of underdeposited material from the platinum substrate. Since two stripping peaks are visible, we would also expect two peaks correlating to zinc UPD. In this instance, it is probable that both UPD peaks are contained within the potential window of the broad stripping signal observed.

Kolb et al correlated the underpotential shift, ΔE_p, to the difference in work functions of depositing metal and substrate material during a detailed survey of 30 couples in both aqueous and non-aqueous media [13]. ΔE_p is measured experimentally as the potential difference between bulk and UPD stripping processes. These workers found that ΔE_p, which serves as a measure of the difference between adatom-substrate and adatom-adatom interaction energies, varied linearly with the difference between work functions of the metal substrate material, φ_s, and electrodeposited metal, φ_m, according to the empirical expression:

$$\Delta E_p \approx \tfrac{1}{2}(\varphi_s - \varphi_m). \tag{6.3}$$

In the case of multiple oxidation peaks in the underpotential region, ΔE_p is taken as the potential difference between the bulk and most positive underpotential stripping signals. A value of 0.96 V was observed for the underpotential shift of zinc on platinum during the present work. A theoretical value of 0.78 V was calculated using the above correlation on the basis of work functions reported by Michealson [14].

Our experimental value of ΔE_p is consistent with values of ΔE_p reported during previous studies of zinc deposition on platinum. Hussey et al report ΔE_p to be 0.85 V during deposition of zinc from a room temperature molten salt [8]. Aramata et al report underpotential shifts ranging from 0.9 to 1.19 V during the reduction of zinc in aqueous media using a variety of supporting electrolytes and at varying pH [15]. Thus the anomalously high ΔE_p observed experimentally is seen to be a typical feature of zinc UPD on platinum. The excellent agreement observed with previous literature investigations gives credence to the assignment of these peaks as a UPD process.

Deposition of zinc at a platinum substrate has been reported by a number of workers. Studies have been confined to aqueous media together with one example of zinc deposition from a room temperature molten salt. This study therefore represents one of the first investigations of zinc deposition at a platinum electrode in non-aqueous media.

Despic and Pavlovic report the deposition of zinc from a buffered zinc sulphate solution [16]. These workers noted two broad reduction peaks located at –0.42 and –0.8 V versus SCE. These were attributed to zinc UPD and zinc-platinum alloy formation respectively. However, given the above discussion it seems likely that both peaks correspond to UPD processes. Bulk zinc deposition is observed at –1.03 V versus SCE. Upon scan reversal, reoxidation of bulk deposited material occurs at –1.0 V versus SCE. Reoxidation of underdeposited zinc material is observed at –0.9 V and +0.05 V versus SCE.

Aramata et al confined their study of zinc deposition to the UPD region. These workers report a number of zinc deposition studies using a variety of supporting electrolytes at different pHs and in some cases in the presence of added anions [17,18,19,20]. Two deposition and subsequent stripping peaks were observed in each case but peak potentials were noted to vary according to the conditions employed. This reflects the significance of solvent, electrolyte, anion and cation interaction at the electrode surface during the UPD process.

Hussey and Pitner investigated the deposition of electrogenerated Zn^{2+} from the room temperature molten salt aluminium chloride 1-methyl-3-ethylimidazolium chloride using cyclic and RDE voltammetry [8]. Two UPD waves were observed at +1.19 and +1.02 V versus an aluminium wire prior to the onset of bulk deposition at +0.17 V. Upon scan reversal, stripping of the bulk deposited zinc was observed at +0.36 V with subsequent removal of underdeposited material at +1.12 and +1.23 V. The presence of two zinc UPD peaks in each instance is consistent with the observations of the present study.

6.3.2.4 Cyclic voltammetry of Bu^n-ZDTP at variable scan speed

The cyclic voltammetry of a 1 mM Bu^n-ZDTP solution was recorded at decreased scan rates using both glassy carbon and platinum electrodes.

6.3.2.4a Glassy carbon

A cyclic voltammogram recorded for a 1 mM solution of Bu^n-ZDTP at a glassy carbon surface using a scan rate of 20 mV s^{-1} is shown in Figure 6.5. A shifting of oxidation and reduction peaks to more negative and positive values respectively is noted with decreasing scan speed. In the case of Bu^n-ZDTP oxidation, this reflects the chemically irreversible nature of the oxidation process and may also correlate to a degree of electrochemical irreversibility. For Bu^n-ZDTP reduction, this is consistent with a nucleated process where deposition of material can occur at less negative potentials over the longer timescale of the experiment. A slight shift of the stripping signal to more positive peak potential with decreasing scan speed is also noted. This probably correlates to the removal of larger quantities of material from the electrode surface.

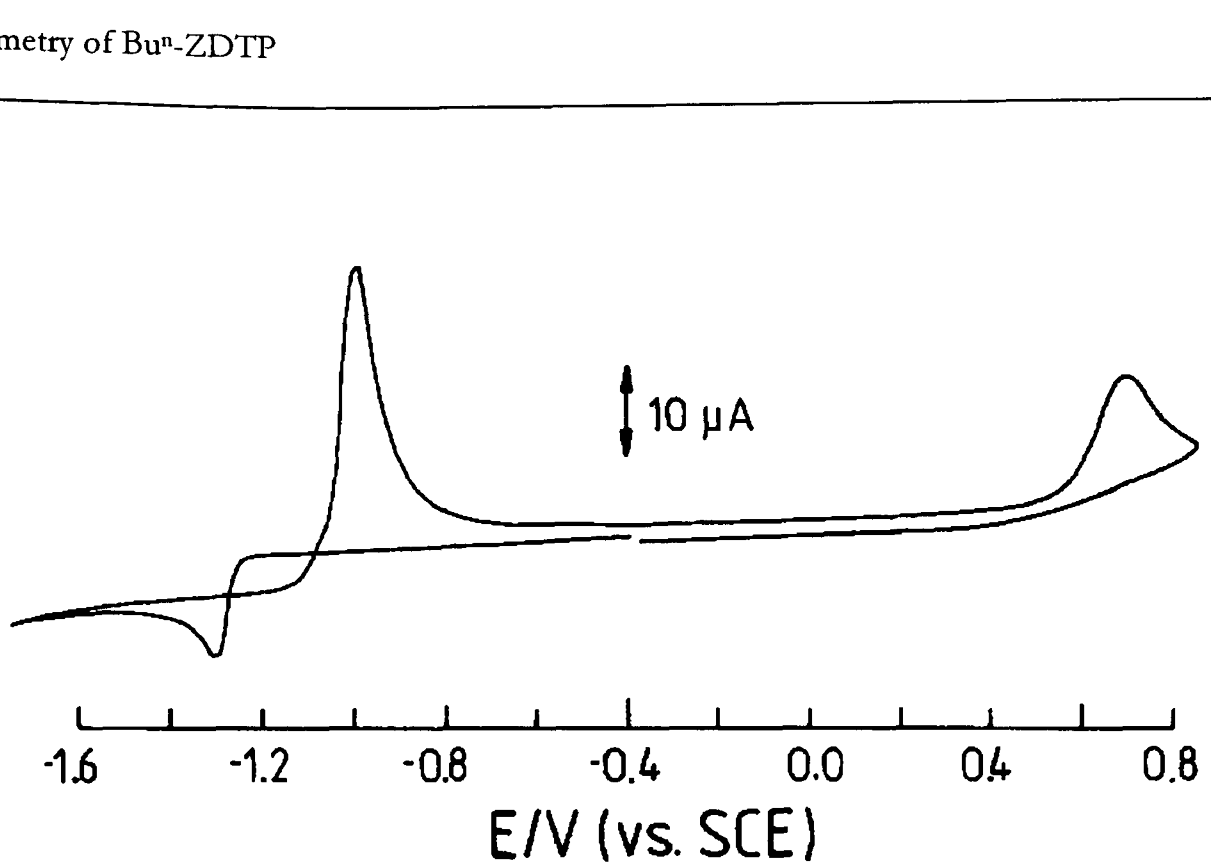

Figure 6.5: Cyclic voltammogram for 1 mM Bu^n-ZDTP in DMF/0.1 NBu_4ClO_4 solution recorded at a 3 mm diameter glassy carbon electrode at 25 °C, scan rate 20 mV s^{-1}.

6.3.2.4b Platinum

Cyclic voltammograms recorded for a 1 mM solution of Bu^n-ZDTP on platinum at scan rates of 20 and 10 mV s^{-1} are shown in Figures 6.6.a and b respectively. A shifting of the oxidation peak potential to more negative values with decreasing scan rate is apparent. As for glassy carbon, this reflects the chemically irreversible nature of the oxidation process and may also correlate to some degree of electrochemical irreversibility.

The reduction signal at –1.34 V versus SCE becomes markedly more defined as scan rate is decreased. In addition, a more well-defined stripping signal is observed at –0.9 V with decreasing scan speed. This is contrary to what we would expect for a diffusion controlled electron transfer process where peak current is correlated to the square root of scan speed as described in §6.3.2.1. These observations lend support to the theory that bulk deposition of zinc on platinum proceeds via overpotential driven nucleation but that the process is less favourable on platinum in comparison to glassy carbon. Increased nucleation is observed with decreasing scan rate since it is possible for a larger number of active nuclei to form over the longer timescale of the experiment. As noted in §6.3.2.3, the characteristic current-loop of the nucleated process appears to be masked in these voltammograms by the UPD peak. As observed for glassy carbon, a shift of the reduction signal to more positive potentials is observed with decreasing scan speed. The UPD of zinc on platinum is apparent in both voltammograms as a broad wave in the potential region –0.6 to –1.1 V versus SCE.

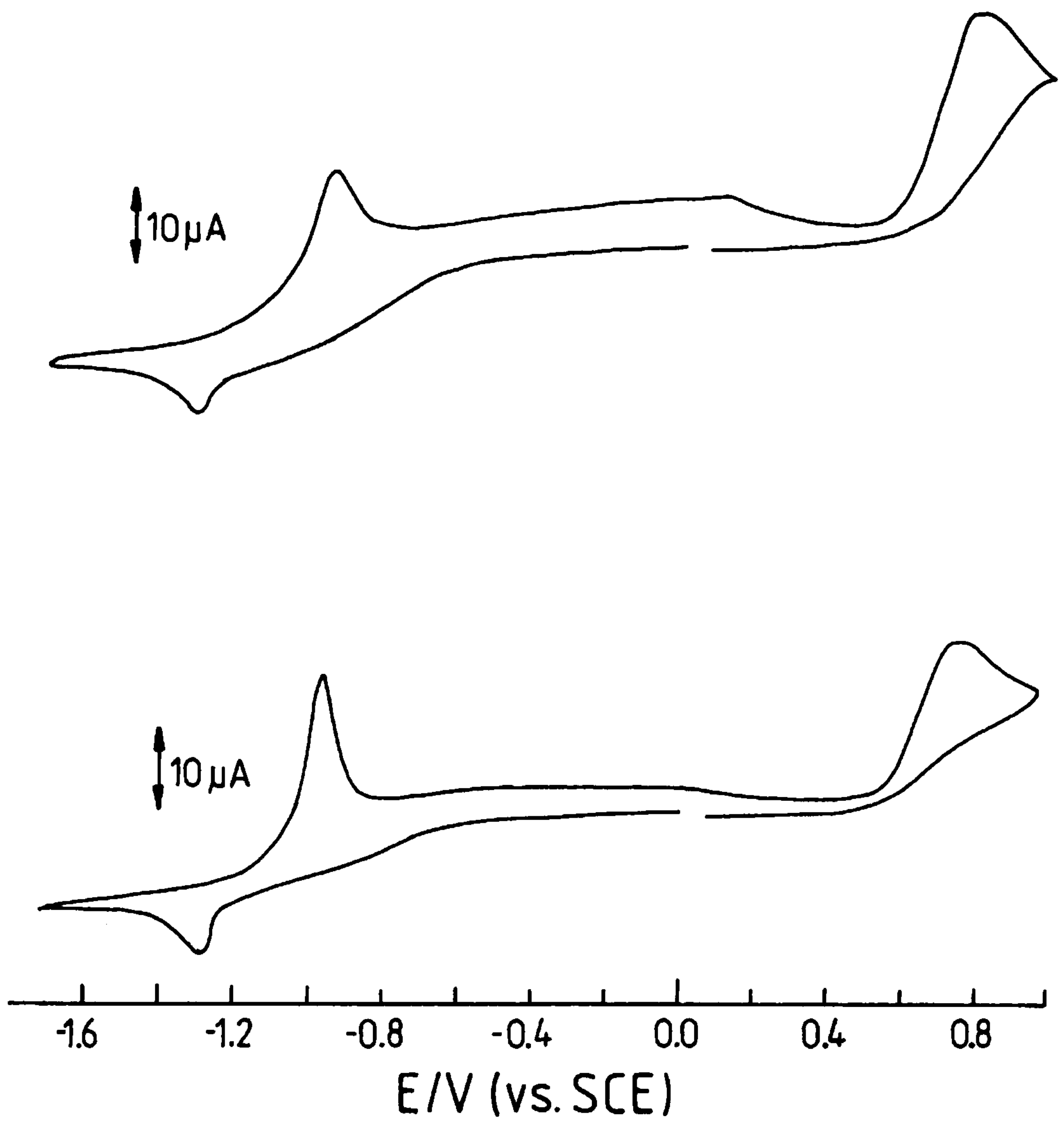

Figure 6.6: Cyclic voltammograms for 1 mM Bu^n-ZDTP in DMF/0.1 NBu_4ClO_4 solution recorded at a 4 mm diameter platinum electrode at 25 °C using scan rates of (a) 20 and (b) 10 mV s^{-1}.

6.3.2.5 Cyclic voltammetry of Bu^n-ZDTP at increased concentration

The cyclic voltammetry of a 5 mM Bu^n-ZDTP solution was recorded at a scan rate of 50 mV s^{-1} using both glassy carbon and platinum surfaces.

6.3.2.5a Glassy carbon

The cyclic voltammogram obtained at a glassy carbon electrode is shown in Figure 6.7. The peak corresponding to zinc nucleation is shifted to a more negative potential of –1.5 V versus SCE. Similarly, the stripping signal is now shifted to a more positive potential of –0.86 V versus SCE. This correlates to the increased energy required to remove the larger quantity of zinc from the electrode surface. In addition, we observe the stripping signal to be more rounded in nature attributable to the removal of a greater volume of zinc from the electrode surface. Increased asymmetry of the stripping peak is also apparent with a significantly greater following "tail". This may suggest increased inefficiency of the stripping process as the quantity of zinc increases.

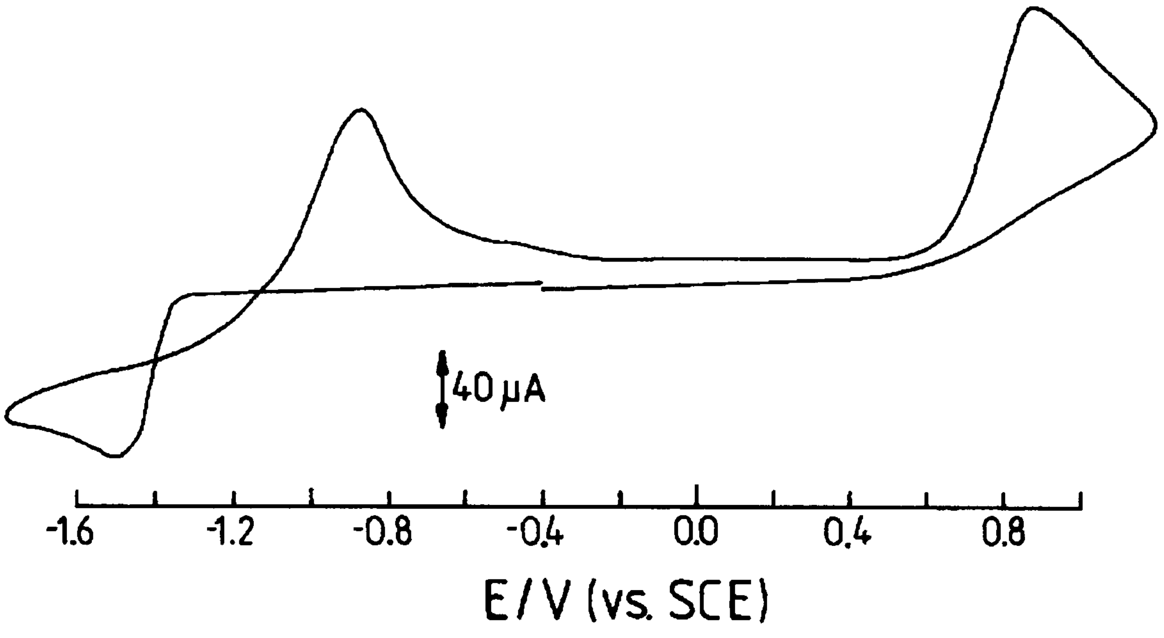

Figure 6.7: Cyclic voltammogram for Bu^n-ZDTP (5 mM) in DMF/0.1 NBu_4ClO_4 solution recorded at a 3 mm diameter glassy carbon electrode at 25 °C, scan rate 50 mV s^{-1}.

6.3.2.5b Platinum

The voltammogram obtained at the platinum surface is shown in Figure 6.8. With increased Bu^n-ZDTP concentration, nucleation of zinc on platinum is evident with the current-loop characteristic of a nucleated process clearly visible. It appears that nucleation is facilitated on the more hostile platinum surface at an increased Bu^n-ZDTP concentration since a greater number of zinc nuclei are able to form as the nucleation overpotential is reached. Reduction of zinc is observed as a sharp peak at −1.4 V versus SCE. Occurrence of this peak at a potential similar to the poorly defined reduction peak at lower Bu^n-ZDTP concentration supports the previous assignment of this wave as a nucleation type process. Stripping of nucleated zinc from the platinum surface is observed at −0.82 V versus SCE. As in the case of glassy carbon, the peak appears rounded with a following "tail" which may suggest some inefficiency in the zinc stripping process

The UPD signal remains evident in the voltammogram recorded for 5 mM Bu^n-

ZDTP. The charge associated with the UPD process was estimated by integration of the peak current to be 127 μC. This is consistent with a UPD process in which deposition of material is normally considered to correspond to monolayer coverage but can extend to two or three monolayers of material. Stripping peaks correlating to the removal of underdeposited material are superimposed onto the bulk stripping tail at −0.3 and +0.2 V versus SCE.

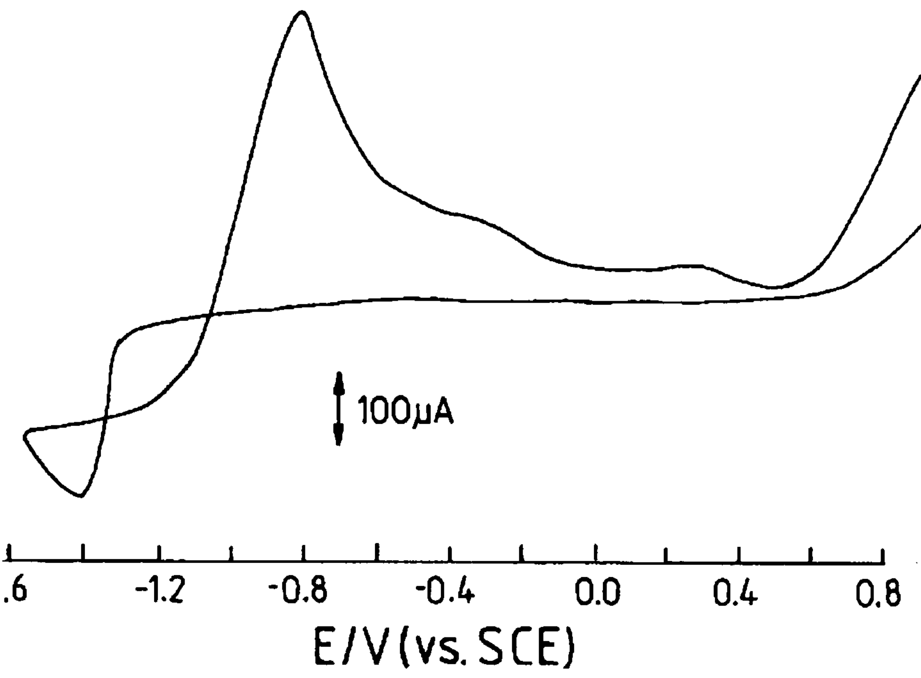

Figure 6.8: Cyclic voltammogram for Bu^n-ZDTP (5 mM) in DMF/0.1 NBu_4ClO_4 solution recorded at a 4 mm diameter platinum electrode at 25 °C, scan rate 50 mV s^{-1}.

6.3.2.6 Multiple scan cyclic voltammetry of Bu^n-ZDTP

Multiple scan cyclic voltammetry of the reductive region was carried out using a 1 mM Bu^n-ZDTP solution as a means of investigating the zinc nucleation process further. Voltammograms were recorded at 50 mV s^{-1} scan speed with the potential cycled repeatedly between 0 and −1.7 V versus SCE for both electrode substrate materials. Results obtained at glassy carbon and platinum electrode surfaces are shown in Figures 6.9.a and b respectively.

6.3.2.6a Glassy carbon

The voltammogram obtained at glassy carbon shows the characteristic nucleation and stripping signals noted previously. For the initial scan, labelled 1 in Figure 6.9.a, these occur at −1.34 and −0.88 V versus SCE respectively. With consecutive scans, the nucleation signal is observed to shift to more positive potentials. In addition, a slight decrease in the intensity of the nucleation signal with each scan is apparent. The stripping signal is also seen to decrease in intensity with consecutive scans. The decrease in stripping signal intensity is more marked than the decrease observed for the nucleation process. We are unable to unambiguously explain these observations but we suggest that passivation of the electrode surface may occur with time. This could arise due to incomplete stripping of zinc material from the electrode surface as reflected in the marked decrease in stripping charge with consecutive scans. Passivated sites may aid nucleation on consecutive scans resulting in the shift of zinc nucleation to more positive potentials as noted. Furthermore, the slight decrease in nucleation current may reflect a lowering of surface activity as a result of passivation.

6.3.2.6b Platinum

The voltammogram obtained at platinum shows the features previously described for cyclic voltammetry of 1 mM Bu^n-ZDTP at 50 mV s^{-1} during the initial scan, labelled 1 in Figure 6.9.b. A wave corresponding to UPD in the potential region −0.6 to −1.1 V together with a poorly-defined nucleation peak at −1.38 V and stripping signals at −0.92 and −0.16 V versus SCE are visible. For the second and subsequent scans, the UPD signal decreases in intensity whereas nucleation and stripping signals become considerably more well-defined. As for glassy carbon, the nucleation peak shifts to more positive potentials with each cycle. On platinum, in contrast to the case for glassy carbon, the intensity of both the nucleation and corresponding stripping signal increases with consecutive scans. However, the characteristic current-loop of the zinc nucleation process remains masked by the UPD peak. We suggest that on platinum, where nucleation does not occur as readily as for glassy carbon, deposition is enhanced by particles of material on the electrode surface which act as nucleation sites. The positive shift of nucleation peak current is also a reflection of the increasing ease with which material can nucleate onto the electrode surface. We are unable to explain the decreased UPD signal observed. However, this may be attributable to blocking of the surface during the passivation process which therefore restricts the available surface area at which UPD can occur.

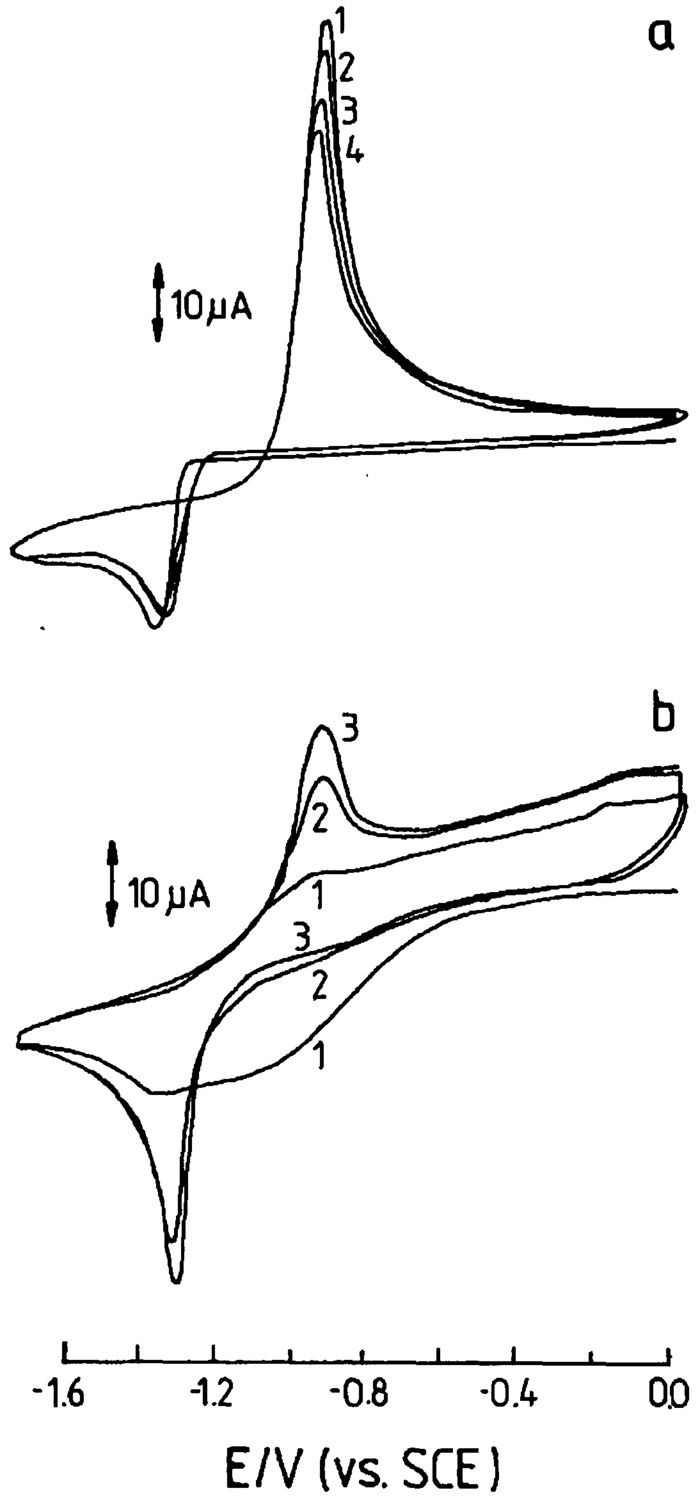

Figure 6.9: Multiple scan cyclic voltammetry of 1 mM Bu^n-ZDTP in DMF/0.1 NBu$_4$ClO$_4$ solution recorded at (a) 3 mm diameter glassy carbon and (b) 4 mm platinum electrodes at 25 °C, scan rate 50 mV s^{-1}.

6.4 RDE voltammetry of Bu^n-ZDTP

6.4.1 Experimental

RDE voltammetric investigations of Bu^n-ZDTP redox activity were conducted using identical experimental conditions to those described for cyclic voltammetric investigation in §6.3.1. Glassy carbon and platinum rotating disc electrodes were used with nominal electrode diameters of 3 and 7 mm respectively. Throughout our investigation, RDE experiments were performed using a scan rate of 5 mV s^{-1}. Rotation rates ranging between 5 and 30 Hz were employed. Waves were recorded by initially scanning positively from 0 V. Upon completion of the positive scan the electrode potential was returned to 0 V and the electrode surface polished to remove any deposited material prior to the reductive scan. The solvent background was measured for each electrode substrate material at rotation rates employed during the investigation. In this manner, limiting currents measured experimentally were corrected for background effects. Voltammograms were obtained initially using a Bu^n-ZDTP concentration of 1 mM and the results obtained for each of the two electrode substrate materials compared. Subsequent investigations were performed using an increased Bu^n-ZDTP concentration of 5 mM.

6.4.2 Results and Discussion

6.4.2.1 Glassy carbon electrode

A representative wave recorded for 1 mM Bu^n-ZDTP using a glassy carbon electrode surface at a rotation speed of 30 Hz is shown in Figure 6.10. A single wave corresponding to Bu^n-ZDTP oxidation is observed with an $E_{1/2}$ of +0.78 V versus SCE. Bu^n-ZDTP reduction comprises a single wave with an $E_{1/2}$ value of –1.3 V versus SCE. The initial steepness of the reduction signal is consistent with an overpotential driven nucleation process where rapid deposition is possible following the initial nucleation of growth sites. Limiting currents obtained at each rotation speed are shown in Table 6.1. I_{lim} values are an average of 3 steady state waves recorded at each rotation speed.

Wave-shape analysis of the Bu^n-ZDTP oxidation wave was carried out using the general current-potential relationship for a reversible wave denoted in Equation 2.29. As previously described in §2.5.3, the slope of E versus $\log(I_{lim}/I-1)$ is indicative of the electrochemical reversibility of the redox process. Figure 6.11 shows E versus $\log(I_{lim}/I-1)$ for the wave obtained at 30 Hz. The slope of 123 ± 8 mV obtained in this instance suggests that, in addition to the chemically irreversible nature of the oxidation process previously deduced during cyclic voltammetric investigation, the oxidation of Bu^n-ZDTP is also electrochemically irreversible.

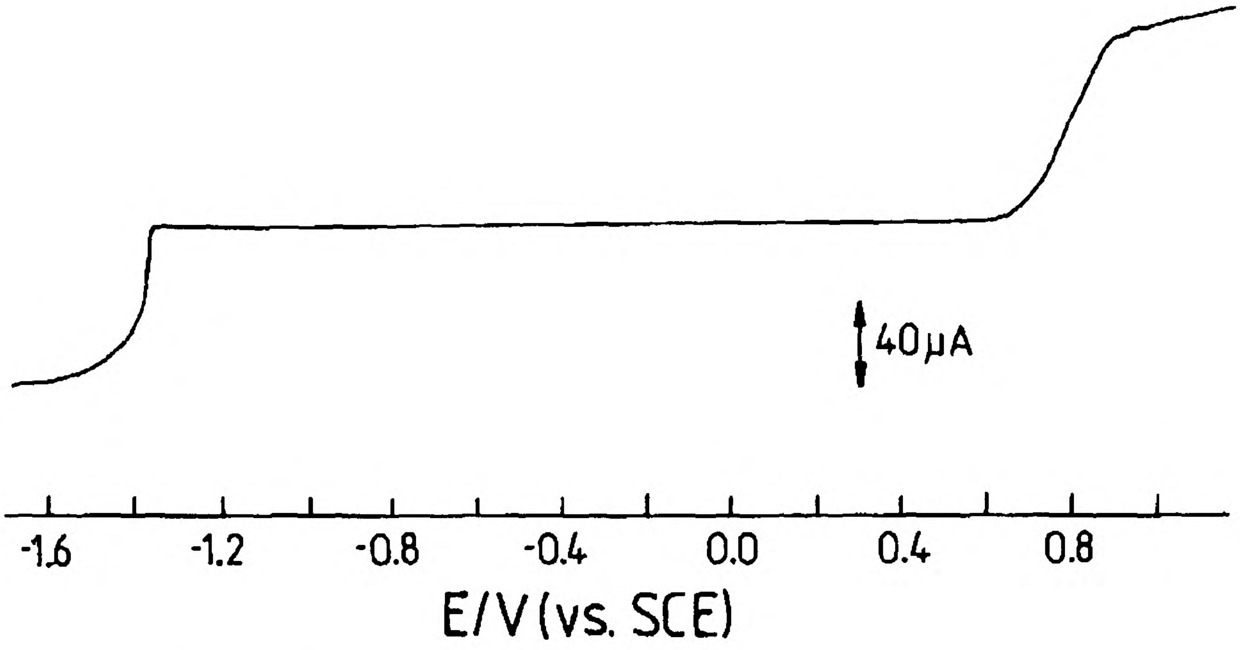

Figure 6.10: Steady state voltammogram for 1 mM Bu^n-ZDTP in DMF/0.1 NBu_4ClO_4 solution recorded during RDE voltammetry at a 3 mm diameter glassy carbon electrode at 25 °C using a rotation speed of 30 Hz and scan rate of 5 mV s^{-1}.

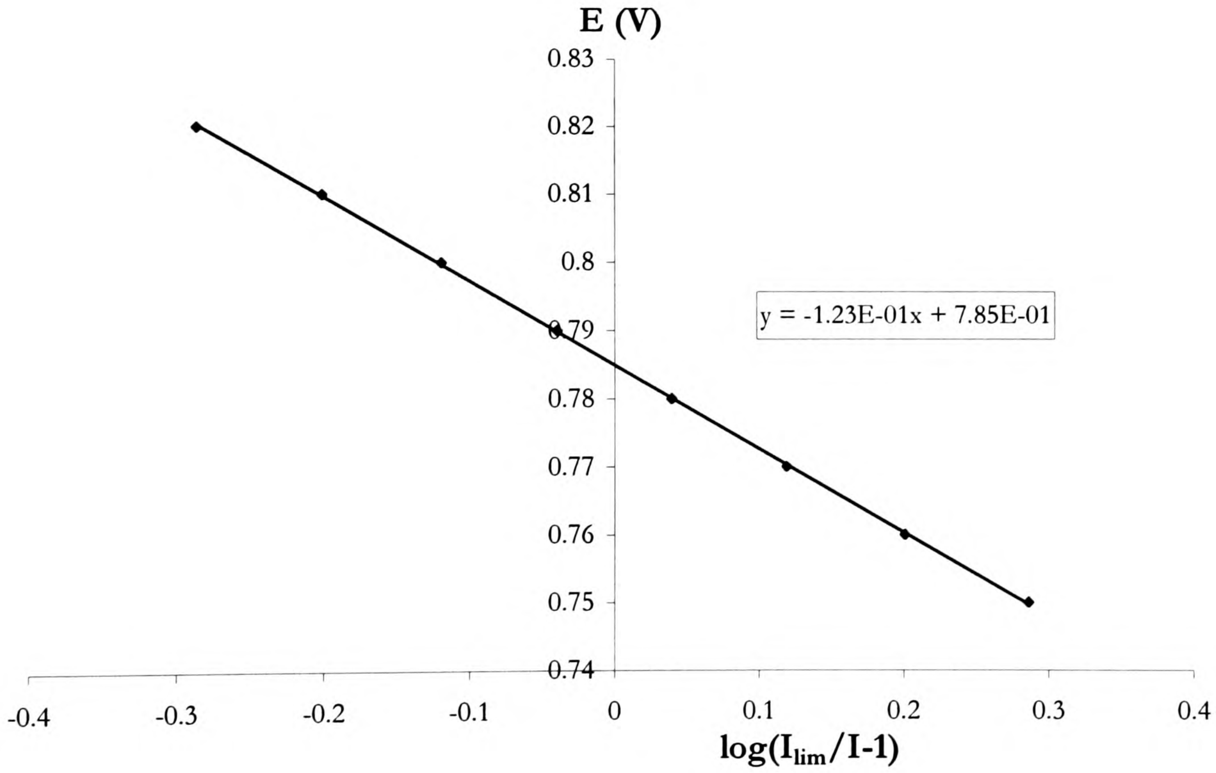

Figure 6.11: E versus log(I_{lim}/I–1) for a steady state voltammogram recorded for 1 mM Bu^n-ZDTP in DMF/0.1 NBu_4ClO_4 solution during RDE voltammetry at a 3 mm diameter glassy carbon electrode at 25 °C using a rotation speed of 30 Hz and scan rate of 5 mV s^{-1}

6.4.2.2 Platinum electrode

A representative wave recorded for 1 mM Bu^n-ZDTP using a platinum electrode surface at a rotation speed of 30 Hz is shown in Figure 6.12. A single wave corresponding to Bu^n-ZDTP oxidation is observed with an $E_{1/2}$ of +0.78 V versus SCE. Bu^n-ZDTP reduction comprises a well-defined wave with an $E_{1/2}$ value of –1.32 V versus SCE attributable to zinc nucleation at the electrode surface. Limiting currents obtained at each rotation speed are shown in Table 6.1. I_{lim} values are an average of 3 steady state waves recorded at each rotation speed. Zinc nucleation on platinum is comparable to that observed for glassy carbon despite the greater hostility of platinum to zinc deposition. This reflects the decreased scan rate of the RDE experiment which allows sufficient time for zinc nuclei to form at the platinum surface once the nucleation overpotential is reached. This is in direct contrast to observations made during cyclic voltammetry of 1 mM Bu^n-ZDTP on platinum where the increased scan rate hindered the formation of growth centres. A broad wave is visible prior to the onset of bulk zinc deposition in the potential region –0.8 to –1.1 V versus SCE. This reflects UPD of zinc on platinum as noted during cyclic voltammetric investigation.

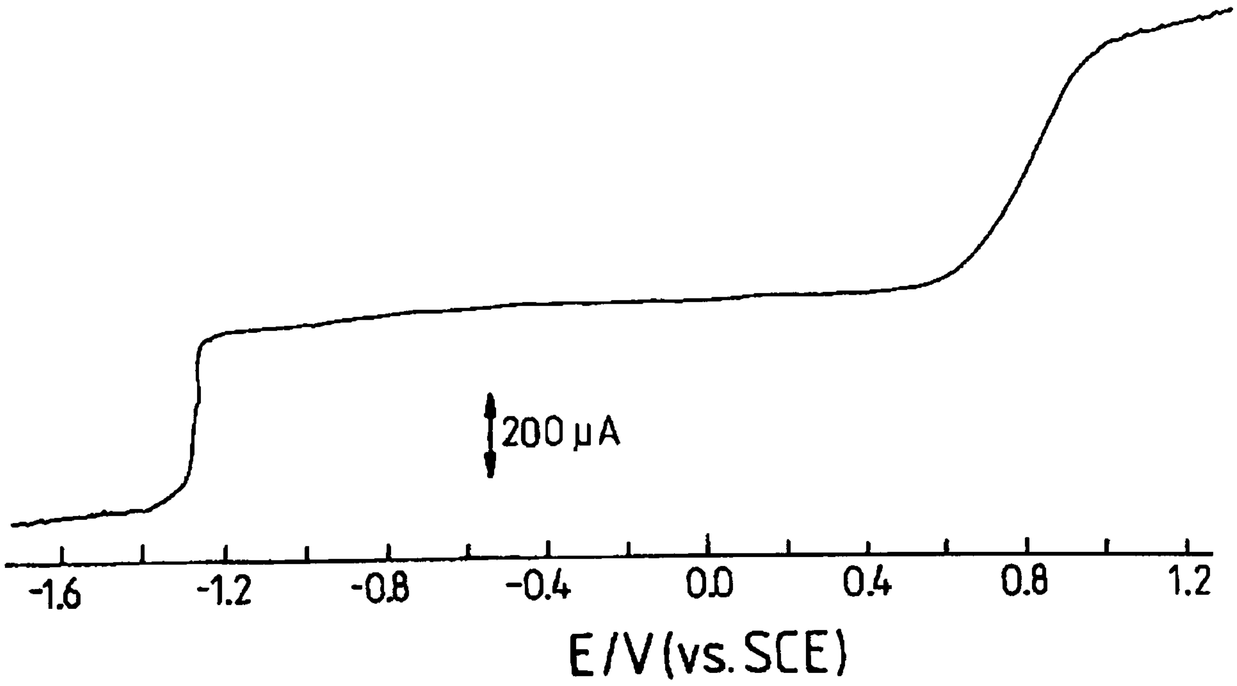

Figure 6.12: Steady state voltammogram for 1 mM Bu^n-ZDTP in DMF/0.1 NBu_4ClO_4 solution recorded during RDE voltammetry at a 7 mm diameter platinum electrode at 25 ^0C using a rotation speed of 30 Hz and scan rate of 5 mV s^{-1}.

6.4.2.3 Levich analysis

Plots showing limiting current versus the square root of rotation speed for Bu^n-ZDTP oxidation and reduction at both glassy carbon and platinum are shown in Figures 6.13.a and b respectively. Plots for both redox processes on each electrode substrate appear linear and are observed to pass through the origin in line with the Levich equation (Equation 2.28). This initially suggests electron transfer processes to be mass transport controlled without mechanistic complication at both electrode substrate materials.

However, we note in Figure 6.13 that for both electrode materials, there is some discrepancy in the slopes obtained for oxidation and reduction. The slope for Bu^n-ZDTP reduction lies below, and has a smaller gradient, than that of Bu^n-ZDTP oxidation. The slope ratios for oxidation:reduction processes are 1.33 and 1.26 on glassy carbon and platinum respectively.

We attribute the discrepancy in oxidation and reduction currents to the nucleation process. Deposition of material will be confined to active growth centres on the electrode surface. Furthermore, the concentration depletion around growing centres will reduce the probability of nucleation in the vicinity of each nucleus. Nucleation will therefore be confined to active centres that are not located within an existing exclusion zone. Since some of the surface area remains inactive during the reduction process, reduction currents obtained will be lower than those recorded for oxidation where the entire electrode area remains electroactive. Thus, the plot of I_{lim} versus $w^{1/2}$ cannot be viewed as a true Levich plot.

Good agreement is observed between the limiting currents measured for Bu^n-ZDTP oxidation at the glassy carbon and platinum surfaces upon taking into account differences in electrode area. The correlation between reduction data recorded at the two electrode materials is less precise reflecting the random nature of the nucleation process.

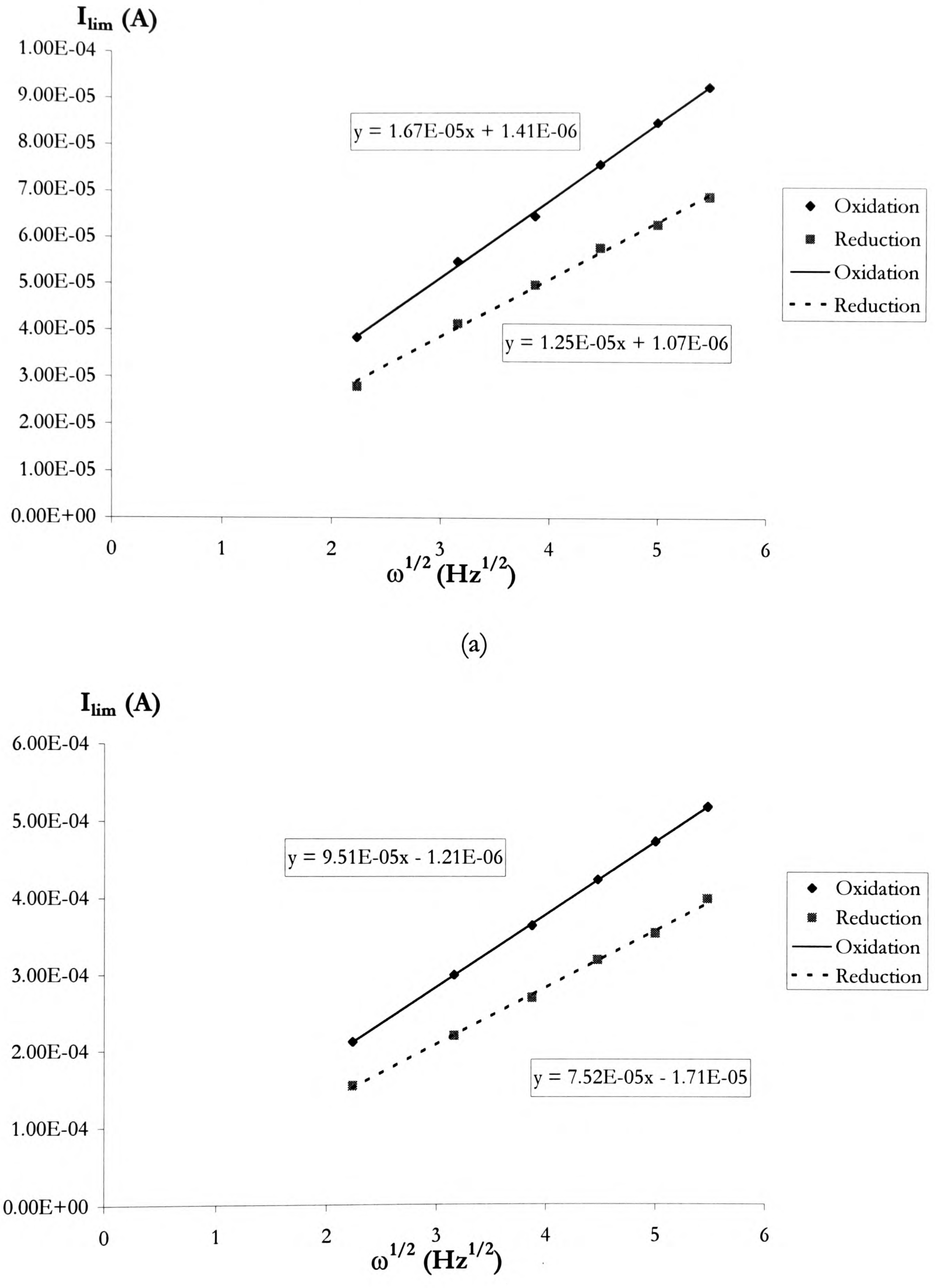

(a)

(b)

Figure 6.13: Limiting current versus square root of rotation speed for oxidation and reduction of 1 mM Bu^n-ZDTP in DMF/0.1 NBu$_4$ClO$_4$ solution during RDE voltammetry at (a) 3 mm diameter glassy carbon and (b) 7 mm diameter platinum electrodes at 25 ^{0}C, scan rate 5 mV s^{-1}.

6.4.2.4 RDE voltammetry at increased Bu^n-ZDTP concentration

RDE voltammetry was performed at both glassy carbon and platinum electrode surfaces using an increased Bu^n-ZDTP concentration of 5 mM. Voltammograms were similar in appearance to those previously observed for 1 mM Bu^n-ZDTP. Limiting currents recorded for each rotation rate at both electrode substrate materials are given in Table 6.1. I_{lim} versus $w^{1/2}$ for Bu^n-ZDTP oxidation and reduction at both glassy carbon and platinum are shown in Figures 6.14.a and b respectively. We note that upon comparison with plots for 1 mM Bu^n-ZDTP, the discrepancy between oxidation and reduction slopes is decreased. Ratios of 1.10 and 1.11 are obtained for the ratio of oxidation to reduction slopes on glassy carbon and platinum respectively. This reflects the increased number of nuclei that can deposit from a solution of higher concentration once the nucleation overpotential is reached.

Rotation speed (Hz)	Limiting current (A)							
	1 mM Bu^n-ZDTP				5 mM Bu^n-ZDTP			
	Glassy carbon		Platinum		Glassy carbon		Platinum	
	Oxidation	Reduction	Oxidation	Reduction	Oxidation	Reduction	Oxidation	Reduction
5	$3.85x10^{-5}$	$2.80x10^{-5}$	$2.12x10^{-4}$	$1.54x10^{-4}$	$1.47x10^{-4}$	$1.25x10^{-4}$	$9.20x10^{-4}$	$8.60x10^{-4}$
10	$5.50x10^{-5}$	$4.15x10^{-5}$	$3.00x10^{-4}$	$2.20x10^{-4}$	$2.25x10^{-4}$	$1.90x10^{-4}$	$1.28x10^{-3}$	$1.18x10^{-3}$
15	$6.48x10^{-5}$	$5.00x10^{-5}$	$3.65x10^{-4}$	$2.70x10^{-4}$	$2.85x10^{-4}$	$2.45x10^{-4}$	$1.62x10^{-3}$	$1.46x10^{-3}$
20	$7.60x10^{-5}$	$5.80x10^{-5}$	$4.25x10^{-4}$	$3.20x10^{-4}$	$3.35x10^{-4}$	$2.95x10^{-4}$	$2.00x10^{-3}$	$1.73x10^{-3}$
25	$8.50x10^{-5}$	$6.30x10^{-5}$	$4.75x10^{-4}$	$3.55x10^{-4}$	$3.75x10^{-4}$	$3.30x10^{-4}$	$2.13x10^{-3}$	$1.95x10^{-3}$
30	$9.23x10^{-5}$	$6.90x10^{-5}$	$5.20x10^{-4}$	$4.00x10^{-4}$	$4.15x10^{-4}$	$3.60x10^{-4}$	$2.38x10^{-3}$	$2.18x10^{-3}$

Table 6.1: *Limiting currents obtained for RDE voltammetry of a) 1 mM and b) 5 mM Bu^n-ZDTP in DMF/0.1 M NBu_4ClO_4 solution at glassy carbon and platinum electrodes with diameters of 3 and 7 mm respectively, temperature 25 ^{0}C, scan rate 5 mV s^{-1}*

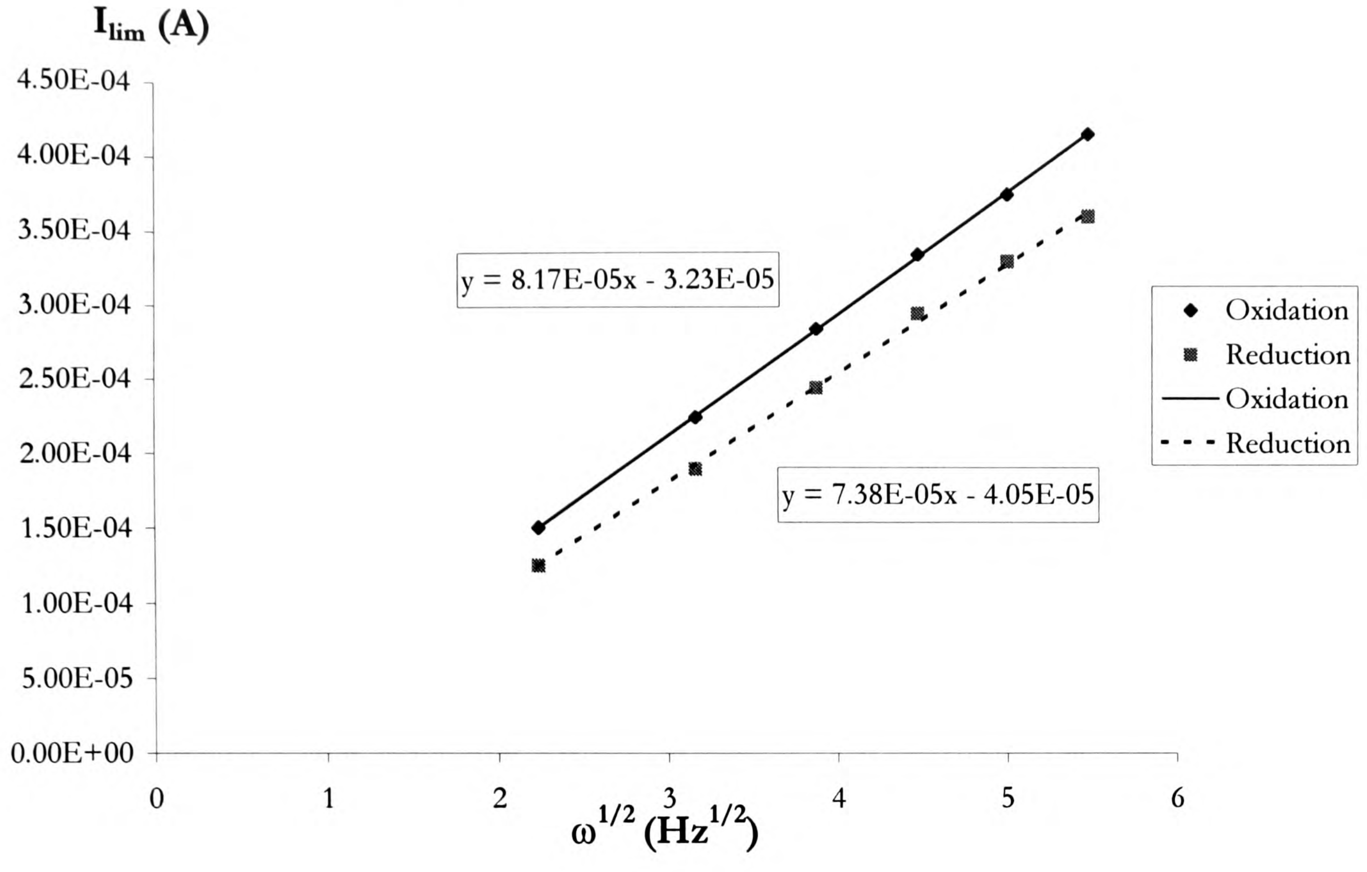

(a)

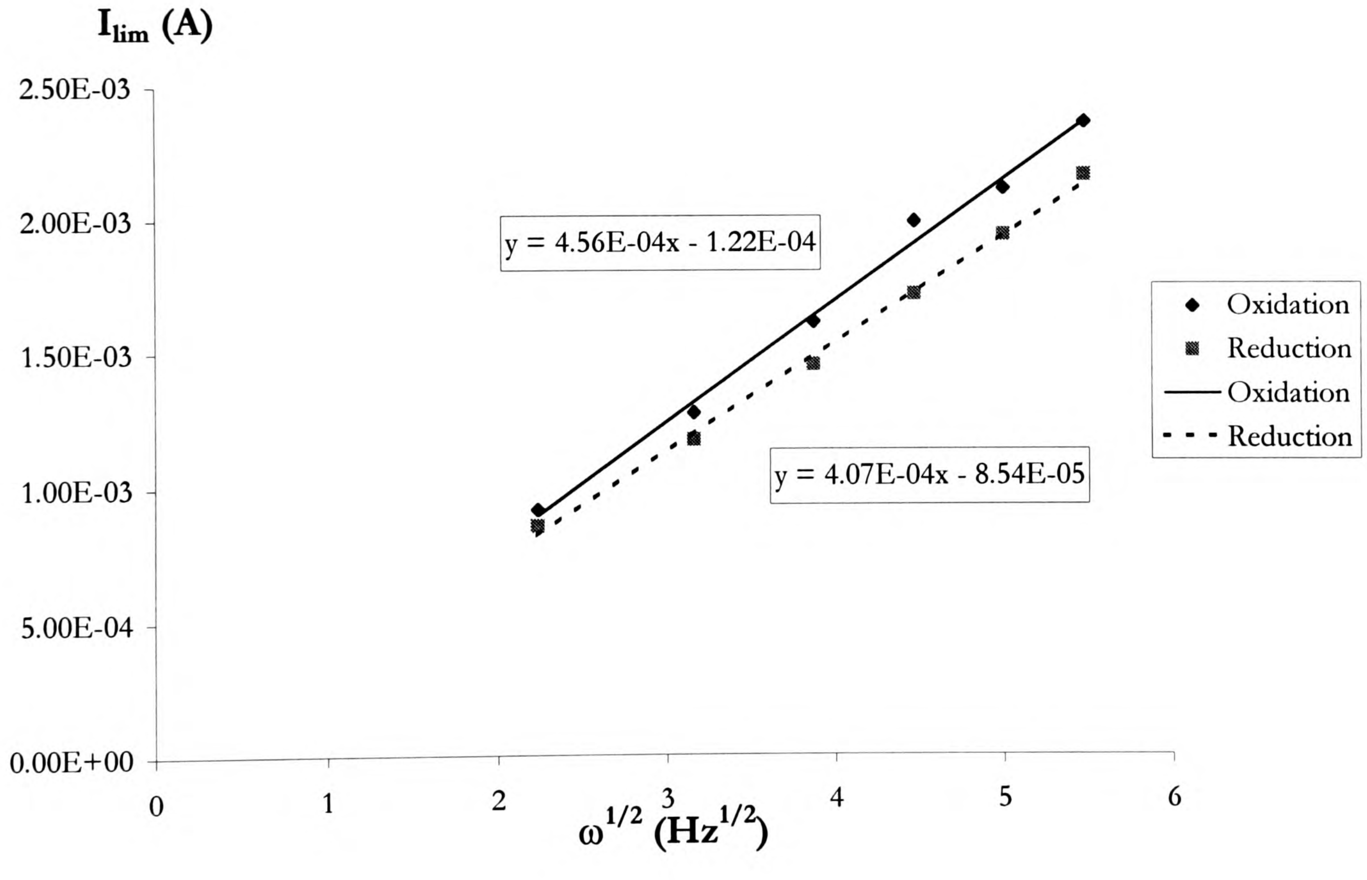

(b)

Figure 6.14: Limiting current versus square root of rotation speed for oxidation and reduction of 5 mM Bu^n-ZDTP in DMF/0.1 NBu_4ClO_4 solution during RDE voltammetry at (a) 3 mm diameter glassy carbon and (b) 7 mm diameter platinum electrodes at 25 °C, scan rate 5 mV s^{-1}.

6.4.2.5 Calculation of diffusion coefficients

As noted previously in §2.5.3, a value for the diffusion coefficient can be extracted from the slope of the Levich plot which is equivalent to:

$$\text{slope} = 1.554nFAD^{2/3}v^{-1/6}c. \qquad (6.4)$$

As described in §6.4.2.3, oxidation of Bu^n-ZDTP appears to conform to the Levich behaviour of a diffusion controlled process. This is supported by cyclic voltammetric investigation where a linear correlation between peak current and square root of scan rate was observed. Reduction data cannot be used for the calculation of the diffusion coefficient in this case since the electron transfer process is complicated by nucleation. Using the Levich plots shown in Figures 6.13.a and b and 6.14.a and b, the values of D calculated from 1 mM and 5 mM Bu^n-ZDTP solutions at both glassy carbon and platinum electrode substrate materials are recorded in Table 6.2.

Bu^n-ZDTP concentration (mM)	**Electrode substrate**	**D (cm^2 s^{-1})**
1	Glassy carbon	$6.67\text{x}10^{-6} \pm 0.5\text{x}10^{-6}$
	Platinum	$6.87\text{x}10^{-6} \pm 0.5\text{x}10^{-6}$
5	Glassy carbon	$6.53\text{x}10^{-6} \pm 0.5\text{x}10^{-6}$
	Platinum	$6.50\text{x}10^{-6} \pm 0.5\text{x}10^{-6}$

Table 6.2: Diffusion coefficients extracted from Levich plots for oxidation of (a) 1 and (b) 5 mM Bu^n-ZDTP in DMF/0.1 M NBu$_4$ClO$_4$ solution at glassy carbon and platinum electrode surfaces, temperature 25 °C, scan rate 5 mV s^{-1}

Wilke-Chang theory has previously been introduced in §5.2.4 as a theoretical basis for the estimation of diffusion coefficients in solution. Using the Wilke-Chang correlation, we estimate the diffusion coefficient of Bu^n-ZDTP in DMF solution to be $4.8\text{x}10^{-6}$ cm^2 s^{-1}. We note a good correlation between this value and the experimentally determined diffusion coefficients reported in Table 6.2 which were calculated assuming a 2 electron transfer process. Values in the region of $1.3\text{x}10^{-5}$ cm^2 s^{-1} are obtained if the oxidation step is assumed to be one electron. Since this is significantly larger than theory predicts, we propose an overall 2 electron process for the oxidation of Bu^n-ZDTP. This contrasts with the 1 electron transfer process proposed by Stezeryanskii et al for the oxidation of iso-octyl ZDTP [1]. We note that the only previously determined value of D in the case of a ZDTP compound was reported by these workers. Using cyclic voltammetry, Stezeryanskii et al determined the diffusion coefficient of iso-octyl ZDTP in DMF solution to be 5.6x10^{-5} cm^2 s^{-1}. On the basis of theoretical and experimental values determined for the diffusion coefficient of Bu^n-ZDTP during the present work, we suggest that the value reported by Stezeryanskii et al is unrealistically large. Values of D obtained at each of the two Bu^n-ZDTP concentrations using both glassy carbon and platinum electrodes are in good agreement.

6.5 Summary

Our investigation of Bu^n-ZDTP under standard electrochemical conditions is by far the most comprehensive voltammetric investigation of a ZDTP compound reported to date. During cyclic voltammetric investigation of Bu^n-ZDTP in DMF solution, we noted chemically irreversible oxidation of this species at both glassy carbon and platinum electrode surfaces. Peak current was observed to vary as the square root of scan rate indicative of a diffusion controlled process without mechanistic complication. Bu^n-ZDTP reduction proceeded via zinc nucleation at both electrode substrate materials with the platinum surface more hostile to zinc deposition than glassy carbon. In addition, the UPD of zinc material was apparent at the platinum electrode surface.

RDE voltammetric investigation of Bu^n-ZDTP at a glassy carbon electrode showed single waves for both the oxidation and reduction processes. A wave corresponding to UPD of zinc at the electrode surface was also apparent on platinum. Wave shape analysis of the Bu^n-ZDTP oxidation wave showed this process to be electrochemically irreversible. Plots for Bu^n-ZDTP oxidation and reduction at both glassy carbon and platinum surfaces showed the current for Bu^n-ZDTP reduction to be lower than that of oxidation. We attribute this to some inactivity in the electrode surface area during the zinc nucleation process. Since Bu^n-ZDTP oxidation has been shown to be under diffusion control without mechanistic complication, we used Levich analysis to derive a value of 6.7x10^{-6} ± 0.5x10^{-6} cm^2 s^{-1} for the diffusion of Bu^n-ZDTP in DMF solution. By correlation with Wilke-Chang theory, we propose a 2 electron transfer for the oxidation of Bu^n-ZDTP.

References

[1] E. A. Stezeryanskii, K. I. Litovchenko, V. S. Kublanovsky, J. Electroanal. Chem., 1995, **390**, 143

[2] R. L. Blankespoor, Inorg. Chem., 1985, **24**, 1126

[3] A. J. Bard, L. R. Faulkner, Electroanalytical Methods, Wiley, New York, 1980, p218

[4] A. M. Shafiqul Alam, J. M. Martin, Ph. Kapsa, Analytica Chemica Acta, 1979, **107**, 391

[5] M. J. Hutchings, G. J. Moody, J. D. R. Thomas, The Analyst, 1987, **112**, 601

[6] S. Fletcher, C. S. Halliday, D. Gates, M. Westcott, T. Lwin, G. Nelson, J. Electroanal. Chem., 1983, **159**, 267

[7] P. J. Sonneveld, W. Visscher, E. Barendrecht, Electrochimica Acta, 1992, **37**, 7, 1199

[8] W. R. Pitner, C. L. Hussey, J. Electrochem. Soc., 1997, **144**, 9, 3095

[9] A. R. Despic, Comprehensive Treatise of Electrochemistry, (eds. B. E. Conway, J. O'M Bockris, E. Yeager, S. U. M. Khan, R. E. White), Plenum Press, New York, 1983, p.451

[10] J. A. Rodriguez, M. Kuhn, J. Chem. Phys., 1995, **102**, 10, 4279

[11] M. M. Nicholson, J. Amer. Chem. Soc., 1957, **79**, 7

[12] V. A. Vicente, S. Bruckenstein, J. Electroanal. Chem., 1977, **82**, 187

[13] M. Kolb, M. Przasnyski, H. Gerischer, Electroanal. Chem., 1974, **54**, 39

[14] H. B. Michaelson, J. Appl. Phys., 1950, **21**, 536

[15] A. Aramata, M. A. Quaiyyum, W. A. Balais, T. Atoguchi, M. Enyo, J. Electroanal. Chem., 1992, **338**, 367

[16] A. R. Despic, M. G. Pavlovic, Electrochimica Acta, 1982, **27**, 11, 1539

[17] S. Taguchi, A. Aramata, M. A. Quaiyyum, M. Enyo, J. Electroanal. Chem, 1994, **374**, 275

[18] A. Aramata, S. Terui, S. Taguchi, T. Kawaguchi, K. Shimazu, Electrochimica Acta, 1996, **41**, 5, 761

[19] S. Taguchi, A. Aramata, J. Electroanal. Chem, 1995, **396**, 131

[20] M. A. Quaiyyum, A. Aramata, S. Moniwa, S. Taguchi, M. Enyo, J. Electroanal. Chem, 1994, **373**, 61

Chapter 7

Chronoamperometric studies of Bu^n-ZDTP

7.1 Introduction

We have noted in Chapter 6 that reduction of Bu^n-ZDTP proceeds via nucleation and growth of zinc at the electrode surface. This chapter describes chronoamperometric experiments which were undertaken as a means of investigating the mechanism of nucleation at both electrode substrate materials further. First we give a broad overview of the generally accepted theory developed for nucleation processes in §7.2. A review of the literature pertaining to the study of zinc nucleation is then presented in §7.3. An introduction to the experimental procedures undertaken during this chapter is given in §7.4. §7.5 describes the results obtained at both glassy carbon and platinum electrode surfaces. Modelling of current-time transients is discussed in §7.6 including a description of the theoretical model implemented in this investigation and its application to the present system. A summary of conclusions drawn is presented in §7.7.

7.2 Theoretical treatment of nucleation and growth

Nucleation of material at a foreign electrode substrate is complex and a number of models to describe the nucleation process have been postulated. Broadly speaking, the nucleation mechanism is considered to progress via the following stages:

1. diffusion of ions in solution to the electrode interface,
2. electron transfer,
3. surface diffusion of ad-atoms,
4. clustering of ad-atoms to form critical nuclei,
5. incorporation of further ad-atoms into the nuclear lattice.

Models for nuclear growth are based on the description of current-time transients which serve as a convenient method for the investigation of nucleation. Theoretical treatments have been developed for a variety of nuclear growth types based on the generation of simplified models which can provide analytical expressions for the current during the nucleation process.

Theoretical treatments of nuclear growth have considered geometry of the growth centre and the rate determining step of the nucleation process. First, we consider geometry of the growth centre. The 2-Dimensional (2-D) nucleation model involves growth of the deposit from nucleation centres which can be considered as one atom or molecule thick. Growth centres subsequently expand and coalesce to form the monolayer deposit. Further deposition of material requires the nucleation of new growth centres onto the freshly generated surface. Expansion of the nucleus requires incorporation of atoms or molecules at the periphery of the expanding growth centre which gives rise to the 2-D growth pattern described. In contrast, a 3-Dimensional (3-D) nucleation model incorporates growth of material in a direction perpendicular to the electrode substrate in addition to the peripheral growth of expanding nuclear centres. In the case of 3-D nucleation, a number of theoretical treatments have been described based on the shape of the growth centre. Secondly, we consider the nature of the rate determining stage. For electrochemical nucleation, it is generally assumed that electron transfer and subsequent changes in solvation are rapid. Nucleation therefore can be either kinetically controlled, in which the rate determining stage in the reaction process is incorporation of material into the nuclear lattice, or under diffusion control.

Models which have been reported in the literature consider nuclear growth in terms of the rate of formation of stable growth centres. If we define the number of active nuclei under particular experimental conditions as N_0, the rate of appearance of stable growth centres is expected to follow first order kinetics in which the nuclear number density is defined as:

$$N(t) = N_0\{1 - \exp(-At)\} \tag{7.1}$$

where A corresponds to the first order nucleation rate constant and t denotes time. For a large value of At, Equation 7.1 becomes:

$$N(t) = N_0 \tag{7.2}$$

Conversely, for small values of At, the nuclear number density is given by:

$$N(t) = N_0At. \tag{7.3}$$

These two cases give rise to the two extremes of nuclear formation rate described as instantaneous and progressive nucleation respectively. Instantaneous nucleation corresponds to formation of a fixed number of active sites at the onset of nucleation. Progressive nucleation describes the continued formation of growth centres throughout the nucleation process.

In general nucleation theories are based on a consideration of the amount of current into a specific surface area coupled with the increase in size of this area as nuclear growth occurs. To obtain the overall current of the nucleation process for the total number of nuclear entities across the electrode surface, this value is multiplied by N and ANt in the case of instantaneous and progressive nucleation respectively. For N centres randomly distributed across the electrode surface, the Avrami theorem is invoked to account for overlap of diffusion zones so that the actual fraction of area covered, θ, is described by [1,2,3]:

$$\theta = 1 - \exp(-\theta_{ex}). \tag{7.4}$$

θ_{ex} denotes the extended surface coverage which correlates to the fraction of area covered by diffusion zones without taking overlap into account.

Fleischmann et al first developed models for the change of current with time for both 2-D and 3-D nucleation under conditions of rate limited growth [4,5]. Nuclei were based on hemispherical and cylindrical approximations assuming constant rate of growth in all dimensions. Subsequent investigators have proposed theoretical models for the 3-D growth of more complex shapes incorporating growth at different rates in varying crystallographic directions. Thirsk et al based their theoretical treatment of 3-D nucleation on a model incorporating the representation of nuclei as right circular cones [5,6]. Growth of the nucleus in directions parallel and perpendicular to the substrate were assumed to be separate and as such the current expression incorporated two rate constants for nuclear expansion.

Astley et al derived expressions for the theoretical current-time transients for growth of 3-D hemispherical nuclei under diffusion limited control assuming transport of material to the surface via planar diffusion [7]. This model was subsequently modified by Hills et al who suggested a hemispherical diffusion regime to be more appropriate for the development of 3-D growth centres [8]. However in both cases, overlap of neighbouring growth centres was not taken into account. Scharifker and Hills extended the model further with the application of the Avrami theorem to allow for nuclear overlap [9,10].

7.3 Overview of nucleation studies of zinc

A number of previous studies reported in the literature have sought to elucidate the nature of the zinc nucleation process from a variety of different media using chronoamperometric techniques together with theoretical models of nucleation described above. Relevant literature associated with nucleation of zinc at the electrode substrate materials used during this investigation, namely glassy carbon and platinum, are now discussed. During the study of zinc reduction from the room temperature molten salt aluminium chloride 1-methyl-3-ethylimidazolium chloride described previously in §6.3.2.1, Hussey and Pitner modelled the nucleation of zinc which was observed on glassy carbon [11]. Current-time transients were found to fit the theoretical description proposed by Scharifker and Hills for the progressive nucleation of hemispherical growth centres under diffusion control [9,10]. As noted in §6.3.2.3, deposition of zinc at a platinum electrode from this medium was observed to proceed without any noticeable nucleation effects.

McBreen and Gannon investigated the nucleation mechanism of zinc deposition on a glassy carbon electrode from $ZnCl_2$ and $ZnBr_2$ molten salts [12]. Using models developed by Fleischmann for 3-D nucleation under kinetic control [4,5], current-time transients for zinc deposition from $ZnCl_2$ were found to fit the theoretical description for instantaneous nucleation of circular cone-shaped nuclei. A similar relationship was observed for the nucleation of zinc from $ZnBr_2$ at low overpotentials. However, at higher overpotentials a close fit to the theoretical description for progressive nucleation was apparent. This was not supported by scanning electron microscopy where all nuclei were observed to be of a similar size suggesting an instantaneous nucleation process. These workers suggested that the onset of diffusion limitations at high current densities produced the deviation from the theoretical model observed.

During the study of Sonneveld et al of zinc nucleation at a glassy carbon electrode substrate from a zincate solution described in §6.3.2.1 [20], current-time transients were found to fit the theoretical description of Scharifker and Hills for instantaneous nucleation of hemispherical growth centres under diffusion control [9,10].

7.4 Experimental

Chronoamperometric investigations were conducted under identical conditions to those employed for voltammetric investigations outlined in Chapter 6. Glassy carbon and platinum electrodes were used with nominal electrode diameters of 3 and 1 mm respectively, with an accurate value obtained using the travelling microscope prior to use. Potential steps were chosen with reference to reduction wave potentials measured during cyclic voltammetric investigation as described in Chapter 6. In general, potential steps from 0 V versus SCE, well before the onset of zinc deposition at the electrode surface, to a range of potentials in the region of the reduction peak were investigated. These included step potentials to a number of points sampled along the nucleation wave together with values immediately prior to and following the nucleation peak for comparison. Transients were initially recorded using a Bu^n-ZDTP concentration of 1 mM and results obtained at each of the two electrode substrate materials compared. The effect of increased Bu^n-ZDTP concentration at the platinum electrode was subsequently investigated.

7.5 Results

7.5.1 Glassy carbon

A series of transient measurements recorded at potential steps ranging between –1.0 and –1.6 V versus SCE using a 1 mM Bu^n-ZDTP solution at a glassy carbon electrode surface is shown in Figure 7.1. The transient measured with the current step at –1.0 V versus SCE shows a falling current-spike at very short time-scales corresponding to charging of the double layer. The current is observed to decay towards zero. We note in Figure 7.1 that the current levels out to a value of approximately 1 µA attributable to background processes. Effects of nucleation are not apparent in this transient which reflects a potential step prior to the onset of the nucleation wave.

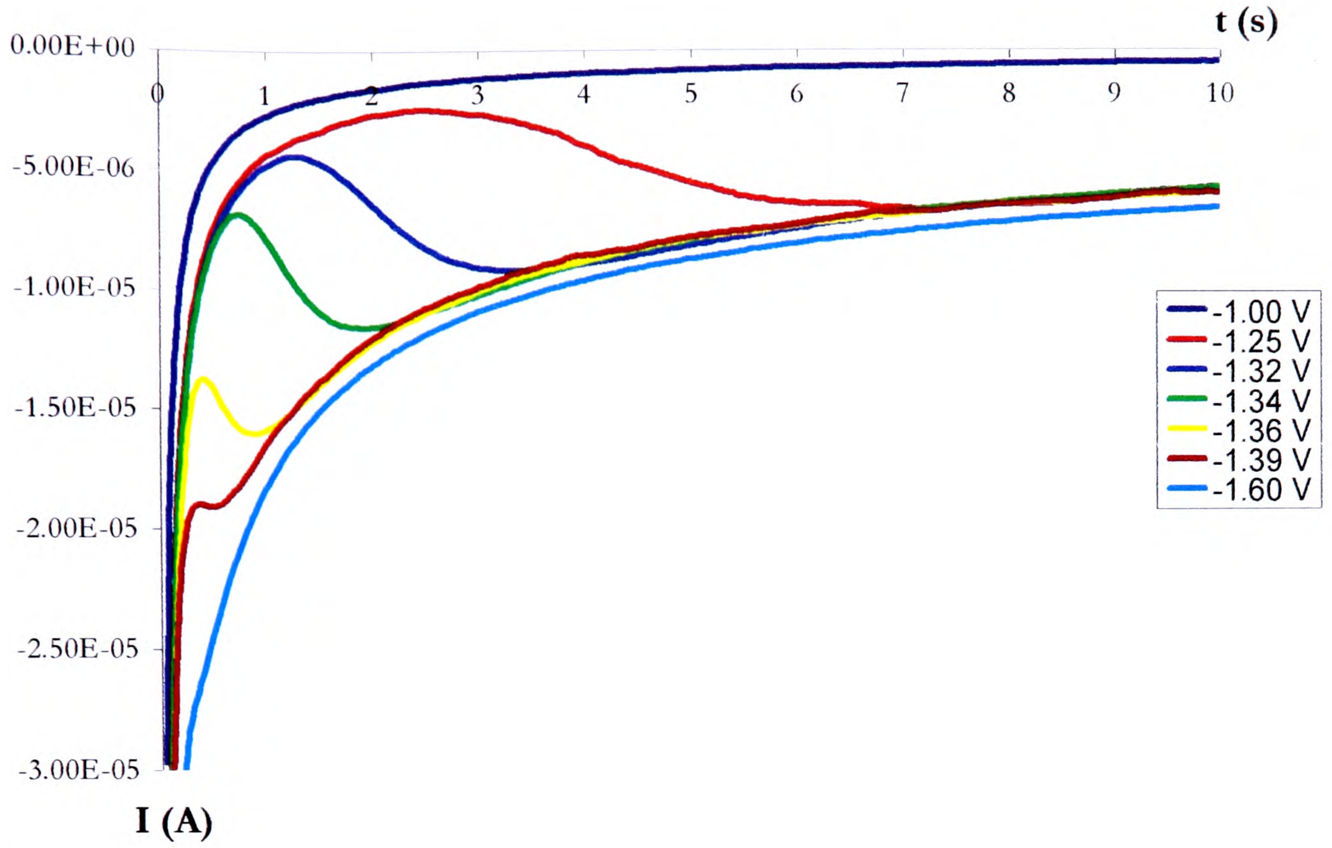

Figure 7.1: Current-time transients recorded for 1 mM Bu^n-ZDTP in DMF/0.1 M NBu_4ClO_4 solution at a glassy carbon electrode with steps from 0 V to potentials ranging from -1.00 to -1.60 V versus SCE

With the potential step to a more negative value at –1.27 V versus SCE, the current-decay arising from double layer charging is visible initially in the transient response as observed with the potential step to –1.0 V. However, a subsequent increase in current is observed, to reach a maximum value after approximately 2 seconds with subsequent decay to a limiting value of around 15 μA. The current increase after a period of time is viewed as evidence for a nucleation mechanism [9]. It supports the assignment of zinc nucleation on glassy carbon made during cyclic voltammetric investigations as described in Chapter 6. An increase in current with time is observed following the onset of nucleation due to an increase in electroactive area via the growth of nuclei and in the case of progressive nucleation through the further generation of active sites. The subsequent current decrease to a constant value suggests growth of 3-D nuclei under diffusion control. Diffusion to the nuclei can be approximated in terms of radial diffusion to individual growth centres with each nucleus having its own diffusion zone [9]. As these grow, radii of diffusion zones overlap and hemispherical mass transfer gives way to a linear regime at an effectively planar surface. As this occurs, the current falls, to give rise to a transient maximum, and approaches a limiting value which corresponds to the rate of linear mass transport to the electrode surface. For a nucleation process in which incorporation of material into the lattice is rate determining, we would expect an increase in current following the onset of nucleation as for the diffusion limited case. However, current levels out to an approximately constant value as rate of incorporation of material into the lattice limits nuclear growth. Ultimately current will gradually decrease as neighbouring nuclei coalesce which limits growth of active sites to a direction perpendicular to the electrode surface [19]. For a 2-D nucleation process, we would expect a transient containing a series of current-time maxima corresponding to nucleation and growth of successive monolayers of material [19].

As the potential is stepped to increasingly negative values along the reduction wave, transient maxima correspondingly move to shorter timescales. This reflects the increasing ease of the nucleation process at greater overpotential values. With a potential step of −1.6 V versus SCE which is well beyond the peak maximum observed during cyclic voltammetry, onset of nucleation is sufficiently rapid that an observable current maximum is not visible. However, the transient tends to a limiting value comparable to transients recorded at lower overpotentials corresponding to the diffusion limited current at the effectively planar nucleated surface.

7.5.2 Platinum

A series of transient measurements recorded for a 1 mM Bu^n-ZDTP solution at a platinum electrode is shown in Figure 7.2. Potential steps to −1.1 −1.3, −1.4 and −1.6 V were used corresponding to potentials immediately prior to the onset of nucleation, at two points along the nucleation wave and a site well beyond the reduction peak respectively. All four current-time transients exhibit the decaying current-spike attributable to double layer charging. The characteristic rising current of the nucleation and growth process is not apparent. This suggests the absence of zinc deposition via nucleation under these conditions. This supports observations made during cyclic voltammetric investigations in which platinum appeared to be more hostile to the nucleation of zinc in comparison to glassy carbon. In all four cases the decaying current spike levels out to a current value in excess of 0 A with increasing current correlated to increased overpotential values. The current observed corresponds to the sum of the current associated with the UPD of zinc at the platinum surface in addition to background processes. Increasing current with overpotential is attributable to the exaggeration of background effects as the voltage is increased.

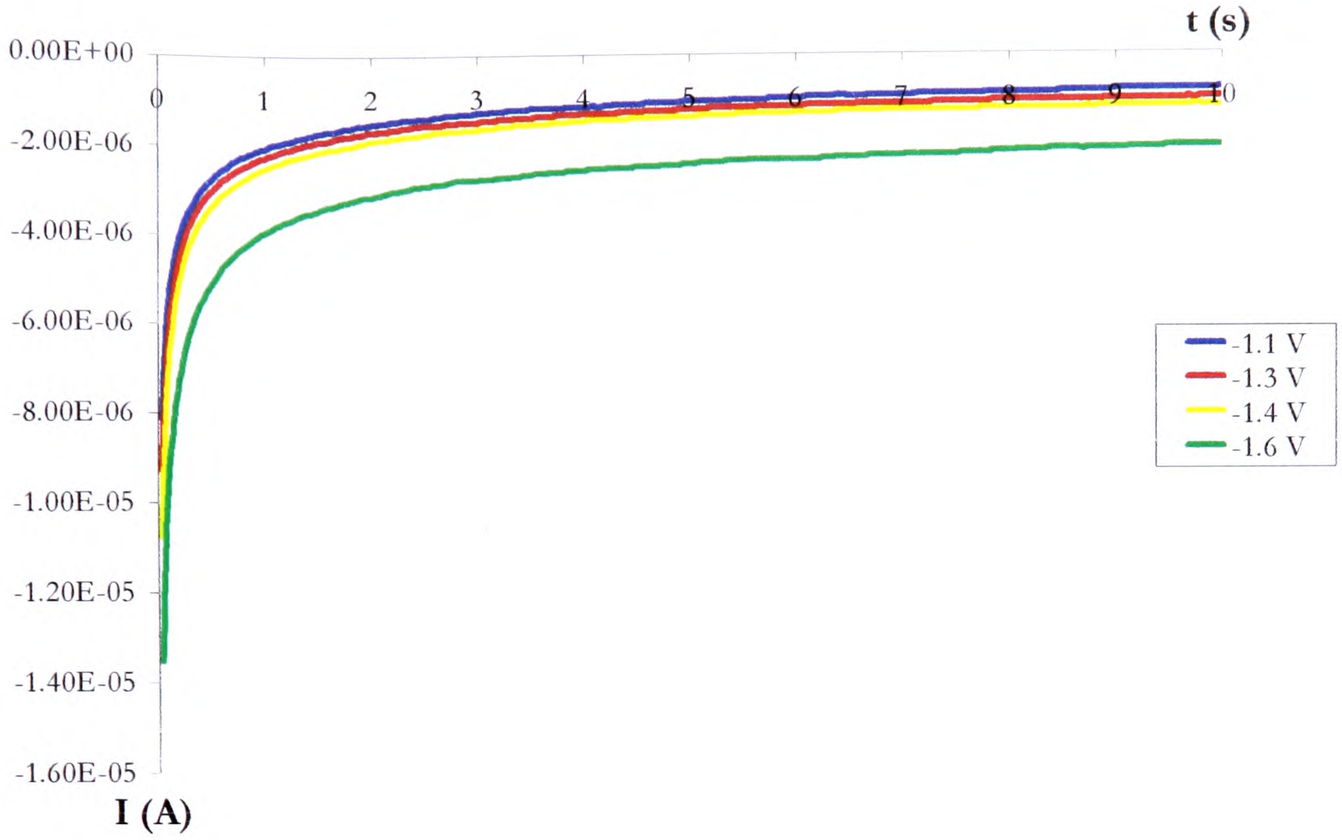

Figure 7.2: Current-time transients recorded for 1 mM Bu^n-ZDTP in DMF/0.1 M NBu$_4$ClO$_4$ solution at a platinum electrode with steps from 0 V to potentials ranging from −1.10 to −1.60 V versus SCE

In contrast, transients recorded at a platinum electrode from a 5 mM Bu^n-ZDTP solution are shown in Figure 7.3. Potential steps of −1.18 V, −1.25, −1.29 −1.35, −1.4 and −1.5 V were used corresponding to voltages prior to the onset of nucleation, four sampled points along the reduction wave and a site beyond the reduction wave respectively. The current-time response obtained at a potential step of −1.18 V shows the initial current-spike consistent with double-layer charging. The current decays to approximately 2.5 μA reflecting the current associated with UPD of zinc on the platinum surface together with background effects. Current-time responses recorded for potential steps at sites sampled along the reduction wave exhibit the current maxima associated with nucleation processes. In addition, transient maxima are observed to move to progressively shorter times as potential step values become increasingly negative. This reflects increasing speed at which nuclei are able to form with increasing nucleation overpotential as described for glassy carbon above. Such observations are consistent with results of cyclic voltammetric studies in Chapter 6 where reduction peaks attributable to zinc nucleation became visible at increased Bu^n-ZDTP concentration.

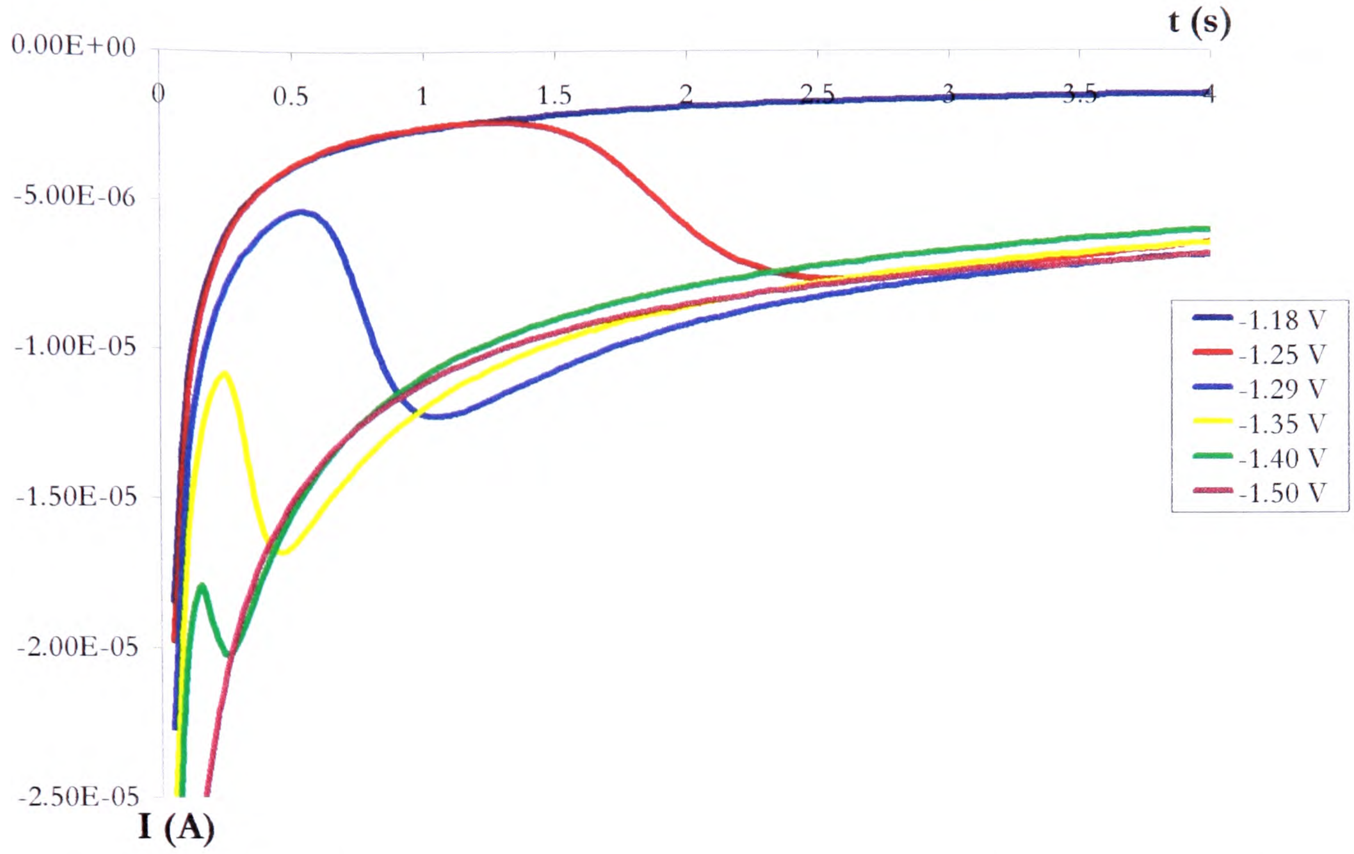

Figure 7.3: Current-time transients recorded for 5 mM Bu^n-ZDTP in DMF/0.1 M NBu$_4$ClO$_4$ solution at a platinum electrode with steps from 0 V to potentials ranging from −1.18 to −1.50 V versus SCE

7.6 Modelling of the nucleation process

We noted in §7.4 that the shape of current-time transients reflected growth of nuclei under diffusion limited conditions. Modelling of the current-time response was carried out according to the theoretical treatment by Scharifker and Hills describing growth of hemispherical nuclei under diffusion limited conditions [9,10].

7.6.1 Theoretical model for the growth of hemispherical nuclei under diffusion limited conditions

According to Scharifker and Hills, a hemispherical diffusion zone grows at a radial velocity so that its radius, δ, is described as a function of time, t, by:

$$\delta(t) = (kDt)^{1/2}, \qquad (7.5)$$

where k is a numerical constant described by the conditions of the experiment. The planar area of a single diffusion zone is given by:

$$S(t) = \pi\delta^2(t) = \pi kDt. \qquad (7.6)$$

For instantaneous nucleation, if N centres are nucleated following t=0, then at a later time t:

$$\theta_{ex} = N\pi kDt, \tag{7.7}$$

Employing the Avrami theorem to account for overlap of diffusion zones as given in Equation 7.4, the actual fraction of area covered, θ, is described by:

$$\theta = 1 - \exp(-N\pi kDt). \tag{7.8}$$

Radial flux density through the boundaries of the diffusion zones will be given by the equivalent planar diffusive flux to the electrode of fractional area θ, thus:

$$I = \frac{zFD^{1/2}c\theta}{\pi^{1/2}t^{1/2}} = \frac{zFD^{1/2}c}{\pi^{1/2}t^{1/2}}[1 - \exp(-N\pi kDt)] \tag{7.9}$$

where zF defines the molar charge of the electrodepositing species and other symbols take their usual meanings. At very short times, $N\pi kDt \ll 1$ and

$$1 - \exp(-N\pi kDt) \approx N\pi kDt. \tag{7.10}$$

Thus, Equation 7.10 becomes:

$$I = zFD^{3/2}c\pi^{1/2}Nkt^{1/2}. \tag{7.11}$$

The current density will be equivalent to the flux of material to N isolated hemispherical nuclei. Hills et al have derived the expression for the current associated with growth of individual nuclei under a hemispherical diffusion regime [8]. The current flux will be equivalent to the current required for nuclear growth. Thus:

$$I = zF2\pi rDc = \frac{zF\rho}{M}\frac{\partial V}{\partial T} \tag{7.12}$$

where V is the volume of the hemisphere, M and ρ denote the molecular weight and density of the deposited material respectively and other symbols take their usual meanings. It follows that:

$$zF2\pi rDc = \frac{zF\rho}{M}2\pi r^2\frac{\partial r}{\partial t}. \tag{7.13}$$

Upon rearrangement, this yields:

$$r\partial r = \frac{DcM}{\rho}\partial t, \tag{7.14}$$

and by integration:

$$r^2 = \frac{2DcMt}{\rho}. \tag{7.15}$$

Substituting for r in the original expression for hemispherical diffusion flux (Equation 7.12) and multiplying by N_0 as the number of growth centres formed in the instantaneous nucleation process yields the potentiostatic time transient:

$$I = \frac{zFN_0\pi(2Dc)^{3/2}M^{1/2}t^{3/2}}{\rho^{1/2}}. \tag{7.16}$$

Combining Equations 7.11 and 7.16 defines k as:

$$k = (8\pi cM/\rho)^{1/2}. \tag{7.17}$$

For progressive nucleation, $N(t)=AN_0t$, thus the rate of change of the amount and size of nucleation sites with time is given by:

$$\theta_{ex} = \int_0^t AN\pi k'Dtdt = AN_0\pi k'Dt^2/2. \tag{7.18}$$

By applying the Avrami theorem to account for nuclear overlap and taking the flux density to be equivalent to planar diffusion to an electrode of fractional area θ as in the case of instantaneous nucleation, we find that:

$$I = \frac{zFD^{1/2}c}{\pi^{1/2}t^{1/2}}[1-\exp(-AN_0\pi k'Dt^2/2)]. \tag{7.19}$$

Correspondingly, at the limit where $AN_\infty t$ tends to 0, Equation 7.19 becomes:

$$I = \frac{zFD^{3/2}cAN_0k'\pi^{1/2}}{2}t^{3/2}. \tag{7.20}$$

For progressive nucleation where all nuclei are assumed to grow independently of one another, current density was obtained by Hills et al by substitution for r into the expression for hemispherical diffusion at a single nucleus and multiplication by AN_0t followed by integration with respect to t to yield [8]:

$$I = \frac{2zFAN_0\pi(2Dc)^{3/2}M^{1/2}t^{3/2}}{3\rho^{1/2}} \tag{7.21}$$

From Equations 7.20 and 7.21, k' is defined by the relation:

$$k' = \frac{4}{3}(8\pi cM/\rho)^{\frac{1}{2}}. \tag{7.22}$$

The current, I_m, and time, t_m, corresponding to the transient maximum for both progressive and instantaneous nucleation was evaluated by equating the first derivative of the relevant I-t relation to zero. Corresponding theoretical dimensionless expressions for the current-time transient are given in Equations 7.23 and 7.24 for instantaneous and progressive nucleation respectively:

$$\frac{I^2}{I^2_m} = \frac{1.9542}{t/t_m}\{1-\exp[-1.2564(t/t_m)]\}^2 \tag{7.23}$$

$$\frac{I^2}{I^2_m} = \frac{1.2254}{t/t_m}\{1-\exp[-2.3367(t/t_m)^2]\}^2 \tag{7.24}$$

Current-time transients can be plotted in non-dimensional form as I^2/I_m^2 versus t/t_m and compared to the theoretical plots obtained using Equations 7.23 and 7.24 as a useful diagnostic criterion of nucleation type without the need for knowledge of values of k, k$'$, AN_0 or N. However, we note that this treatment is approximate and is also limited by its definition of the nucleation process as either of the two limiting cases, instantaneous and progressive, which are likely to be extremes of a general mechanism which involves continued development and exhaustion of surface active sites.

7.6.2 Previous applications of model

The model proposed by Scharifker et al for the 3-D growth of hemispherical nuclei under diffusion limited conditions has frequently been applied in the description of metal nucleation at foreign substrate materials. Numerous examples pertaining to deposition from both aqueous and molten salt media are reported in the literature. As detailed in §7.3, Hussey and Pitner [11] and Sonneveld et al [20] were able to describe zinc nucleation on glassy carbon from molten salt and aqueous zincate solution respectively using this theoretical approach. Similarly Hussey and Xu found this model to be appropriate for the description of lead nucleation at a glassy carbon surface [13]. Deposition of lead from a solution of $PbCl_2$ in a room temperature molten salt medium was observed to follow a progressive pathway. Legrand et al used this model to assign the electrodeposition of aluminium on tungsten from a $DMSO_2$ electrolyte as a 3-D progressive nucleation process under diffusion limited growth [14]. Fabricus et al report that the nucleation of copper from acidic sulphate solutions of copper ions at a palladium substrate can be described by a 3-D instantaneous diffusion controlled mechanism [15]. Hussey and Xu report a comparative study of silver nucleation from molten salt media at glassy carbon and tungsten surfaces using the model developed by Scharifker and Hills [16]. Instantaneous nucleation was found to dominate at a glassy carbon electrode whereas deposition at tungsten was observed to occur via a progressive mechanism. Trejo et al conducted an investigation of the effects of temperature on gold electrodeposition at a glassy carbon electrode from Au(I) ammoniacal solution [17]. Using the theoretical framework proposed by Scharifker and Hills, these workers noted diffusion limited progressive nucleation at 30 and 40 ^{0}C with instantaneous behaviour at 50 ^{0}C.

7.6.3 Application of model to deposition of Bu^n-ZDTP

7.6.3.1 Glassy carbon

Current-time transients obtained on glassy carbon using a 1 mM Bu^n-ZDTP solution at potential steps of −1.27, −1.32, −1.33, −1.34, −1.36, and −1.39 V were plotted in dimensionless form and compared with the theoretical responses for progressive and instantaneous nucleation derived using Equations 7.23 and 7.24. In order to make an effective comparison between theory and experiment, previous investigations using this model have suggested that account must be made for the delay time which precedes the onset of nucleation following application of the potential step [13, 14, 16, 18]. For a given delay time t_0, the time axis is redefined as $t^/=t-t_0$ and the time to the maximum current as $t_m^/=t_m-t_0$. t_0 values were obtained by linear regression of the rising portion of the current-time transient. Values of t_0 obtained at each of the potential step values under investigation are recorded in Table 7.1. Dimensionless plots incorporating t_0 values at each potential step are shown in Figures 7.4.a to f along with theoretical responses for instantaneous and progressive nucleation.

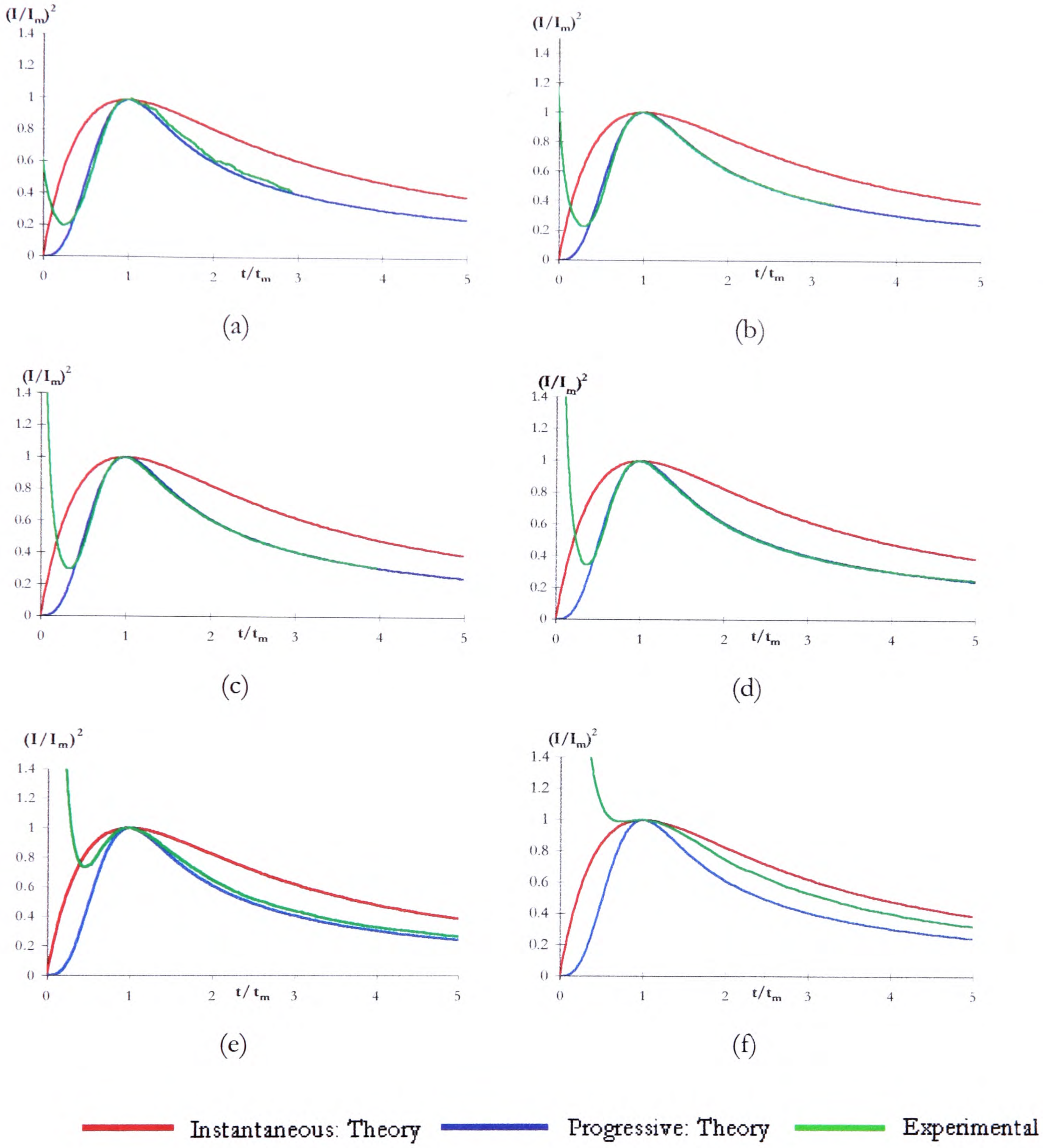

Figure 7.4: Current-time transients recorded for 1 mM Bu^n-ZDTP in DMF/0.1 M NBu$_4$ClO$_4$ solution at a glassy carbon electrode plotted in dimensionless form for potential steps from 0 V to a)–1.27 V, b)–1.32 V, c)–1.33 V, d)–1.34 V, e)–1.36 V and f)–1.39 V versus SCE in comparison to the theoretical responses for instantaneous and progressive diffusion limited nucleation

Potential step (V)	t_0 (s)
−1.270	0.80
−1.320	0.40
−1.330	0.10
−1.340	0.05
−1.360	~0
−1.390	~0

Table 7.1: Delay times which proceed onset of zinc nucleation at a glassy carbon electrode surface from 1 mM Bu^n-ZDTP in DMF/0.1 M NBu_4ClO_4 solution at 25 °C following application of each potential step

---

The experimental transients obtained for potential steps of −1.32, −1.33 and −1.34 V are observed to be in excellent agreement with the theoretically predicted response for progressive nucleation. This suggests a nucleation mechanism in which zinc growth centres are continually being formed throughout the deposition process. For the transients recorded at greater overpotential steps of −1.36 and −1.39 V, progressive behaviour is dominant although a tendency to instantaneous behaviour at the onset of the nucleation process is observed. We attribute this to the initial formation of a large number of nuclei upon application of a significantly high overpotential so that rate of deposition of zinc via growth of these nuclei is comparable to rate of formation of new active sites. Over time, continued exhaustion of nuclei gives rise to progressive behaviour in which generation of new active sites is the dominant form of zinc deposition. The current-time response recorded at a low overpotential of −1.27 V suggests progressive behaviour although the fit to theory is poorer than for the current-time transients recorded at higher overpotential values. Such an anomaly may arise from slow rate of growth centre formation during the progressive nucleation process upon application of a significantly low overpotential.

7.6.3.2 Platinum

Current-time transients obtained on platinum using a 5 mM Bu^n-ZDTP solution at potential steps of −1.29, −1.35, −1.38, −1.39, −1.40, and −1.42 V versus SCE were plotted in dimensionless form and compared with the theoretical responses for progressive and instantaneous nucleation. As for glassy carbon, the time axis was redefined taking into account the delay time proceeding the onset of nucleation following application of the potential step. Values of t_0 obtained via linear regression of the rising portion of the current-time transient at each potential step value are recorded in Table 7.2. Dimensionless plots incorporating t_0 values at each potential step are shown in Figures 7.5.a to f along with theoretical responses for progressive and instantaneous nucleation.

Potential step (V)	**t_0 (s)**
−1.29	0.60
−1.35	0.10
−1.38	0.03
−1.39	0.02
−1.40	0.02
−1.42	0.01

Table 7.2: Delay times which proceed onset of zinc nucleation at a platinum electrode surface from 5 mM Bu^n-ZDTP in DMF/0.1 M NBu$_4$ClO$_4$ solution at 25 ^{0}C following application of each potential step

The experimental transients recorded at potential steps of −1.38, −1,39, −1.40 and −1.42 V are observed to be in excellent agreement with the theoretical response for progressive nucleation. Thus nucleation of zinc on platinum following reduction of Bu^n-ZDTP proceeds via an identical mechanism to glassy carbon. Similar to the case for glassy carbon, the transient obtained at a low overpotential value shows a poorer fit to the theoretically predicted response which may arise from the slow rate of active site formation upon application of a significantly low overpotential. A tendency to instantaneous behaviour at the onset of the nucleation process at significantly high overpotentials was not apparent on platinum in contrast to the results obtained on glassy carbon. This may be due to the fact that onset of nucleation is sufficiently rapid at overpotentials where initial instantaneous behaviour occurs so that an observable current maximum is not apparent.

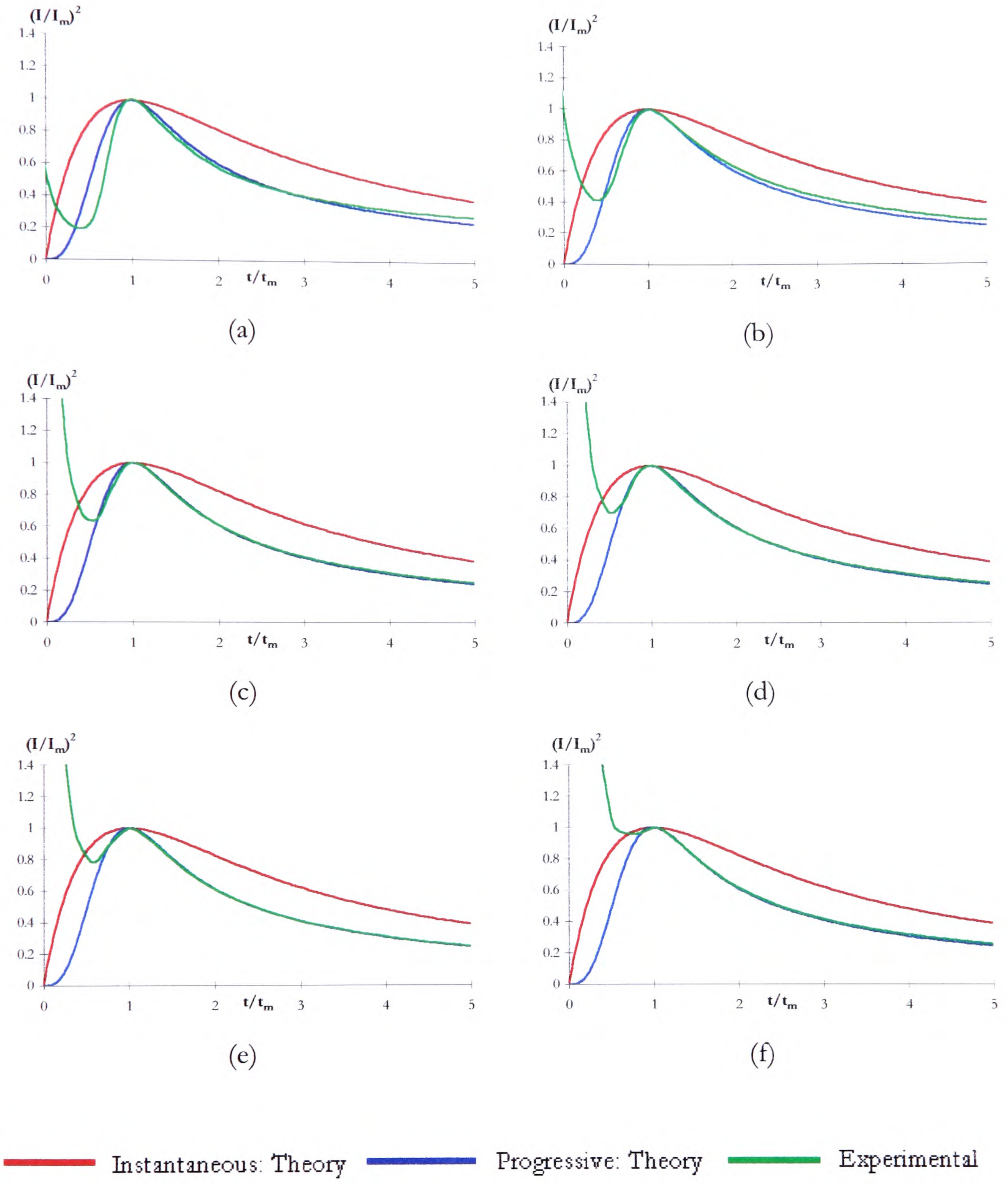

Figure 7.5: Current-time transients recorded for 5 mM Bu^n-ZDTP in DMF/0.1 M NBu$_4$ClO$_4$ solution at a platinum electrode plotted in dimensionless form for potential steps from 0 V to a)–1.29 V, b)–1.35 V, c)–1.38 V, d)–1.39 V, e)–1.40 V and f)–1.42 V versus SCE in comparison to the theoretical responses for instantaneous and progressive diffusion limited nucleation

7.6.3.3 Calculation of diffusion coefficients

Using values of I_m and t_m derived for progressive and instantaneous nucleation, Scharifker and Hills suggested that the product $I_m^2t_m$ serves as a convenient method for the determination of the diffusion coefficient of the substrate material without the need for knowledge of k, k$'$, N and AN_∞. Expressions for $I_m^2t_m$ for instantaneous and progressive nucleation are given in Equations 7.25 and 7.26 respectively:

$$I_m^2 t_m = 0.1629(zFc)^2 D, \tag{7.25}$$

$$I_m^2 t_m = 0.2598(zFc)^2 D. \tag{7.26}$$

If the overpotential applied to the electrode surface is sufficiently high so as to effectively reduce surface concentrations of the electroactive species to zero, the concentration term will correspond to the bulk solution concentration to provide a valid determination of D. Furthermore for a true diffusion limited process, D will be independent of applied overpotential since the current-time transient will not reflect nucleation and growth rates.

Using the expression for progressive nucleation, diffusion coefficients for the Bu^n-ZDTP species were calculated at a range of potential step values for glassy carbon and platinum where true progressive behaviour was indicated by the dimensionless plots shown in Figures 7.5 and 7.6. Diffusion coefficients calculated for each potential step along with transient maxima used to calculate D values are recorded in Table 7.3. Values at both electrode substrate materials are independent of applied potential concurrent with a diffusion limited nucleation and growth process. A good correlation is observed between diffusion coefficients obtained at the two electrode substrate materials. Furthermore, values of D are observed to be in excellent agreement with the diffusion coefficients calculated from Levich analysis of Bu^n-ZDTP oxidation data as recorded in Table 6.3. Since zinc deposition from Zn^{2+} is clearly a 2 electron process, the correlation between values of D obtained from reduction and oxidation data validates our assignment of Bu^n-ZDTP oxidation as a 2 electron transfer process.

7.7 Summary

In this chapter we have presented a study of zinc nucleation which occurs at glassy carbon and platinum electrode surfaces during Bu^n-ZDTP reduction. Nucleation of zinc on glassy carbon has previously been studied via chronoamperometric techniques from molten salt materials and from aqueous media. As far as we know, this study represents the first investigation of zinc deposition at a glassy carbon surface from non-aqueous solution. Nucleation of zinc on platinum has previously not been reported, instead electrodeposition of zinc on platinum has been observed to proceed via a bulk deposition process. This work therefore comprises the first reported observation and study of zinc nucleation at a platinum electrode.

Current-time transients suggested nucleation of zinc at both electrode substrate materials to be under diffusion control. Current-time responses were modelled in terms of a previously reported model describing the growth of hemispherical nuclei under mass transport limited conditions. Transients plotted in dimensionless form for both electrode substrate materials were observed to be in excellent agreement with the theoretical response for progressive nucleation and growth. Diffusion coefficients calculated from the current-time maxima showed a close correlation to values of D calculated from RDE voltammetric investigation of Bu^n-ZDTP oxidation thereby validating our previous assignment of Bu^n-ZDTP oxidation as a 2 electron process.

E (V)	I_m (A cm^{-2})	t_m (s)	t_0 (s)	$I^2_m t_m$ (A^2 cm^{-4} s^{-1})	D (cm^2 s^{-1})
Glassy Carbon					
-1.32	1.31x10^{-4}	3.35	0.4	5.10x10^{-8}	6.20x10^{-6}
-1.33	1.45x10^{-4}	2.60	0.1	5.32x10^{-8}	6.47x10^{-6}
-1.335	1.59x10^{-4}	2.10	0.05	5.15x10^{-8}	6.27x10^{-6}
-1.34	1.66x10^{-4}	1.95	0.05	5.22x10^{-8}	6.35x10^{-6}
Platinum					
-1.38	2.36x10^{-3}	0.32	0.03	1.61x10^{-6}	6.65x10^{-6}
-1.39	2.48x10^{-3}	0.29	0.02	1.66x10^{-6}	6.88x10^{-6}
-1.40	2.58x10^{-3}	0.25	0.02	1.54x10^{-6}	6.35x10^{-6}
-1.42	2.85x10^{-3}	0.20	0.01	1.55x10^{-6}	6.39x10^{-6}

***Table 7.3:** Current-time transient data for the reduction of Bu^n-ZDTP in DMF/0.1 M NBu_4ClO_4 solution at (a) 3 mm glassy carbon (1 mM Bu^n-ZDTP solution) and b) 1 mm platinum (5 mM Bu^n-ZDTP solution) electrodes at 25 ^{0}C*

References

[1] M. Avrami, J. Chem, Phys., 1939, **7**, 1103

[2] M. Avrami, J. Chem, Phys., 1940, **8**, 212

[3] M. Avrami, J. Chem, Phys., 1941, **9**, 177

[4] M. Fleischmann, H. R. Thirsk, Advances in Electrochemistry and Electrochemical Engineering, (Ed. P. Delahay), Vol. 3, Interscience, New York, 1963, ch.3

[5] J. A. Harrison, H. R. Thirsk, Electroanalytical Chemistry, (Ed. A. J. Bard), Vol. 5, Marcel Dekker, New York, 1971, p67

[6] R. D. Armstrong, M. Fleishmann, H. R. Thirsk, J. Electroanal. Chem., 1966, **11**, 208

[7] D. J. Astley, J. A. Harrison, H. R. Thirsk, Trans. Faraday. Soc., 1968, **64**, 198

[8] G. J. Hills, D. J. Schiffrin, J. Thompson, Electrochimica Acta, 1974, **19**, 675

[9] B. Scharifker, G. Hills, Electrochimica Acta, 1983, **28**, 7, 879

[10] G. Gunawardena, G. Hills, I. Montenegro, B. Scharifker, J. Electroanal. Chem., 1982, **138**, 225

[11] W. R. Pitner, C. L. Hussey, J. Electrochem. Soc., 1997, **144**, 9, 2020

[12] J. McBreen, E. Gannon, J. Electrochem. Soc., 1983, **130**, 8, 1667

[13] X-H Xong, C. L. Hussey, J. Electrochem. Soc., 1991, **138**, 7, 1886

[14] L. Legrand, A. Tranchent, R. Messina, J. Electrochem. Soc., 1994, **141**, 2, 378

[15] G. Fabricus, K. Konturri, G. Sundholm, Electrochimica Acta, 1994, **39**, 16, 2353

[16] X-H Xong, C. L. Hussey, J. Electrochem. Soc., 1992, **139**, 5, 1295

[17] G. Trejo, A. F. Gil, I. Gonzâlez, J. Electrochem. Soc., 1995, **142**, 10, 3404

[18] P. M. Rigano, C. Mayer, T. Chierchie, J. Electroanal. Chem., 1988, **248**, 229

[19] Southampton Electrochemistry Group, Instrumental Methods in Electrochemistry, Ellis Horwood, UK, Ch9

[20] P. J. Sonneveld, W. Visscher, E. Barendrecht, Electrochimica Acta, 1992, **37**, 7, 1199

Chapter 8

Atomic Force Microscopy of Bu^n-ZDTP

8.1 Introduction

This chapter describes the first reported application of atomic force microscopy to the study of ZDTP compounds. We implement this technique in an investigation of Bu^n-ZDTP reduction as a means of directly visualising deposited zinc material at the electrode surface. We begin in §8.2 with a brief survey of the literature pertaining to the study of metal deposition using atomic force microscopy including a detailed review of zinc electrodeposition studies using the AFM. We then move on to consider AFM studies undertaken as part of this thesis. An introduction to the applications of atomic force microscopy to the study of Bu^n-ZDTP activity is given in §8.3. The implementation of atomic force microscopy in an ex-situ study comparing zinc deposit morphology under cyclic and RDE voltammetric conditions is then described. Atomic force microscopy in conjunction with cyclic and RDE voltammetry are considered in §8.4 and 8.5 respectively. §8.6 briefly considers attempts to implement an in-situ electrochemical AFM study of Bu^n-ZDTP reduction. We conclude the chapter with a brief summary of the results obtained in §8.7.

8.2 Survey of literature relating to AFM studies of metal electrodeposition

We noted in §2.8.3.3 that numerous studies concerned with the imaging of metal electrodeposition processes using atomic force microscopy have been reported in the literature. Previous investigations have focussed on both UPD and bulk growth of material at the electrode surface. Reported work encompasses both in-situ and ex-situ electrochemical AFM studies. In this section, we present a more detailed survey of the literature pertaining to AFM studies of metal electrodeposition.

Ex-situ atomic force microscopy has been widely implemented in the study of bulk metal electrodeposition processes. Penner et al describe an ex-situ electrochemical

AFM study of silver deposition at a graphite electrode from aqueous $AgNO_3$ solution containing KNO_3 as electrolyte [1]. These workers noted the appearance of silver nuclei both at scratch lines and on the basal plane of the electrode surface. All nuclei appeared similar in size consistent with current-time transient measurements which suggested an instantaneous nucleation and growth mechanism.

Darrort et al used ex-situ atomic force microscopy to examine the morphology of nickel electrodeposits formed from an aqueous acidified $NiSO_4$ and $NiCl_2$ solution at pH5 on a polycrystalline copper electrode surface [2]. Bulk nickel deposition in the absence of additives was compared with deposits formed in the presence of saccharin and 2-butyne-1,4-diol additive species. Large facetted crystals were observed in the absence of additives. A roughness value of 160 nm was evaluated for the deposits covering the electrode surface. By comparison, nickel deposits obtained in the presence of additives were noticeably smoother. In the presence of saccharin, nickel deposits appeared as smooth undulations at the electrode surface with a roughness value of 13 nm. In the presence of 2-butyne-1,4-diol and a mixture of 2-butyne-1,4-diol and saccharin, a fine-grained flat nickel deposit was observed with a roughness value of 8 nm in both cases. A decrease in grain size was correlated to an inhibitory effect of each additive species on nickel reduction observed during voltammetric investigation.

Wouters et al investigated tin electrodeposition on NiP electrodes from acidified aqueous $SnSO_4$ solution [3]. Bulk tin deposition was investigated in the presence of a variety of commercial additive species which are added during industrial tin deposition processes as a means of avoiding dendritic tin growth. Using ex-situ atomic force microscopy, bulk growth of material was observed to proceed via island formation in the initial stages of growth for all commercial additive packages under study. Island height poses a lower limit to the thickness of tin multilayers formed via electrolytic synthesis. As a means of increasing growth uniformity, the influence of two novel additives on the tin deposition process was evaluated. One of these was observed to give increased uniformity of the tin deposits obtained. However this was also observed to have decreased stability which may limit its possible commercial application.

The advent of in-situ atomic force microscopy has allowed direct observation of electrochemical processes occurring at the solid liquid interface. The technique has been widely applied to the study of UPD and bulk metal deposition. One of the first investigations of metal deposition at an electrode surface to use in-situ atomic force microscopy was reported by Gewirth et al. These workers described deposition of copper at a gold (111) electrode surface [4]. Deposition of copper from solutions containing different electrolyte species, namely perchlorate and sulphate, was compared. In perchlorate solution, underpotential deposited copper formed a close-packed adlattice on the gold substrate material. A copper atom separation of 0.29 ± 0.02 nm was noted with the lattice at a 30^0 rotation from the underlying gold surface. UPD from the sulphate containing medium yielded a more open $(\sqrt{3}x\sqrt{3})R30^0$ overlayer structure with a copper atom separation of 0.49 ± 0.02 nm. For bulk deposited material, copper atoms converged to a (111)-oriented layer with a lattice spacing of 0.26 ± 0.02 nm in both electrolytic systems.

Subsequent investigations have considered deposition of a variety of metals at a range of substrate materials. Examples of in-situ AFM reports concerned with metal electrodeposition follow. Both Ikeyami et al [5] and Chen et al [6] have described deposition of silver on gold using in-situ atomic force microscopy. Ikeyami et al considered UPD of silver from acidified aqueous Ag_2SO_4 and $AgClO_4$ solutions at the Au(100) face [5]. Identical adlattice structures were obtained for each of the two electrolyte systems. Deposition was observed to proceed via an initial $c(\sqrt{2}x5\sqrt{2})R45^0$ structure corresponding to 0.6 monolayer coverage followed by a pseudomorphic (1x1) adlayer at more negative potential. Bulk silver deposition was investigated in sulphate solution and was observed to proceed via preferential nucleation of silver at imperfection sites on the electrode surface with subsequent lateral growth of films. Layer-by-layer growth in this manner formed the bulk silver deposit. Chen et al investigated UPD of silver at a Au(111) surface from aqueous silver solutions containing sulphate, perchlorate, nitrate, carbonate and acetate electrolytes [6]. In contrast to studies of the Au(100) surface described above, differences in monolayer adlattice structure were apparent in different electrolytic solutions. Silver showed a (3x3) overlayer in sulphate solution and a (4x4) adlattice in nitrate and carbonate containing electrolytes. In perchlorate solution, the overlayer structure was unresolved but packing density appeared similar to that observed in nitrate solution. In acetate, a close-packed (1x1) monolayer was observed. Monolayer structures and associated packing densities were correlated to electrolyte size suggesting that anion adsorption at the Au(111) surface prior to silver deposition was influential in monolayer structure. A similar relationship was not observed for the deposition of silver in different electrolytes at the Au(100) surface. This suggested that anion adsorption was not prominent at this surface [5]. At potentials negative of bulk deposition, growth of the Ag(111) lattice was observed on Au(111) for all electrolyte systems with 0.29 nm atomic spacing.

Gewirth and co-workers describe lead deposition from an aqueous $Pb(ClO_4)_2$ perchlorate solution at a Au(111) surface [7]. These workers observed growth of the underpotential deposited monolayer via island formation. The full monolayer of lead atoms grows via further deposition at step edges to form a hexagonal close-packed structure with interatomic separation 0.35 ± 0.02 nm.

An investigation of the bulk deposition of lithium at polycrystalline copper electrodes from $LiClO_4$ and $LiPF_6$ propylene carbonate solutions has been reported by Aurbach and Cohen [8]. These workers describe rounded agglomerates of lithium distributed across the electrode surface upon deposition of material from $LiClO_4$ solution. In contrast, lithium deposition from $LiPF_6$ solution resulted in significantly smoother bulk deposits at the electrode surface.

Chen et al report an in-situ AFM study of mercury deposition at a Au(111) surface [9]. Deposition was from aqueous HgO solution and compared sulphate, nitrate, perchlorate and acetate electrolytes. In sulphate, perchlorate and nitrate solution, a hexagonal underdeposited adlattice was observed with atomic spacing 0.58 ± 0.02 nm. Just prior to bulk deposition, a mercury-gold surface alloy was observed with interatomic spacing 0.29 ± 0.03 nm. In acetate solution, a hexagonal lattice with atomic spacing 0.75 ± 0.05 nm was observed immediately following the UPD signal, a rhombic lattice with atomic spacing 0.43 ± 0.02 nm was seen at more negative potentials and a hexagonal lattice with 0.30 ± 0.03 nm spacing was found prior to bulk deposition. The nature of mercury deposition in acetate solution was attributed to complexation between the adatom and anion species.

Gewirth at al report an in-situ AFM study of underpotentially and bulk deposited cadmium at a Cu(111) surface [10]. Deposition was from aqueous $Cd(ClO_4)_2$ solution. The UPD adlattice was observed to form a (4x4) structure with atomic spacing 0.343 ± 0.06 nm. Bulk cadmium deposition proceeded via preferential nucleation of material at defects and step edges. Growth continued epitaxially to yield a close-packed hexagonal crystalline structure with interatomic separation 0.304 ± 0.02 nm.

Farrington et al have used in-situ atomic force microscopy to visualise the bulk deposition of silver from an acidified aqueous Ag_2SO_4 solution at a platinum surface [11].

Comparison between silver deposits obtained at different sweep rates was made. At slow sweep rates, two crystal types were visible. Large crystals formed at scratch lines together with smaller deposits at uniformly distributed sites. With increasing sweep rate, a more uniform deposit was observed. This was attributed to the preferential deposition of silver at scratch-lines with subsequent longer growth time resulting in increased crystal size. At faster sweep rates, crystals formed preferentially at scratch-lines had less time to grow. These crystals were therefore less easily distinguished from other silver deposits.

8.2.1 Literature reports of AFM studies of zinc electrodeposition

Despite the plethora of literature concerned with the AFM study of metal electrodeposition, reports concerned with the deposition of zinc are few. Kondo et al describe zinc electrodeposition from zinc sulphate solution at a steel substrate material in the presence and absence of an Sn^{2+} additive [12]. These workers report that the initial zinc deposit both with and without Sn^{2+} comprises hexagonal platelet crystals of the $(0001)_{\eta}$ crystal plane oriented ten or twenty degrees to the surface. Continued growth in the absence of Sn^{2+} occurs via the deposition of material at the edge of the plane opposite to the substrate. Thus, platelet crystals ultimately become aligned perpendicular to the substrate material. In contrast, deposition of zinc in the presence of Sn^{2+} occurs at the edge of the plate closest to the substrate. This results in the formation of hexagonal platelet crystals in alignment with the substrate material.

Other reported AFM studies of zinc deposition are confined to the deposition of zinc alloy materials. Gómez report deposition of a zinc-cobalt alloy from an aqueous $ZnCl_2.6H_2O$ and $CoCl_2.6H_2O$ solution (ratio 1:9) at a highly ordered pyrolytic graphite (HPOG) surface via ex-situ atomic force microscopy [13]. Deposition was investigated in conjunction with potentiostatic experiments. Current-time transients revealed two distinct regions. Initially slow current increase was observed followed by a region of steep current growth. AFM analysis of the electrode surface in the region of slow current increase revealed the presence of isolated growth centres across the electrode surface. Related compositional investigation via x-ray microanalysis indicated growth centres to be composed primarily of zinc suggesting preferential deposition of zinc versus cobalt [14]. AFM investigation during the second zone of the current-time transient showed the dendritic growth of electrodeposited material. Compositional analysis showed dendrites to be composed primarily of cobalt [14].

Harris et al describe deposition of a zinc-cobalt alloy from a solution identical to that of Gómez et al using ex-situ atomic force microscopy. These workers showed the growth of deposits with approximate height 50 nm during the early stages of alloy formation [15]. The continued deposition of material in a lateral direction at step edges was noted.

Kondo et al report studies of zinc-iron alloy deposition from aqueous zinc and iron sulphate solution containing an Sn^{2+} additive at a steel substrate [16]. Using ex-situ atomic force microscopy, these workers report the growth of hexagonal columnar crystals. The top surface of the crystal was observed to be covered with lateral macrosteps and nanometer-sized microsteps suggesting lateral growth of the crystal structure. X-ray diffraction indicated alloys to be 96.6% zinc rich.

An ex-situ AFM study by Park et al investigated zinc-iron alloy electrodeposition at a steel substrate from an identical solution in the absence of Sn^{2+} [17,18]. These workers described a fish-scale like alloy structure across the electrode surface.

8.3 Application of atomic force microscopy to the study of zinc deposition in the present work

The voltammetric techniques we have implemented for the study of Bu^n-ZDTP redox activity have provided information averaged over the entire electrode surface. Complimentary to such methods, the AFM is a valuable tool for the study of electrode processes providing site specific information at high resolution. We have applied atomic force microscopy to the direct observation of zinc nucleation at both glassy carbon and platinum electrode substrate materials during Bu^n-ZDTP reduction.

Previous studies describing the morphology of zinc electrodeposition processes can be found in the literature. However, these reports are largely confined to scanning electron (SEM) [19,20,21,22] and transmission electron micrographic techniques (TEM) [23,24,25]. These methods can only provide resolution on a scale of μms [8]. Furthermore, UHV conditions are required and imaging of surfaces is consequently limited to ex-situ conditions. In contrast, the AFM permits in-situ imaging of electrode surfaces at a resolution in the region of nms [8]. In addition to the reported use of SEM and TEM in the study of zinc electrodeposition, the use of atomic force microscopy has been described. AFM studies of zinc electrodeposition have been reviewed in §8.2.1. We note that reports are confined to ex-situ investigations. One study considers deposition of zinc while the remainder are concerned with the formation of zinc-alloy deposits. The work described in this chapter therefore represents one of the first applications of atomic force microscopy to the study of zinc electrodeposition.

We applied ex-situ atomic force microscopy to the study of Bu^n-ZDTP reduction at both glassy carbon and platinum electrode surfaces. Nucleation morphology under cyclic and RDE voltammetric conditions at both electrode substrate materials are compared. We also sought to implement in-situ electrochemical atomic force microscopy for the direct observation of the zinc nucleation process during Bu^n-ZDTP reduction. We note that these investigations represent the first reported application of atomic force microscopy to the study of the filming action of a ZDTP compound.

8.4 Ex-situ atomic force microscopy in conjunction with cyclic voltammetry

8.4.1 Experimental

Ex-situ AFM imaging of zinc nucleation following Bu^n-ZDTP reduction under cyclic voltammetric conditions was carried out at both glassy carbon and platinum surfaces using the electrode construction described in §3.3.4. This electrode configuration allowed for attachment to the AFM head assembly following removal of the electrode from solution. Glassy carbon and platinum surfaces of nominal diameters 3 and 4 mm were used respectively. Prior to Bu^n-ZDTP reduction, the electrode was polished using the procedure detailed in §3.3.2 to ensure a flat surface area. The electrode surface was imaged prior to zinc deposition to show the absence of nucleation features on the electrode surface.

Deposition of zinc was carried out under conditions identical to those previously employed for the cyclic voltammetric study of Bu^n-ZDTP in §6.3.1. This facilitated correlation of results obtained with those previously described. Thus zinc reduction was carried out using a 1 mM Bu^n-ZDTP solution in DMF containing 0.1 M NBu_4ClO_4 as supporting electrolyte. A scan rate of 50 mV s^{-1} was employed. A temperature of 25 ^{0}C was maintained throughout. The working electrode was scanned reductively from 0 V to a potential of –1.7 V well beyond the voltage at which the zinc deposition process occurs. The potential was held at –1.7 V and the electrode disconnected from the potentiostat for transfer to the AFM instrument.

8.4.2 Results

8.4.2.1 Glassy carbon

AFM images of the glassy carbon electrode surface prior to and at two different magnifications following zinc deposition are shown in Figures 8.1.a to c respectively. The surface image recorded before Bu^n-ZDTP reduction confirms the absence of nucleation features. The electrode appears flat with the most pronounced surface feature at a height of 17 nm. Scratch lines on the electrode which result from the surface polishing procedure are clearly visible.

Following zinc deposition, the appearance of nucleated sites on the electrode surface are observed with a maximum height of 202 nm. A range of different sized nuclei are apparent concurrent with the progressive nuclear growth mechanism described in §7.6.3.1. Approximate nuclear diameters observed in Figure 8.1.c range between 50 and 300 nm. Nucleated sites appear to be distributed randomly across the entire electrode surface.

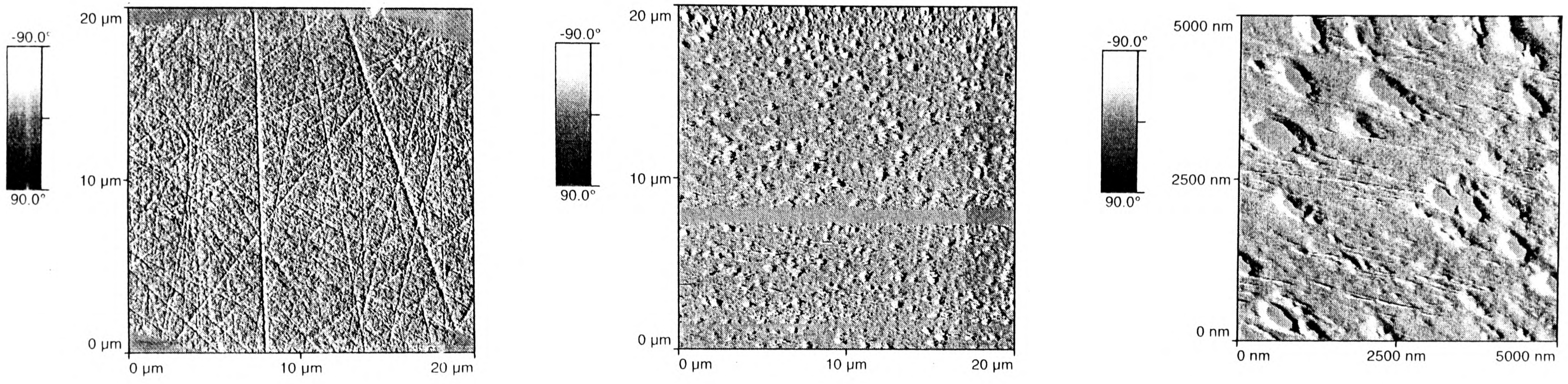

(a)

(b)

(c)

Figure 8.1: AFM image of a glassy carbon electrode surface (a) prior to and (b,c) following zinc deposition via reduction of 1 mM Bu^n-ZDTP in DMF/0.1 M NBu_4ClO_4 solution under cyclic voltammetric conditions employing a potential scan of 0 to −1.7 V versus SCE, scan rate 50 mV s^{-1}. Scales of 20 and 5 µm are shown in (b) and (c) respectively.

8.4.2.2 Platinum

AFM images of the platinum surface prior to and following Bu^n-ZDTP reduction are shown in Figures 8.2.a and b. As for glassy carbon, the electrode surface shows the absence of nucleation features before zinc deposition. The electrode is flat with the most pronounced surface feature at a height of 50 nm. Scratch lines arising from the electrode polishing procedure are clearly visible.

Following Bu^n-ZDTP reduction, the majority of the platinum electrode surface appears bare. It is likely that a monolayer of deposited zinc material is covering the electrode surface as indicated by cyclic voltammetry but that this remains unresolved at the resolution of this image. A small amount of nucleated material is clearly visible concentrated along a scratch line. This is in contrast to the case for glassy carbon where nucleated sites appeared to be distributed randomly across the electrode surface. This is consistent with cyclic voltammetry at the platinum electrode where a small peak correlating to zinc nucleation was apparent. It appears that nucleation of zinc on platinum under these experimental conditions is confined to scratch line sites. Zinc nuclei have a maximum height of 113 nm.

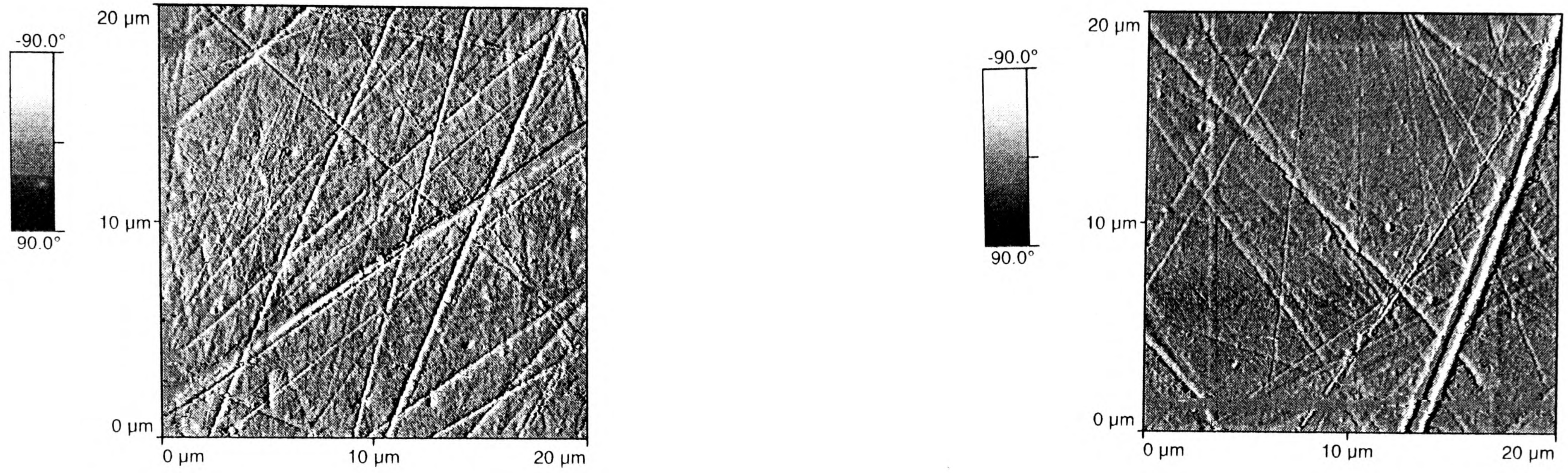

(a)

(b)

Figure 8.2: AFM image of a platinum electrode surface (a) prior to and (b) following zinc deposition via reduction of 1 mM Bu^n-ZDTP in DMF/0.1 M NBu_4ClO_4 solution under cyclic voltammetric conditions employing a potential scan of 0 to –1.7V versus SCE, scan rate 50 mV s^{-1}.

8.5 Ex-situ atomic force microscopy in conjunction with RDE voltammetry

8.5.1 Experimental

Ex-situ AFM imaging of zinc nucleation following Bu^n-ZDTP reduction under RDE voltammetric conditions was carried out at both glassy carbon and platinum surfaces using the electrode construction described in §3.4.4. As for cyclic voltammetry, the electrode was polished prior to Bu^n-ZDTP reduction using the procedure detailed in §3.3.2 to ensure a flat surface area. The electrode surface was imaged prior to zinc deposition to confirm the absence of nucleation features.

Deposition of zinc was carried out under conditions identical to those previously employed for the RDE voltammetric study of ZDTP described in §6.4.1. This facilitated correlation of results to those previously obtained. Thus zinc reduction was carried out using a 1 mM Bu^n-ZDTP solution in DMF containing 0.1 M NBu_4ClO_4 as supporting electrolyte. Investigations employed a scan rate of 5 mV s^{-1} and a rotation speed of 30 Hz. A temperature of 25 ^{0}C was maintained throughout. The working electrode was scanned reductively from 0 V to a potential of –1.7 V well beyond the voltage at which the zinc deposition process occurs. The potential was held at –1.7 V and the electrode disconnected from the potentiostat and RDE holder for transfer to the AFM instrument.

8.5.2 Results

8.5.2.1 Glassy carbon

AFM images of the glassy carbon electrode surface prior to and at two different magnifications following zinc deposition are shown in Figures 8.3.a to c respectively. The surface image recorded before Bu^n-ZDTP reduction confirms the absence of nucleation features. The electrode appears flat with the most prominent surface feature at a height of 13 nm.

Following zinc deposition, nucleated sites are clearly visible with active sites distributed randomly across the entire electrode surface. Upon comparison with Figures 8.1.b and c for zinc deposition under cyclic voltammetric conditions, we note that the density of growth sites is increased. This reflects the nature of the RDE experiment where continued growth of active sites is possible. This is in contrast to cyclic voltammetry where nuclear growth is limited by mass transport control. As for cyclic voltammetry at a glassy carbon surface, a range of nuclear sizes are observed consistent with a progressive nucleation and growth mechanism. A maximum nuclear height of 623 nm is observed with approximate nuclear diameters ranging between 200 and 700 nm.

8.5.2.2 Estimation of electroactive surface area

We noted a discrepancy between the limiting currents obtained for oxidation and reduction of Bu^n-ZDTP during the RDE voltammetric investigation described in §6.4.2.3. Both redox processes comprise the transfer of 2 electrons but the current for Bu^n-ZDTP reduction was significantly lower than that observed for oxidation. This was attributed to the nature of the nucleation process where deposition is confined to growth centres which effectively limit the electroactive area of the electrode.

Using Figure 8.3.b, an estimate of the electroactive area in terms of percentage nucleated surface was made. An areal density of approximately 70% is observed. This correlates well to limiting currents measured for Bu^n-ZDTP oxidation and reduction under identical conditions at a glassy carbon RDE where a reduction:oxidation current ratio of 0.75 was obtained.

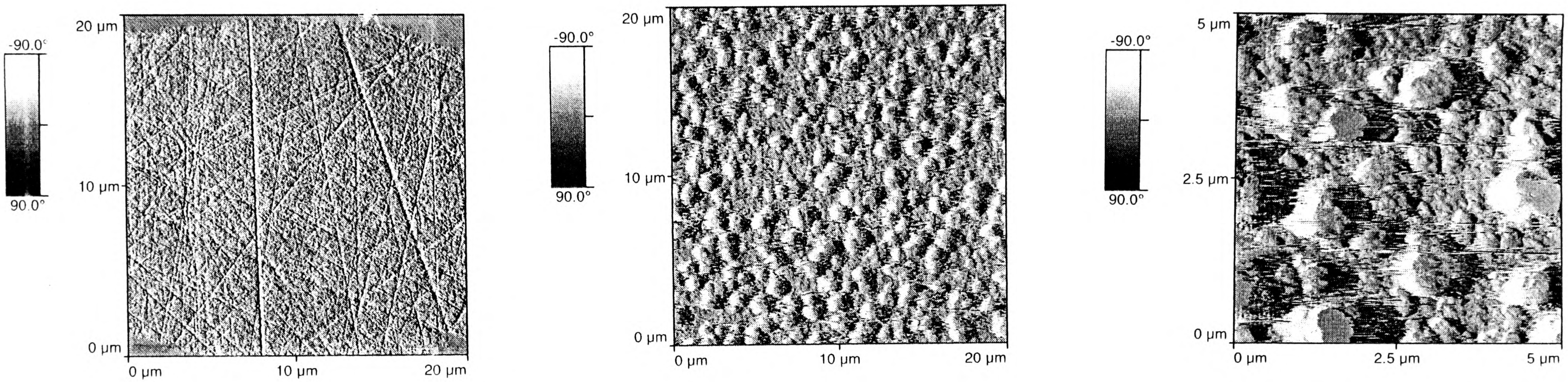

(a) (b) (c)

Figure 8.3: AFM image of a glassy carbon electrode surface (a) prior to and (b,c) following zinc deposition via reduction of 1 mM Bu^n-ZDTP in DMF/0.1 M NBu_4ClO_4 solution under RDE voltammetric conditions employing a potential scan of 0 to −1.7 V versus SCE, scan rate 5 mV s^{-1}. Scales of 20 and 5 µm are shown in (b) and (c) respectively.

8.5.2.3 Platinum

AFM images of the platinum surface prior to and following zinc deposition are shown in Figures 8.4.a and b. The surface image recorded prior to Bu^n-ZDTP reduction confirms the absence of nucleation features. The electrode appears flat with the most pronounced surface feature at a height of 50 nm.

Following reduction of Bu^n-ZDTP, zinc nuclei are observed to be distributed across the electrode surface. This is in contrast to the largely bare electrode surface observed following Bu^n-ZDTP reduction at a platinum electrode under cyclic voltammetric conditions. We attribute the ability of zinc to nucleate at the platinum surface under RDE voltammetric conditions to the decreased scan rate which allows sufficient time for zinc nuclei to form once the nucleation overpotential is reached. This reflects observations of cyclic and RDE voltammetry reported in §6.3.2.3 and 6.4.2.2.

As observed during zinc deposition under cyclic voltammetric conditions, a concentration of nuclear features is observed along scratch lines. In contrast to cyclic voltammetry, the remainder of the electrode surface is also covered with nuclear features with a number of significantly large zinc nuclei visible. Growth sites have a maximum height of 353 nm. Well-developed nuclei have approximate diameters in the range 100 to 600 nm. It is possible that these are associated with scratch lines at the electrode surface. The majority of nuclear sites across the platinum surface have approximate diameters of less than 50 nm. These nuclei appear less well-developed than those observed for Bu^n-ZDTP reduction under identical conditions on glassy carbon. This may reflect the increased hostility of the platinum surface to zinc deposition in comparison to glassy carbon which was noted in §6.3.2.3.

We were unable to make an accurate estimate of electroactive area in terms of percentage surface coverage as for glassy carbon. This was due to the large number of poorly defined nuclei covering the electrode surface in Figure 8.4.b.

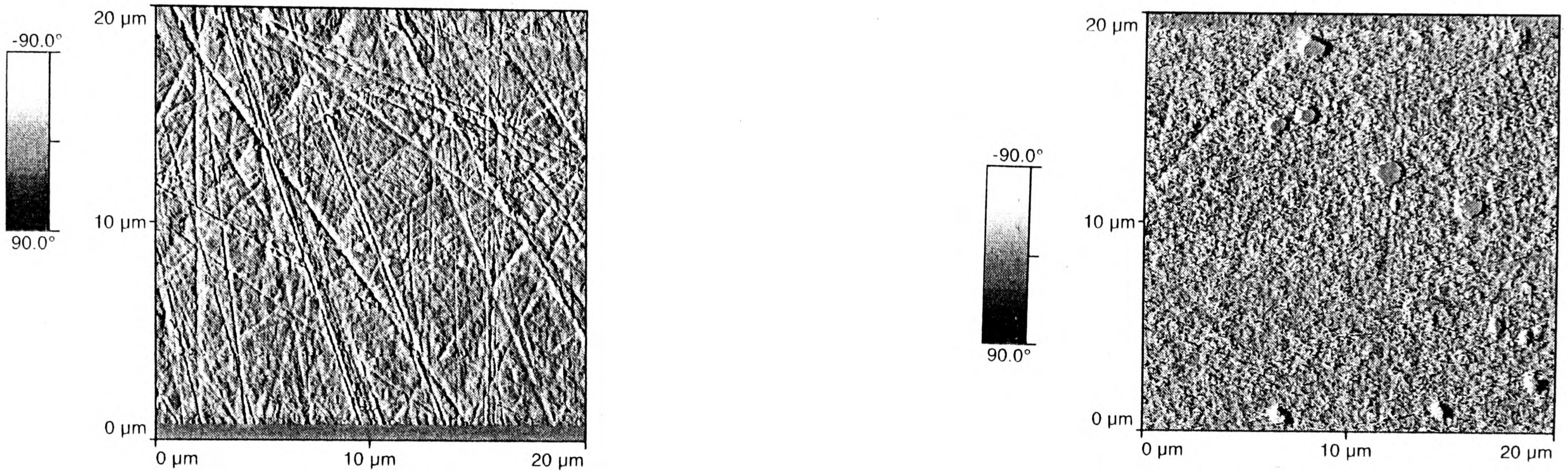

(a)

(b)

Figure 8.4: AFM image of a platinum electrode surface (a) prior to and (b) following zinc deposition via reduction of 1 mM Bu^n-ZDTP in DMF/0.1 M NBu_4ClO_4 solution under RDE voltammetric conditions employing a potential scan of 0 to −1.7 V versus SCE, scan rate 5 mV s^{-1}.

8.5.2.4 Comparison of zinc nucleation at glassy carbon and platinum surfaces

We have noted significant differences in zinc deposition at glassy carbon and platinum electrode surfaces. Nucleation on glassy carbon was observed to proceed across the entire electrode surface. Preferential deposition at scratch lines was not apparent.

In general, the platinum electrode appeared more hostile to zinc nucleation than glassy carbon. This is consistent with observations made during the voltammetric investigations described in Chapter 6. The AFM image following Bu^n-ZDTP reduction under cyclic voltammetric conditions revealed an electrode surface predominantly free of nucleation although some zinc growth centres were visible at scratch line sites. Bu^n-ZDTP reduction during RDE voltammetry revealed nucleation across the platinum surface but growth sites were considerably smaller than those previously observed on glassy carbon. We attribute the greater hostility of the platinum surface in comparison to glassy carbon to differences in surface energy of the two electrode substrate materials.

In contrast to observations of zinc nucleation on glassy carbon, we have noted the preferential deposition of zinc material at scratch lines on the platinum surface. We saw in §6.3.2.1 and 6.3.2.3 during cyclic voltammetric investigation at both electrode substrate materials that zinc deposition occurred at a lower overpotential of –1.34 V versus SCE on platinum in comparison to glassy carbon where a reduction potential of –1.41 V was observed. Since we would expect a lower overpotential to be associated with greater ease of deposition at the electrode surface, this is in direct contrast to the observations that platinum appears more hostile to zinc deposition than glassy carbon. The lower overpotential of Bu^n-ZDTP deposition on platinum may reflect preferential deposition of zinc at platinum scratch lines in comparison to the glassy carbon electrode surface.

8.6 In-situ atomic force microscopy

In-situ electrochemical AFM experiments were attempted for the direct visualisation of the zinc nucleation process. Experimental protocol comprised an in-situ AFM cell fabricated by the Physical and Theoretical Chemistry Laboratory Workshops of Oxford University. Cell design was based on the commercial in-situ electrochemical AFM cell produced by Topometrix (supplied by Topometrix, Santa Clara, CA, USA). It consisted of a fluid filled compartment containing silver/silver chloride reference and platinum counter electrodes with external electrical contacts. The working electrode comprised a disc of electrode substrate material set into a flat disc of Teflon. The working electrode was sealed into the cell and connected to a metal plate for attachment to the holding magnet on the AFM head using latex. Attachment also formed external electrical contact. Latex allowed for movement of the electrode inside the cell both in a lateral direction relative to the tip during scanning and vertically in response to tip-sample force interactions. The AFM tip was located at the base of the working electrode and was held in a stable position by means of a magnet sealed into the cell. A silica window formed the front of the cell which permitted the focus of laser light onto the cantilever to facilitate imaging of the sample. In-situ experiments were performed with the main AFM head located within an inert atmosphere to permit the rigorous exclusion of oxygen. An inert atmosphere was maintained using an argon filled Atmosbag™ (supplied by Aldrich, UK) which consisted of an inflatable polyethylene chamber containing gloves for manipulation of equipment. Control of potential was achieved using a commercial electrochemical package (supplied by Topometrix, Santa Clara, CA, USA).

We found the above experimental set-up to be unsuitable for the study of the experimental system under consideration. This was because the latex working electrode seal swelled in the presence of DMF solution over the timescale of the experiment. Further investigation is required in order to optimise cell conditions for this particular experimental system.

8.7 Summary

This work describes the first reported application of atomic force microscopy to the study of a ZDTP compound. The potential of this method as a promising technique for the study of ZDTP filming action has been demonstrated.

We have described the application of ex-situ atomic force microscopy to the study of zinc deposits formed during Bu^n-ZDTP reduction at both glassy carbon and platinum electrode surfaces. Nucleation morphology under cyclic and RDE voltammetric conditions at both electrode substrate materials was compared. Deposition of zinc from a 1 mM Bu^n-ZDTP solution on glassy carbon during cyclic voltammetry revealed isolated growth centres distributed across the electrode surface consistent with a nucleated process. Active sites varied in size concurrent with a progressive nucleation mechanism. Reduction of Bu^n-ZDTP under the same conditions on platinum showed the absence of nucleation features over most of the electrode surface. Some nucleation was visible at scratch lines. The presence of underdeposited zinc material is not visible due to insufficient resolution of the AFM image.

Deposition of zinc on glassy carbon from a 1 mM Bu^n-ZDTP solution during RDE voltammetry revealed an increased density of growth sites at the electrode surface. This reflects the nature of the RDE experiment where continued growth of active sites is possible. This is in contrast to cyclic voltammetry where nuclear growth is limited by mass transport control. An estimate of the electroactive area in terms of percentage nucleated surface correlated well with the observed discrepancy of Bu^n-ZDTP oxidation and reduction currents reported in Chapter 6. Bu^n-ZDTP reduction on platinum under identical conditions revealed the growth of zinc nuclei across the electrode surface but these were mostly less well developed than nuclei observed on glassy carbon.

We have described attempts to obtain in-situ AFM images of zinc deposition at both glassy carbon and platinum electrode substrate materials. These investigations proved unsuccessful due to equipment failure.

References

[1] J. V. Zoval, R. B. Stiger, P. R. Biernacki, R. M. Penner, J. Phys. Chem., 1996, **100**, 837

[2] V. Darrort, M. Troyan, J. Ebothé, C. Bissieux, C. Nicollin, Thin Solid Films, 1995, **265**, 52

[3] G. Wouters, M. Bratoeva, J.-P. Celis, J. R. Roos, Electrochimica Acta, 1995, **40**, 10, 1434

[4] S. Manne, P. K. Hansma, J. Massie, V. B. Elings, A. A. Gewirth, Science, 1991, **251**, 183

[5] N. Ikemiya, K. Yamada, S. Hara, Surface Science, 1996, **348**, 253

[6] Ch. Chen, S. M. Vesecky, A. A. Gewirth, J. Am. Chem. Soc., 1992, **114**, 451

[7] Ch. Chen, N. Washburn, A. A. Gewirth, J. Phys. Chem., 1993, **97**, 9754

[8] D. Aurbach, Y. Cohen, J. Electrochem. Soc., 1996, **143**, 11, 3525

[9] Ch. Chen, A. A. Gewirth, Phys. Rev. Lett., 1992, **68**, 10, 1571

[10] M. Ge, A. A. Gewirth, Surface Science, 1995, **324**, 140

[11] K. Kowal, L. Xie, R. Huq, G. C. Farrington, J. Electrochem. Soc., 1994, **141**,1, 116

[12] K. Kondo, T. Murakami, F. Czerwinski, K. Shinohara, ISIJ International, 1997, **37**, 2, 140

[13] E. Gómez, E. Vallés, P. Gorostiza, J. Servat, F. Sanz, J. Electrochem. Soc., 1995, **142**, 12, 4091

[14] M. L. Alcalá, E. Gómez, E. Vallés, J. Electroanal. Chem., 1994, **370**, 73

[15] S. J. Harris, F. B. Li. I. R. McColl, P. J. Borden, The Electrochemical Soc. Extended Abstract, 1995, Oct., Chicago

[16] F. Czerwinski, K. Kondo, J. A. Szpunar, , J. Electrochem. Soc., 1997, **144**, 2, 481

[17] H. Park, F. Czerwinski. J. A. Szpunar, Proceedings of the Electrochemical Society, Second Symposium

on Electrochemically Deposited Thin Films II (Editor M. Psunovic), PV 94-31, NJ, 1994

[18] H. Park, F. Czerwinski. J. A. Szpunar, Mater. Sci. Forum, 1996, **204-206**, 703

[19] K. Kamei, Y. Ohmori, J. Appl. Electrochem., 1987, **17**, 821

[20] Y. Ohmori, K. Nakai, H. Ohtsubo, T. Yagi, T. Matsumoto, ISIJ Int., 1993, **33**, 11, 1196

[21] Y. Ohmori, K. Nakai, H. Ohtsuba, T. Yagi, T. Matsumoto, ISIJ Int., 1994, **34**, 12, 1002

[22] K. Kamei, J. Jpn. Inst. Met., 1988, **52**, 743

[23] A. Seki, K. Kamei, ISIJ Int., 1992, **32**, 12, 1306

[24] H. Yan, J. Downes, P. J. Boden, S. J. Harris, Philosphical Magazine A, 1994, **70**, 2, 391

[25] H. Yan, J. Downes, P. J. Boden, S. J. Harris, J. Electrochem. Soc., 1996, **143**, 5, 1577

Chapter 9

Preliminary studies of Bu^n-ZDTP voltammetry at elevated temperatures and in resistive solvent media

9.1 Introduction

Last, we sought to extend the study of Bu^n-ZDTP redox activity under standard electrochemical conditions to investigations more typical of the engine environment. This chapter describes preliminary studies of Bu^n-ZDTP redox activity at elevated temperatures and in resistive solvent media. In §9.2 we describe application of the elevated temperature voltammetric apparatus to the study of Bu^n-ZDTP redox behaviour. We then move to consider voltammetry in the resistive solvent medium toluene in §9.3. We conclude the chapter with a summary of conclusions drawn in §9.4.

9.2 High temperature investigations

9.2.1 Application of the elevated temperature voltammetric apparatus to the study of Bu^n-ZDTP

Since we know that ZDTPs perform both anti-wear and anti-oxidant functions at the elevated temperatures of an engine environment, we implemented the novel elevated temperature voltammetric apparatus in a study of Bu^n-ZDTP redox chemistry. This served as a more meaningful investigation of Bu^n-ZDTP voltammetry in relation to working environment than that conducted under standard electrochemical conditions in Chapter 6.

9.2.2 Experimental

Steady-state voltammograms were recorded for a 1 mM solution of Bu^n-ZDTP in DMF using 0.1 M NBu_4ClO_4 as supporting electrolyte. Waves were obtained at temperatures ranging between 20 and 80 ^{0}C using a 10 μm diameter platinum working electrode. An accurate value for the electrode diameter was obtained via electrochemical calibration prior to use using a standard ferrocene solution.

9.2.3 Results

9.2.3.1 Bu^n-ZDTP oxidation

The single Bu^n-ZDTP oxidation wave was observed at an $E_{1/2}$ value of + 0.63 V versus the platinum pseudo reference electrode. A representative voltammogram recorded at a temperature of 21 ^{0}C is shown in Figure 9.1. The $E_{1/2}$ obtained is in good agreement with the E_p and $E_{1/2}$ values recorded for Bu^n-ZDTP oxidation during cyclic and RDE voltammetric investigations described in §6.3 and 6.4 respectively. Limiting currents obtained for the oxidation of Bu^n-ZDTP at each temperature are given in Table 9.1. Reported I_{lim} values are an average of 5 steady state waves recorded for each temperature. Diffusion coefficients calculated using the theoretical expression for the diffusion limited current at a microelectrode previously defined in Equation 2.33 are also recorded in Table 9.1. In line with the RDE investigation reported in §6.4.2.5, a 2 electron transfer step was assumed.

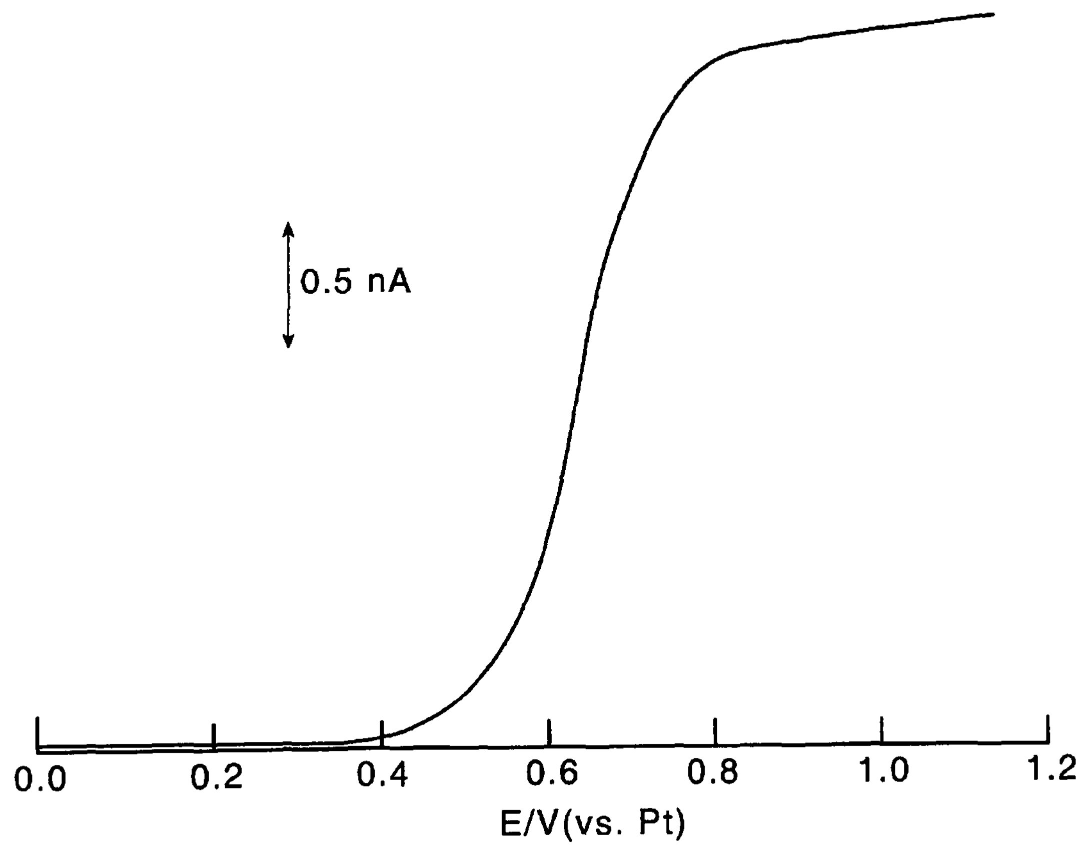

Figure 9.1: Steady state voltammogram for oxidation of 1 mM Bu^n-ZDTP in DMF/0.1 M NBu_4ClO_4 solution recorded using a 10 μm diameter platinum microelectrode at 21 ^{0}C, scan rate 10 mV s^{-1}.

Temperature (^{0}C)	I_{lim} (A)	D (cm^2 s^{-1})
21	2.64×10^{-9}	$6.44\times10^{-6} \pm 0.5\times10^{-6}$
30	3.14×10^{-9}	$7.67\times10^{-6} \pm 0.6\times10^{-6}$
40	3.72×10^{-9}	$9.08\times10^{-6} \pm 0.7\times10^{-6}$
50	4.30×10^{-9}	$1.05\times10^{-5} \pm 0.8\times10^{-6}$
60	4.95×10^{-9}	$1.21\times10^{-5} \pm 1.0\times10^{-5}$
70	5.87×10^{-9}	$1.43\times10^{-5} \pm 1.1\times10^{-6}$
80	6.64×10^{-9}	$1.62\times10^{-5} \pm 1.3\times10^{-6}$

Table 9.1: Limiting currents and diffusion coefficients obtained for oxidation of 1 mM Bu^n-ZDTP in DMF/0.1 M NBu$_4$ClO$_4$ solution using a 10 μm diameter electrode at temperatures ranging from 21 to 80 ^{0}C

We note that the diffusion coefficient obtained at 21 ^{0}C is in good agreement with previous values measured via RDE voltammetry and chronoamperometry at 25 ^{0}C as described in §6.4.2.5 and 7.6.3.3 respectively. An Arrhenius plot of ln D versus 1/T gave the linear correlation shown in Figure 9.2. From this graph, the activation energy for diffusion of Bu^n-ZDTP in DMF was estimated to be 13.4 ± 1.0 kJ mol^{-1}. This is in good agreement with the E_a of 14.4 ± 1.2 kJ mol^{-1} reported for the diffusion of ferrocene in DMF in §5.4.6.

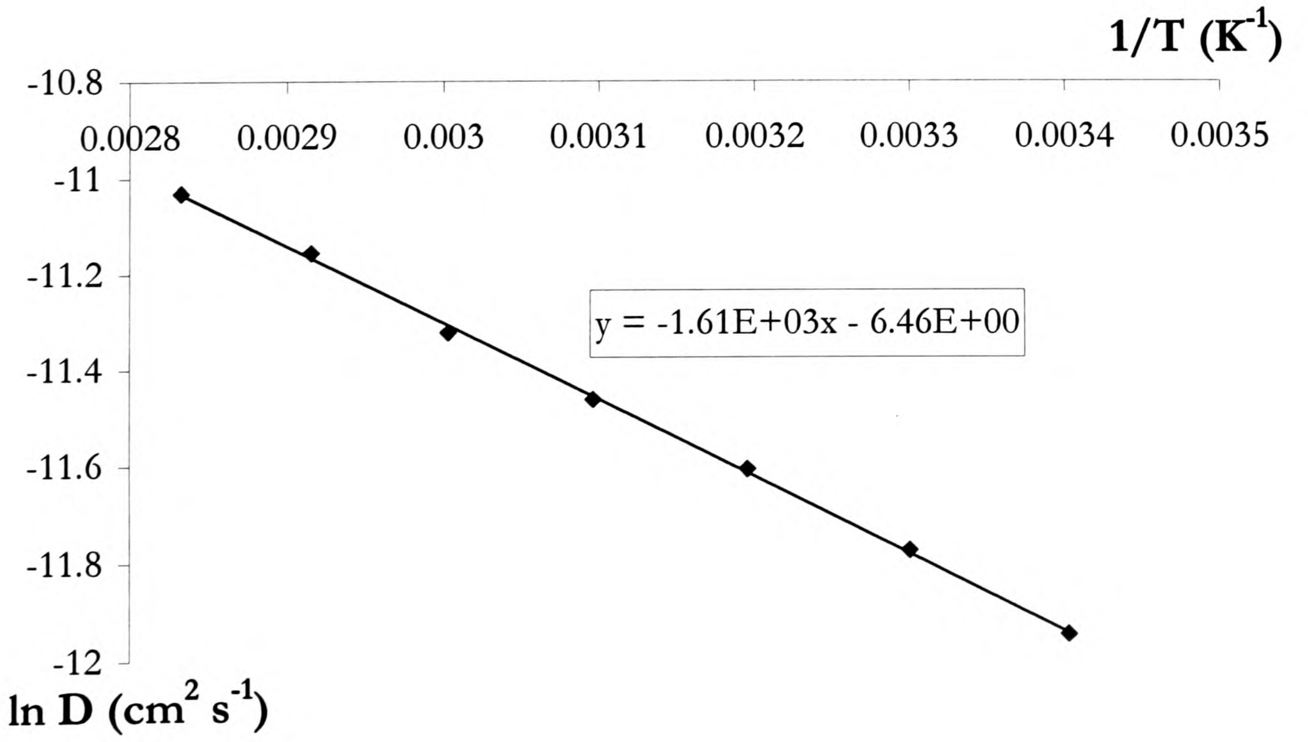

Figure 9.2: ln D versus 1/T for Bu^n-ZDTP in DMF/0.1 M NBu$_4$ClO$_4$ solution

9.2.3.2 Bu^n-ZDTP reduction

Under the conditions employed during our investigation, Bu^n-ZDTP reduction waves appeared irreproducible and poorly defined. Thus no meaningful data was obtained. We attributed this to fouling of the electrode during zinc deposition. Furthermore, during voltammetry at ambient temperatures, we noted that thorough solution degassing was necessary in order to obtain reproducible reduction data. It is therefore likely that the zinc reduction process is very sensitive to the presence of adventitious oxygen which we were unable to remove from our experimental system.

9.2.4 Conclusions

We have described application of the elevated temperature microelectrode apparatus to the study of Bu^n-ZDTP. This investigation represents the first attempt, as far as we are aware, to mimic the engine environment during the voltammetric study of a ZDTP compound.

Limiting currents for Bu^n-ZDTP oxidation were recorded at temperatures ranging between 21 and 80 ^{0}C. From these, diffusion coefficients at each temperature were calculated. The diffusion coefficient obtained at 21 ^{0}C was in good agreement with values of D previously measured for this compound at room temperature via alternative techniques. An Arrhenius plot of ln D versus 1/T yielded the E_a for diffusion of Bu^n-ZDTP in DMF solution as being 13.4 ± 1.0 kJ mol^{-1}.

Investigation of the Bu^n-ZDTP reduction process via this technique gave poorly defined and irreproducible steady state waves. We attributed the poor quality of the data obtained to electrode fouling during zinc deposition and the presence of adventitious oxygen which we were unable to remove from our experimental system. Possible improvements to our experimental design as a means of investigating Bu^n-ZDTP reduction at elevated temperatures are considered in Chapter 10.

9.3 Resistive solvent investigations

9.3.1 Application of resistive solvents to the study of Bu^n-ZDTP

As a first step to conducting a study of Bu^n-ZDTP redox activity in oil, we attempted to investigate the voltammetry of this compound in toluene. This solvent has a dielectric constant of 2.38 at 20 ^{0}C in contrast to values of 37.5 and 36.7 reported for acetonitrile and DMF respectively [1] and therefore serves as a suitable model for a poorly-conducting oil medium. In addition, a number of literature studies have considered voltammetry in toluene and have described the necessary conditions. A survey of the literature pertaining to voltammetric investigation in toluene follows.

9.3.2 Literature reports of voltammetry in toluene

We noted previously in §1.8.1 the difficulties associated with voltammetry in resistive media where current-voltage curves appear greatly distorted from the reversible Nernstian shape as a result of ohmic drop. We also described the application of microelectrodes to the study of redox processes in poorly conducting media. A summary of the literature concerned with the application of microelectrodes to voltammetric investigation in resistive solvents has been presented in §1.8.1. A more detailed review of the literature pertaining to voltammetric investigation in toluene follows.

Bond and Mann report the oxidation of ferrocene in toluene solution with 0.1 M $NHex_4ClO_4$ as supporting electrolyte using platinum microelectrodes at a range of diameters and varying ferrocene concentrations [2]. Current-voltage curves recorded at a concentration of 1 mM were observed to be grossly distorted from the reversible diffusion controlled shape with the slope of E versus $\log(I_{lim}/I-1)$ in the region of 200 mV. Essentially distortion free voltammograms were obtained with electrode diameters less than or equal to 1 μm and ferrocene concentrations in the region of 0.1 mM. Increased electrode sizes up to 25 μm in diameter gave an ideal result when ferrocene:electrolyte support ratios were increased by lowering the ferrocene concentration to 0.01 mM.

The same research group describe copper diethyldithiocarbamate $Cu(dedtc)_2$ redox activity in toluene at 10 μm platinum microelectrodes using $NHex_4ClO_4$ and $NHex_4PF_6$ as supporting electrolytes [3]. Near ideal responses were obtained using 1 mM $Cu(dedtc)_2$ and 0.1 M concentrations of electrolyte. Decreasing electrolyte concentrations showed increasing iR drop effects with no useful redox response observed below 0.01 M.

In a further study, Bond's group attributed the requirement of high support ratios to the low permittivity of the toluene solvent which acts as an inhospitable environment to ions with subsequent ion pairing and a decrease in the availability of ions for conduction of current [4]. These workers examined the redox activity of $Cu(dedtc)_2$, $NHex_4Br$ and $AgClO_4$. Voltammograms were recorded at 10 μm diameter platinum microelectrodes using $NHex_4PF_6$ as supporting electrolyte. For all species, voltammograms were recorded over a range of support ratios. At ratios in excess of 100, distortion free voltammograms were observed. With decreasing supporting electrolyte, waves became increasingly drawn out as a result of ohmic distortion. Effects of support ratio on limiting current were also investigated. In the case of the neutral $Cu(dedtc)_2$ species, I_{lim} appears to be independent of electrolyte concentration. Thus for an uncharged species undergoing reduction or oxidation to a charged species, I_{lim} is diffusion controlled and independent of the extent of ion pairing in the supporting electrolyte. By contrast, voltammetry of the charged Br^- and Ag^+ species showed a decrease in I_{lim} as the support ratio was increased. This reflects the diffusivity of the ion pair formed between the electroactive ion and counter ion of the supporting electrolyte at increased electrolyte concentration.

Murray et al report voltammetry in toluene for a range of different species at 0.01 mM concentrations using 10 μm diameter platinum microelectrodes and 0.1 M $NHex_4ClO_4$ as supporting electrolyte [5]. In a further study using identical reaction conditions, these workers report voltammetry of tetraphenylporphyrin complexes in toluene as a means of comparing ligand complexation and acid-base phenomena with reactivity noted in less resistive solvents [6]. No obvious signs of solution resistance in the voltammograms was reported.

Amatore and Pflüger report oxidation of tetrakis(triphenylphosphine)-palladium(0), $Pd^0(PPh_3)_2$, in toluene solution [7]. This study was conducted as part of an investigation to measure rates of oxidative addition of iodobenzenes to the $Pd^0(PPh_3)_2$ species. Voltammograms for the oxidation of $Pd^0(PPh_3)_2$ were recorded at 10 μm platinum microelectrodes using 0.06 M $NHex_4BF_4$ as electrolyte. The decrease in I_{lim} in the presence of known quantities of various iodonitrobenzenes was monitored as a measure of rate of oxidative addition. These workers report some ohmic distortion at the substrate:electrolyte support ratios used.

9.3.3 Experimental

During our study of Bu^n-ZDTP voltammetry in toluene we chose to use $NHex_4PF_6$ as the supporting electrolyte. This compound has been shown by a number of workers to be suitable for voltammetric work in toluene since it gives a 4 V potential range, is easily handled and has adequate solubility at ambient temperatures [3,4]. Steady state waves were recorded using toluene solutions containing 0.01 mM Bu^n-ZDTP together with 0.1 M $NHex_4PF_6$ to give substrate:electrolyte support ratios of 10000. Such support ratios have previously been shown by Bond et al to give voltammograms which are essentially free of ohmic effects [2,3,4]. Solutions were made up via dilution of 1 ml aliquots of a 0.5 mM Bu^n-ZDTP/toluene solution to ensure accuracy at such low concentrations of Bu^n-ZDTP. Waves were recorded using a 10 μm diameter platinum microelectrode. An accurate value was determined prior to use via electrochemical calibration at 25 ^{0}C using a standard ferrocene/acetonitrile solution. The temperature of the solution was maintained at 25 ^{0}C throughout the investigation. Voltammograms were recorded versus a platinum pseudo reference electrode.

9.3.4 Results

9.3.4.1 Voltammetry of ferrocene in toluene using microelectrodes of variable radii

We first aimed to reproduce the voltammetry of ferrocene in toluene described by previous investigators [2,5]. Although microelectrode voltammetry of ferrocene in toluene has been reported by both Bond et al and Murray et al, their discussions have been limited to a consideration of wave shape and peak potential respectively. In contrast, we report limiting currents obtained at variable electrode radii as a means of estimating the diffusion coefficient of ferrocene in toluene.

Steady-state voltammograms were recorded for a 0.01 mM ferrocene solution with 0.1 M $NHex_4PF_6$ as supporting electrolyte. Waves were obtained using microelectrodes with nominal electrode diameters ranging between 5 and 50 μm with the temperature of the solution maintained at 25 ^{0}C throughout. Accurate values for electrode radii were obtained prior to use via electrochemical calibration using a standard ferrocene/acetonitrile solution.

A single wave was observed for ferrocene oxidation with an $E_{1/2}$ of +0.5 V versus the platinum pseudo reference electrode. This compares to a value of +0.9 V versus a pseudo silver reference electrode reported by Murray et al using 0.1 M $NHex_4ClO_4$ as supporting electrolyte [5]. Limiting currents obtained for the oxidation of ferrocene at each electrode radius are given in Table 9.2. Reported I_{lim} values are an average of 5 steady state waves recorded for each electrode.

Electrode diameter (μm)	I_{lim} (A)
5.3	$1.76x10^{-11}$
10.0	$3.00x10^{-11}$
25.2	$8.35x10^{-11}$
50.2	$1.67x10^{-10}$

Table 9.2: Limiting current values obtained for oxidation of 0.01 mM ferrocene in toluene/0.1 M $NHex_4PF_6$ solution using microelectrodes of variable diameter at 25 ºC

From the theoretical expression for the diffusion limited current at a microdisc electrode previously given in Equation 2.33, a plot of I_{lim} versus 4nFca will have a slope equivalent to D. I_{lim} versus 4nFca for the values recorded in Table 9.2 is shown in Figure 9.3, from which the diffusion coefficient for ferrocene in toluene is estimated as being $1.74x10^{-5} \pm 1.4x10^{-6}$ cm^2 s^{-1}. This represents, to the best of our knowledge, the first reported value of D for ferrocene in this solvent medium.

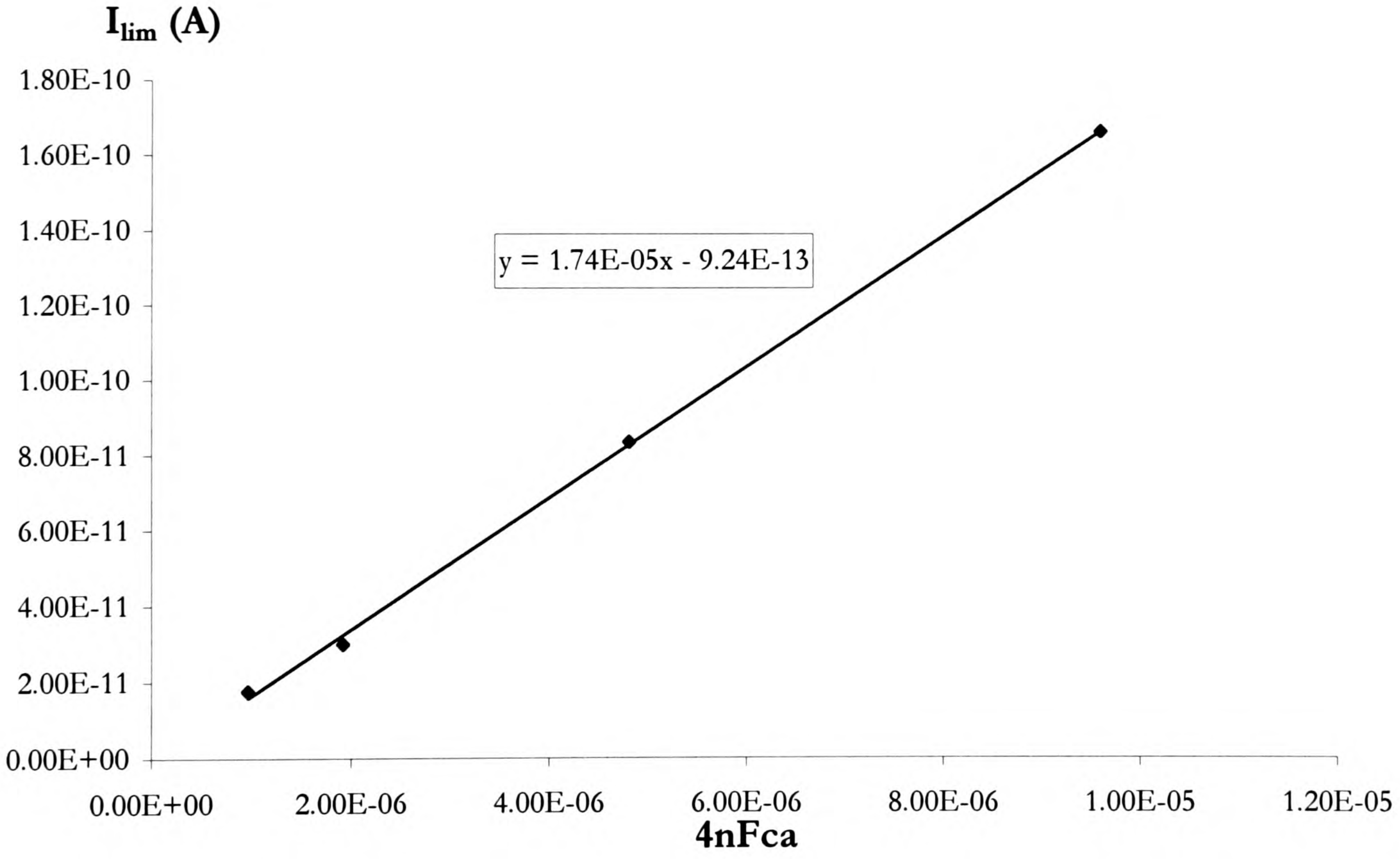

Figure 9.3: I_{lim} versus 4nFca for oxidation of 0.01 mM ferrocene in toluene/0.1 M $NHex_4PF_6$ solution using microelectrodes of variable diameter at 25 ºC

9.3.4.2 Bu^n-ZDTP in toluene

We confined our study to Bu^n-ZDTP oxidation since this has been shown in

Chapter 6 to proceed via a simple 2 electron transfer in DMF without complicating nucleation processes attendant during reduction. We were, however, unable to investigate oxidation of Bu^n-ZDTP in toluene due to the presence of a solvent contaminant peak in the potential region expected for the Bu^n-ZDTP response. Although the peak current of the contaminant species was low, of the order of 0.7 nA, it was significant in terms of the low concentrations of Bu^n-ZDTP which must necessarily be used in order to overcome ohmic distortion.

We suggest that for the further study of Bu^n-ZDTP redox activity in toluene, solvent purification is necessary. Increasing the concentration of Bu^n-ZDTP as a means of increasing measurable oxidation current is not possible since this will lower substrate:electrolyte support ratios thereby introducing ohmic distortion into the redox response. Increasing the concentration of supporting electrolyte is not an option due to the limited solubility of tetrahexylammonium salts in toluene at room temperature [2,3,6,7]. Possible experimental strategies which could be implemented as a means of overcoming solvent contamination are considered in Chapter 10.

9.3.5 Conclusions

From a review of the literature and by an investigation of ferrocene oxidation in toluene, we have shown that voltammetry in toluene is possible with the application of microelectrodes and using $NHex_4PF_6$ as supporting electrolyte. Using microelectrodes of varying diameters, we have obtained, as far as we are aware, the first reported value for the diffusion coefficient of ferrocene in this solvent medium. We were, however, unable to investigate oxidation of Bu^n-ZDTP in toluene due to the presence of a contaminant peak in the potential region of the Bu^n-ZDTP response.

9.4 Summary

During this chapter we have described a preliminary investigation of Bu^n-ZDTP redox activity under conditions typical of an engine environment, namely at elevated temperatures and in resistive solvent media.

Using the novel variable temperature apparatus previously described in Chapter 4, limiting currents for the oxidation of Bu^n-ZDTP in DMF have been measured at temperatures ranging between 21 and 80 ^{0}C. From this data, the activation energy for diffusion of Bu^n-ZDTP through this solvent medium has been calculated. Our investigation of Bu^n-ZDTP reduction at elevated temperatures was less successful since waves appeared irreproducible and poorly defined. We attributed this to electrode fouling and the presence of oxygen which we were unable to completely remove from the apparatus prior to the experiment.

Voltammetry of Bu^n-ZDTP in the resistive solvent toluene was attempted as a convenient model for oil. The oxidation of ferrocene in toluene was studied as a means of assessing our experimental procedure prior to the investigation of Bu^n-ZDTP. Limiting currents obtained using microelectrodes of varying radii were used to estimate the diffusion coefficient of ferrocene which represents, to the best of our knowledge, the first reported value of D for ferrocene in this solvent medium. We were, however, unable to investigate Bu^n-ZDTP oxidation due to the presence of a solvent contaminant which was redox active at a similar potential to Bu^n-ZDTP.

We stress that this work has served as a preliminary investigation of Bu^n-ZDTP redox activity at elevated temperatures and in resistive solvents. A consideration of the future directions which this work can take is given in Chapter 10.

References

[1] C.R.C. Handbook of Chemistry and Physics (74th Edition), CRC Press, Cleveland, Ohio, USA, 8-55

[2] A. M. Bond, T. F. Mann, Electrochimica Acta, 1987, **32**, 6, 863

[3] J. H. Santos, A. M. Bond, J. Mocak, T. J. Cardwell, Anal. Chem., 1994, **66**, 1925

[4] K. B. Oldham, T. J. Cardwell, J. H. Santos, A. M. Bond, J. Electroanal. Chem., 1997, **430**, 39

[5] L. Geng, A. G. Ewing, J. C. Jernigan, R. W. Murray, Anal. Chem., 1986, **58**, 853

[6] L. Geng, R. W. Murray, Inorg. Chem., 1986, **25**, 3115

[7] C. Amatore, F. Pflüger, Organometallics, 1990, **9**, 2276

Chapter 10

Conclusions and future directions

10.1 Introduction

In this chapter we present a summary of the work undertaken during the course of this thesis and review the conclusions drawn in §10.2. Avenues open for further investigation are considered in §10.3. We conclude with a summary of the contributions of this thesis in §10.4.

10.2 Review

We began with a brief description of lubricant composition. A detailed review of ZDTP lubricant additives was presented including an account of anti-wear and anti-oxidant behaviour. It was noted that despite the long-standing inclusion of these types of additives in engine lubricant formulations, their mode of action is poorly defined. A summary of literature investigations pertaining to the study of ZDTPs was given as an illustration of the wide range of techniques which have been applied. We stressed that examples relating to the study of the electrochemical behaviour of ZDTPs were few. In addition, previous investigations suggest conflicting assignments of ZDTP redox activity. Through this we recognised the need for a more detailed study of ZDTP redox behaviour.

The application of voltammetric techniques as a tool in ZDTP analysis was then introduced. The importance of conducting such studies under conditions typical of a working engine environment was noted. Since we aimed to study Bu^n-ZDTP redox activity at elevated temperatures and in resistive solvent media, experimental requirements for voltammetry were discussed and an introduction to the literature related to voltammetric analysis under these conditions given.

An overview of electrochemical methods implemented during this thesis was presented in Chapter 2. The nature of electron transfer processes was introduced and a discussion of the mass transfer processes operative in an electrochemical cell given. The general requirements of a voltammetric investigation were illustrated. A detailed description of the theory behind and applications of the techniques used during this investigation, namely cyclic voltammetry, RDE voltammetry, chronoamperometry, microelectrode voltammetry and atomic force microscopy was then presented.

In Chapter 3, we described the experimental protocol for standard electrochemical techniques utilised during the course of this work. The source and purity of chemicals employed was given.

Chapter 4 described development of the elevated temperature microelectrode apparatus designed for use in conjunction with resistive solvent media. We recognised the need for :

1. Incorporation of microdisc electrodes into the design and minimisation of distance between working and reference electrodes as a means of overcoming ohmic distortion.
2. A robust structure at temperatures up to 200 ^{0}C.
3. Temperature stability and accuracy of the voltammetric unit whilst allowing for quick and easy temperature control.
4. A flow system to ensure a fresh supply of electrolytic solution was maintained to the electrode surface and to facilitate removal of waste products with delivery of electrolytic solution in a quantifiable and easily controlled manner.
5. A computer system for the control and measurement of voltammetric parameters.

A detailed description of apparatus design based on the above requirements was given as divided into the four main components of the unit, namely the heated voltammetric cell, temperature control system, flow system and computer control system. Experimental characterisation of the apparatus in terms of stability of the temperature control system, and the effects of flow on solution temperature stability and limiting current was described.

The potential of the novel variable temperature steady state approach was illustrated in Chapter 5. Application of the technique to a range of electrochemical problems was demonstrated. Areas in which application of the apparatus has significant advantages over previously applied techniques were highlighted. Studies of TMPD and TBPA oxidation yielded diffusion coefficients at elevated temperatures from which activation parameters for diffusion of each compound in solution were obtained. Variation of D with temperature was compared to predicted theory according to the Stokes-Einstein and Wilke-Chang relationships. Correlation of experimental results with both theories was linked to diffusional behaviour of each of these species according to a "slip" or "stick" type model.

Studies of oBNB and 9-ArCl reduction demonstrated the elevated temperature microelectrode apparatus as a viable method for the interrogation of rapid kinetic processes. Both compounds are reduced via an ECE mechanism where halide bond cleavage constitutes the chemical step. Since the use of a microelectrode permits the "outrunning" of electrode kinetics to gave an n_{eff} of less than two, rate constants for the halide bond cleavage process at varying temperatures were evaluated. Arrhenius plots were used to determine the energy and entropy of halide bond cleavage in both compounds. For oBNB in particular, this technique has allowed determination of parameters which to date have eluded analysis.

The nature of Bu^n-ZDTP redox activity under standard electrochemical conditions was thoroughly investigated in Chapter 6. The work described represents one of the first applications of electrochemical techniques to the study of ZDTP activity and certainly the most comprehensive. Cyclic voltammetry of Bu^n-ZDTP in DMF solution was described at two different electrode substrate materials, namely glassy carbon and platinum. Bu^n-ZDTP oxidation was observed to proceed via an irreversible electron transfer process at both electrode surface materials. Bu^n-ZDTP reduction at glassy carbon appeared as a single wave exhibiting the cross-over between forward and reverse scans characteristic of a nucleation controlled process. Stripping of zinc material from the electrode surface was apparent on scan reversal. Bu^n-ZDTP reduction on platinum was more complex with UPD of zinc material visible at potentials positive of bulk deposition. In addition, the platinum surface appeared more hostile to zinc nucleation in comparison to glassy carbon with nucleation only apparent at decreasing scan rates or at increased concentrations of Bu^n-ZDTP. An RDE voltammetric study of this complex at both glassy carbon and platinum electrodes was also described. Levich analysis of Bu^n-ZDTP oxidation at both electrode substrate materials was carried out. By correlation with Wilke-Chang theory, we deduced a 2 electron transfer process for the oxidation of Bu^n-ZDTP. A diffusion coefficient of 6.7×10^{-6} cm^2 s^{-1} at 25 ^0C was calculated. Work undertaken has demonstrated voltammetric techniques to be a promising method for studying redox activity of ZDTPs and will form the basis of future voltammetric work aimed at elucidating the redox behaviour of this compound under more typical engine conditions.

A more thorough investigation of the zinc nucleation process arising from Bu^n-ZDTP reduction via chronoamperometric techniques was described in Chapter 7.

Current-time responses at both glassy carbon and platinum electrode substrate materials indicated nucleation and growth of material to be under diffusion limited control. Transients plotted in dimensionless form were compared to a theoretical model describing growth of hemispherical nuclei under mass transport limited conditions. A close correlation between the experimental data and the theoretical response for a progressive nucleation mechanism was observed.

The potential of atomic force microscopy as a promising technique for the imaging of ZDTP filming action has been demonstrated in Chapter 8. Ex-situ atomic force microscopy of a glassy carbon electrode following reduction of $\mathrm{Bu^n}$-ZDTP under both cyclic and RDE voltammetric conditions revealed the presence of isolated zinc nuclei of varying sizes randomly distributed across the electrode surface. This is consistent with the progressive nucleation process deduced via chronoamperometry. Atomic force microscopy of a platinum electrode following reduction of $\mathrm{Bu^n}$-ZDTP illustrated the greater hostility of the platinum surface to zinc nucleation versus glassy carbon. The surface remained largely bare with only a small amount of nucleation at scratch lines visible.

Chapter 9 described initial attempts to introduce typical engine conditions to the voltammetric investigation of $\mathrm{Bu^n}$-ZDTP. Application of the novel elevated temperature microelectrode apparatus was illustrated. Steady state data was recorded for oxidation of $\mathrm{Bu^n}$-ZDTP at temperatures ranging between 21 and 80 ^{0}C. Application of this technique to $\mathrm{Bu^n}$-ZDTP reduction was less successful due to electrode fouling and oxygen contamination. We suggest that further modifications to our experimental design will be necessary to take account of these limitations.

Voltammetry in the resistive solvent toluene was attempted as a convenient model for oil. An initial study of ferrocene oxidation was made using microdisc electrodes of varying diameters. The diffusion coefficient of ferrocene in toluene was determined to be $1.74\mathrm{x}10^{-5}$ cm^2 s^{-1} at 25 ^{0}C. This represents the first value of D recorded for ferrocene in this solvent medium. We were unable to measure voltammetry of $\mathrm{Bu^n}$-ZDTP oxidation in toluene due to the presence of a contaminant species which was redox active at the potential of $\mathrm{Bu^n}$-ZDTP.

10.3 Future directions

We divide this section into two parts. We first consider possible extensions to the investigation of ZDTP redox activity in §10.3.1. We then consider refinements to the elevated temperature apparatus which will be necessary for the implementation of further ZDTP studies in §10.3.2.

10.3.1 Extension of ZDTP studies

We have reported a comprehensive investigation of Bu^n-ZDTP redox activity under standard electrochemical conditions. An extension to this work could take the form of voltammetric investigation of other ZDTP compounds including an assessment of the influence of the alkyl substituent on redox chemistry. An investigation could take the form of a comparison between aryl and alkyl ZDTPs, for example.

As an extension to the AFM work, we anticipate that this technique can be implemented for the examination of ZDTP films formed ex-situ under typical engine conditions, such as in a load bearing high pressure apparatus. Furthermore, development of the technique for the in-situ investigation of ZDTP reduction will form the basis of ultimately investigating redox reactions of ZDTP under more authentic engine conditions, such as in resistive media.

A natural extension of the work reported in this thesis would be a more comprehensive investigation of Bu^n-ZDTP redox activity at elevated temperatures and in resistive media. We first direct our attention to an extension of the work reported during this thesis in the resistive solvent toluene.

With the use of elevated temperatures, the ionic conductivity of a solution is substantially increased. Furthermore, at elevated temperatures enhanced electrolyte solubility will permit the use of increased electrolyte concentrations. For example, Bond et al report that at 50 ^{0}C enhanced electrolyte solubility permits the solution of 0.8 M $NHex_4ClO_4$. At such electrolyte concentrations, cyclic voltammetry of $Cu(dedtc)_2$ was possible using a 1 mm diameter platinum electrode [1]. Murray et al describe voltammetry of a 1 mM ferrocene solution using 0.7 M $NHex_4ClO_4$ as supporting electrolyte at 45 ^{0}C [2]. The enhanced ionic conductivity under these conditions permitted cyclic voltammetry of ferrocene at a 0.25 cm diameter platinum electrode. The reversible nature of the ferrocene wave was clearly apparent as evidenced by a reverse wave in the voltammogram obtained.

Given an increased supporting electrolyte concentration, a considerable increase in the concentration of electroactive substrate which can be used without associated ohmic distortion is possible. This approach should facilitate a more convenient experimental procedure. For example, the problem encountered during the investigation described in this thesis, namely the presence of a contaminant peak at the potential of Bu^n-ZDTP oxidation with peak current significant in terms of the 0.01 mM concentration of Bu^n-ZDTP utilised, can more readily be overcome. We anticipate that this approach can also be implemented in a study of Bu^n-ZDTP reduction.

We propose that our experimental procedure can be adapted for the investigation of Bu^n-ZDTP redox activity in oil. Farrington and Slater have described voltammetry in mineral oil by minimisation of the distance between working and reference electrodes [3]. A more detailed description of their experimental approach in the context of possible modification to the elevated temperature microelectrode apparatus is presented in §10.3.2.

We also consider future directions of the investigation of Bu^n-ZDTP voltammetry at elevated temperatures. Our investigation of Bu^n-ZDTP reduction was limited by electrode fouling and oxygen contamination. We propose apparatus modification as a means of addressing these limitations to be a natural extension of our investigation. Refinement of the apparatus is considered in detail in §10.3.2. Furthermore, our investigation of Bu^n-ZDTP redox activity was confined to temperatures ranging between 20 and 80 ^{0}C. We suggest that a more thorough investigation over a greater temperature range would be valid with the implementation of higher boiling point solvents, such as mineral oil.

10.3.2 Refinement of elevated temperature apparatus for the study of ZDTPs

In §9.2.3 we introduced the elevated temperature microelectrode apparatus to the study of Bu^n-ZDTP. We highlighted two areas which limited application of the apparatus to Bu^n-ZDTP reduction. Steady state waves appeared poorly-defined and irreproducible which we attributed to electrode fouling and incomplete removal of oxygen from the apparatus prior to the experiment. Modifications to the apparatus must necessarily take these factors into account if a study of Bu^n-ZDTP redox activity is to be successfully implemented at elevated temperatures. Possible improvements to apparatus design are now considered.

It is clear that if a modified elevated temperature apparatus is to be used with resistive solvents, microelectrodes must remain fundamental to experiment design. In addition, Farrington and Slater have recently described voltammetry in mineral oil with $LiClO_4$ as supporting electrolyte [3]. This was achieved using a 5 μm diameter gold microelectrode and minimisation of working/reference electrode separation to a distance of 5 μm via incorporation of a silver reference wire adjacent to the working electrode within a novel microelectrode assembly. Separation of electrodes in our current apparatus is 2 mm. Given that microelectrode wires must by necessity be encased in an insulating material, decreasing the separation between the two electrodes whilst they remain as separate constructions is problematic. We suggest that the electrode construction suggested by Farrington and Slater has laid the foundations toward a more useful approach to minimising working/reference electrode separation.

We now address the two major limitations of the current apparatus, namely electrode fouling and oxygen contamination. To alleviate electrode fouling, it would be an advantage for the apparatus to have the facility for electrode removal between scans to enable cleaning. To overcome oxygen contamination problems, we propose that a modified elevated temperature apparatus should incorporate a facility for in-situ degassing of the Bu^n-ZDTP solution inside the voltammetric cell.

With these two requirements in mind, we suggest that the voltammetric unit should take the form of a sealed cylinder with a removable lid. The lid should contain a gas inlet which could be attached to a needle like structure underneath the lid for direct input of gas into the solution. The lid should also have a hole for insertion of the working/reference electrode assembly. To provide a seal whilst facilitating removal of the electrode between scans, the hole should be tight-fitting to the electrode. A permanent counter electrode should be incorporated inside the unit structure. We anticipate that a flow system would not be necessary in this instance since the degassing procedure would ensure transport of fresh electrolytic solution to the electrode surface.

In order to achieve the rapid and easily controlled temperature applications of the previously employed system, a modified elevated temperature microelectrode apparatus should incorporate a similar heating system to that previously described. This comprised heating wire wrapped around the voltammetric cell controlled by a PID system with a platinum resistor as the temperature sensor. Insulation of the heated unit took the form of a double layer of 'Armiflax' pipe-lagging material. Incorporation of a computer system for the control of voltammetric parameters and acquisition of data identical to that implemented previously would be an advantage.

For work at increased temperatures, we propose that apparatus construction should take the form of a metal container. As for the elevated temperature microelectrode apparatus described in this thesis, testing of the apparatus would be necessary to ensure temperature stability at increased temperatures.

10.4 Major contributions of this thesis

The major contributions of this thesis are summarised as follows:

1. We have described development of a novel technique facilitating microelectrode studies at elevated temperatures.
2. The potential of this novel experimental approach for the study of electrochemical processes has been clearly demonstrated.
3. The most comprehensive voltammetric study to date of a ZDTP compound under standard electrochemical conditions has been presented.
4. We describe the first reported application of atomic force microscopy to the study of ZDTP compounds. The potential of this method as a promising technique for the study of ZDTP filming action has been demonstrated.
5. The concept of ZDTP voltammetry under conditions more representative of an engine environment has been introduced.

References

[1] J. H. Santos, A. M. Bond, J. Mocak, T. J. Cardwell, Anal. Chem., 1994, **66**, 1925

[2] L. Geng, A. G. Ewing, J. C. Jernigan, R. W. Murray, Anal. Chem., 1986, **58**, 853

[3] A. M. Farrington, J. M. Slater, The Analyst, 1997, **122**, 593

Appendix A

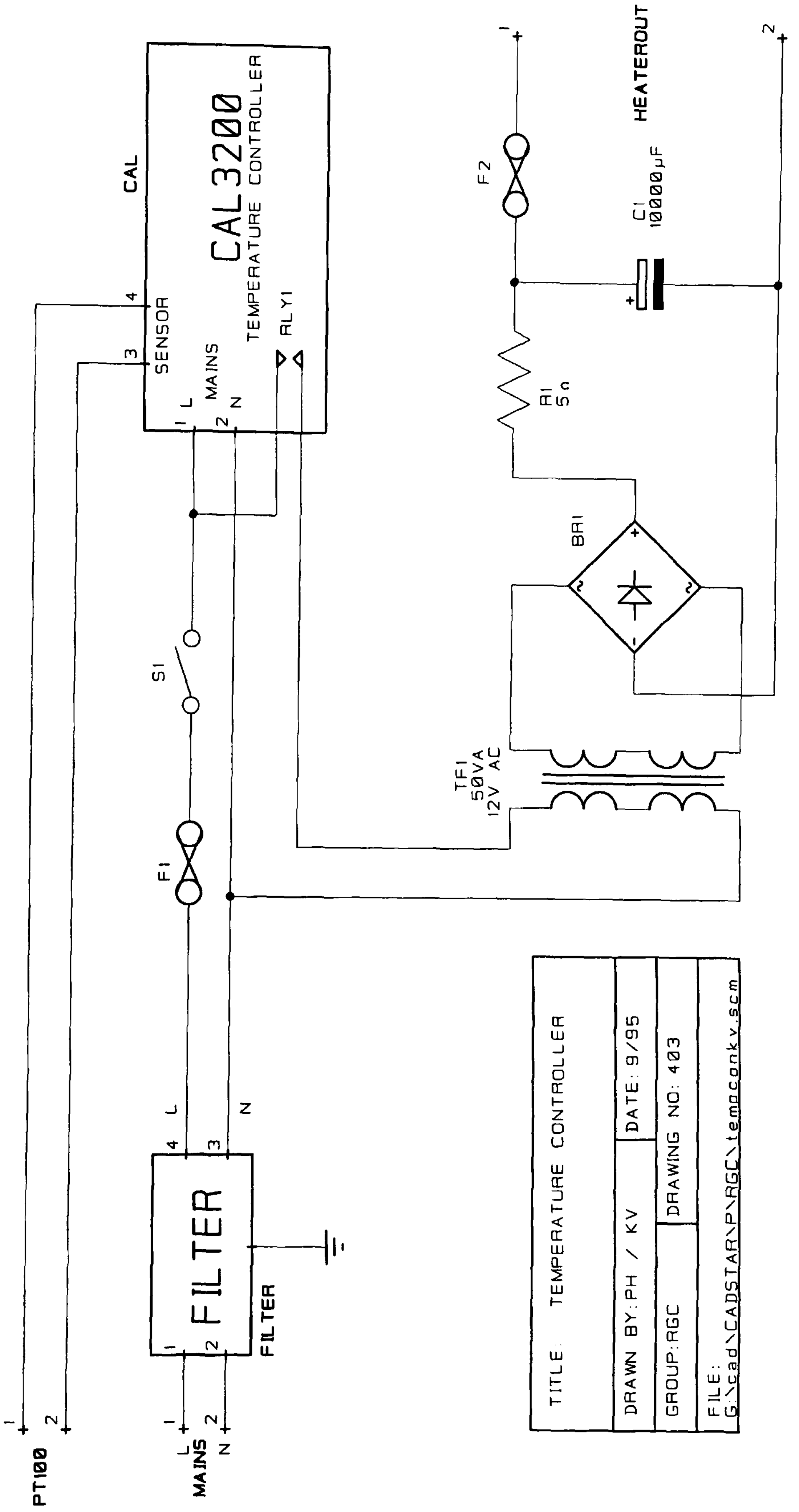
CAL
CAL3200
TEMPERATURE CONTROLLER
4
3
SENSOR
1 L
2 N
MAINS
RLY1
F2
1
2
HEATEROUT
C1
10000µF
+
R1
5Ω
BR1
S1
TF1
50VA
12V AC
F1
FILTER
FILTER
4 L
3 N
1
2
PT100
1
2
MAINS
L 1
N 2
TITLE: TEMPERATURE CONTROLLER
DRAWN BY: PH / KV
DATE: 9/95
GROUP: RGC
DRAWING NO: 403
FILE: G:\cad\CADSTAR\P\RGC\tempconkv.scm